Optimisation and integration of catalytic porous structures into structured reactors for CO conversion to methane

Simge Danaci

Communauté
UNIVERSITÉ Grenoble Alpes

THÈSE

Pour obtenir le grade de

DOCTEUR DE LA COMMUNAUTÉ UNIVERSITÉ GRENOBLE ALPES

Spécialité : MEP : Mécanique des fluides Energétique, Procédés

Arrêté ministériel : 25 mai 2016

Présentée par

Simge DANACI

Thèse dirigée par **Philippe MARTY**, Professeur, UGA

et codirigée par Dr. Lidia PROTASOVA
Ing. Alain BENGAOUER

préparée au sein du **Laboratoire VITO- Vlaamse Instelling voor Technologisch Onderzoek - Belgium, MAT** et **Laboratoire CEA Grenoble/DRT/LITEN/DTBH/SCTR/LER** dans **l'École Doctorale I-MEP2 - Ingénierie - Matériaux, Mécanique, Environnement, Energétique, Procédés, Production**

Optimisation et intégration de catalyseurs structurés en réacteurs structurés pour la conversion de CO_2 en méthane

Optimisation and integration of catalytic porous structures into structured reactors for CO_2 conversion to methane

Thèse soutenue publiquement le **19 octobre 2017**,
devant le jury composé de :

Monsieur Philippe MARTY
Professeur, Laboratoire LEGI, Université Grenoble Alpes, Directeur de thèse
Madame Anne-Cécile ROGER
Professeur des Universités, Université de Strasbourg, Président du jury
Monsieur Jorg THöMING
Professeur, Universität Bremen, Rapporteur
Monsieur Camille SOLLIEC
Maître-Assistant, IMT Atlantique France, Rapporteur
Madame Vesna MIDDELKOOP
Chargée de Recherche, VITO Belgique, Examinateur
Monsieur Alain BENGAOUER
Ingénieur de Recherche, CEA France, Co-Directeur de thèse
Madame Lidia PROTASOVA
Chargée de Recherche, ASML Netherlands, Co-Directeur de thèse

Science is the most reliable guide in life.

M.K. ATATURK

Acknowledgements

This collaborative PhD project was supported by Atomic and Alternative Energy Commission - CEA Liten in Grenoble, France and Flemish Institute for Technological Research – VITO in Mol, Belgium. This PhD has been a great experience in my life and it would not have been possible to do it without the support and guidance that I received from many people.

First of all, I would like to thank my academic promoter Prof. Philippe Marty for the supervision of my PhD. I will be always thankful to my mentors Eng. Alain Bengaouer and Dr. Lidia van Lent-Protasova and for their priceless guidance, sharing their experience all along. I would like to thank Alain for his wise guidance and mentoring. I would like to specially thank Lidia for sharing her expertise and continuous energetic motivation. I have experienced to combine the perspective of engineering and science on my study with contribution of both of you.

I would like to thank Dr. Eng. Jasper Van Noyen and Eng. Laurent Bedel for being startuppers of this project, also to Prof. Richard Guilet. I would like to thank Frederic Ducros, Mieke Quaghebeur and Pieter Vercaemst for giving me the opportunity to join this project and to work in their teams and laboratories with highly qualified engineers and researchers.

I would like to thank CEA methanation team members: Genevieve, Pierre, Julien, Georges, Albin, Benoit and Isabelle. I would like to thank especially my cheerful officemates Rasmey, Alban and Michel for their linguistic support but also for our lunch breaks, running and badminton. Without you guys nothing would be: *J`ai la patate*!

I would like to thank VITO material team members: Marijn, Myrjam, Annemie, Wim, Luc, Pieter, Jan, Mon, Dirk, Frans, Bart, Marijke, Elena, Joran, Angelika and Marleen for becoming my family in Belgium, for sharing their knowledge & experience, and for making VITO a very special place to me. I would like to thank Vesna & Steven for sharing their scientific knowledge and support all along. I especially thank my officemates Jasper, Judith and Pieter. I thank Igor - ‘plazmatic’ friend but also as a colleague during the PhD, for crazy scientific ideas shared at coffee breaks.

I also kindly express my gratitude to all jury members, Prof. Jorg Thöming, Prof. Anne-Cécile Roger and Dr. Camille Solliec.

I would like to thank all my friends and a specially thanks to Boeretang Kingdom members who became my lifelong friends. I also would like to thank you John, I send you my love for being with me and supporting me all the time with all of your patience. Finally, I would like to thank my family, Anne, Baba ve Övünç sizi çok seviyorum, for their love, endless support and encouragement during my PhD abroad.

Simge Danaci
Grenoble, August 2017

Optimization and integration of structured catalysts into structured reactor for CO_2 conversion

Abstract – In this doctoral study, the three dimensional fibre deposition (3DFD) technique has been applied to develop and manufacture advanced multi-channelled catalytic support structures. By using this technique, the material, the porosity, the shape and size of the channels and the thickness of the fibres can be controlled. The aim of this research is to investigate the possible benefits of 3D-designed structured supports for CO_2 methanation in terms of activity, selectivity and stability and the impact of specific properties introduced in the structural design of the supports.

Keywords: Methanation of CO_2, additive manufacturing, structured support, structured catalyst, structured reactor, coating.

Résumé – Dans cette étude de doctorat, la technique de dépôt tridimensionnel de fibres (3DFD) a été appliquée pour développer et fabriquer des structures de support catalytique multi-canaux avancées. En utilisant cette technique, le matériau, la porosité, la forme et la taille des canaux et l'épaisseur des fibres peuvent être contrôlées. L'objectif de cette recherche est d'étudier les performances des supports structurés 3D conçus pour la méthanation du CO_2 en termes d'activité, de sélectivité de stabilité et d'étudier l'impact des propriétés spécifiques introduites dans la conception structurale des supports.

Mots-clefs: Méthanation du CO_2, fabrication additive, réacteur structuré, catalyseur structuré, revêtement.

Table of Contents

Nomenclature

Latin

A	Arrhenius factor	-
a	Fibre thickness	m
C_p	Specific heat capacity	$J.kg^{-1}.K^{-1}$
c	Stacking factor	m
D_{tube}	Tube diameter	m
d_p	Particle diameter	m
E_A	Activation Energy	$J.mol^{-1}$
$F_{i,\ in}$	Flux of species i at inlet of the reactor	$mol.s^{-1}$
$F_{i,\ out}$	Flux of species i at outlet of the reactor	$mol.s^{-1}$
$G_{support}$	Weight of the structured support	kg
h	Time	$hours$
K	Permeability	m^2
k	Kinetic rate constant	-
L	Height of the sample	m
M	Axial centre difference between two fibres	m
m_{Ni}	Gram of nickel	kg
n	Inter-fibre distance	m
P	Pressure	$bars$
P_{CH4}	Methane productivity	$mmol.g_{cat.}^{-1}.h^{-1}$
Q	Power	W
R	Ideal gas constant	$8.314\ J.mol^{-1}.K^{-1}$
Re	Reynolds number	-
r	Rate of the reaction	$mol.m^{-3}s^{-1}$
S	Selectivity	$\%$
S_t	Top surface area of the sample	m^2
S_r	Rear surface area of the sample	m^2
s	Uncertainty	$\%$
T	Temperature	$°C$
T_1	Top surface temperature	K
T_2	Rear surface temperature	K
T_M	Max. temperature of the surface	K
t	Time	s
X	Conversion	$\%$
V	Fluid superficial velocity	$m.s^{-1}$
$V_{support}$	Volume of the structured support	cm^3
Y	Yield	$\%$
ΔG	Gibbs free energy	$kJ.mol^{-1}$
ΔH	Enthalpy change	$kJ.mol^{-1}$
ΔP	Pressure drop	Pa

Greek symbols

α	Thermal diffusivity	m^2s^{-1}
β	Forcheimer coefficient	
ε	Macro-porosity	$\%$
$\lambda_{SS\ 316L}$	316L Stainless steel thermal conductivity	$W.m^{-1}K^{-1}$
λ_{axial}	Axial ETC	$W.m^{-1}K^{-1}$
λ_{eff}	Effective thermal conductivity	$W.m^{-1}K^{-1}$
λ_{radial}	Radial ETC	$W.m^{-1}K^{-1}$
μ	Air dynamic viscosity	$Pa.s$
ρ	Density	$kg.m^{-3}$
ω	Dimensionless time	

Abbreviations

AM	Additive manufacturing
ASTM	American society for testing materials
BET	Brunauer–Emmett–Teller
CFD	Computational fluid dynamics
CNC	Computer numerical control
CNT	Carbon nanotube
CP	Coprecipitation
CS	Conventional sintering
DTGA-MS	Differential thermo-gravimetric analysis - mass spectroscopy
DME	Dimethyl ether
EASE	European association for storage of energy
EBM	Electron beam melting
ETC	Effective thermal conductivity, $Wm^{-1}K^{-1}$
FBR	Fluidized-bed reactor
FID	Flame ionization detector
FTS	Ficher-tropsch synthesis
GHSV	Gas hourly space velocity, h^{-1}
HEX	Heat exchanger
HMCR	Hybrid micro-channel reactor
IMP	Impregnation
IP	Impregnation-precipitation
LOHC	Liquid organic hydrogen carriers
LS	Laser sintering
MeOH	Methanol
MFC	Mass flow controller
MFEC	Micro-fibrous entrapped catalyst
MR	Microchannel reactor
MTO	Methanol-to-olefins
OCF	Open-cell foam
OFA	Open frontal area, *%*
OM	Optical microscopy
PEC	Pulse electric current
PtG	Power-to-gas
PBR	Packed-bed reactor
PI	Process intensification
PtL	Power-to-liquids
PVA	Poly-vinyl alcohol
RTD	Residence time distribution
RWGS	Reverse water-gas shift
R&D	Research and development
SEM	Scanning electron microscopy
SLS	Selective laser sintering
SLM	Selective laser melting
SNG	Synthetic natural gas
SPIRE	Sustainable process industry resource and energy Efficiency
SSA	Specific surface area, mm^{-1}
STP	Standard temperature and pressure
TCD	Thermal conductivity detector
TGA	Thermo-gravimetric analysis
TPR	Temperature-programmed reduction
XRD	X-ray diffraction
WGS	Water-gas shift
WHSV	Weight hourly space velocity, h^{-1}
3DFD	3-Dimensional Fibre Deposition

3D-Cu	3DFD manufactured copper
3D-SS	3DFD manufactured stainless steel

General introduction

The increase of CO_2 emissions into the atmosphere increases the effect of global warming. In the last decade, various strategies were proposed to reduce the carbon dioxide level in the atmosphere, e.g. the use of renewable energy sources, CO_2 storage and conversion. The increase use of intermittent renewable energy sources causes a power balance problem in the network. The Power-to-Gas (PtG) concept opens a route to the increasing use of renewable energy systems by linking the power and the gas network by converting the excess power into a gas or vice versa. Among catalytic reactions, catalytic CO_2 conversion to methane has become of crucial importance since it can offer a solution for Synthetic Natural Gas (SNG) production for storage or conversion to further valuable chemicals.

CO_2 conversion to methane, also called methanation reaction, is a highly exothermic reaction. The reaction is thermodynamically favoured at low temperatures and high pressures. The reaction kinetics is favoured at high temperatures, however, it is necessary to control the catalyst temperature to prevent catalyst deactivation. In recent years, it was proved that the advanced temperature control could be achieved by using structured reactors and catalysts such as monoliths, foams, channelled plates etc. The aim of this thesis is the implementation of innovative additive manufactured catalytic supports into chemical reactors. 3D-structured catalysts were integrated into a tubular reactor, and CO_2 methanation reaction tests were performed at lab- and pilot scales.

The thesis consists of 5 chapters. Chapter 1 presents the motivation of this study and a review of methanation catalysts and processes. Chapter 2 is dedicated to the optimization of coating suspensions for the coating of structured supports and CO_2 methanation tests on 3D-structured catalysts made of different architectures. Chapter 3 is devoted to the study of 3D-supports and their heat transport and hydrodynamic properties. Chapters 4 is dedicated to the manufacture of copper supports and CO_2 methanation experiments with 3D-structured catalysts in a laboratory scale reactor. Chapter 5 presents the CO_2 methanation experimental results with 3D-structured catalysts in a pilot-scale reactor. The lab- and pilot-scale experimental results are compared and discussed, some recommendations for further works are finally presented. The details of the chapters are as follows:

In **Chapter 1**, an overview of the recent developments of structured reactors with several processing routes and their limitations are given. Structured reactors and catalysts such as monoliths, foams, channelled plates etc. are reviewed. The reactors are classified according to the basic design of the support. Several other aspects are highlighted, i.e. CO_2 methanation reaction mechanisms, catalysts and their deactivation, industrial processes. A special attention is paid to additive manufacturing technologies and coating processes for the manufacture of the structured catalysts.

Chapter 2 is devoted to the study of CO_2 methanation reaction using 3D-manufactured stainless steel structures post-coated with Ni/Al_2O_3 catalyst. The results were benchmarked with the conventional Ni/Al_2O_3 powder catalyst which was prepared by impregnation and characterized by several

physico-chemical techniques. Catalytic structures were tested in a lab-scale tubular reactor in CO_2 methanation reaction. This study showed the effect of the coating suspension composition on the properties of catalytic coatings, as well as how CO_2 conversion, methane selectivity and catalyst stability are affected by the architecture of the structured catalyst.

In **Chapter 3**, since the heat transfer and pressure drop are main limitations in the case of conventional packed bed reactors, heat transport and pressure drop properties of 3D-manufactured stainless steel structures are described based on experimental and modelling data. The effective thermal conductivity was determined by diffusimetry over the solid matrix. The pressure drop was measured by a manometer using air as a fluid gas. The effect of unit cell geometry (fibre stacking) and coating thickness on pressure drop was studied experimentally. The effect of geometry (architecture of the structure, fibre diameter and macro-porosity) on the effective thermal conductivity was experimentally determined and compared to modelling results.

In **Chapter 4**, copper 3D-structures were manufactured and tested in CO_2 methanation conditions. The influence of the sintering temperature, atmosphere and technique (pulsed electrical current sintering *vs* conventional furnace sintering) on the properties of copper structures was investigated. The microstructural evolution of the support was analysed by low-temperature N_2 adsorption, SEM, OM and XRD. Adhesion strength of the Ni/Al_2O_3 catalytic coating on copper supports was benchmarked with stainless steel supports. Both coated structured supports and conventional packed-bed catalyst were examined in CO_2 conversion to methane.

Chapter 5 presents the study of structured catalysts in a pilot-scale tubular reactor for CO_2 methanation. 12 wt.%Ni/Al_2O_3 catalysts were synthesized by conventional impregnation method using two different alumina powders. Catalysts were characterized by N_2 adsorption, XRD, XPS, TPR and TGA. Lab- and pilot scale experiments were performed, and the results were compared by means of methane productivity. Stability test was performed during 80 h time-on-stream with pure reactants under pressure of 15 bars on pilot scale.

Chapter 1

Catalytic porous structures and structured reactors for CO_2 methanation: a review

In the last decades, increasing CO_2 levels in the atmosphere have contributed to an increase of the greenhouse effect. The utilization of lower carbon intensive energy sources such as wind and solar energy is essential. Unfortunately, these energy sources are intermittent and therefore the PtG concept was proposed to store excess energy, as a balancing link between the power and the gas networks. PtG uses renewable energy sources to produce hydrogen via electrolysis or for the conversion of further valuable fuels and chemicals for storage in the gas grid. Among catalytic reactions, CO_2 conversion to methane has become important since it can offer a solution for SNG production for storage or conversion. Temperature control is the main issue of the methanation process. In recent years, it was proved that the advanced temperature control could be achieved by using structured reactors and catalysts such as monoliths, foams, channelled plates etc. Chapter 1 presents an overview of the industrial methanation reactors. The reactors are classified according to their design. Reaction mechanisms for methanation reaction, methanation catalysts and their deactivation are also described. Special attention is paid to the structured catalysts. Innovative additive manufacturing technologies and coating processes for the manufacture of the supports and catalysts are presented.

1.1. Introduction

Carbon dioxide is the main contributor to the greenhouse effect. Before the industrial revolution in the 19th century, global average atmospheric CO_2 concentration was about 280 ppm, today it is determined to be above 400 ppm due to increasing human activities (transportation, industry, electricity etc.) [1]. Over the last decades, several ways have been investigated in order to decrease CO_2 levels in the atmosphere: (a) using low carbon intensive energy sources, (b) storage of CO_2 known as CCS (Carbon Capture and Storage), (c) conversion of CO_2 known as CCU (Carbon Capture and Usage).

In recent years, renewable energy sources for generating electricity, e.g. the wind and solar energy, have become more important. It was reported that the share of low carbon intensive energy sources producing electricity was estimated to increase to nearly 80 % in 2030 [2]. However, with the increasing use of intermittent renewable energy sources, fluctuation in the electricity grid is becoming a major issue. In this case, PtG technology provides a solution to long-term energy storage and long-distance energy transportation.

A power-to-gas plant consists of water electrolysis units and conversion installations. A general view of the PtG concept is shown in Figure 1-1. This concept was proposed to use renewable energy sources to produce hydrogen via electrolysis for storage into the gas grid or conversion to further chemicals. It is notewrothy that the potential storage capacity of hydrogen in the gas infrastructure is significantly lower than the total storage capacity of methane. Thus, only a limited amount of H_2 can be stored in the gas grid due to its lower density in comparison with other fuels. Due to this limitation, the methanation process is currently more promoted. Methane has 3.5 times higher volumetric energy than hydrogen and can be injected much easier into the gas grid. Therefore, it can be stored in a gas network without any limitations or used for heating, as a fuel for transportation and for the production of more valuable chemicals, e.g. MeOH, dimethyl ether (DME), Fischer-Tropsch products or electricity generation (Gas-to-Power).

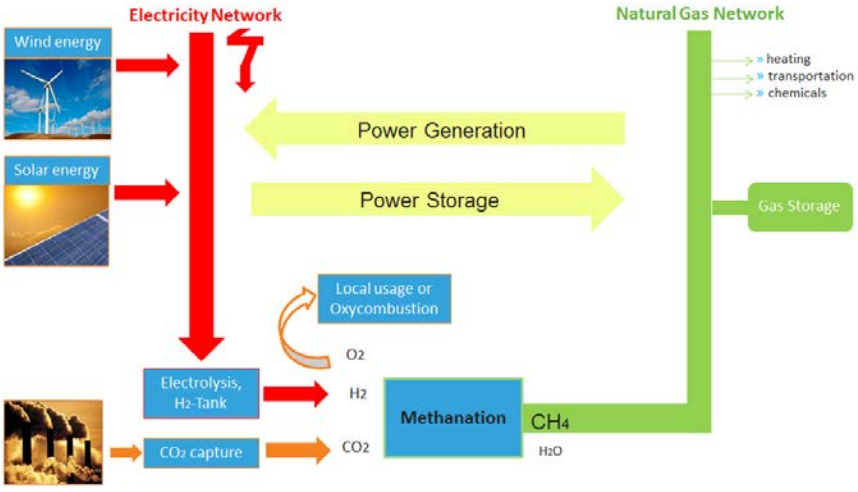

Figure 1-1. Diagram of the power-to-gas approach.

The first idea of combining water electrolysis with gas-fired power plants for storing renewable electricity was proposed in 1991 by Dunbar *et al.* [3]. Hashimoto *et al.* had proposed a global CO_2 recycling using sea water and built a pilot plant in Japan in 2003 [4]. In 2004, the installation of the Utsira full-scale combined wind power and hydrogen plant in Norway was completed [5]. In recent years, several PtG pilot plants have been reported in the press, mass media and literature which are being planned or have already been built worldwide. In the case of methane production, several ongoing projects have been identified mainly in Europe: Germany (7), France (1), Netherlands (1), Austria (1), Italy (1) [6,7] but also in the USA and Canada [8]. One of the planned PtG platform is the Jupiter 1000 project where the installations will be built at the *Fos sur Mer* harbour nearby Marseille in France in 2020 [9]. The R&D and reactor technology will be provided by CEA Liten, Grenoble. An intensified reactor will be used for the methanation process, in which CO_2 from industrial flue gas will be employed, and the produced methane will be injected into the natural gas grid.

The catalytic hydrogenation of carbon dioxide to methane is a well-known catalytic process ($\Delta H_{298K} = -165\ \mathrm{kJ/mol}$). This reaction is usually operated under high pressures and temperatures between 250 and 500°C. So far, catalytic methanation has been widely investigated in fixed-bed and fluidised-bed reactors with conventional catalytic materials [10]. For exothermic reactions, the heat removal in a fixed-bed reactor is difficult, so hot spots are often encountered. These hot-spots can lead to the catalyst deactivation due to the thermal sintering and carbon deposition. Moreover, fixed-bed reactors packed with conventional catalysts show high pressure drops related to both catalyst particle size/shape and packing of the catalytic bed [11]. To overcome the mentioned limitations mainly the temperature regulation due to the exothermicity of the reaction and pressure drop, improvements of the design and configuration of catalysts/reactors are crucial.

Above-mentioned limitations can be overcome by using structured reactors and catalysts. For example, intensified milli- and micro-channel reactors were successfully implemented for CO_2 methanation [12,13]. In recent years, the use of metal based structured catalysts such as metallic plates [14], foils [15,16], micro-fibrous materials [17], monoliths [18] and foams [19,20] attracted a lot of attention due to their higher heat transfer properties. However, these structured catalysts and micro-reactors have limitations such as low catalyst loading, high manufacturing price, scale-up challenges etc.

It has to be mentioned that a number of studies related to methanation reactions were reported in recent years. However, most of the studies are focused on CO methanation. This is because of the high accessibility of syngas ($CO+H_2$) in industry due to the historical development of coal to gas processes and more recently investigations on biomass and waste gasification processes. In this chapter, the fundamentals of CO_2 methanation reactions were explored. Industrial methanation reactors are reviewed and the current state of methanation technology is summarised by reviewing the

recent developments of heat transfer improved structured reactors. Catalysts and catalyst deactivation phenomena were presented. We also paid attention on the innovative structured reactors made by additive manufacturing techniques.

1.2. Fundamentals: Carbon Dioxide Methanation

This section presents the theoretical background of the methanation reaction and proposed mechanisms. Fundamental studies on thermodynamic equilibrium, kinetics, catalysts and catalysts deactivation are highlighted.

1.2.1. Thermodynamics

The methanation reaction, also called Sabatier reaction, was discovered by the French chemist Paul Sabatier in the 1910s [23]. The catalytic hydrogenation of carbon dioxide to methane and water is a thermodynamically favourable process at low temperature and high pressure. The methanation reaction is highly exothermic and the Gibbs free energy is negative depending on the temperature (ΔG_{298K} = -113.5 kJ·mol^{-1}, 1 atm). CO_2 methanation is a reversible reaction, and the reverse reaction is called 'methane steam reforming'.

$$CO_2 + 4H_2 \leftrightarrow CH_4 + 2H_2O \qquad \Delta H_{298K} = -165\ kJ \cdot mol^{-1} \tag{1-1}$$

Besides the methanation reaction, the hydrogenation of carbon monoxide and reverse water-gas shift (rWGS) reactions can take place.

$$CO + 3H_2 \leftrightarrow CH_4 + H_2O \qquad \Delta H_{298\,K} = -206\ kJ \cdot mol^{-1} \tag{1-2}$$

$$CO_2 + H_2 \leftrightarrow CO + H_2O \qquad \Delta H_{298\,K} = 41\ kJ \cdot mol^{-1} \tag{1-3}$$

Figure 1-2 shows the CO_2 conversion versus temperature at the thermodynamic equilibrium for the pure feed gas with the following composition: H_2:CO_2=4:1 (CO_2, CO, H_2, CH_4 and H_2O at 1-10 bars). Conversion of CO_2 and CH_4 selectivity were calculated according to the equations 1-4 and 1-5. The methanation reaction temperature usually ranges between 250 and 500°C. According to Le Chatelier's principle, low temperatures and high pressures shift the equilibrium to the product side. The highest yield and the highest methane selectivity are obtained at relatively low temperatures and high pressures. As it can be seen in Figure 1-2, obtaining CO_2 conversion higher than 95 % at atmospheric pressure requires reaction temperatures below 290°C. When the pressure increases from 1 to 10 bars at 290°C, the conversion increases from 95.5 % to 98.1 %. With increasing temperature, the Gibbs free energy increases rapidly, and at >500°C becomes positive and the reaction path changes to methane reforming. Therefore, the increase of the temperature reduces the conversion rate. Gao *et al.* reported that H_2:CO_2 ratio has a remarkable effect on CO_2 conversion and CH_4 selectivity. High H_2:CO_2 ratio leads to high CO_2 conversion and CH_4 selectivity at pressures of 1 to 30 bars [24].

$$X_{CO_2} = \frac{F_{CO_{2in}} - F_{CO_{2outlet}}}{F_{CO_{2in}}} \quad (1\text{-}4)$$

$$S_{CH_4} = \frac{F_{CH_{4outlet}}}{F_{CO_{2in}} - F_{CO_{2outlet}}} \quad (1\text{-}5)$$

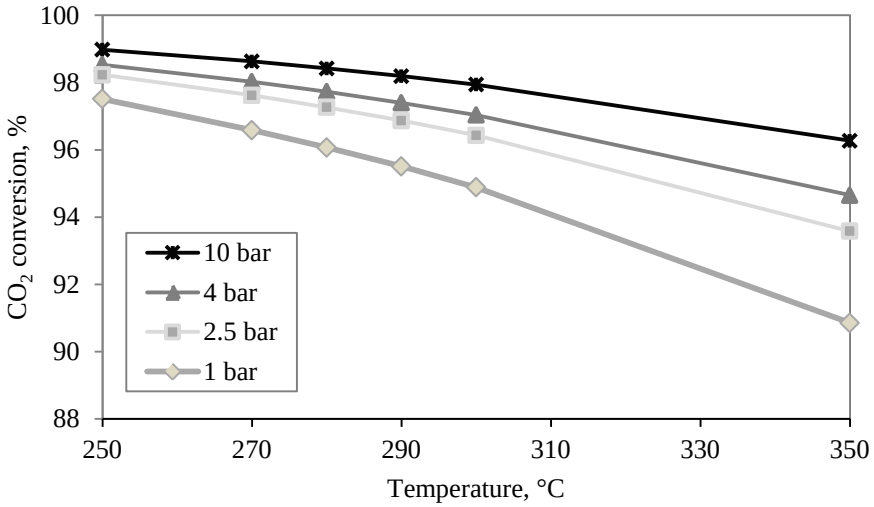

Figure 1-2. Thermodynamic equilibrium of CO_2 conversion.

Carbon monoxide plays an important role in CO_2 methanation. The thermodynamics of CO_2 conversion in the presence of CO are confirmed by the experiments of Beus *et al.* with Rh/γ-Al_2O_3 catalyst [25]. Results showed that when CO_2 was fed with a small amount of CO, the methanation of CO was favoured. The presence of CO has an inhibitive effect on the CO_2 methanation. In the case of pure CO_2 methanation, CO formation becomes significant at temperatures above 500°C. From a thermodynamic point of view, in order to gain a better CH_4 yield, side reactions such as rWGS (equation 1-3) can be avoided by choosing the reaction conditions such as temperature, H_2:CO_2 ratio and more selective catalysts.

1.2.2. Kinetics

The proposed reaction mechanisms for CO_2 methanation fall into two main categories. The first one involves the conversion of CO_2 to CO, and the subsequent reactions follow the same mechanism as for CO methanation. The other one involves direct hydrogenation of CO_2 to methane without the formation of CO as an intermediate. It is noteworthy that even for CO methanation, there is still no agreement on the kinetics and mechanism. Koschany *et al*. summarised proposed kinetic models since 1950s [26]. Due to the economic feasibility, methanation reaction is mainly studied using nickel based catalysts. An overview of kinetic models for CO_2 methanation over nickel based catalysts is given in Table 1-1. In equation 1-6, k is the kinetic rate constant, E_A is the activation energy, R is the gas constant, T is the temperature.

$$k = A\ exp\ (-\frac{E_A}{RT}) \quad (1\text{-}6)$$

According to the Arrhenius law, rate constant *k* is directly linked with the temperature. Besides of the temperature, kinetics depend on many other parameters such as nature of the nature, dispersion and size of the active material of the catalyst, oxide support etc. Reaction rates (equation 1-7) are generally formulated as:

$$r\ = \frac{(kinetic\ factor,\ \ k) * (driving\ force)}{(adsorption\ term)} \quad (1\text{-}7)$$

Table 1-1. Overview of kinetic models for methanation on nickel based catalysts [26].

Catalyst (Ni wt.%)	T (°C)	P_{max} (bars)	Rate equation	EA (kJ/mol)	Ref
Ni/SiO_2 (60)	280-400	30	$r_{CH_4} = \frac{kP_{co2}P_{H_2}^4}{(1+K_{H_2}P_{H_2}+K_{CO_2}P_{CO_2})^5}$	55-58	[27]
Ni/Al_2O_3 (28)	200-230	1	$r_{CH_4} = \frac{kP_{co2}}{(1+A_{CO_2}+P_{co2})}$	106	[28]
Ni/SiO_2 (3)	227-327	1.4	$r_{CH_4} = \frac{kP_{co_2}^{0.5}P_{H_2}^{0.5}}{(1+K_1P_{co_2}^{0.5}P_{H_2}^{0.5}+K_2P_{co_2}^{0.5}P_{H_2}^{0.5}+K_3P_{co})^2}$	94	[29]
Ni/SiO_2 (58)	275-320	17	$r_{CH_4} = kP_{co_2}^{0.66}P_{H_2}^{0.21}$ $r_{CH_4} = \frac{kP_{CO_2}P_{H_2}}{(1+K_{H_2}P_{H_2}+K_{CO_2}P_{CO_2})}$	61 19	[30]
Ni	250-350	-	$r_{CH_4} = \frac{kP_{H_2}P_{CO_2}^{1/3}}{1+K_{CO_2}P_{CO_2}+K_{H_2}P_{H_2}+K_{H_2O}P_{H_2O})}$	-	[31]
$Ni/La_2O_3/Al_2O_3$ (17)	240-320	1	$r_{CH_4} = \frac{kP_{H_2}^{1/2}P_{CO_2}^{1/3}}{(1+K_{H_2}P_{H_2}^{1/2}+K_{CO_2}P_{co_2}^{1/2}+K_{H_2O}P_{H_2O})^2}$	72.5	[32]
$Ni/MgAl_2O_4$ (15)	300-400	10	$r_1 = \frac{k_1}{P_{H2}^{2.5}}P_{CH4}P_{H2O} - \frac{P_{H2}^3P_{CO}}{K_1}\ DEN^2$ $r_2 = \frac{k_2}{P_{H2}}P_{Co}P_{H2O} - \frac{P_{H2}P_{CO2}}{K_2}\ DEN^2$ $r_3 = \frac{k_3}{P_{H2}^{3.5}}P_{CH4}P_{H2O}^2 - \frac{P_{H2}^4P_{CO2}}{K_3}\ DEN^2$ $DEN = 1+K_{CO}P_{CO}+K_{H2}P_{H2}+K_{CH4}P_{CH4}+K_{H2O}P_{H2O}P_{H2}$	240.1 67.13 243.9	[33]

The main detailed kinetic investigations and models were developed by Weatherbee & Bartholomew and Xu & Froment [29,33]. A kinetic model of the rate determining step was proposed by Weatherbee and Bartholomew in 1982 [29] on Ni/SiO_2 catalysts at highly diluted gas mixture. The rate of CO_2 methanation was measured as a function of pressure (1.4 bars), temperature (227-327°C) and reactant concentration (space velocities between 9 000 and 30 000 h^{-1}). Dilution gas (N_2) was used to minimize the heat and mass transfer limitations. It was proposed that both CO and CO_2 methanation reactions follow similar paths with different rate determining steps. It was found that even a ppm level

of CO could inhibit the CO_2 methanation due to the slower adsorption rate of CO_2 on the catalyst surface. However, relatively low partial pressure of reactant gases which was considered in the model is away from the implementation of methanation process in SNG industry. Further kinetic model on steam reforming, CO_2 methanation and WGS on 15 % $Ni/MgAl_2O_4$ catalyst was proposed by Xu and Froment in 1989 [33]. Eleven probable reactions were proposed, however only three of them play a substantial role, i.e. CO methanation (I), rWGS (II) and CO_2 methanation (III). This model was proposed for temperatures between 300 and 400°C (Figure 1-3). The activation energies of the CO methanation, rWGS and CO_2 methanation reactions were determined as EA_1 = 240.1, EA_2 = 67.13 and EA_3 = 243.9 $KJ.mol^{-1}$. Reactions were performed at pressures of 3-10 bars without dilution gas which was closer to the industrial implementation of CO_2 methanation.

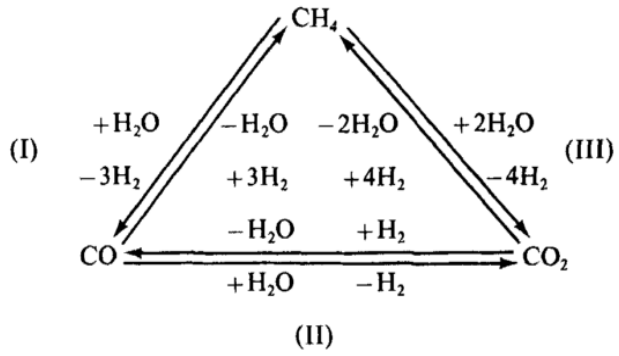

Figure 1-3. Kinetic model proposed by Xu and Froment [33].

A reaction mechanism for the CO_2 methanation on 2% Ru/TiO_2 catalyst at 383K was proposed by Marwood *et al.* in 1997 [34]. The proposed mechanism is given in Figure 1-4. The methanation reaction rate is reported to be inhibited by water. Therefore, a water trap was needed at the inlet of the reactor. Methanation of CO_2 is inhibited by CO as described by Weatherbee *et al*. In contrary, Beuls *et al.* [25] reported that low amount of oxygen has a positive effect on the CO_2 methanation on $Rh/\gamma\text{-}Al_2O_3$ catalyst. Recently, Koschany *et al.* defined a model for CO_2 methanation with non-diluted H_2/CO_2 reactants in 2016. The comparison of the kinetic predictions is shown in Figure 1-5.

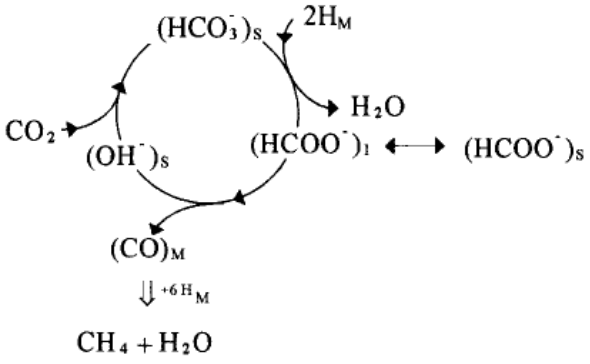

Figure 1-4. Reaction mechanism of CO_2 methanation proposed by Marwood *et al.* [34].

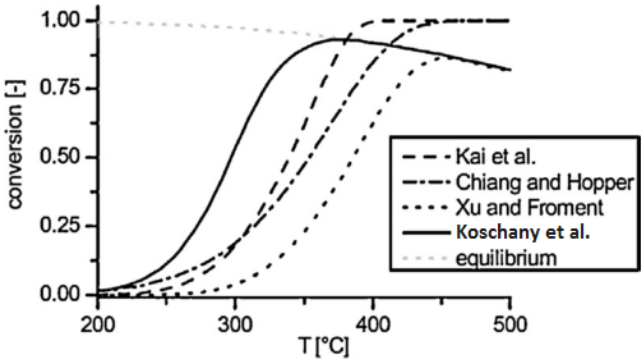

Figure 1-5. Comparison of the kinetic predictions in literature [26].

1.2.3. Catalysts

The catalysts for the methanation reaction are prepared by various methods such as impregnation (IMP) [35–37], co-precipitation (CP) [38,39], impregnation-precipitation (IP) [40], sol-gel [41–43] etc. However, the most commonly used preparation technique is the impregnation due to its simplicity. The 3 main steps of impregnation can be summarised as follows: the first step is the contact between the support (Al_2O_3, SiO_2, CeO_2 etc.) and the impregnating solution (water or organic solvent based) of precursors (metal nitrate, sulphate, acetate etc.). The second step is separation of the impregnated catalyst from the solution and drying (freeze drying, evaporation etc.). The final step is the thermal treatment (calcination) followed by the catalyst reduction or other appropriate activating treatment. The general scheme of the impregnation procedure steps is given in Figure 1-6.

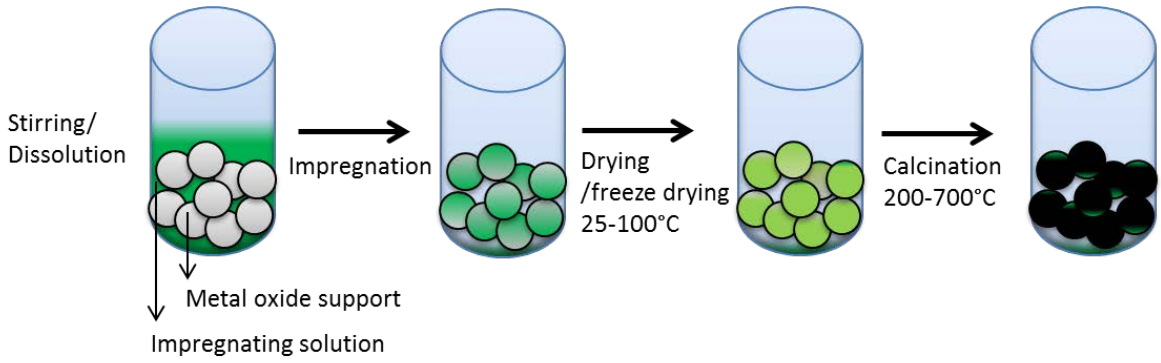

Figure 1-6. General steps in catalyst synthesis via impregnation method.

Conventional catalysts that are mostly used in packed-bed reactors have different shapes. Final shape of the catalyst can be as follows: irregular granules, spheres, pellets, cylindrical, cubic or rings depending on the manufacturing procedure and application. Catalyst spheres can be made by aging liquid droplets (200-2500 µm) or by spray-drying technique (<500 µm), pellets are manufactured mostly by pressing (tableting), extrudes are made by extrusion of the paste through a nozzle with given size and shape.

The group of VIII, IX, X and XI transition metals have been widely investigated for CO_2 methanation. Previous studies showed that ruthenium catalysts supported on Al_2O_3 are highly selective towards methane in CO_2 methanation [44]. However, nickel-based catalysts are the most widely studied for the methanation reaction due to their high activity and competitive cost. Typical nickel loading in Ni-containing catalysts ranges from 1 to 20 wt.%. A study published in 2003 showed that high Ni loading (up to 20 wt.%) enhanced the activity and selectivity of the catalyst (Figure 1-7). However, further increase of Ni content leads to the decrease of the activity and gives no more improvement to the methane yield [45]. In another study, the influence of Ni loading (10 to 25 wt.%) on CO_2 conversion and CH_4 selectivity was investigated on Ni/Al_2O_3 catalysts. The results revealed that the catalyst with 20 wt.% Ni possessed high activity and stability in CO_2 methanation [46].

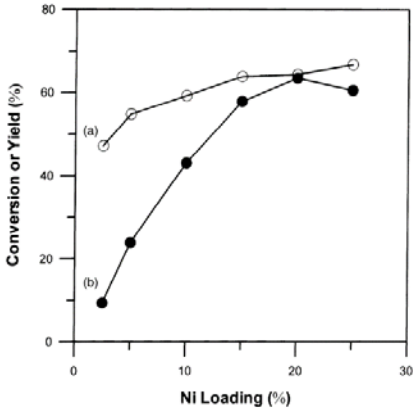

Figure 1-7. Effect of nickel loading on CO_2 conversion (a) and CH_4 yield (b) for CO_2 hydrogenation on Ni/RHA-Al_2O_3 catalysts [35].

Nature of the catalytic support (Al_2O_3, SiO_2, CeO_2, ZrO_2, TiO_2, activated carbon, zeolite etc.) plays a crucial role in the metal-support interactions. For example, it was reported for CO_2 methanation that the addition of 2 wt.% CeO_2 to Al_2O_3 support has a significant effect on the interactions between Ni and Al_2O_3, leading to an excellent catalytic performance and low carbon deposition [47]. It was shown that more intimate interactions between active metals and support materials resulted in higher catalytic activity [48–50]. Furthermore, active oxygen sites (oxygen vacancies) in support materials can interact with active metals to improve the performances of the catalysts as well [51]. It was reported that 10 %Ni/La_2O_3 catalysts exhibited excellent performance for CO_2 methanation and gave a high yield of methane even at low temperatures (< 350°C) due to the strongly bonded NiO to La_2O_3 support. Under the same reaction conditions, the 10 %Ni/γ-Al_2O_3 catalyst gave lower activity [52]. The formation of active sites due to interactions between Ni and La_2O_3 on the surface was proposed as a possible reason for the excellent catalytic performance of 10 %Ni/La_2O_3 catalysts. Another study showed that at the temperatures <350°C, Ru/SiO_2 gave higher CO conversion and higher selectivity than Ru/Al_2O_3 catalyst [16]. Recently, nickel and cerium supported on multi-walled carbon nanotubes (CNTs) were investigated in CO_2 methanation and compared to the conventional Ni/Al_2O_3 catalyst by Wang *et al.* [53]. CNTs supported catalysts

exhibited ca. 20 % higher CO_2 conversion than Al_2O_3 supported catalysts at 400°C. H_2-TPR analysis showed that CNTs supported catalysts had more active sites than Al_2O_3 supported ones.

During the last decades, bimetallic catalysts were investigated for methanation reactions. Conversion of CO_2 on 0.5wt.% Rh and Ru loaded on Ni–$Ce_xZr_{1-x}O_2$ (Ni-CZ) was studied by Ocampo *et al.* Results showed that bimetallic Ni-Rh-CZ and Ni-Ru-CZ catalysts exhibited higher conversion than Ni-CZ at low temperatures (250-300°C) [42]. Mono- and bimetallic (Ni–Fe/Al_2O_3) catalysts were tested for CO_2 methanation as well as for simultaneous CO and CO_2 methanation. It has been shown that the conversion of CO_2 to methane significantly increased on the bimetallic Ni-Fe alloy catalysts compared to the pure nickel catalyst [48].

Few papers reported about CO_2/H_2 methanation using trimetallic catalysts. It was found by Zamani et al. that the addition of Cu, Mn and Ru to Mn/Cu–Al_2O_3 catalyst would assist the catalyst stability during the reaction [54]. A similar study showed that presence of zirconia in Ni/ZrO_2-Al_2O_3 catalyst is beneficial for improving the catalytic activity and stability [55].

Besides the effect of active metal and metal oxides, it was observed that conversion of CO_2 and the yield of CH_4 are strongly dependent on catalyst calcination and reduction temperatures. Calcination is needed for the formation and interaction of active species and decomposition/removal of additives, e.g. thermal decomposition of $Ni(NO_3)_2 \cdot 6H_2O$ takes place at ca. 300°C [56]. CO_2 methanation on Pd/Ru/Ni(2:8:90)/Al_2O_3 catalyst calcined at different temperatures (300, 400, 500, 700 and 1000°C) was reported [57]. The highest CO_2 conversion of 43.6 % was obtained on the catalyst calcined at 400°C. Increasing calcination temperature can lead to a decrease of the surface area and consequently lower nickel dispersion, resulting in a negative effect on catalytic performance [46]. The reduction of NiO to Ni on methanation catalysts usually takes place in a hydrogen atmosphere at temperatures of 300 to 600°C. A TPR analysis provides information about hydrogen consumption at different temperatures and thus can indicate the suitable reduction temperature. Reduction temperature increases with increasing interaction (between active metal and metal oxide support and decreasing metal (Ni, Ru etc.) loading [58].

1.2.4. Catalyst deactivation

Catalyst deactivation is a loss of catalytic activity during the reaction. Deactivation is commonly divided into four categories: poisoning, coking/fouling, phase transformation and sintering [59]. The main reasons for catalyst deactivation during the methanation reaction are sintering and coking.

Poisoning is the activity loss due to the chemisorption of components from the feed stream on active sites of catalysts [60]. Sulphur and sulphur containing components are known as poison for nickel catalysts used for methanation reactions. It was confirmed that there is a rapid adsorption of

sulphur onto the nickel surface. In the presence of impurities (H_2S, other sulphur containing components and NO_2), conversion of CO_2 to CH_4 is influenced negatively due to the poisoning and blocking the active sites of the catalyst. Therefore, high purity of CO_2 is needed for the efficient CO_2 methanation [61]. Typical requirements for H_2S contaminant concentration in syngas methanation is ca. 1ppm [62]. Thus, the feed gas used for methanation process must be cleaned upstream of the methanation reactor(s). An effect of O_2, NO_2 and SO_2 impurities on methanation on Ni-based catalyst was reported by Müller *et al.* [63]. The CO_2 conversion decreased in the presence of oxygen, but selectivity to methane remains high. In the case of NO_2, no significant effect on selectivity was observed. Figure 1-8 shows a catalytic performance as a function of time with SO_2 contaminated (516 ppm) gas flow. The conversion dropped by 17 % in 12.5 h due to the strong bonding of sulphur on nickel sites.

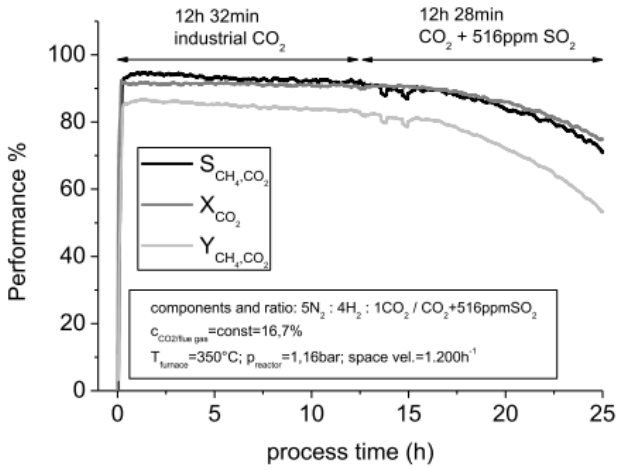

Figure 1-8. CO_2 (with SO_2 impurity) methanation on Ni-based catalyst versus time [63].

Coke and carbon formations decrease the activity of the catalysts by blocking active sites, encapsulating metal particles, plugging of micro- and meso-pores, and building-up carbon filaments that could destroy the catalytic support [64]. In the case of fixed-bed reactors, the presence of higher hydrocarbons is also an issue since they can decompose at temperatures above ca. 500°C forming coke on the catalyst surface [29]. It is important to mention that nickel promotes carbon deposition from CH_4 or CO via the reactions shown in equations 1-8 and 1-9, at temperatures between 345 and 370°C [64].

$$CH_4 \leftrightarrow C + 2H_2 \qquad \Delta H° = -41\ kJ/mol \tag{1-8}$$

$$2CO \leftrightarrow C + CO_2 \qquad \Delta H° = -173\ kJ/mol \tag{1-9}$$

According to the equation 1-9, dissociation of CO or hydrocarbons on the metal surface leads to the formation of α-carbon which can then polymerize to undesirable carbon forms such as graphite

or carbon filaments. The latter coke formation occurs by a series of free radical carbocation reactions on acid sites including dehydrogenation, oligomerization, cyclization, aromatization, and formation of poly-nuclear aromatics. Furthermore, during methanation formation and hydrogenation of deposited carbons (e.g. alpha and beta carbons) on catalyst can take place. When gasification rate exceeds deposition rate, there will be no carbon deposition. While below 330°C there is only α-carbon accumulation, α-carbon is converted to beta-carbon polymeric chain or film which deactivates the nickel catalyst >330°C. The carbon species formed by decomposition of CO on nickel at different temperatures are given in Table 1-2.

Table 1-2. Decomposition of CO over Nickel catalyst at different temperatures [64].

Deposited form of carbon	Formation temperature (°C)	H_2-TPR peak (temperature, °C)
Absorbed carbon (C_α)	200-400	200
Polymerized carbon (C_β)	250-500	400
Fibre carbon (C_v)	300-1000	400-600
Nickel carbide (C_γ)	150-250	275
Crystalline carbon (C_c)	500-550	550-850

The catalysts with carbon deposits can be regenerated by exposing to air at elevated temperatures to burn the carbon. The temperature control to avoid local high temperatures is important for regeneration processes. Another source of the deactivation is sintering which is mainly an irreversible process. Sintering can occur on the metal oxide support or on the active metal due to the atomic and crystallite migration Figure 1-9.

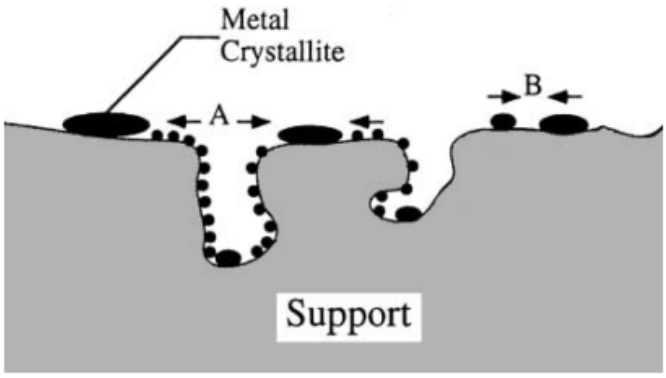

Figure 1-9. A crystallite growth due to the sintering by (A) atomic migration;
(B) crystallite migration [64].

Experimental observations showed that sintering rate of supported metal catalyst is strongly affected by the temperature and water vapour. For example, at the temperature above 500°C nickel crystallites migration occurs due to the more stable metal-metal bonding and this formation is

accelerated by the presence of water vapour [64]. Depending on the reaction conditions, several complex reactions can occur (e.g. re-dispersion). In order to minimize the rate of metal sintering, operation temperatures should be 0.3–0.5 times lower than the melting point of the active metal [65]. The addition of noble metals with higher melting point (such as rhodium or ruthenium) to a nickel catalyst increases the thermal stability of the material [66]. Mechanisms of catalyst deactivation were summarized in detail by Bartholomew [64].

Several studies focused on the stability of the catalysts in methanation reaction have been published in recent years [37,43,47,67,68]. It can be concluded that carbon deposition on different catalytic supports can be very different. Liu *et al.* studied the CO_2 methanation on Ni/Al_2O_3 and $Ni\text{-}CeO_2/Al_2O_3$ catalysts at GHSV = 15000 $mL \cdot g_{cat}^{-1} h^{-1}$ at 350°C for 120 h [47]. The CO_2 conversion on Ni/Al_2O_3 catalyst decreased by 4.2 % after 120 h time-on-stream. $Ni\text{-}CeO_2/Al_2O_3$ catalyst exhibited high stability under the selected operating conditions due to the addition of CeO_2.

Recently, a Ni-based catalyst was studied in CO methanation to address the sintering and the carbon deposition over time, which both hinder the stability and the efficiency of the catalyst [69]. The following process to produce an advanced catalyst with anti-coking and anti-sintering properties was reported: the Ni core of about 170 nm was protected by a 30-40 nm microporous SiO_2 layer from coking. This porous layer allows the gases to permeate, and completely inhibits particle-particle sintering.

In another study, 0.4 wt.% boron modified Ni/Al_2O_3 was compared to Ni/Al_2O_3 catalyst in CO methanation in the presence of ethylene [70]. The boron-modified Ni/Al_2O_3 catalyst exhibited enhanced carbon resistance. While Ni/Al_2O_3 catalyst lost approximately 20 % of its initial activity within 4 h, boron-modified catalyst only lost 4 % of the initial activity.

1.3. Industrial methanation reactors

Methanation reactors can be classified according to their reactor configuration or their development stage as follows: fixed-bed, fluidised-bed and intensified reactors or commercialised, demonstration [71] and research and development (R&D) stage reactors, respectively.

Starting from 20th century, fixed bed methanation reactors are integrated as gas cleaning units in various processes, e.g. ammonia plants [7]. Methanation reaction has been used for elimination of CO from gas stream to avoid catalyst deactivation. In the case of methanation unit, operating pressures range between 10-77 bars. The industrial lifetime of conventional nickel-alumina catalyst is usually between 2 and 4 years [72]. Generally, GHSV can be varied from 1.000 to 10.000 h^{-1}. GHSV can be calculated as follows: $GHSV = \frac{F_{feed\ gas}}{V_{reactor}}$.

The reactor types with increasing heat transfer properties are given in Figure 1-10. In industrial processes, there are mainly two strategies to deal with the catalysts deactivation. The first one is using dilution with product gases (CH_4, H_2O) or multi-injection of the reactant gases. The second one is using diluted catalysts with inert materials (such as in TREMP process). The state-of-the-art of methanation reactors is reviewed in this section; the advantages and disadvantages of different reactor types for both CO and CO_2 methanation are discussed. An overview of existing CO methanation industrial processes is given in Table 1-3.

Table 1-3. An overview of CO methanation industry.

Process	Process stage	Catalyst	Temperature (°C)	Pressure $(bars)_{max}$	Proposed lifetime	Ref
Lurgi Process	2	20 wt.% Ni/Al_2O_3 G1–85 (BASF)	260-450 280-650	18	1.8 years 5 years	[73]
TREMP **(Haldor Toposøe)**	4	wt.%23 PK-7R MCR-2X & MCR4	250-430 430-700	30 70	10 years 11 years	[74–76]
HICOM process	4	n.a.	230-640	70	2 years	[77]
Ralph M. Parsons	4-6	n.a.	315-780	77	n.a.	[78]
Imperial Chemical Industries	3	NiO 60%	400-700	n.a.	n.a.	[76]
Foster wheeler & VESTA	3	Clariant's ShiftMax®	260-670	30-60	4 years	[79]
Linde	2	n.a.	n.a.	n.a.	n.a.	[76]
Etogas	n.a.	Clariant's SNG cat.	n.a.	7-8 bar	20 years	[80,81]
Johnson Matthey	3	CRG-S2S CRG-S2C	250-700	n.a.	30 years	[80,82]

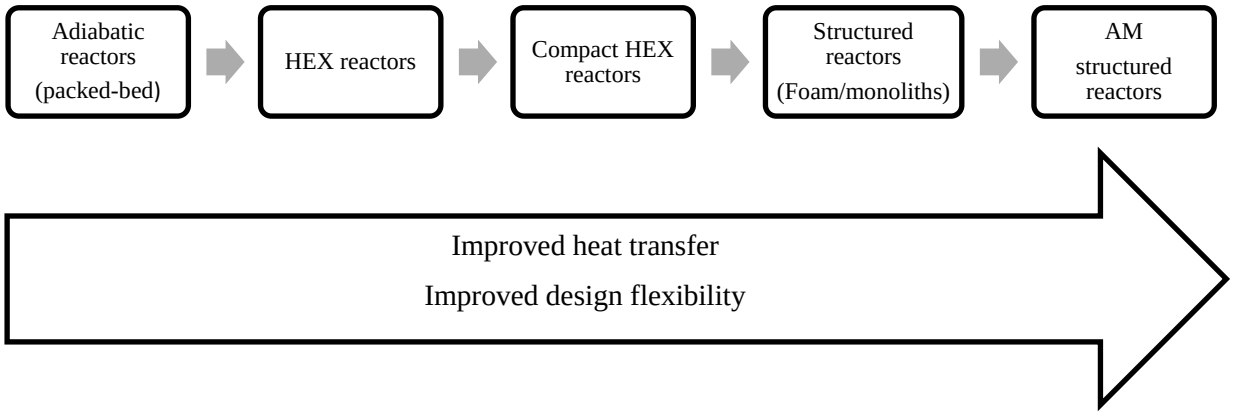

Figure 1-10. Type of reactors with increasing heat transfer performances.

1.3.1. Packed-bed reactors (PBRs)

Packed-bed reactors are usually tubular reactors filled with catalytic particles. These reactors are the most common for chemical industrial applications because of high catalyst loading and the ease of operation [83]. For large scale productions, the fixed bed reactors are usually made of stainless steel which is resistant to operations under high pressures. At laboratory scale, reactors are usually

made of less reactive materials such as glass [36,84], quartz [85] and rarely stainless steel [86]. Figure 1-11 shows the general scheme of a single-bed reactor.

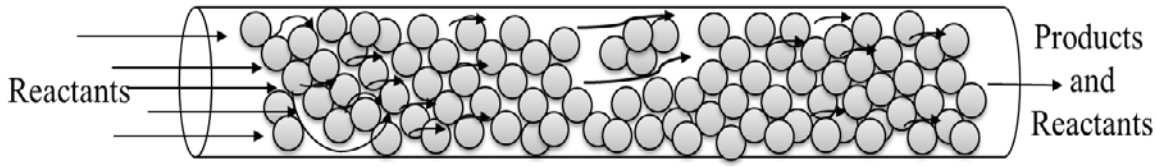

Figure 1-11. General scheme of a basic adiabatic packed-bed reactor and reactant flow in the catalyst bed.

The advantages of the fixed-bed reactors are: higher conversion per unit mass of catalyst (in comparison with e.g. fluidized-bed reactors), low operating cost, continuous operation, simple design, easy cleaning and replacement of the catalyst. The disadvantages of the fixed-bed reactors are: undesired heat gradients resulting in hot-spots formation, uneven flow distribution and high pressure drop. When reactor packing is uneven, the reacting fluid usually does not flow uniformly through the reactor due to channelling and by-pass phenomenon. Consequently, the molecules are following different pathways and do not spend equal time at the catalyst surface (Figure 1-11). Therefore, this leads to a non-uniform residence time of reactant gases. Furthermore, fixed bed reactors suffer from high pressure drops that are related to both the particle size of the catalyst and its shape and packing [11]. Larger particles will produce less pressure drop, but more diffusion limitations. In the case of small particles, pressure drop problem is encountered, especially if higher gas flow rates are used.

The catalytic reactors can be also classified adiabatic and non-adiabatic or heat-exchanger (HEX) reactors; or considering the process stage such as single-stage and multi-stage reactors etc. The HEX reactors, multistage and multi-tubular reactors are preferred for exothermic reactions [83]. In a HEX reactor, heat removal is ensured by the presence of the cooling channels. Heat exchanger can be integrated around the reactive channels with the circulating cooling fluid nearby the reactive channels as an internal exchanger (intercooling) or implemented externally to maintain the temperature at certain level. Micro-channelled packed-bed reactors, plate HEX reactors, structured reactors can be implemented in HEX configuration.

Adiabatic fixed-bed reactor (without any cooling) is the oldest and basic fixed-bed reactor configuration which has been used starting from Lurgi process. These reactors were chosen due to their easy operation and design because of the absence of radial heat transfer. There are several ways to control the temperature reported in literature. For example, temperature control can be ensured by recycling an excess of any of products with the mixture of reactant gases or dilution of reactants with an inert/steam gas. In a single adiabatic reactor, the highest possible conversion is the equilibrium conversion.

An example of an adiabatic fixed-bed reactor and its axial temperature profile is given in Figure 1-12 and 1-13. It is desirable to reduce the reaction rate at the position where the heat releases fast. Considering the above mentioned limitation of the methanation reaction, a model with separated H_2 and CO_2 feed streams was developed by Schlereth *et al.* [87]. The goal was to keep temperature below 510°C. Results indicated that the methanation reaction is fast without a product recycle or dilution by water or methane in the beginning section of the reaction channel, with diminishing rates in the downstream sections of the reaction channel. Modelled reactor with separate feeding of the components enables a high temperature control for CO_2 methanation.

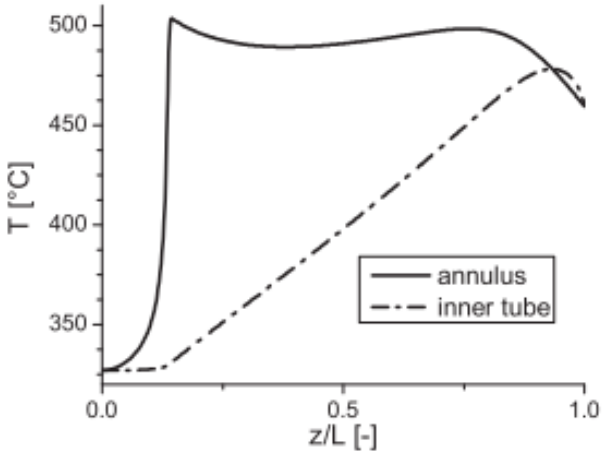

Figure 1-12. Axial temperature profile of the fixed-bed membrane reactor.

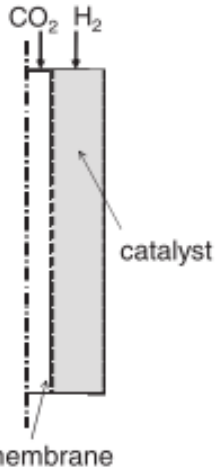

Figure 1-13. Fixed-bed membrane reactor design.

Besides the recycle of product gases with reactant gases, diluting the reacting CO and H_2 gaseous mixture with CO_2 would also help to control the temperature rise in the reactor. The effect of CO_2 addition was studied for CO methanation reaction by modelling in 2013 [88]. Modelling results showed that dilution of inlet feed stream with CO_2 increased the yield of methane as well as decreased outlet gas temperature. Another approach was proposed by Eigenberger *et al.* [83] that catalysts with different activities can be placed along the length of the reactor to control the temperature. In another study, modelling of adiabatic and isothermal methanation processes with different gas compositions and inlet gas dilution with N_2 were investigated at Riga Technical University in 2011. The increase of nitrogen concentration impacts the methanation process efficiency due to the decrease of the temperature indirectly. It was reported that the composition of the products has more effect on methane yield in adiabatic methanation than in isothermal methanation [89]. It is noteworthy to mention that dilution with inert gases results in further issues such as separation problems on industrial scale.

Lurgi process

Lurgi process was developed for coal gasification and methanation reaction in Germany in the 1930s. Two semi-commercial methanation pilot plants have been operated for 1.5 years with two

adiabatic fixed bed reactors with internal recycle [73,90]. One plant, designed and erected by Lurgi and South African Coal, Oil and Gas Corporation (SASOL), was operated as a side stream plant of a commercial Fischer-Tropsch Synthesis (FTS) plant. The other plant, a joint effort of Lurgi and El Paso Natural Gas Corporation, was operated at the same time at Petrochemie in Austria. Two demonstration plants have been operated to find optimal design parameters. Process scheme is given in Figure 1-14.

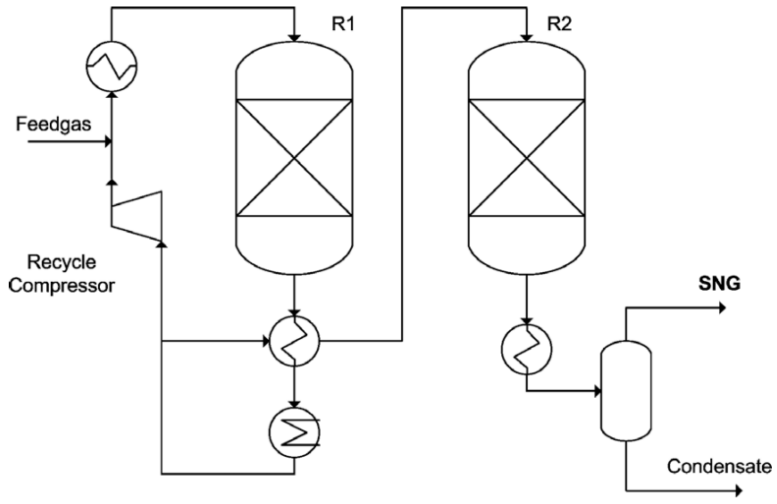

Figure 1-14. Process flow diagram of Lurgi methanation unit [90].

The first developed rectors were adiabatic in order to minimize operating and investment costs. Catalyst G1-85 of BASF, inlet temperatures of 260-300°C and outlet temperature of 450-500°C was found to be acceptable. Lifetime of the process with optimized design was expected to be around 2 years. This technology is still commercially available from Air Liquide.

TREMP process (Haldor Topsøe)

Haldor Topsøe initiated research and development in methanation field in the 1970s [75]. Haldor Topsøe has developed a unit which can convert desulphurised H_2 and CO with the ratio 3:1 into methane. This SNG plant was designed with a production rate of 1.4 billion Nm^3/year SNG [75,91]. Multiple stage methanation process was proposed, with the number of methanation reactors that depends on the operating conditions. Both Ni-based and a Ni-free catalysts were used. In TREMP multistage reactors, two type of catalysts are used: PK-7R and MCR-2X catalysts for low and high temperature methanation, respectively. Multi-stage process diagram is given in Figure 1-15.

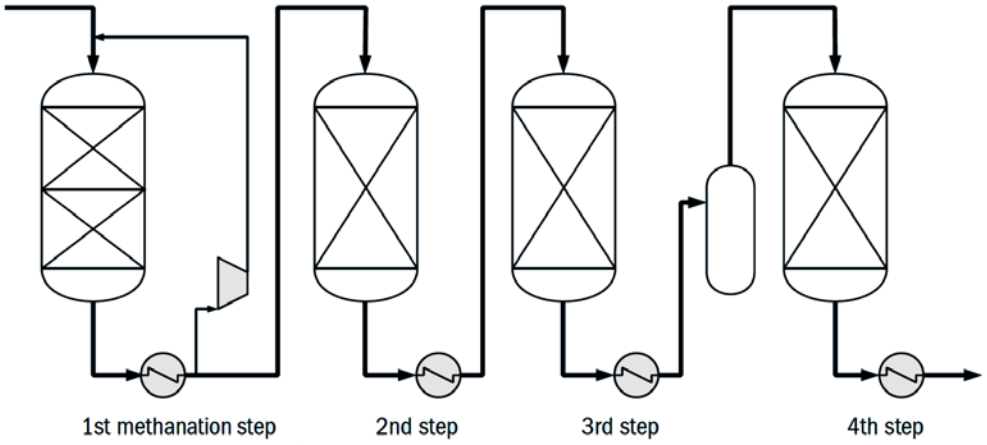

Figure 1-15. Process flow diagram of the TREMP process [91].

HICOM process

HICOM process was developed by British Gas Corporation. The temperature is controlled by recycling the cooled product gas. Excess steam is added to the first methanation reactor to avoid carbon deposition. However, the excess steam reduces the thermal efficiency and may cause catalyst sintering. A part of the product gas from the main methanation reactors is recycled and the other part is passed through one or more low temperature fixed bed methanation reactors. In the latter, the remaining CO and H_2 are converted to CH_4 and CO_2. Process scheme is given in Figure 1-16. The pilot plant consisted of 37 mm diameter tubular reactors for long term tests under near-commercial conditions. Operating conditions of the pilot tests with catalyst pellets of 3.2 mm and 5.4 mm are given in Table 1-3.

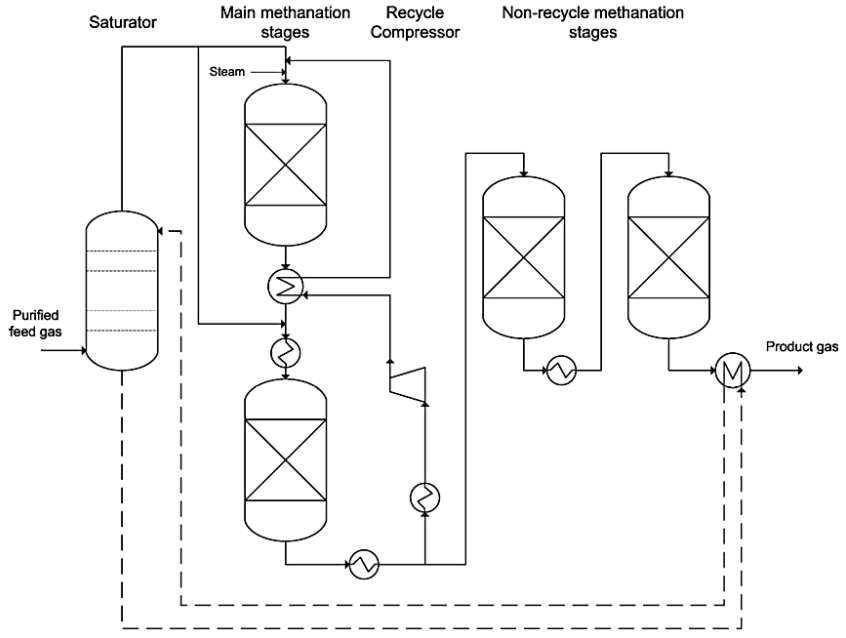

Figure 1-16. Diagram of the HICOM process [92].

Ralph M. Parsons technology

A high temperature methanation unit without gas recycle was proposed by the Ralph M. Parsons Company (Figure 1-17). The methanation unit consisted of 4 to 6 adiabatic fixed bed methanation reactors in series with intermediate gas cooling [78]. Temperature control was done by steam addition. There was no gas recycle and therefore no recycle compressor was needed in the process. No data about the catalyst was published.

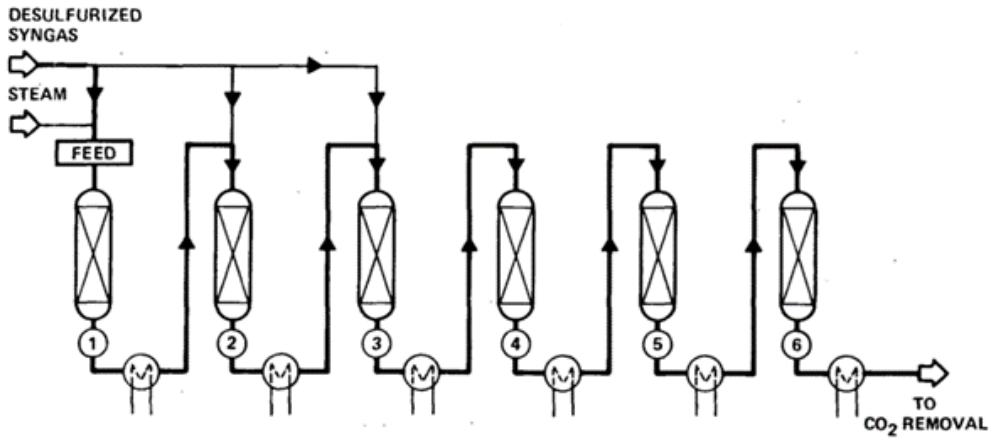

Figure 1-17. Process flow diagram of the RMP process [78].

Imperial Chemical Industries

This process consisted of three adiabatic fixed reactors in series with intermediate gas cooling. No large scale plant has been built.

Foster Wheeler& Vesta technology

A SNG methanation plant was built in China by Clariant and Foster Wheeler and started-up in July 2014. The pilot plant was designed for a production capacity of 100 Nm^3/h of SNG [93]. This process consists of three fixed-bed reactors in series with steam or CO_2 addition for the temperature control [79] (Figure 1-18). However, reacted gas recycling requires recycle compressors leading to increased operating costs. In the first reactor, high-temperature WGS reaction takes place on Clariant's ShiftMax® catalyst. The stream leaving the shift reactor is sent to the methanation reactors operated using Clariant's SNG catalyst beds.

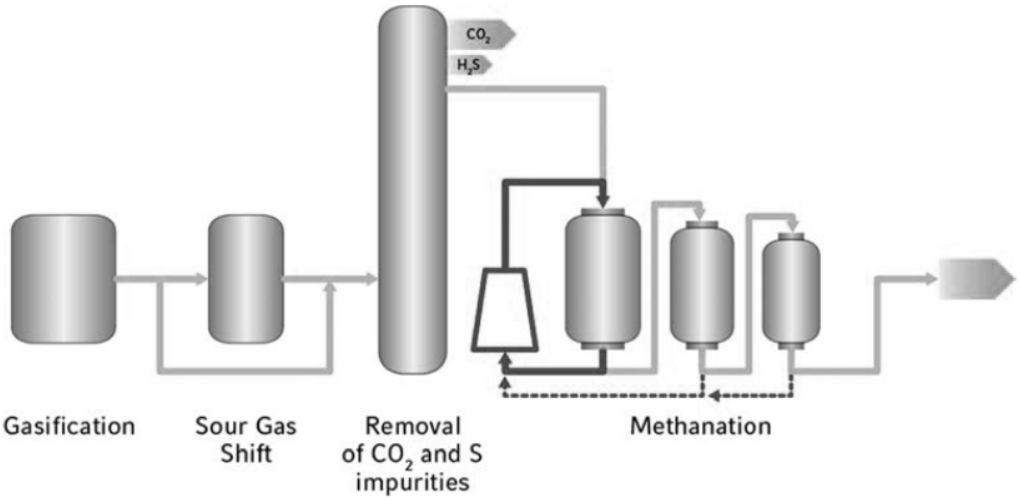

Figure 1-18. Three stages methanation for SNG production - VESTA [93].

Linde process

In the 1970s, Linde AG (Germany) developed an isothermal fixed bed reactor with indirect heat exchange. The plant consisted of an isothermal and an adiabatic methanation reactors as shown in Figure 1-19. For the isothermal reactor, the cooling tube bundles are embedded in the catalyst bed as shown in Figure 1-20. The reactor itself was supposed to produce steam from the heat of the exothermic methanation reaction. There was also the possibility to feed a part of the resulting product gas of the isothermal reactor into the adiabatic reactor to increase the methane yield. The product gases of both reactors are finally mixed, cooled, and produced water is condensed. No information can be found about the temperature, pressure and catalyst. Today, the Linde isothermal reactors are in operation in methanol synthesis plants [76].

Johnson Matthey (Davy Technologies)

Johnson Matthey has announced the contract with Qianan Hong Ao Industrial Trade Co. Ltd to operate a methanation plant in China. Davy technology uses the proprietary CRG methanation process technology from Johnson Matthey. The CRG family of methanation catalysts (CRG-S and CRG-SR) with high nickel content was used. The concept is the use of three adiabatic fixed-bed reactors with intermediate gas cooling and recycling [80].

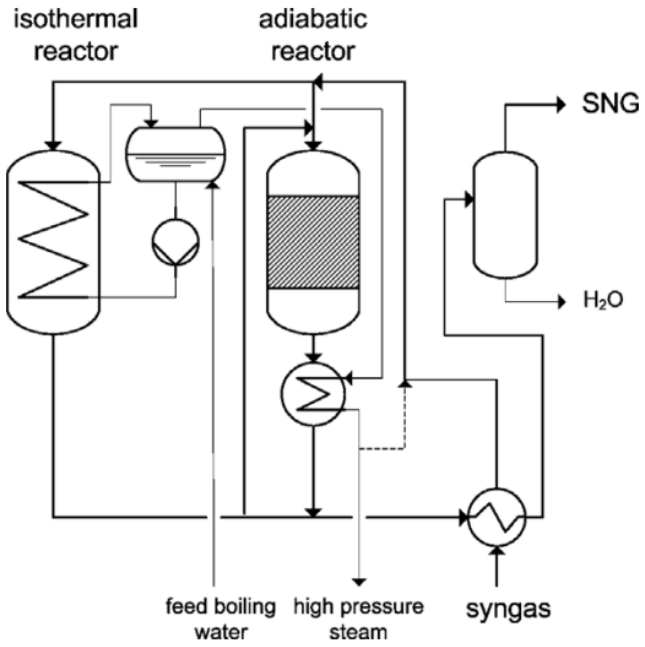

Figure 1-19. Flow diagram of Linde process [76].

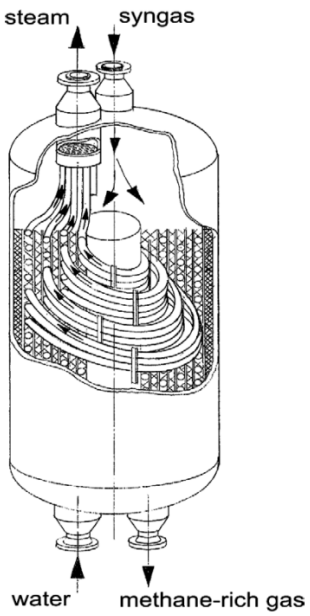

Figure 1-20. Scheme of the isothermal Linde reactor [76].

Etogas

The PtG power plant from ETOGAS for Audi AG in Werlte, Germany is operated for thermochemical methanation in a tube bundle reactor with molten salt [80,81]. This plant has 6.3 MW capacity and production of around 1000 tons of synthetic methane per year [45]. Clariant has supplied the methanation catalyst. Process is fed by a biogas plant (scheme is given in Figure 1-21). To the best of our knowledge, the process used at Werlte now takes place in the new Viessmann facility for biological methanation process [94].

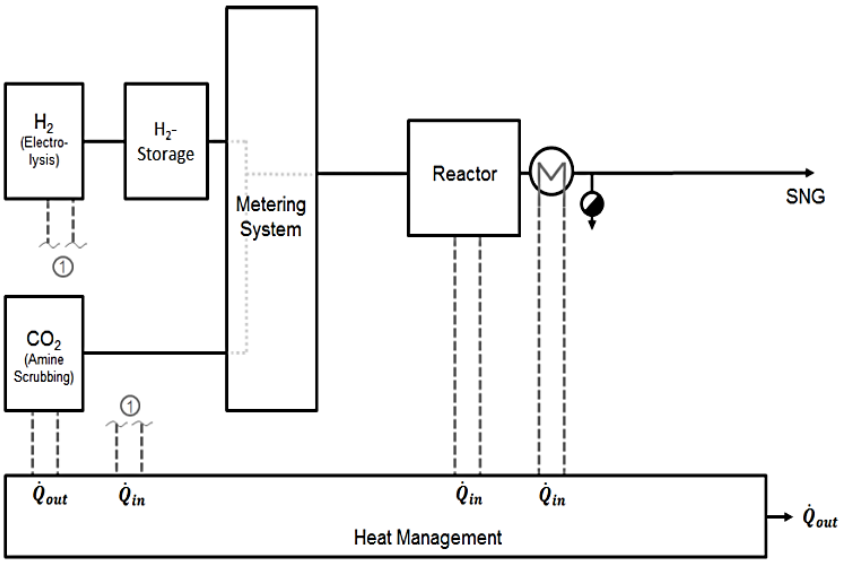

Figure 1-21. ETOGAS process [95].

1.3.2. Fluidized bed reactors (FBRs)

In a fluidized bed reactor (see Figure 1-22), a flow of gas or liquid is directed through the catalyst. The fluidized bed reactor has to be designed considering the fluid flowrate to be sufficient to suspend the catalyst particles. The size of the particles is typically in the range between 10 and 500 μm [80,96]. These reactors provide extensive homogeneous mixing resulting in excellent temperature stability and increased mass-transfers. Fluidized bed reactors typically have a porous plate located at the bottom of the reactor, known as a gas distributor. Basic contact between the catalyst and reactant gas occurs in fluid phase of the reactor. Fluidized bed reactors are suitable for handling large amounts of feed and catalyst. The advantages of the fluidized-bed reactors are eliminated hot spots via the heat distribution, continuous operation, more efficient reactants contact, and better mass transfer compared to fixed bed reactors. However, there are some disadvantages of fluidized-bed reactors such as erosion of the reactor walls and separation of fine particles due to the attrition of the catalysts.

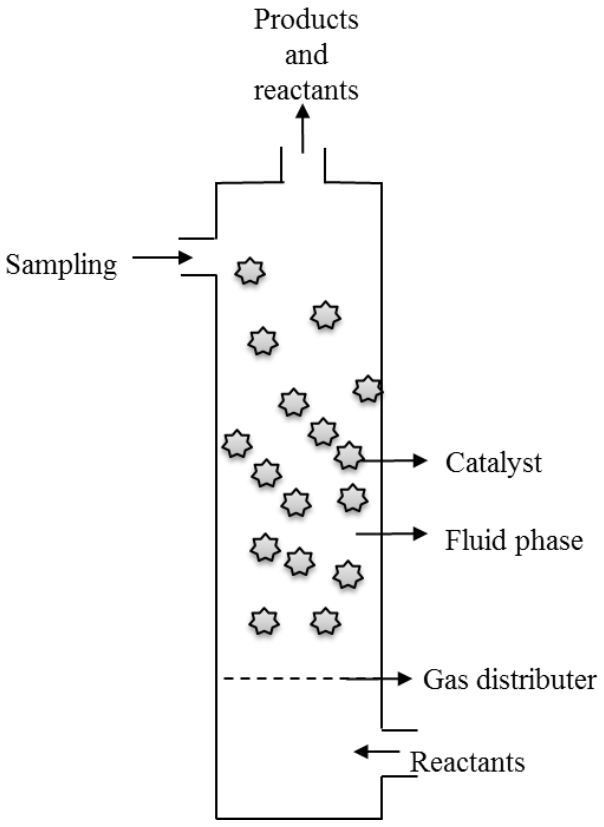

Figure 1-22. General scheme of a fluidized bed reactor.

Kopyscinski *et al.* investigated the heat- and mass-transfer and hydrodynamics of CO methanation reaction in a fluidized-bed reactor [10]. The high space velocity leads to higher heat transfer and less hotspot formation. However, gas bypassing through the reactor bed took place. At laboratory scale, the comparison of the syngas methanation in fluidized-bed and packed-bed reactors was described by Liu *et al.* [97]. It was shown that the fluidized-bed reactor gave higher CH_4 yield and lower bed temperatures, thus lower coke formation than in the packed-bed reactor. Moreover, the

syngas methanation in the fluidized bed reactor was studied in various reaction conditions, e.g. different space velocities of 40-120 $L \cdot g^{-1} \cdot h^{-1}$, gas compositions and temperatures (480 - 550°C) [98]. It was shown that composition of the feed gas (CO_2 content) affects the conversion and CH_4 selectivity.

As for industrial processes, one of the first fluidized-bed methanation processes was developed by the Bituminous Coal Research Inc. in 1963 (USA, Bi-Gas-Process) [99]. Between 1975 and 1986, the Thyssengas GmbH (Germany) and University of Karlsruhe (Germany) designed a fluidised bed methanation reactor to produce SNG from coal gasification [80]. Starting from 1960s, processes for SNG production from coal and dry biomass were reviewed in detail by Kopyscinski *et al.* [76].

1.4. Intensified compact reactors

1.4.1. Milli-channel HEX reactors

The typical channel diameter of a milli-structured reactor is larger than 1000 µm. A HEX reactor combines a reactor and a heat exchanger in one unit. The heat transfer efficiency is up to 20 times higher than in conventional reactors [100]. The heat removal from the catalyst to the cooled walls is essential to ensure high conversion rates and limit the catalyst deactivation. Lowering the reaction temperature prevents thermal runaways but requires more catalyst resulting in a larger reactor size. Therefore, intensified reactors offer better thermal control of the reaction, high surface-to-volume ratio, narrow RTD of reactants, reduced reactor size, quick response time (start-up and shut-down), and easy scale-up. However, increased number of channels increases the manufacturing costs.

A milli-structured compact reactor was successfully designed at CEA Liten, Grenoble and studied for CO_2 methanation by Ducamp in 2015 [101]. A photograph of the milli-structured HEX reactor is given in Figure 1-23.

Figure 1-23. A photograph of the milli-structured HEX reactor [101].

This reactor consists of 20 reactive parallel channels with a length of 240 mm surrounded by cooling channels. The reactor was equipped with 15 thermocouples for the continuous temperature screening. The CO_2 methanation was performed using commercial Ni/alumina (Evonik) catalyst packed in the milli-structured reactor at temperatures of between 270-300°C under pressures of 1-5 bars. Results were compared with the annular packed-bed reactor. It was reported that ca. 90 % of CO_2 conversion was achieved with the milli-structured reactor at a lower pressure (<5 bars), a lower maximum bed temperature (<500°C) and ca. 4 times higher GHSV than annular packed-bed reactor.

1.4.2. Micro-channel reactors (MRs)

The typical channel diameter of a microchannel reactor, also known as a micro reactor, is in the range of 50 to 1000 µm. Due to their small channel diameters, microchannel reactors usually work under laminar flow conditions [102,103]. In micro reactors, the catalyst particles have diameters in the range between 50 and 75 µm [104]. Comprehensive reviews of micro reactor designs and applications were published by Kolb & Hessel and Kiwi-Minsker & Renken [102,105,106]. The advantages of using micro reactors are temperature control affecting conversion, selectivity, yield, the narrow RTD and high surface-to-volume ratio: in the range of 10.000-50.000 $m^2 \cdot m^{-3}$.

A micro reactor design was studied for Sabatier and WGS reactions by TeGrotenhuis *et al.* [107]. Methanation reactions in the micro reactor were performed at isothermal and adiabatic conditions. Figure 1-24 shows the conversion and selectivity versus contact time at 400°C. Equilibrium conversion was obtained with a contact time of ca. 400 ms. The microchannel cooling enhances the equilibrium and the temperature control and therefore, conversion and selectivity of the catalyst/reactor.

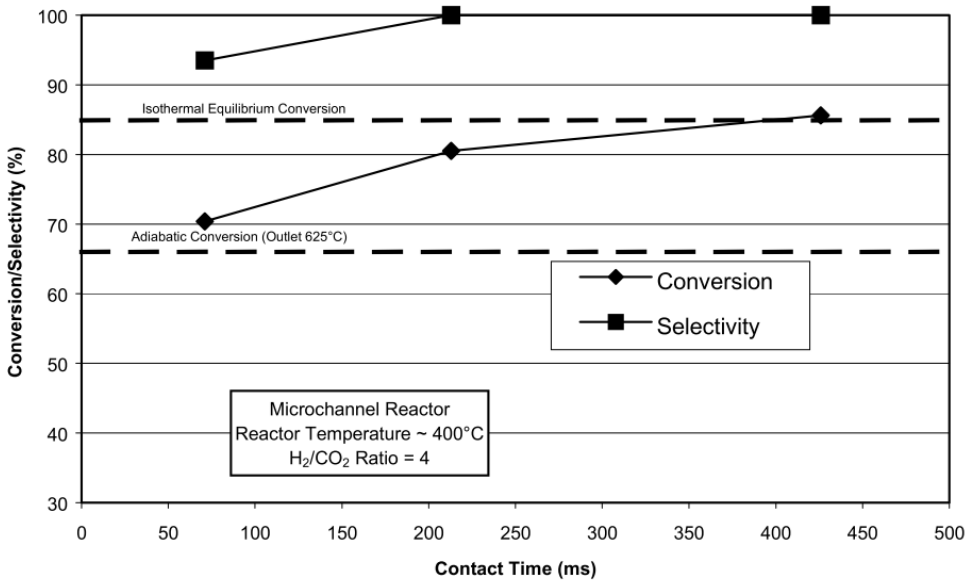

Figure 1-24. Conversion and selectivity results of the Sabatier reaction performed in a N_2 cooled micro-reactor [107].

A study published by Lee *et al.* [108] is devoted to a hybrid micro-channel reactor (HMCR) designed for CO methanation and oxidation reactions. The micro reactor was made of 316L stainless steel with a volume of 1.67 cm^3. The reactor bed was separated from the micro-channel heat exchanger with a separator sheet, and contained two different catalysts that promote preferential oxidation and methanation of CO in series. In the case of methanation, results showed excellent efficiency and stability in a wide temperature range (214-277°C). Along with micro channel packed-bed systems, catalytically active walls were proposed as an alternative in order to improve the heat transfer and to avoid high pressure drops.

1.4.3. Wall-coated reactors

In a wall-coated reactor, catalytic layer is supported on the wall of the microchannel. A remarkable study for CO methanation in presence of CO_2 and O_2 was published by Görke *et al.* [16]. The micro-channels were coated by dip-coating with a Ru/SiO_2 and a Ru/Al_2O_3 catalysts. It was found that CO methanation is more favoured at temperatures between 200 and 250°C, and CO_2 methanation dominates at temperatures >250°C. Highly selective methanation was achieved by the use of a microchannel reactor coated with Ru/SiO_2 catalyst. Wall coating optimization in microchannel reactors is discussed in details by Stefanescu *et al.* [109].

An extensive experimental study of methanation and WGS reactions in a 130 mm long catalytic plate reactor was reported by Kopyscinski *et al.* [110]. The reactor consisted of a metal plate coated with commercial nickel-based catalysts. Mass transfer effect at temperatures of 280-360°C was investigated by modelling. Concentration profiles at different axial positions were calculated. Results showed that at high temperatures (above 340°C) depending on the reactor and reaction conditions, pore diffusion limitations possibly occurred in the first 30 millimetres of the catalytically coated area.

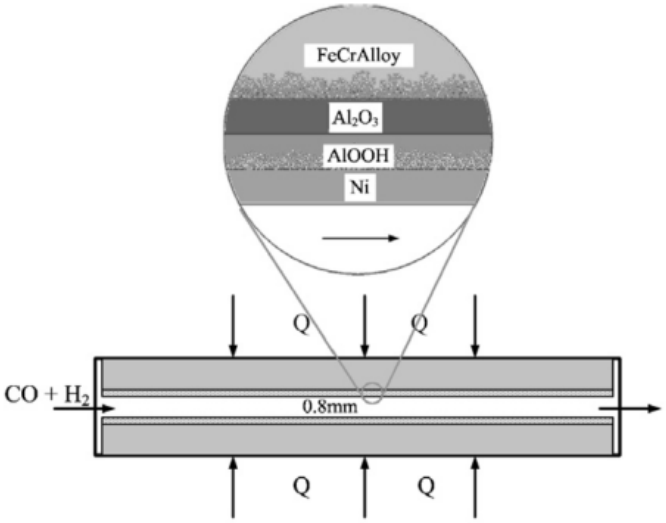

Figure 1-25. Wall-coated micro channel reactor [14].

Another remarkable study of methanation reaction in a wall coated micro-channel reactor was published by Liu *et al.* The scheme of the micro-channel reactor is given in Figure 1-25. Metal-ceramics complex substrate consisted of FeCr-alloy and thermally sprayed γ-alumina nano-particles. The substrate was impregnated with nickel-containing solution. This microchannel reactor was tested for a long term CO conversion at temperatures between 350 and 550°C and pressures up to 30 atm, and at a high GHSV of 71.000 h^{-1}. It was reported that coated plates showed excellent catalytic performance in methanation reaction during long-term stability test. Even at 550°C conversion still remained high [14]. If we compare conventional methanation reactors with coated microchannel reactors, the latter allow better temperature control and lower pressure drop. However, wall-coated micro-reactors suffer from low catalyst loading, difficult catalyst loading-unloading, re-use and challenging scale-up.

1.5. Structured reactors

Structured reactors/catalysts consist of a metallic or ceramic support and an active catalytic layer on the support surface. In contrast to packed-bed catalysts, structured catalysts provide higher mass- and heat-transfers and lower pressure drops [83]. However, the manufacturing cost is high and the low catalyst loading limits the integration of structured catalysts in industrial applications due to higher gas velocity requirements. Nevertheless, structured catalysts and reactors are attractive for industrial reactor engineering with their potentially smaller reactor sizes, easy catalyst replacement, high surface-to-volume ratio, easy scale-up and flexible operation conditions. This section presents a review of existing metallic plates, monoliths, foams, foils, micro-fibrous materials (felts) and additive manufactured structured reactors/catalysts. The comparisons between structured reactors/catalysts and conventional systems are shown in Table 1-4 [11].

Table 1-4. Comparison of the reactors [11].

	Packed-bed reactors	Fluidized bed reactors	Structured reactors
Energy requirement	High	Medium	Low
Pressure Drop	High-medium (depends on particle size)	Medium	Low
Heat transfer	Low	Medium	Medium-high (depends on support material)
Catalyst separation	Easy	Costly	Easy
Reactor size	Small-large scale	Small-large scale	Compact reactor
Experience	High (Industrial)	High (Demonstration)	Developing (R&D), small pilot
Catalyst loading	High	Medium	Medium-Low

1.5.1. Monoliths

A large number of studies have already been performed on monolithic structures since the 1990s. Monolithic catalysts were originally developed as catalytic converters for the automotive

industry [111]. Later, these structures found a wide range of applications in industrial chemical processes [112] and catalytic reactors [113,114].

Monolithic reactors can be manufactured from the various materials (metallic/ceramic) as shown in Figure 1-26 [114]. Ceramic monoliths are mainly produced by extrusion technique. The shape of the channels can be circular, square, triangular, rectangular, hexagonal ("honeycomb" monoliths), sinusoidal etc. Cordierite was found to be the most appropriate ceramic material for combustion applications. In non-adiabatic applications, the use of cordierite is limited by its low thermal conductivity.

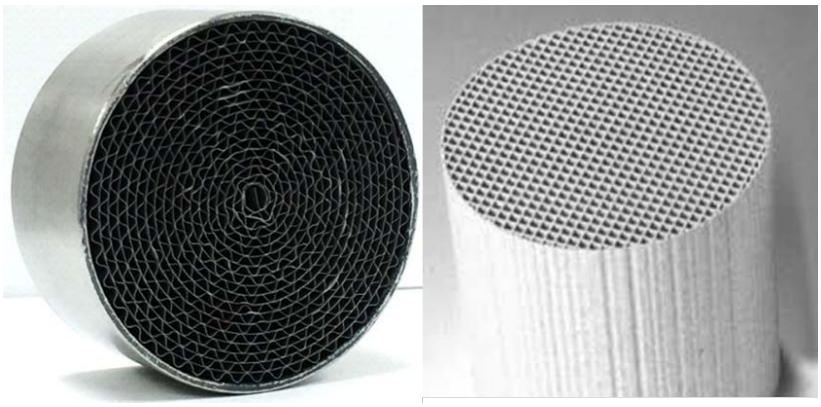

Figure 1-26. Metallic (left) and ceramic (right) monoliths.

Metallic monoliths have attracted a great interest in the beginning of 80s, especially for non-adiabatic processes. Metallic monoliths are usually made of stainless steel [11]. The use of conductive monoliths as catalytic supports for highly exothermic reactions was suggested in 2005 [115,116]. The monoliths made of high intrinsic conductivity materials like copper and aluminium were investigated by Groppi *et al.* for exothermic reactions [115]. It was confirmed with a model that near-isothermal reactor operation could be achieved with monolithic reactors for exothermic oxidation of methanol to formaldehyde. Boger and Heibel [116] compared the heat transfer in cordierite, aluminium and copper monoliths. Their study showed that low thermal conductivity of cordierite allows only very limited radial conductive heat transfer, while conductive monoliths achieved very high conductive heat transfer. Visconti *et al.* [117] developed a detailed model to estimate the effective axial and radial thermal conductivities of honeycomb monoliths with square channels. In their model, a wash-coated catalyst layer on the monolith channels was also taken into account. Recently, Sanz *et al.* [118] studied the effective thermal conductivity (ETC) of metallic monoliths considering methanol steam reforming (endothermic reaction) reaction. Simulation and experimental results confirmed the fundamental role of thermal conductivity. The pronounced effect of the cell density of the monolith on methanol conversion was observed.

Methanation reaction in a metallic honeycomb structured reactor was simulated in 2010 [119]. The effect of gas space velocity on conversion and temperature profiles was discussed. High CO

conversion (83 %) was obtained in a presence of CO_2. Higher gas flow rate results in the shift of the hot-spots towards the end of the catalyst bed. Temperature increase generated by the reaction heat was found to be lower, that slowed down the reaction. It was concluded that the thermal runaway during CO methanation can be overcome by using monoliths.

A remarkable modelling study on the comparison of metallic honeycombs with fixed bed reactors for CO_2 methanation was presented by Schlereth *et al.* [120] in 2015. Heat transfer in fixed bed reactors is dominated by the convection which is a strong function of the particle Reynolds number. In honeycomb monolith reactors, this value depends on gap resistance – the resistance of heat transfer caused by the gap between the honeycomb and the tube, void fraction, and thermal conductivity of the solid material. It was concluded that honeycomb reactors are able to maintain isothermicity at higher temperatures than fixed bed reactors. The idea of the integration of two reactor types was proposed in this study. Honeycombs can be exploited in a first reactor, operated at a level of intermediate conversions with well-controlled temperatures. Then, a fixed bed reactor can be installed as the second reactor since it offers higher catalyst loadings. Heat removal is expected to be less critical because the gas is already diluted by product gases which slow down the reaction rates.

Recently, methanation tests were performed on honeycomb monoliths and on the commercial bulk catalyst of the same volume [121]. Cordierite type monolith was wash-coated with commercial nickel-based catalyst. Methanation reaction was performed with a gas mixture of H_2, CO_2 and CO (total flow 50 $Nl \cdot min^{-1}$) at 20 bars and 350°C. This study showed that at GHSV of 2000 h^{-1} commercial bulk catalyst gave ca. 90 % conversion, while honeycomb catalyst reached only ca. 70 % due to the limited catalyst loading at the same volume of the reactor. This 20 % difference in conversion decreased to 10 % at higher GHSVs (6000 h^{-1}). Comparison of the structured and conventional catalyst can be challenging: either the same volume of the catalyst/reactor with different amount of catalyst is used, or the same amount of catalyst has to be taken, but then it has to be diluted with non-active material to achieve the same reactor volume.

1.5.2. Open-cell foams (OCF)

Open-cell foams, also called solid sponges, are irregular structures belonging to the family of cellular materials. A metallic/ceramic foam consists of a metal or ceramic material containing a large volume fraction of air-filled pores (see Figure 1-27). Foams are divided in closed-cell or open-cell, corresponding of their sealed or interconnected pore cells, respectively. Manufacturing process of a ceramic foam is based on impregnation of the open-cell polymers with ceramic slurry and then firing the polymer in a furnace to obtain only ceramic material. Ceramic foams are used as filters for molten metals [122,123], catalytic combustion devices [124] and catalytic supports [125]. Metallic foams are made by mixing metal powders with a blowing agent, compacting the mixture, and then foaming it by melting. Closed-celled metal foams are commonly made by injecting a gas or mixing a foaming agent into molten metal. Metallic foams are used as high-temperature filters [126], heat exchangers

[127,128] and catalytic supports [129]. The detailed description of various methods for foam manufacturing was discussed by Banhard [130].

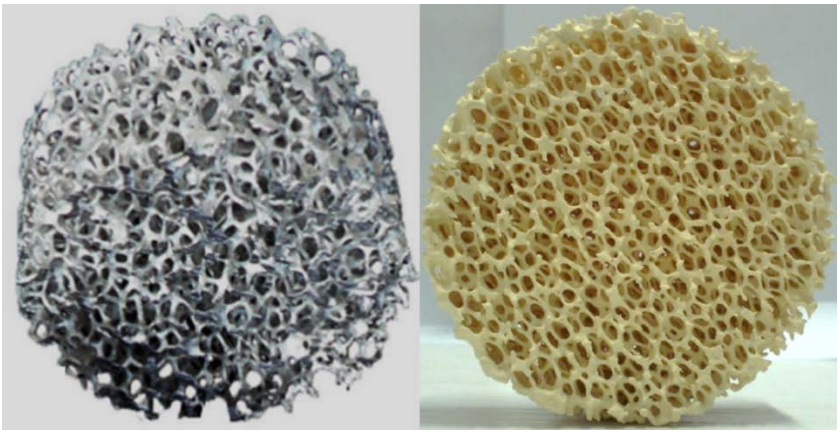

Figure 1-27. Metallic (left) and ceramic (right) foams.

Maestri *et al.* [131] studied catalytic partial oxidation of methane by modelling using three different types of ceramic catalyst supports (foam of 25 ppi, honeycomb monolith of 400 ppi and spheres with a diameter of 1.3 mm). The heat and mass transfer coefficients of these three configurations were determined at increasing gas flow rate. It was reported that the foam exhibited the highest values of heat and mass transfer coefficients in the whole range of flow rates investigated. In the case of honeycomb and spheres, at low flow rates the honeycomb monolith showed better transport properties than the packed bed of spheres. However, at higher gas velocities the transport coefficients in the packed bed exceeded those of the monolith due to the negligible dependence of the latter on gas velocity. Figure 1-28 shows the results of the modelling heat and mass transfer coefficients of samples at different flow rates.

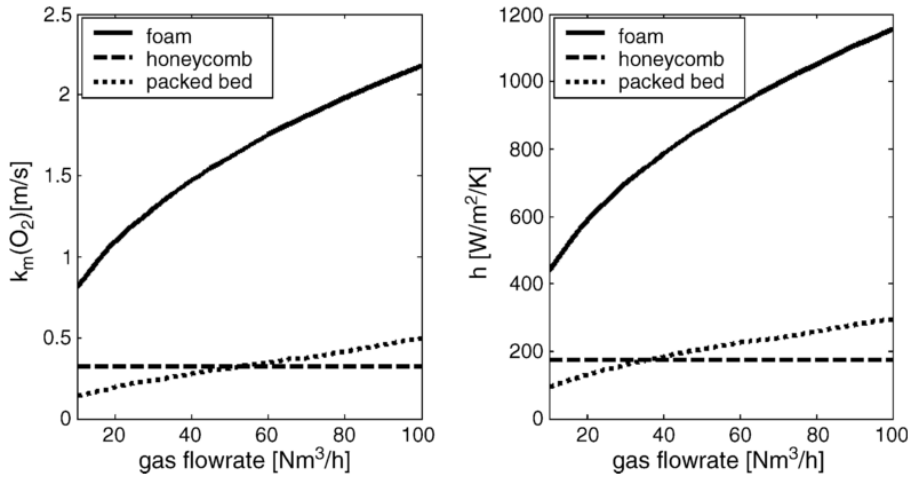

Figure 1-28. Comparison of mass- and heat-transfer properties of different supports in partial oxidation of methane at various gas flow rates (T = 620 K, P = 1.5 bar) [131].

Heat transfer on metallic FeCrAlY and aluminium open-cell foams for strongly exo- / endothermic catalytic processes (e.g. methanation, selective oxidation, Fischer–Tropsch synthesis (FTS)) was experimentally and theoretically investigated by Bianchi *et al.* [132]. The heat transfer properties of the foams (porosity of 89-95 %) in tubular reactor were examined at gas (nitrogen) velocities of 15-35 $Nl \cdot min^{-1}$ at the temperatures from 127 to 527°C. Closer to the inlet of the tubular reactor, the tube outer temperature is higher than the temperature of the flowing gas, so the temperature decreases radially from the wall to the centre of the bed, while it increases axially towards the test tube exit. With increasing the flow rate, the inlet temperature decreases because of the reduced residence time in the preheater of the foam bed. Furthermore, radial effective thermal conductivity of the samples was investigated, depending on the operation conditions. The estimated radial effective thermal conductivity values of FeCrAlY (porosity of 95%) and aluminium samples (porosity of 89%) were found to be 0.3–0.9 and 7.7 $W.m^{-1} \cdot K^{-1}$, respectively. Radial effective thermal conductivity was found to be weakly dependent on the operation conditions. It was suggested that thermal conduction plays a determining role, especially for Al foams. It was shown that it is possible to improve the effective thermal conductivity coefficients of foams simply by increasing the volume fraction and/or the conductivity of the foam material.

CO_2 methanation reaction on ceria-zirconia-SiC foams and powder catalysts at temperatures between 250 and 400°C and atmospheric pressure was studied by Frey *et al.* [20]. Foam catalysts were impregnated with the same amount of active phase (nickel + ruthenium). A platelet milli-reactor was used to compare the foams and powder catalysts of the same volume. At the temperature of 250°C, the powder catalyst showed higher CO_2 conversion than foams, due to higher catalyst loading, i.e. conversion was found to be 2.5 and 5.0 %, respectively. It was concluded that better comparison between foam and powder can be made by calculating productivity. The productivity of the ceria–zirconia-based foam and the powder catalyst of the same composition at temperature 400°C was found to be 2.6 and 1.8 $mol_{CH4} \cdot g_{Ni+Ru}^{-1} . h^{-1}$, respectively. Later, methanation reaction on SiC, alumina and aluminium supported catalysts was studied using an infrared camera [133]. The CO_2 conversion rates on SiC, Al_2O_3 and Al were found to be 7.8, 3.7 and 2.3, respectively, for a flow rate of 2 $L \cdot h^{-1}$. Lower specific surface area led to lower active phase dispersion and therefore to a smaller number of active sites and weaker catalytic activity. The direct effect of the exothermic methanation reaction on the foam's surface temperature was recorded in this study. The SiC based catalyst showed the highest catalytic activity and the highest amount of hotspots. Al_2O_3 based catalyst exhibited lower catalytic activity than SiC but still showed some hotspots. As for aluminium based catalyst, hot spot formation couldn't be clearly observed due to low conversion rate which resulted in less heat production during the reaction. In their recent study, CO_2 methanation reactions were performed on ceria-zirconia (CZ) coated OFC catalysts in a pilot scale reactor [134]. At 300°C, methane productivity of OFC and packed-bed catalyst were found to be 580 and 500 $mmol_{CH4} \cdot g_{Ni} . h^{-1}$, respectively. However, CZ-OFC structured catalysts exhibited much lower temperature increases during the reaction, and lower

pressure drop. At operation temperatures between 270-318°C, the maximum temperature increase was recorded as 25°C which can be considered as negligible in comparison with conventional packed-bed reactor configuration.

Experimental and modelling study of the methanation reaction on metallic foams was published by Ducamp in 2015 [101]. A commercially available aluminium foam was loaded with 43 $kg \cdot m^{-3}$ of commercial Ni/alumina (Evonik) catalyst. Conversion of CO_2 was measured experimentally at temperatures between 280 and 325°C, pressures of 5 to 15 bars with GHSV of 2600 to 8800 h^{-1}. CO_2 conversion was found to be 42 % (330°C, 5 bars, 1 $Nl \cdot min^{-1}$ gas velocity). Selectivity was recorded as 95 %. Furthermore, it was found that increasing the pressure from 5 to 15 bars at 325°C increases the CO_2 conversion by 14 %.

Recently, the effects of the reaction temperature, pressure and GHSV on the performance of Ni-Al_2O_3 coated catalytic supports (Ni-foam, Cu-foam and Cu-Ni alloy foam) in syngas methanation were investigated by Li *et al.* [135]. The experiments at 350°C and GHSV of 5000 h^{-1} showed that Ni-Al_2O_3/Ni-foam gave much higher activity and CH_4 selectivity than Ni-Al_2O_3/Cu-foam and Ni-Al_2O_3/CuNi-foam, that was expected to be due to the higher surface amount of nickel in the Ni-foam. Additionally, temperature difference between the reactor wall and the catalyst-bed was analysed on Ni-Al_2O_3/Ni-foam and Ni/Al_2O_3 packed bed catalyst at 350°C by CFD simulation and monitored experimentally. It was observed that in the case of Ni-Al_2O_3/Ni-foam the temperature difference was always lower than in the case of Ni/Al_2O_3 packed bed in the whole temperature range due to highly enhanced heat transfer.

To summarize, the literature studies show that the radial heat transport is important for the design of chemical reactors with structured catalyst, especially on the industrial scale. Better heat transfer properties of metal foams are expected to limit the sintering of the catalyst and/or fast coking due to heat generated during the reaction.

1.5.3. Micro-fibrous materials

Micro-fibrous materials were patented by Auburn University in 2010 [136]. These materials are made of micron-sized highly conductive fibres where various reactive materials including catalysts can be immobilized. Micro fibrous felt materials enable the temperature control and provide uniform temperature profile for highly endo/exothermic chemical reactions. A unique felt structured catalyst was developed by Hu *et al.* for methanation and rWGS reactions in a micro-channelled reactor [17]. A porous FeCrAlY felt was used as a substrate, methanation catalysts were introduced by wash-coating technique. In the case of methanation reaction, structured catalysts achieved 78 % conversion at GHSV of 18.000 h^{-1} and temperature of 300°C which was giving the same performance as powder catalyst.

Commercial sintered metallic micro-fibres were used as catalyst supports in a model reaction (CO oxidation) by Groppi *et al.* [137]. The fibres had high porosity (86 %) and extremely high surface

area per unit volume (22400 $m^2 \cdot m^{-3}$). CO conversion reached 90 % at very high space velocities (>10^6 h^{-1}) in the catalytic bed with only 1mm depth. However, it was shown that gas/solid mass transfer data for micro-fibres exhibit negative deviations, similar to those observed in packed beds of particles at very low Re numbers.

A potentially interesting system for the efficient thermal control in the microchannel reactor was designed and implemented for CO_2 methanation by Brooks *et al.* [12]. Rh or Ru/titania catalysts with metal loadings between 1 and 6 wt.% supported on FeCrAlY felts were used. Structured felt catalysts were placed within each channel of the micro reactor. Microchannel wall temperature was maintained by a counter-flow of oil (see Figure 1-29). Reactor was operated at the inlet temperature of 400°C, and the temperature decreased linearly to 300°C at the channel exit. The improved performance (10 % higher yield) of the felt microchannel reactor was reported due to its controlled temperature.

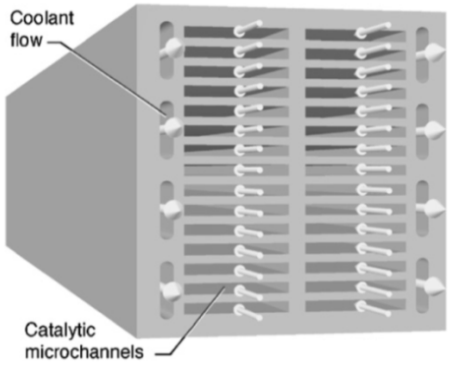

Figure 1-29. Cross section of the microchannel reactor with counter-flow oil [12].

A copper micro-fibrous structure coated with 15 wt.% Co/Al_2O_3 catalyst was tested in a tubular reactor with an inner diameter of 41 mm for FTS, and results were compared with Co/Al_2O_3 catalyst particles in packed bed configuration by Sheng *et al.* [138]. While the maximum temperature difference from the centreline to the reactor wall was only 6.4°C in the case of copper micro-fibrous entrapped catalyst (MFEC), for the packed bed it was measured to be 460°C. The uniform temperature profile of copper MFEC resulted in higher selectivity to longer chain hydrocarbons and less catalyst deactivation. The use of copper MFEC led to less hot spot formation during the start-up, prevented thermal runaway, provided a wider operational temperature range, and offered the possibility of using reactors with larger diameters. Furthermore, comparison in micro-scale heat transfer between packed bed and MFEC was reported by the same research group [139]. Copper MFEC demonstrated an excellent intra-bed heat transfer ability for FTS [140]. Figure 1-30 shows the photographs and SEM images of copper microfiber media before and after loading with catalyst particles. Figure 1-30D shows catalyst particles immobilized by the sintered microfiber. MFEC approach enabled FTS to be carried out in a larger tubular reactor (34 mm inner diameter) without comprising the production rate

and selectivity to the desired product. The maximum temperature difference along the radial direction was recorded to be less than 5°C for all MFEC structures, as for the packed bed, this temperature difference was around 54°C under the same conditions.

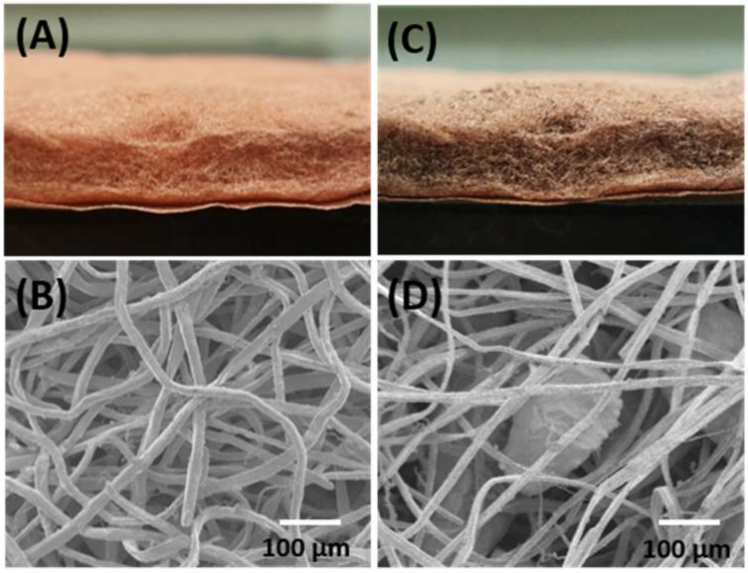

Figure 1-30. Images of Cu MFEC structure: (A) photograph before catalyst loading; (B) SEM image of before catalyst loading; (C) photograph after catalyst loading; (D) SEM image after catalyst loading [140].

Additionally, the enhanced heat transfer characteristics of copper MFEC were studied by experimental determination of thermal parameters. Copper MFEC demonstrated 56 times higher radial effective thermal conductivity (9.05 $W \cdot m^{-1}K^{-1}$), and more than 10 times higher wall heat transfer coefficient (235 $W \cdot m^{-2}K^{-1}$) than the traditional alumina-packed bed [141]. The axial effective thermal conductivity (0.951 $W \cdot m^{-1}K^{-1}$) was found to be much lower than the radial effective thermal conductivity. The effect of sintering temperature and sintering time of Cu MFM on the effective thermal conductivity was also investigated [142]. It was shown that higher sintering temperature and longer sintering time improved the junction factor and effective thermal conductivity. Recently, a study related to the effective thermal conductivity of a porous stainless steel fibre felt (condensed/pressed metallic fibres) with different fibre diameter and porosity under different operating pressures has been published [143]. It was found that when the fibre diameter increases under fixed porosity, thermal radiation and solid conduction plays more dominant role than natural air convection. Fibre diameter was found to be the major factor that determines the thermal radiation and affects the total effective thermal conductivity.

A remarkable study of CO_2 methanation reaction was published by NASA [144]. Conventional monolith reactor was compared with an improved Microlith™ reactor which was developed for long term space mission. Figure 1-31 shows the Microlith™ proposed as a support material with active Ru and Rh catalytic layers deposited on the surface of the fibres. Results showed

that improved Microlith™ reactor has a significant impact on the performance due to its better heat and mass transfer, high surface area and lower pressure drop compared to the traditional packed-bed reactor. CH_4 selectivity of ca. 100 % was achieved at space velocities of 30.000 - 60.000 h^{-1}.

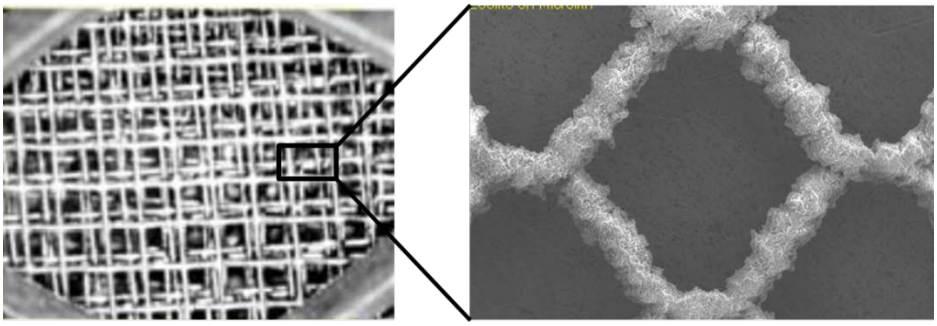

Figure 1-31. Photograph of Microlith™ (left) and catalytic coating on the fibres (right).

Figure 1-32 illustrates the difference in a boundary layer formation in a conventional monolith and Microlith™. It is noteworthy that the heat- and mass-transfer coefficients depend on the boundary layer thickness. In the case of a conventional long channel honeycomb monolith, a fully developed boundary layer is present over a considerable length of the catalytic surface, thus limiting the rate of reactant transport to the active sites. It was reported that this effect can be avoided when short channel length catalytic screens (e.g. Microlith™) are used.

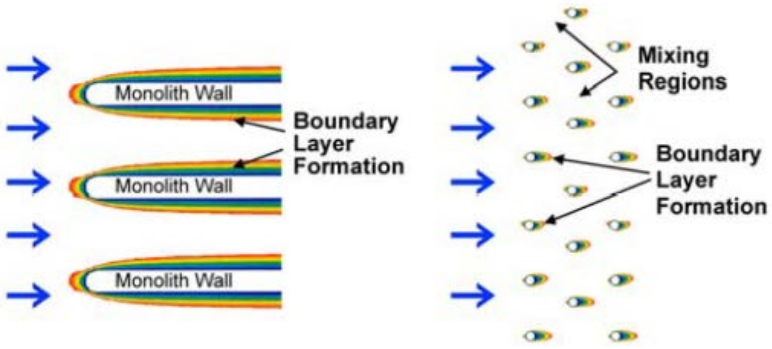

Figure 1-32. CFD analysis of boundary layer formation for a conventional monolith (left) and three Microlith™ screens (right) [144].

1.5.4. Additive manufacturing materials: state-of-the-art

Industrial application of additive manufacturing (AM) processes started at the end of 1980s [145], initially called ‘rapid prototyping’. AM technologies are used to manufacture materials for a wide range of applications such as biological applications [146, 147], (aero) space [148], automotive [149] industries and for other commercial consumer products (food, customized jewellery, watches etc.). AM route is already used for many years for the shaping polymeric materials. However in recent years, technology has been amplified to shape also metallic and ceramics materials.

In 2010, the American Society for Testing and Materials (ASTM) group developed a set of standards to classify the AM processes into 7 categories. In this section, main focus is given to AM processes for metals and alloys. Following categories are reviewed: selective laser sintering/melting (SLS/SLM), electron beam melting (EBM) and 3-Dimensional fibre deposition (3DFD).

Table 1-5. Additive manufacturing technologies for metallic/ceramic structures.

Technique	**Selective laser melting/sintering (SLM/SLS)**	**Electron beam melting (EBM)**	**3-Dimensional fibre deposition (3DFD)**
Formation process	powder bed fusion	powder bed fusion	paste extrusion
Shaping source	laser	electron beam	conventional sintering
Product	plastics, ceramics & metals	metals & alloys	ceramics, metals & alloys
Vacuum	-	+	-
Post-treatment[1]	+	+	-
Shrinkage	+	-	+
Dense material	-	+	+
Micro porosity	-	-	+
Reference	[150,151]	[152]	[153]

[1] – post treatment refers to polishing, ultrasonic cleaning, painting, heat-treatment etc.

Table 1-5 presents the characteristics of a few main AM technologies for the fabrication of metal structures. Presented technologies are based on the concept of "layer-by-layer" manufacturing, however, the material processing makes these techniques different [154]. The abovementioned techniques are based on powder laser melting/sintering and metal paste extrusion. The difference between the SLM and SLS processes is while in SLM process, metal powder melts entirely to create a homogenous structure, in SLS process, powder particles fuse together on molecular level but not fully melt. In the case of SLM/SLS techniques, the powder is spread uniformly by a wiper or roller. A high power-density laser melts the pre-deposited powder layer. The melted particles fuse and solidify to form a layer of the component. The main drawbacks of SLS/SLM techniques are poor surface quality, dimensional inaccuracy of the surface and pores caused by unmolten powder, limited cell (fibres/interfibre distances) dimensions, high costs of the equipment and materials (loss of powder) [155]. Moreover, post-surface treatment and post-cleaning to remove the non-sintered powder particles is necessary. The main drawbacks of EBM technique are cleaning and utrasonic treatment of the final structure in order to remove powder particles from the surface, especially for sharply shaped structures. Detailed explanation of SLS and EBM techniques can be found elsewhere [156–158].

For the first time, catalytic application of structures made by AM (Inkjet printing, IJP) technology was successfully demonstrated in 2007 [159]. In this study, the highly precise IJP technique allowed the control of the catalyst deposition (ultra-low platinum loading) on a polymer electrolyte. Recently, AM is started being used for the manufacture of the macro-structured catalytic supports for highly exothermic and highly endothermic reactions. The choice of the correct geometry

of the structure according to the application is as important as the material itself. The main benefit of the use of AM technologies is the manufacture of catalytic supports with the flexible design of possible complex geometries, material variability as well as adjustable porosity of the structures.

3DFD is one of the unique techniques to control the 3D-porosity in macro structured supports via controlled distances between the support struts, and stacking. This technique is based on the micro-extrusion: metallic or ceramic pastes are extruded through a thin nozzle, and the structure is built layer-by-layer. After being printed, 3DFD manufactured 'green' sample needs subsequent heat treatment (e.g. de-binding, calcination) by sintering at high temperature ovens, in air or under inert/reducing gas atmosphere, depending on the material. Furthermore, precise manufacturing is possible with 3DFD technique without any post-treatment. Structured catalysts can be manufactured by direct printing of catalytic material or in two steps: manufacture of the support structure and then deposition of the active catalytic layer. Figure 1-33 presents some metallic and ceramic samples manufactured by 3DFD technique.

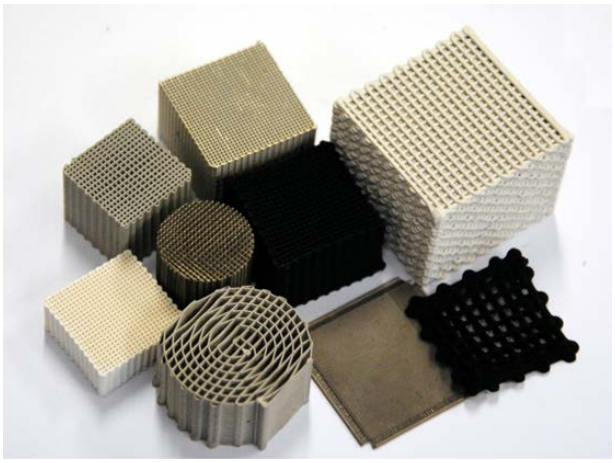

Figure 1-33. 3DFD manufactured metallic and ceramic structures.

The 3DFD manufactured structured catalysts were investigated for the conversion of methanol to light olefins (MTO) by Lefevere *et al.* in 2013 [22]. Manufactured supports were coated by wash-coating with zeolite layer ZSM-5 layer. The coated 3DFD structures of different geometries, coated cordierite monolith and powder catalyst were tested in MTO reaction at WHSV of 4.6-27.4 h^{-1}, at 350°C. At the lowest WHSV, the packed bed gave 85 % conversion while all structured catalysts showed ca. 90% conversion of methanol. At high WHSV, only 3DFD structured catalyst with 'zig-zag' channel geometry showed substantial conversion of methanol. This study proved the influence of the architecture on the catalytic performance. In another study, a ZSM-5 zeolite structure was manufactured by 3DFD technique and tested for CO_2 adsorption in 2017 by Couck *et al.* [160]. Results proved the excellent separation potential of porous materials. The structures showed a slight decreased in adsorption capacity compared to the pure powder, which is mainly due to the binder (35 wt.%) used for making monolithic structures. Recently, structured catalysts made by AM were

tested in Ullmann reactions by Tubio *et al.* [161]. Alumina based structured catalyst was manufactured by 3D-printing technique. Catalytic species (Cu) were immobilized in Al_2O_3 matrix. The Cu/Al_2O_3 3D-structured catalyst exhibited excellent catalytic performance in different Ullmann reactions without leaching. In a similar study, 13X and 5A zeolite monoliths fabricated by 3D-printing technique were tested for CO_2 removal from air [162]. The adsorption capacities of 5A and 13X monoliths were found to be 1.59 and 1.60 $mmol \cdot g^{-1}$, respectively, at 5000 ppm CO_2 in nitrogen at room temperature. In comparison with the packed bed, CO_2 breakthrough times on zeolite powders was found to be sharper indicating less mass transfer resistance in monolithic beds.

1.6. Catalytic coating on structured materials

Catalytic coating is used for the impregnation of catalysts onto structured support/reactor walls [102,109,163]. The choice of the coating procedure is crucial importance to achieve adhesive coating onto structured supports/reactors walls due to different adhesion strength of coatings on different support materials (e.g. ceramics, metals). Several coating techniques can be used depending on the application, type of the material, catalyst properties etc.

Coating procedure depends on type and geometry of the supports as well as on the surface properties. Materials with rough surface (e.g. ceramics) are easier to coat than materials with smoother surfaces (e.g. metals). In general, before coating, surface pre-treatment (thermal or chemical) of the support should be done in order to increase the surface roughness and the adhesion strength of the coating. For example, during the surface pre-treatment - calcination in air under high temperature - of Al contain alloys, micrometer alumina whiskers are formed on the surfaces which greatly enhance the surface roughness, therefore, increases the adhesion of the coating [164].

Quality of the coating is crucial for the life time of the structured catalyst. Different techniques can be applied to deposit the coating onto support materials, e.g. wash-coating, sol-gel coating, hydrothermal coating [165]. For example, in the case of flat geometries (planar plates), spray coating, electrochemical coating are the most suitable. Due to its easy application procedure, dip-coating is the most popular coating technique on lab and pilot-scale. For structures with complex geometries, dip-coating is recommended. The coating suspension can consist of ready catalyst particles or support materials, that can be further impregnated with an active phase (e.g. metal salt solution).

1.6.1. Dip-coating technique

Dip-coating is widely used to deposit active materials since it provides a uniform coating on complex-structured substrates. Dip-coating procedure consists of two steps: The first step is the preparation of the coating suspension and the immersion of the support structure for a certain time into it. The second step is the elimination of the excess suspension from the structure with subsequent drying or centrifugation. The scheme of a dip coating process is shown in Figure 1-34. The main parameters affecting the coating properties are the coating suspension composition and its rheological

properties. The standard ingredients of the coating slurry are powder (catalyst), binder, dispersant and water or organic solvent. Parameters such as particle size, viscosity, solid loading, pH and binder content are crucial to obtain the coating with desired thickness, good adhesion and uniformity [163].

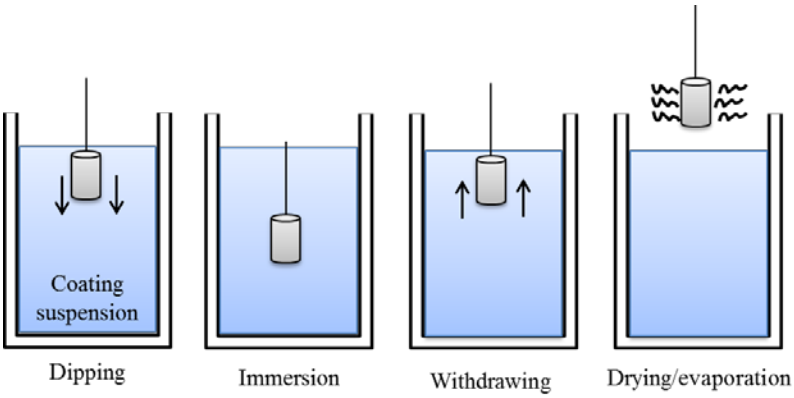

Figure 1-34. Dip-coating procedure.

Alumina is one of the commonly used support materials for catalytic applications. Hydrated aluminas are often used as an alumina precursor for wash-coating, because of their good dispensability in water and high surface area [166]. It was shown that the use of the powder particle size below 10 μm results in more homogenous coating [165]. It was reported by different research groups that too thick coating can lead to diffusion limitations, and thus to low catalyst performance [167]. Almedia *et al.* studied the influence of the catalytic layer thickness on monoliths for FTS [163]. Results showed that wash-coated layers thicker than 50 μm resulted in diffusion limitations. In a similar study, monoliths with a wash-coating thicker than 50 μm suffered from decreased CO conversion as a result of diffusion limitations [168].

The rheological properties of the coating suspension are strongly affected by the pH (acid concentration) [169]. A low pH of the coating suspension is needed to reach the maximum surface charge to keep the catalyst powder in its dispersed form, to avoid agglomeration and sedimentation of the suspension [170]. A successful study devoted to the tests of alumina coated metallic slabs and ceramic tubes for the catalytic combustion of CH_4 and CO oxidation reactions was reported by Valentini *et al.* [169]. In this study, structured catalysts were prepared by dip-coating of metallic and ceramic supports; catalyst layer thickness was around 30 μm on both substrates. This study proved that apparent viscosity is strongly affected by the HNO_3 concentration that plays an important role in the gelation/dispersion process.

Viscosity of the suspension is crucial for the quality of the coating: the higher the vicosity the lower the immersion time, thus more efficient coating procedure. However, depending on the support geometry, high viscosity might result in less homogenous coating and diffusion problems in the case of small or tortuous channelled structures, and as a consequence blockage of channels. Low viscosity of the coating slurry increases the immersion time (less loading per immersion), and gives cracks on

the coating surface. Another important requirement is clean and rough surface to achieve the adhesive coating. Furthermore, some small particles of binders (such as colloidal SiO_2) can promote the adhesion between coating and the surface. Regarding the binder content, it was reported that increasing binder concentration in the coating suspension resulted in better adhesion [22].

In another study, the effect of the different solvents on the coating characteristics on honeycomb supports was reported [171]. Results showed that the properties of the coating can be changed using different solvents in coating suspension, e.g. the corner effect can be avoided. Less accumulation of the coating suspension in the corners of the monolith's channels was observed using the suspension prepared with ethanol in comparison with the one with water.

1.6.2. Other coating techniques

Regarding sol-gel coating methods, the precursor material is dissolved in the solvent and not present as suspended particles. A catalytic sol-gel coating on stainless steel supports using thixotropic suspension was described by Truyen *et al.* [172]. It was reported that the coatings obtained by sol-gel method are homogeneous, but often too thin, thus multiple coating runs are needed to achieve the reasonable loading. Hydrothermal coating technique is based on the *in-situ* growth of the active layer on the support surface. The samples are immersed in the coating precursors mixture in a hydrothermal vessel, and excess coating is later removed. This technique is often used to grow zeolite layers on the structured substrates.

1.7. Summaries and outlook

This chapter presents an overview of existing methanation industrial processes, theoretical background and a detailed overview of CO_2 and CO methanation reactions on conventional and structured reactors/catalysts. Fundamental studies on methanation reaction kinetics, catalysts and catalyst deactivation are highlighted. Advanced types of reactors with improved heat transfer characteristics are reviewed. Different research groups showed that limitations of packed-bed reactors such as undesired heat gradients, uneven flow distribution and high pressure drops can be overcome by using structured catalysts/reactors. Structured reactors with improved heat transfer properties including metallic plates, monoliths, foams, and felts are described and compared with conventional systems. The main limitations of the structured catalysts/reactors are limited catalysts loading and high manufacturing costs.

Additional attention was paid to the innovative structured catalysts manufactured by AM techniques. The benefits of the use of AM technologies for manufacturing catalytic supports are flexible design of complex geometries, material variability as well as adjustable porosity of the structures. Several coating techniques for the integration of the catalysts onto the structured support/reactor walls were described. The effect of parameters such as particle size, viscosity, solid loading, pH and binder content was reported.

1.8. References

[1] E.S.R.L. US Department of Commerce, NOAA, NOAA Earth System Research Laboratory, Http://www.esrl.noaa.gov/. (n.d.). http://www.esrl.noaa.gov/ (accessed May 23, 2017).

[2] A roadmap for moving to competitive low carbon economy in 2050, European Commision, (2011) 112, 2011.

[3] W.R. Dunbar, N. Lior, R.A. Gaggioli, Combining fuel cells with fuel-fired power plants for improved exergy efficiency, Energy. 16 (1991) 1259–1274. doi:10.1016/0360-5442(91)90155-F.

[4] K. Hashimoto, N. Kumagai, K. Izumiya, H. Takano, Z. Kato, The production of renewable energy in the form of methane using electrolytic hydrogen generation, Energy. Sustain. Soc. 4 (2014) 17. doi:10.1186/s13705-014-0017-5.

[5] I. Partnership, Renewable Hydrogen Report, 2011. http://www.utcpower.com.

[6] Power-to-Gas Demonstration Projects, (n.d.). https://www.google.com/maps/d/viewer?mid=1G6iHbCZd91DCmJEIiv2EmGVDdno&ll=52.36212476985405%2C12.248792809472661&z=5 (accessed July 25, 2017).

[7] T. Schaaf, J. Grünig, M.R. Schuster, T. Rothenfluh, A. Orth, Methanation of CO_2 - storage of renewable energy in a gas distribution system, Energy. Sustain. Soc. 4 (2014) 1–14. doi:10.1186/s13705-014-0029-1.

[8] G. Gahleitner, Hydrogen from renewable electricity: An international review of power-to-gas pilot plants for stationary applications, Int. J. Hydrogen Energy. 38 (2013) 2039–2061. doi:10.1016/j.ijhydene.2012.12.010.

[9] The project Jupiter 1000, Demonstr. Massive Renew. Energy Storage into Transm. Gas Grid. (2017). http://www.jupiter1000.com/en/projet.html (accessed May 24, 2017).

[10] J. Kopyscinski, T.J. Schildhauer, S.M.A. Biollaz, Methanation in a fluidized bed reactor with high initial CO partial pressure: Part I-Experimental investigation of hydrodynamics, mass transfer effects, and carbon deposition, Chem. Eng. Sci. 66 (2011) 924–934. doi:10.1016/j.ces.2010.11.042.

[11] V. Tomašić, F. Jović, State-of-the-art in the monolithic catalysts/reactors, Appl. Catal. A Gen. 311 (2006) 112–121. doi:10.1016/j.apcata.2006.06.013.

[12] K.P. Brooks, J. Hu, H. Zhu, R.J. Kee, Methanation of carbon dioxide by hydrogen reduction using the Sabatier process in microchannel reactors, Chem. Eng. Sci. 62 (2007) 1161–1170. doi:10.1016/j.ces.2006.11.020.

[13] J. Ducamp, A. Bengaouer, P. Baurens, Modelling and experimental validation of a CO_2 methanation annular cooled fixed-bed reactor exchanger, Can. J. Chem. Eng. 9999 (2016) 1–12. doi:10.1002/cjce.22706.

[14] Z. Liu, B. Chu, X. Zhai, Y. Jin, Y. Cheng, Total methanation of syngas to synthetic natural gas over Ni catalyst in a micro-channel reactor, Fuel. 95 (2012) 599–605. doi:10.1016/j.fuel.2011.12.045.

[15] R. Zapf, C. Becker-Willinger, K. Berresheim, H. Bolz, H. Gnaser, V. Hessel, G. Kolb, P. Löb, A.-K. Pannqitt, A. Ziogas, Alumina-based catalyst coatings within microchannels and their testing, 81 (2003) 721–729.

[16] O. Görke, P. Pfeifer, K. Schubert, Highly selective methanation by the use of a microchannel

reactor, Catal. Today. 110 (2005) 132–139. doi:10.1016/j.cattod.2005.09.009.

[17] J. Hu, K.P. Brooks, J.D. Holladay, D.T. Howe, T.M. Simon, Catalyst development for microchannel reactors for martian in situ propellant production, Catal. Today. 125 (2007) 103–110. doi:10.1016/j.cattod.2007.01.067.

[18] C. Janke, M.S. Duyar, M. Hoskins, R. Farrauto, Catalytic and adsorption studies for the hydrogenation of CO_2 to methane, Appl. Catal. B Environ. 152–153 (2014) 184–191. doi:10.1016/j.apcatb.2014.01.016.

[19] C.Y. Zhao, Review on thermal transport in high porosity cellular metal foams with open cells, Int. J. Heat Mass Transf. 55 (2012) 3618–3632. doi:10.1016/j.ijheatmasstransfer.2012.03.017.

[20] M. Frey, D. Édouard, A.-C. Roger, Optimization of structured cellular foam-based catalysts for low-temperature carbon dioxide methanation in a platelet milli-reactor, Comptes Rendus Chim. 18 (2015) 283–292. doi:10.1016/j.crci.2015.01.002.

[21] S. Danaci, L. Protasova, J. Lefevere, L. Bedel, R. Guilet, P. Marty, Efficient CO_2 methanation over Ni/Al_2O_3 coated structured catalysts, Catal. Today. 273 (2016) 234–243. doi:10.1016/j.cattod.2016.04.019.

[22] J. Lefevere, M. Gysen, S. Mullens, V. Meynen, J. Van Noyen, The benefit of design of support architectures for zeolite coated structured catalysts for methanol-to-olefin conversion, Catal. Today. 216 (2013) 18–23. doi:10.1016/j.cattod.2013.05.020.

[23] J.B. Sabatier, P., Senderens, New synthesis of methane, Comptes Rendus 134. 134 (1902) 514–516.

[24] J. Gao, Y. Wang, Y. Ping, D. Hu, G. Xu, F. Gu, F. Su, A thermodynamic analysis of methanation reactions of carbon oxides for the production of synthetic natural gas, RSC Adv. 2 (2012) 2358. doi:10.1039/c2ra00632d.

[25] A. Beuls, C. Swalus, M. Jacquemin, G. Heyen, A. Karelovic, P. Ruiz, Methanation of CO_2: Further insight into the mechanism over $Rh/\gamma\text{-}Al_2O_3$ catalyst, Appl. Catal. B Environ. 113–114 (2012) 2–10. doi:10.1016/j.apcatb.2011.02.033.

[26] F. Koschany, D. Schlereth, O. Hinrichsen, On the kinetics of the methanation of carbon dioxide on coprecipitated NiAl(O)x, Appl. Catal. B Environ. 181 (2016) 504–516. doi:10.1016/j.apcatb.2015.07.026.

[27] J.N. Dew, R.R. White, C.M. Sliepcevich, Hydrogenation of carbon dioxide on Nickel-kieselguhr catalyst, Ind. Eng. Chem. 47 (1955) 140–146. doi:10.1021/ie50541a044.

[28] T. Van Herwijnen, H. Van Doesburg, W. a De Jong, Kinetics of the methanation of CO and CO_2 on a nickel catalyst, J. Catal. 28 (1973) 391–402. doi:10.1016/0021-9517(73)90132-2.

[29] G.D. Weatherbee, C.H. Bartholomew, Hydrogenation of CO_2 on Group VIII Metals, J. Catal. 77 (1982) 460–472. doi:doi:10.1016/0021-9517(81)90040-3.

[30] J.H. Chiang, J.R. Hopper, Kinetics of the hydrogenation of carbon dioxide over supported nickel, Ind. Eng. Chem. Prod. Res. Dev. 22 (1983) 225–228. doi:10.1021/i300010a011.

[31] H. Inoue, M. Funakoshi, Kinetics of methanation of carbon monoxide and carbon dioxide., J. Chem. Eng. Japan. 17 (1984) 602–610. doi:10.1252/jcej.17.602.

[32] K. Takami, T. Takeshige, Kinetics of the methanation of carbon dioxide over a supported $Ni\text{-}La_2O_3$ catalyst, Can. J. Chem. Eng. 66 (1988) 343–347.

[33] J. Xu, G.F. Froment, Methane steam reforming , methanation and water-gas shift : 1 . intrinsic kinetics, Am. Inst. Chem. Eng. J. 35 (1989) 88–96. doi:10.1002/aic.690350109.

[34] M. Marwood, R. Doepper, A. Renken, In-situ surface and gas phase analysis for kinetic studies under transient conditions The catalytic hydrogenation of CO_2, Appl. Catal. A Gen. 151 (1997) 223–246. doi:10.1016/S0926-860X(96)00267-0.

[35] F.W. Chang, M.S. Kuo, M.T. Tsay, M.C. Hsieh, Hydrogenation of CO_2 over nickel catalysts on rice husk ash-alumina prepared by incipient wetness impregnation, Appl. Catal. A Gen. 247 (2003) 309–320. doi:10.1016/S0926-860X(03)00181-9.

[36] W.A. Wan Abu Bakar, R. Ali, N.S. Mohammad, The effect of noble metals on catalytic methanation reaction over supported Mn/Ni oxide based catalysts, Arab. J. Chem. (2013). doi:10.1016/j.arabjc.2013.06.009.

[37] A.H. Zamani, R. Ali, W.A.W.A. Bakar, The investigation of Ru/Mn/Cu-Al_2O_3 oxide catalysts for CO_2/H_2 methanation in natural gas, J. Taiwan Inst. Chem. Eng. 45 (2014) 143–152. doi:10.1016/j.jtice.2013.04.009.

[38] M. Behrens, Coprecipitation: An excellent tool for the synthesis of supported metal catalysts - From the understanding of the well known recipes to new materials, Catal. Today. 246 (2015) 46–54. doi:10.1016/j.cattod.2014.07.050.

[39] A.E. Aksoylu, Z.I. Önsan, Hydrogenation of carbon oxides using coprecipitated and impregnated Ni/Al_2O_3 catalysts, Appl. Catal. A Gen. 164 (1997) 1–11. doi:10.1016/S0926-860X(97)00151-8.

[40] F. Meng, Z. Li, F. Ji, M. Li, Effect of ZrO_2 on catalyst structure and catalytic methanation performance over Ni-based catalyst in slurry-bed reactor, Int. J. Hydrogen Energy. (2015) 1–11. doi:10.1016/j.ijhydene.2015.05.057.

[41] F. Ocampo, B. Louis, A.-C. Roger, Methanation of carbon dioxide over nickel-based $Ce_{0.72}Zr_{0.28}O_2$ mixed oxide catalysts prepared by sol–gel method, Appl. Catal. A Gen. 369 (2009) 90–96. doi:10.1016/j.apcata.2009.09.005.

[42] F. Ocampo, B. Louis, L. Kiwi-Minsker, A.C. Roger, Effect of Ce/Zr composition and noble metal promotion on nickel based $Ce_xZr_{1-x}O_2$ catalysts for carbon dioxide methanation, Appl. Catal. A Gen. 392 (2011) 36–44. doi:10.1016/j.apcata.2010.10.025.

[43] M.A.A. Aziz, A.A. Jalil, S. Triwahyono, R.R. Mukti, Y.H. Taufiq-Yap, M.R. Sazegar, Highly active Ni-promoted mesostructured silica nanoparticles for CO_2 methanation, Appl. Catal. B Environ. 147 (2014) 359–368. doi:10.1016/j.apcatb.2013.09.015.

[44] M. Kuśmierz, Kinetic study on carbon dioxide hydrogenation over Ru/γ-Al_2O_3 catalysts, Catal. Today. 137 (2008) 429–432. doi:10.1016/j.cattod.2008.03.003.

[45] Lukas Grond, Paula Schulze, Johan Holstein, Final Report: Systems Analyses Power to Gas, 2013.

[46] S. Rahmani, M. Rezaei, F. Meshkani, Preparation of highly active nickel catalysts supported on mesoporous nanocrystalline γ-Al_2O_3 for CO_2 methanation, J. Ind. Eng. Chem. 20 (2014) 1346–1352. doi:10.1016/j.jiec.2013.07.017.

[47] H. Liu, X. Zou, X. Wang, X. Lu, W. Ding, Effect of CeO_2 addition on Ni/Al_2O_3 catalysts for methanation of carbon dioxide with hydrogen, J. Nat. Gas Chem. 21 (2012) 703–707. doi:10.1016/S1003-9953(11)60422-2.

[48] J. Sehested, K.E. Larsen, A.L. Kustov, A.M. Frey, T. Johannessen, T. Bligaard, M.P. Andersson, J.K. Nørskov, C.H. Christensen, Discovery of technical methanation catalysts based on computational screening, Top. Catal. 45 (2007) 9–13. doi:10.1007/s11244-007-0232-9.

[49] G. Du, S. Lim, Y. Yang, C. Wang, L. Pfefferle, G.L. Haller, Methanation of carbon dioxide on Ni-incorporated MCM-41 catalysts: The influence of catalyst pretreatment and study of steady-state reaction, J. Catal. 249 (2007) 370–379. doi:10.1016/j.jcat.2007.03.029.

[50] A. Karelovic, P. Ruiz, CO_2 hydrogenation at low temperature over Rh/γ-Al_2O_3 catalysts: Effect of the metal particle size on catalytic performances and reaction mechanism, Appl. Catal. B Environ. 113–114 (2012) 237–249. doi:10.1016/j.apcatb.2011.11.043.

[51] H. Zhu, R. Razzaq, C. Li, Y. Muhmmad, S. Zhang, Catalytic methanation of carbon dioxide by active oxygen material $Ce_xZr_{1-x}O_2$ supported Ni-Co bimetallic nanocatalysts, Am. Inst. Chem. Eng. AIChE J. 59 (2013) 2567–2576. doi:10.1002/aic.14026.

[52] H. Song, J. Yang, J. Zhao, L. Chou, Methanation of carbon dioxide over a highly dispersed Ni/La_2O_3 catalyst, Chinese J. Catal. 31 (2010) 21–23. doi:10.1016/S1872-2067(09)60036-X.

[53] W. Wang, W. Chu, N. Wang, W. Yang, C. Jiang, Mesoporous nickel catalyst supported on multi-walled carbon nanotubes for carbon dioxide methanation, Int. J. Hydrogen Energy. 41 (2016) 967–975. doi:10.1016/j.ijhydene.2015.11.133.

[54] A.H. Zamani, R. Ali, W.A.W. Abu Bakar, Optimization of CO_2 methanation reaction over M*/Mn/Cu–Al_2O_3 (M*: Pd, Rh and Ru) catalysts, J. Ind. Eng. Chem. 29 (2015) 238–248. doi:10.1016/j.jiec.2015.02.028.

[55] M. Cai, J. Wen, W. Chu, X. Cheng, Z. Li, Methanation of carbon dioxide on Ni/ZrO_2-Al_2O_3 catalysts: Effects of ZrO_2 promoter and preparation method of novel ZrO_2-Al_2O_3 carrier, J. Nat. Gas Chem. (2011). doi:10.1016/S1003-9953(10)60187-9.

[56] W. Brockner, C. Ehrhardt, M. Gjikaj, Thermal decomposition of nickel nitrate hexahydrate, $Ni(NO_3)_2.6H_2O$, in comparison to $Co(NO_3)_2.6H_2O$ and $Ca(NO_3)_2.4H_2O$, Thermochim. Acta. 456 (2007) 64–68. doi:10.1016/j.tca.2007.01.031.

[57] W.A.W. Abu Bakar, R. Ali, S. Toemen, Catalytic methanation reaction over supported nickel-ruthenium oxide base for purification of simulated natural gas, Sci. Iran. 19 (2012) 525–534. doi:10.1016/j.scient.2012.02.004.

[58] M.B.I. Choudhury, S. Ahmed, M. a Shalabi, T. Inui, Characterization of multi-component methanation catalysts by temperature-programmed reduction method to develop novel type methanation catalyst ., (n.d.) 1–10.

[59] P. Forzatti, Catalyst deactivation, Catal. Today. 52 (1999) 165–181. doi:10.1016/S0920-5861(99)00074-7.

[60] I.C. Mart, Carbon Dioxide Methanation for Intensified Reactors, 2015.

[61] M.K. Mondal, H.K. Balsora, P. Varshney, Progress and trends in CO_2 capture/separation technologies: A review, Energy. 46 (2012) 431–441. doi:10.1016/j.energy.2012.08.006.

[62] M. Mozaffarian, Z. R.W.R., Feasibility Of Biomass / Waste-Related SNG Production Technologies Final report, 2003. doi:249-01-03-12-0001.

[63] K. Müller, M. Fleige, F. Rachow, D. Schmeißer, Sabatier based CO_2-methanation of flue gas emitted by conventional power plants, Energy Procedia. 40 (2013) 240–248.

doi:10.1016/j.egypro.2013.08.028.

[64] C.H. Bartholomew, Mechanism of catalyst deactivation, Appl. Catal. A Gen. 212 (2001) 17–60. doi:http://dx.doi.org/10.1016/S0926-860X(00)00843-7.

[65] M. Argyle, C. Bartholomew, Heterogeneous catalyst deactivation and regeneration: A review, Catalysts. 5 (2015) 145–269. doi:10.3390/catal5010145.

[66] C.H. Bartholomew, Catalyst deactivation 1994, Proceedings of the 6th International Symposium, Elsevier, 1994. doi:10.1016/S0167-2991(08)62726-3.

[67] J. Zhang, Z. Xin, X. Meng, Y. Lv, M. Tao, Effect of MoO_3 on the heat resistant performances of nickel based MCM-41 methanation catalysts, Fuel. 116 (2014) 25–33. doi:10.1016/j.fuel.2013.07.102.

[68] R. Razzaq, C. Li, M. Usman, K. Suzuki, S. Zhang, A highly active and stable Co_4N/γ-Al_2O_3 catalyst for CO and CO_2 methanation to produce synthetic natural gas (SNG), Chem. Eng. J. 262 (2015) 1090–1098. doi:10.1016/j.cej.2014.10.073.

[69] M.A. Lucchini, A. Testino, A. Kambolis, C. Proff, C. Ludwig, Sintering and coking resistant core-shell microporous silica-nickel nanoparticles for CO methanation: Towards advanced catalysts production, Appl. Catal. B Environ. 182 (2016) 94–101. doi:10.1016/j.apcatb.2015.09.012.

[70] A. Kambolis, D. Ferri, Y. Lu, S.N. Yannopoulos, S. Pokrant, D. Rentsch, O. Kröcher, Structural Modification of Ni/γ-Al_2O_3 with Boron for Enhanced Carbon Resistance during CO Methanation, ChemCatChem. 7 (2015) 3261–3265. doi:10.1002/cctc.201500567.

[71] M. Götz, J. Lefebvre, F. Mörs, A. McDaniel Koch, F. Graf, S. Bajohr, R. Reimert, T. Kolb, Renewable Power-to-Gas: A technological and economic review, Renew. Energy. 85 (2016) 1371–1390. doi:10.1016/j.renene.2015.07.066.

[72] L.F. Albright, Albright's Chemical Engineering Handbook, CRC Press, 2008. https://books.google.com/books?id=HYB3Udjx_FYC&pgis=1 (accessed May 22, 2016).

[73] K.-H. Eisenlohr, F.W. Moeller, M. Dry, Influence of certain reaction parameters on methanation of coal to SNG, n.d.

[74] H. Iskov, N. Rasmussen, Global screening of projects and technologies for Power-to-Gas and Bio-SNG, 2013. https://www.energinet.dk/SiteCollectionDocuments/Engelske dokumenter/Forskning/global_screening_08112013_final.pdf.

[75] J.H. Jensen, J.M. Poulsen, N.U. Andersen, From coal to clean energy, Nitrogen+Syngas 310. (2011).

[76] J. Kopyscinski, T.J. Schildhauer, S.M. a Biollaz, Production of synthetic natural gas (SNG) from coal and dry biomass - A technology review from 1950 to 2009, Fuel. 89 (2010) 1763–1783. doi:10.1016/j.fuel.2010.01.027.

[77] M. Sudiro, a Bertucco, Synthetic Natural Gas (SNG) from coal and biomass: a survey of existing process technologies, open issues and perspectives, Nat. Gas. (2010) 105–127. doi:10.5772/9835.

[78] W. G.A., R. T.R., S. D.W., The RMP process, A.C.S. Fuels Div. Prepr. 19 (1974) 57–69.

[79] B. Luigi, A new, safe & cost-effective route to SNG Foster Wheeler VESTA technology, (2014) 2014.

[80] S. Rönsch, J. Schneider, S. Matthischke, M. Schlüter, M. Götz, J. Lefebvre, P. Prabhakaran, S. Bajohr, Review on methanation – From fundamentals to current projects, Fuel. 166 (2016) 276–296. doi:10.1016/j.fuel.2015.10.111.

[81] B. G., B. J., R. R.B., SGC report: Power-to-Gas – A technical review, 2013. doi:SGC Rapport 2013:284.

[82] Johnson Matthey Process Technologies, (n.d.). http://www.jmprotech.com/ (accessed March 15, 2016).

[83] G. Eigenberger, C. Verfahrenstechnik, U. Stuttgart, Fixed-Bed Reactors, 1992.

[84] B.Y. Traa, J. Weitkamp, Kinetics of the methanation of carbon dioxide over ruthenium on titania, Chem. Eng. Commun. 21 (1999) 291–293.

[85] M.M. Zyryanova, P. V. Snytnikov, Y.I. Amosov, V.A. Kuzmin, V.A. Kirillov, V.A. Sobyanin, Design, scale-out, and operation of a preferential CO methanation reactor with a nickel-ceria catalyst, Chem. Eng. J. 176–177 (2011) 106–113. doi:10.1016/j.cej.2011.03.085.

[86] S. Huang, Y. Zhang, S. Chen, M. Shang, Effect of promoter on performance of CuO-ZnO-Al_2O_3 catalyst for CO_2 hydrogenation to methanol, Shiyou Huagong/Petrochemical Technol. 39 (2011) 912–917. doi:10.1016/S1872-5813(12)60002-4.

[87] D. Schlereth, O. Hinrichsen, A fixed-bed reactor modeling study on the methanation of CO_2, Chem. Eng. Res. Des. 92 (2014) 702–712. doi:10.1016/j.cherd.2013.11.014.

[88] N.R. Parlikkad, S. Chambrey, P. Fongarland, N. Fatah, A. Khodakov, S. Capela, O. Guerrini, Modeling of fixed bed methanation reactor for syngas production: Operating window and performance characteristics, Fuel. 107 (2013) 254–260. doi:10.1016/j.fuel.2013.01.024.

[89] J. Porubova, G. Bazbauers, D. Markova, Modeling of the adiabatic and isothermal methanation process, Sci. J. Riga Tech. Univ. Environ. Clim. Technol. 6 (2011) 79–84. doi:10.2478/v10145-011-0011-5.

[90] J. Kopyscinski, Production of synthetic natural gas in a fluidized bed reactor, 19AD. doi:10.3929/ethz-a-006031831.

[91] N.B. Rasmussen, toposoe Technologies relevant for gasification and methanation in Denmark, (2012) 1–38.

[92] S.H. Ensell RL, The British gas HICOM methanation process for SNG production., in: Proc. Int. Gas Res. Conf., British Gas Corporation UK, 1983: pp. 472–81.

[93] L. Romano, F. Ruggeri, Methane from syngas – status of amec Foster Wheeler VESTA technology development, Energy Procedia. 81 (2015) 249–254. doi:http://dx.doi.org/10.1016/j.egypro.2015.12.092.

[94] Audi e-gas project, AUDI AG, (n.d.). http://www.audi.com/corporate/en/corporate-responsibility/we-live-responsibility/product/audi-e-gas-project.html#fullwidthpar__ah_2 (accessed July 23, 2017).

[95] U. Zuberbühler, M. Specht, 9 . International renewable energy storage conferencePower-to-Gas (P2G®): Technical progress and perspectives, ZSW – Cent. Sol. Energy Hydrog. Res. Stuttgart. (2015).

[96] C.G. Hill, J. Wiley, G. Charles, An introduction to chemical engineering kinetics & reactor design, John Wiley & Sons, 1977.

[97] B. Liu, S. Ji, Comparative study of fluidized-bed and fixed-bed reactor for syngas methanation over Ni-W/TiO_2-SiO_2 catalyst, J. Energy Chem. 22 (2013) 740–746. doi:10.1016/S2095-4956(13)60098-4.

[98] J. Liu, D. Cui, J. Yu, F. Su, G. Xu, Performance characteristics of fluidized bed syngas methanation over Ni–Mg/Al_2O_3 catalyst, Chinese J. Chem. Eng. 23 (2015) 86–92. doi:10.1016/j.cjche.2014.09.038.

[99] R.C. Streeter, Recent developments in fluidized-bed methanation research, Proc. Ninth Synth. Pipeline Gas Symp. (1977) 153–165.

[100] X. Guo, Y. Fan, L. Luo, Multi-channel heat exchanger-reactor using arborescent distributors: A characterization study of fluid distribution, heat exchange performance and exothermic reaction, Energy. 69 (2014) 728–741. doi:10.1016/j.energy.2014.03.069.

[101] J. Ducamp, Conception et optimisation d ’un réacteur-échangeur structuré pour l’hydrogénation du dioxyde de carbone en méthane de synthèse dédié à la filière de stockage d’énergie électrique renouvelable, l’université de Strasbourg, 2015.

[102] L. Kiwi-Minsker, A. Renken, Microstructured reactors for catalytic reactions, Catal. Today. 110 (2005) 2–14. doi:10.1016/j.cattod.2005.09.011.

[103] J.M. Commenge, L. Falk, J.P. Corriou, M. Matlosz, Optimal design for flow uniformity in microchannel reactors, 48 (2002) 345–358. doi:10.1002/aic.690480218.

[104] M.W. Losey, M. a Schmidt, K.F. Jensen, A micro packed-bed reactor for chemical synthesis, in: 3rd Int. Conf. Microreact. Technol., Springer, Heidelberg, 1999: pp. 277–286. doi:10.1007/978-3-642-59738-1.

[105] G. Kolb, V. Hessel, Micro-structured reactors for gas phase reactions, Chem. Eng. J. 98 (2004) 1–38. doi:10.1016/j.cej.2003.10.005.

[106] A. Delparish, A.K. Avci, Intensified catalytic reactors for Fischer-Tropsch synthesis and for reforming of renewable fuels to hydrogen and synthesis gas, Fuel Process. Technol. 151 (2016) 72–100. doi:10.1016/j.fuproc.2016.05.021.

[107] T. W.E., K. D.L., B. K.P., B.J. Golladay, R.S. Wegeng, Optimizing microchannel reactors by trading-off equilibrium and reaction kinetics through temperature management, in: AIChE Spring Natl. Meet. New Orleans, 2002: pp. 1–11.

[108] C.-B. Lee, S.-H. Cho, D.-W. Lee, K.-R. Hwang, J.-S. Park, S.-H. Kim, Combination of preferential CO oxidation and methanation in hybrid MCR (micro-channel reactor) for CO clean-up, Energy. 78 (2014) 421–425. doi:10.1016/j.energy.2014.10.029.

[109] A. Stefanescu, A.C. van Veen, C. Mirodatos, J.C. Beziat, E. Duval-Brunel, Wall coating optimization for microchannel reactors, Catal. Today. 125 (2007) 16–23. doi:10.1016/j.cattod.2007.01.074.

[110] J. Kopyscinski, T.J. Schildhauer, F. Vogel, S.M. a Biollaz, A. Wokaun, Applying spatially resolved concentration and temperature measurements in a catalytic plate reactor for the kinetic study of CO methanation, J. Catal. 271 (2010) 262–279. doi:10.1016/j.jcat.2010.02.008.

[111] I.P. Kandylas, A.M. Stamatelos, Engine exhaust system design based on heat transfer computation, Energy Convers. Manag. 40 (1999) 1057–1072. doi:10.1016/S0196-8904(99)00008-4.

[112] M. Noda, H. Nishitani, Flexible heat exchanger network design for chemical processes with operation mode changes, in: 16th Eur. Symp. Comput. Aided Process Eng. 9th Int. Symp. Process Syst. Eng., 2006: pp. 925–930.

[113] V. Tomašić, Z. Gomzi, S. Zrnčević, Analysis and modeling of a monolithic reactor, Chem. Eng. Technol. 29 (2006) 59–65. doi:10.1002/ceat.200500100.

[114] A. Cybulski, J.A. Moulijn, Monoliths in heterogeneous catalysis, Catal. Rev. 36 (1994) 179–270. doi:10.1080/01614949408013925.

[115] G. Groppi, E. Tronconi, Honeycomb supports with high thermal conductivity for gas/solid chemical processes, in: Catal. Today, 2005. doi:10.1016/j.cattod.2005.06.041.

[116] T. Boger, A.K. Heibel, Heat transfer in conductive monolith structures, Chem. Eng. Sci. 60 (2005) 1823–1835. doi:10.1016/j.ces.2004.11.031.

[117] C.G. Visconti, G. Groppi, E. Tronconi, Accurate prediction of the effective radial conductivity of highly conductive honeycomb monoliths with square channels, Chem. Eng. J. (2013). doi:10.1016/j.cej.2013.02.095.

[118] O. Sanz, I. Velasco, I. Reyero, I. Legorburu, G. Arzamendi, L.M. Gandía, M. Montes, Effect of the thermal conductivity of metallic monoliths on methanol steam reforming, Catal. Today. 273 (2016) 131–139. doi:10.1016/j.cattod.2016.03.008.

[119] M. Sudiro, A. Bertucco, G. Groppi, E. Tronconi, Simulation of a structured catalytic reactor for exothermic methanation reactions producing synthetic natural gas, Comput. Aided Chem. Eng. 28 (2010) 691–696. doi:10.1016/S1570-7946(10)28116-6.

[120] D. Schlereth, P.J. Donaubauer, O. Hinrichsen, Metallic honeycombs as catalyst supports for methanation of carbon dioxide, Chem. Eng. Technol. 38 (2015) 1845–1852. doi:10.1002/ceat.201400717.

[121] M. Lehner, Methanation process development utilizing ceramic honeycomb catalysts, in: 3rd Nuremb. Work. Methanation Second Gener. Fuels, 2016: pp. 1–6.

[122] Z. Taslicukur, C. Balaban, N. Kuskonmaz, Production of ceramic foam filters for molten metal filtration using expanded polystyrene, J. Eur. Ceram. Soc. 27 (2007) 637–640. doi:10.1016/j.jeurceramsoc.2006.04.129.

[123] L.N.W. Damoah, L. Zhang, AlF_3 reactive Al_2O_3 foam filter for the removal of dissolved impurities from molten aluminum: Preliminary results, Acta Mater. 59 (2011) 896–913. doi:10.1016/j.actamat.2010.09.064.

[124] A.K. Ismail, M.Z. Abdullah, M. Zubair, A.R. Jamaludin, Z.A. Ahmad, Effect of ceramic coating in combustion and cogeneration performance of Al_2O_3 porous medium, J. Energy Inst. (2015) 1–13. doi:10.1016/j.joei.2015.01.008.

[125] J.T. Richardson, Y. Peng, D. Remue, Properties of ceramic foam catalyst supports: Pressure drop, Appl. Catal. A Gen. 204 (2000) 19–32. doi:10.1016/S0926-860X(00)00508-1.

[126] R. Poss, B. Kloeden, A. Dreher, G. Walther, High temperature Nickel and Iron-based alloy metal foams for filtration applications, 2010.

[127] Z. Anxionnaz, M. Cabassud, C. Gourdon, P. Tochon, Heat exchanger/reactors (HEX reactors): Concepts, technologies: State-of-the-art, Chem. Eng. Process. Process Intensif. 47 (2008) 2029–2050. doi:10.1016/j.cep.2008.06.012.

[128] S. Mancin, C. Zilio, A. Cavallini, L. Rossetto, Heat transfer during air flow in aluminum

foams, Int. J. Heat Mass Transf. 53 (2010) 4976–4984. doi:10.1016/j.ijheatmasstransfer.2010.05.033.

[129] Enrico Bianchi, An appraisal of the heat transfer properties of metallic open-cell foams for strongly exo-/endo-thermic catalytic processes in tubular reactors, Chem. Eng. J. 198–199 (2012) 512–528.

[130] J. Banhart, Manufacturing routes for metallic foams, JOM. 52 (2000) 22–27. doi:10.1007/s11837-000-0062-8.

[131] M. Maestri, A. Beretta, G. Groppi, E. Tronconi, P. Forzatti, Comparison among structured and packed-bed reactors for the catalytic partial oxidation of CH_4 at short contact times, Catal. Today. 105 (2005) 709–717. doi:10.1016/j.cattod.2005.06.045.

[132] E. Bianchi, T. Heidig, C.G. Visconti, G. Groppi, H. Freund, E. Tronconi, An appraisal of the heat transfer properties of metallic open-cell foams for strongly exo-/endo-thermic catalytic processes in tubular reactors, Chem. Eng. J. 198–199 (2012) 512–528. doi:10.1016/j.cej.2012.05.045.

[133] M. Frey, T. Romero, A.-C. Roger, D. Edouard, Open cell foam catalysts for CO_2 methanation: Presentation of coating procedures and in situ exothermicity reaction study by infrared thermography, Catal. Today. 273 (2016) 83–90. doi:10.1016/j.cattod.2016.03.016.

[134] M. Frey, A. Bengaouer, G. Geffraye, D. Edouard, A.-C. Roger, Aluminium open cell foams as efficient support for CO_2 methanation catalyst: pilot scale reaction results, Energy Technol. (2017). doi:10.1002/ente.201700188.

[135] Y. Li, Q. Zhang, R. Chai, G. Zhao, F. Cao, Y. Liu, Y. Lu, Metal-foam-structured Ni-Al_2O_3 catalysts: Wet chemical etching preparation and syngas methanation performance, Appl. Catal. A Gen. 510 (2016) 216–226. doi:10.1016/j.apcata.2015.11.034.

[136] B. Tatarchuk, H. Yang, R. Kalluri, D. Cahela, Microfibrous media for optimizing and controlling highly exothermic and highly endothermic reactions/processes, 2011.

[137] G. Groppi, E. Tronconi, G. Bozzano, M. Dente, Experimental and theoretical study of gas/solid mass transfer in metallic filters as supports for micro-structured catalysts, Chem. Eng. Sci. 65 (2010) 392–397. doi:10.1016/j.ces.2009.06.038.

[138] M. Sheng, H. Yang, D.R. Cahela, W.R. Yantz, C.F. Gonzalez, B.J. Tatarchuk, High conductivity catalyst structures for applications in exothermic reactions, Appl. Catal. A Gen. 445–446 (2012) 143–152. doi:10.1016/j.apcata.2012.08.012.

[139] M. Sheng, C. Gonzalez, W. Yantz, D. Cahela, H. Yang, D. Harris, B. Tatarchuk, Micro-scale heat transfer comparison between packed beds and micro-fibrous entrained calalysts, Eng. Appl. Comput. Fluid Mech. 7 (2013) 471–485. doi:10.1080/19942060.2013.11015486.

[140] X. Cheng, H. Yang, B.J. Tatarchuk, Microfibrous entrapped hybrid iron-based catalysts for Fischer–Tropsch synthesis, Catal. Today. 273 (2016) 62–71. doi:10.1016/j.cattod.2016.02.048.

[141] M. Sheng, H. Yang, D.R. Cahela, B.J. Tatarchuk, Novel catalyst structures with enhanced heat transfer characteristics, J. Catal. 281 (2011) 254–262. doi:10.1016/j.jcat.2011.05.006.

[142] M. Sheng, D.R. Cahela, H. Yang, C.F. Gonzalez, W.R. Yantz, D.K. Harris, B.J. Tatarchuk, Effective thermal conductivity and junction factor for sintered microfibrous materials, Int. J. Heat Mass Transf. 56 (2013) 10–19. doi:10.1016/j.ijheatmasstransfer.2012.08.015.

[143] W.Q. Li, Z.G. Qu, Experimental study of effective thermal conductivity of stainless steel fiber felt, Appl. Therm. Eng. 86 (2015) 119–126. doi:10.1016/j.applthermaleng.2015.04.024.

[144] C. Junaedi, K. Hawley, D. Walsh, S. Roychoudhury, M.B. Abney, J.L. Perry, Compact and lightweight sabatier reactor for carbon dioxide reduction, in: 41sr Int. Conf. Environ. Syst., 2011.

[145] J.-P. Kruth, M.C. Leu, T. Nakagawa, Progress in additive manufacturing and rapid prototyping, CIRP Ann. - Manuf. Technol. 47 (1998) 525–540. doi:10.1016/S0007-8506(07)63240-5.

[146] S.W. Mok, R. Nizak, S.C. Fu, K.W.K. Ho, L. Qin, D.B.F. Saris, K.M. Chan, J. Malda, From the printer: Potential of three-dimensional printing for orthopaedic applications, J. Orthop. Transl. 6 (2016) 42–49. doi:10.1016/j.jot.2016.04.003.

[147] H. Shao, Y. He, J. Fu, D. He, X. Yang, J. Xie, C. Yao, J. Ye, S. Xu, Z. Gou, 3D printing magnesium-doped wollastonite/β-TCP bioceramics scaffolds with high strength and adjustable degradation, J. Eur. Ceram. Soc. 36 (2015) 1495–1503. doi:10.1016/j.jeurceramsoc.2016.01.010.

[148] R. Liu, Z. Wang, T. Sparks, F. Liou, J. Newkirk, Aerospace applications of laser additive manufacturing, Elsevier Ltd, 2017. doi:10.1016/B978-0-08-100433-3.00013-0.

[149] L.E. Murr, Frontiers of 3D printing/additive manufacturing: From human organs to aircraft fabrication, J. Mater. Sci. Technol. 32 (2016) 987–995. doi:10.1016/j.jmst.2016.08.011.

[150] C.R. Deckard, J.J. Beaman, J.F. Darrah, Method for selective laser sintering with layerwise cross-scanning, 1992.

[151] G. Coykendall, Introduction to additive manufacturing processes and terminology, 2012.

[152] Electron beam melting - EBM process, additive manufacturing | Arcam AB, (n.d.). http://www.arcam.com/technology/electron-beam-melting/ (accessed February 15, 2016).

[153] S.H.R.W. Mullens, I. Thijs, J.R. Luyten, W.L. Bouwen, EP 2 195 131 B1 - Method for producing a three-dimensional macroporous filament construct based on phase inversion and construct thereby obtained CA2696386A1, CA2696386A1, 2009.

[154] R.J. Silva, G.F. Barbosa, J. Carvalho, Additive manufacturing of metal parts by welding, IFAC Proc. Vol. 48 (2015) 2318–2322. doi:10.1016/j.ifacol.2015.06.433.

[155] E.O. Olakanmi, R.F. Cochrane, K.W. Dalgarno, A review on selective laser sintering/melting (SLS/SLM) of aluminium alloy powders: Processing, microstructure, and properties, Prog. Mater. Sci. 74 (2015) 401–477. doi:10.1016/j.pmatsci.2015.03.002.

[156] L. Loeber, S. Biamino, U. Ackelid, S. Sabbadini, P. Epicoco, P. Fino, J. Eckert, Comparison of selective laser and electron beam melted titanium aluminides, 22nd Annu. Int. Solid Free. Fabr. Symp. - An Addit. Manuf. Conf. SFF 2011. (2011) 547–556. http://www.scopus.com/inward/record.url?eid=2-s2.0-84898402503&partnerID=tZOtx3y1.

[157] E. Herderick, Additive manufacturing of metals: A review, Mater. Sci. Technol. Conf. Exhib. 2011, MS T'11. 2 (2011) 1413–1425. http://www.scopus.com/inward/record.url?eid=2-s2.0-84856301323&partnerID=40&md5=e02018d10b2ca37a7e2ae1773e4fcaec.

[158] Joel Fredrick Flumerfelt, Aluminum powder metallurgy processing, 1988.

[159] A.D. Taylor, E.Y. Kim, V.P. Humes, J. Kizuka, L.T. Thompson, Inkjet printing of carbon supported platinum 3-D catalyst layers for use in fuel cells, J. Power Sources. 171 (2007) 101–

106. doi:10.1016/j.jpowsour.2007.01.024.

[160] S. Couck, J. Lefevere, S. Mullens, L. Protasova, V. Meynen, G. Desmet, G. V. Baron, J.F.M. Denayer, CO_2 adsorption with a 3DFD-printed ZSM-5 monolith, Chem. Eng. J. 308 (2017) 719–726. doi:10.1016/j.cej.2016.09.046.

[161] C.R. Tubio, J. Azuaje, L. Escalante, A. Coelho, F. Guitián, E. Sotelo, A. Gil, 3D printing of a heterogeneous copper-based catalyst, J. Catal. 334 (2016) 110–115. doi:10.1016/j.jcat.2015.11.019.

[162] H. V. Thakkar, S. Eastman, A. Hajari, A.A. Rownaghi, J.C. Knox, F. Rezaei, 3D-printed zeolite monoliths for CO_2 removal from enclosed environments, ACS Appl. Mater. Interfaces. 8 (2016) 27753−27761. doi:10.1021/acsami.6b09647.

[163] L.C. Almeida, F.J. Echave, O. Sanz, M.A. Centeno, J.A. Odriozola, M. Montes, Washcoating of metallic monoliths and microchannel reactors, in: Stud. Surf. Sci. Catal., 2010: pp. 25–33. doi:10.1016/S0167-2991(10)75004-7.

[164] Y. Han, D. Xu, C. Lu, N. Li, J. Zhou, Y. Hu, H. Huang, Preparation of alumina coatings on metallic nickel substrate using a room-temperature wet chemical pretreatment method, Mater. Chem. Phys. 127 (2011) 7–11. doi:10.1016/j.matchemphys.2011.01.014.

[165] V. Meille, Review on methods to deposit catalysts on structured surfaces, Appl. Catal. A Gen. 315 (2006) 1–17. doi:10.1016/j.apcata.2006.08.031.

[166] C. Agrafiotis, A. Tsetsekou, The effect of powder characteristics on washcoat quality . Part I : Alumina washcoats, J. Eur. Ceram. Soc. 20 (2000) 815–824.

[167] S. Walter, S. Malmberg, B. Schmidt, M. a. Liauw, Mass transfer limitations in microchannel reactors, Catal. Today. 110 (2005) 15–25. doi:10.1016/j.cattod.2005.09.019.

[168] R.E. Hayes, S.T. Kolaczkowski, Mass and heat transfer effects in catalytic monolithic reactors, Chem. Eng. Sci. 49 (1994) 3587–3599. doi:10.1016/0009-2509(94)00164-2.

[169] M. Valentini, G. Groppi, C. Cristiani, M. Levi, E. Tronconi, P. Forzatti, The deposition of γ-Al_2O_3 layers on ceramic and metallic supports for the preparation of structured catalysts, Catal. Today. 69 (2001) 307–314. doi:10.1016/S0920-5861(01)00383-2.

[170] C. Cristiani, M. Valentini, M. Merazzi, S. Neglia, P. Forzatti, Effect of ageing time on chemical and rheological evolution in γ-Al_2O_3 slurries for dip-coating, Catal. Today. 105 (2005) 492–498. doi:10.1016/j.cattod.2005.06.020.

[171] J.M. Zamaro, M.A. Ulla, E.E. Miró, The effect of different slurry compositions and solvents upon the properties of ZSM5-washcoated cordierite honeycombs for the SCR of NO_x with methane, Catal. Today. 107–108 (2005) 86–93. doi:10.1016/j.cattod.2005.07.066.

[172] D. Truyen, M. Courty, P. Alphonse, F. Ansart, Catalytic coatings on stainless steel prepared by sol-gel route, Thin Solid Films. 495 (2006) 257–261. doi:10.1016/j.tsf.2005.08.200.

Chapter 2

Methanation of CO_2 on macro-porous metal structured supports coated with Ni/alumina catalyst

Chapter 2 presents CO_2 methanation on macro-porous metal structures coated with Ni/Al_2O_3 catalyst. The results were benchmarked with conventional Ni/Al_2O_3 powder catalyst prepared by impregnation and characterized by several physico-chemical techniques. Macro-porous catalytic supports were manufactured by 3DFD technique. Supports were coated with Ni/Al_2O_3 suspension to achieve sufficient catalytic coating. After characterization, catalytic structures were tested in a tubular reactor for CO_2 methanation reactions at temperatures between 250 and 450°C. This study shows the effect of the coating suspension composition on the properties of catalytic coatings, as well as how CO_2 conversion, methane selectivity and catalyst stability are affected by the architecture of the structured catalyst.

This chapter was adapted from the following paper: Danaci S., Protasova L., Lefevere J., Bedel L., Guilet R., Marty P., *Efficient CO_2 methanation over Ni/Al_2O_3 coated structured catalysts,* Catal. Today. 273 (2016) 234–243.

2.1. Introduction

In recent years, CO_2 methanation reaction has drawn great interest in the production of methane and utilization of CO_2 [1–3]. The catalytic conversion (hydrogenation) of carbon dioxide to methane, also called a Sabatier reaction, is reversible and very exothermic reaction (2-1). This reaction is usually operated under moderate pressures (10-30 bars) and temperatures between 250 and 500°C.

$$CO_{2(g)} + 4H_{2(g)} \leftrightarrow CH_{4(g)} + 2H_2O_{(g)} \quad \Delta_r H^{\circ}_{298K} = -165\ \text{kJ} \cdot \text{mol}^{-1} \qquad (2\text{-}1)$$

Catalysts containing transition metals of the VIII, IX, X and XI groups have been investigated for methanation [3–5]. In the last decade, bimetallic catalysts have also attracted a lot of attention due to their higher activity. Previous studies showed that catalysts containing ruthenium supported on Al_2O_3 were highly selective for methane [6–9]. Some studies have shown that active oxygen sites (vacancies) can interact with active metals to improve the performances of catalysts. Therefore, active materials with mobile oxygen (e.g. $Ce_xZr_{1-x}O_2$) and bimetallic catalysts (Ni-Co, Ni–Mo, Ni-Fe) were investigated [10–12]. Recently, the effect of the addition of a second metal (Fe, Co, Cu) to Ni/ZrO_2 catalysts for methanation reaction have been reported. Iron was found to be a suitable second metal for the catalyst for low-temperature CO_2 methanation [13]. Nickel-based catalysts are the most widely studied for the methanation reaction due to their high activity and competitive cost. Among metal oxides, alumina is the most common catalytic support used in heterogeneous catalysis due to its low cost, good thermal stability, high specific surface area and high interaction with deposited metals leading to high catalytic activity [14].

So far, catalytic methanation has been mostly investigated in packed-bed and fluidized-bed reactors [15]. However, on the industrial scale, the Sabatier process is usually performed in packed-bed reactors due to its economic efficiency [3]. Because of the high exothermicity of the Sabatier reaction, temperature control is a challenge. For fast chemical reactions, using a packed-bed reactor can lead to hot spots formation and catalyst deactivation due to the sintering of the catalyst [16]. Therefore it is necessary to remove the heat more efficiently. Furthermore, at high gas space velocities, existing packed-bed systems can lead to high pressure drops which is dependent on the particle size of the catalyst as well as its shape and packing [17]. Flow mal-distribution resulting in non-uniform contact time is an additional disadvantage of the packed-bed systems. Decreasing the particle size improves the activity of the catalyst and mass transfer but leads to even greater increase in pressure drop [18]. Thus, macro-structured supports with catalytically active coatings are seen as an important part of process intensification, as they allow for the controlled mass and heat transfer, low pressure drop and thus better control of the process.

In order to overcome the above mentioned limitations, several improved reactor and catalyst designs have been proposed. One of the possibilities of heat transfer improvement for CO_2 methanation is the use of a structured micro-channel reactor with a thin layer of catalyst on the reactor channel walls that leads to improved heat and mass transfer [19–21]. In the case of heat transfer

improved reactors, metal based supports provide better temperature control in comparison with conventional catalysts. As for structured reactors, metallic plates [21], foils [22,23], felts [24], monoliths [25] and foams [26,27] are used as structured supports.

In recent years, some data related to both CO and CO_2 methanation in structured reactors have been published. However, most of the published studies are focused on CO methanation due to high accessibility of the syngas ($CO + H_2$) in industry. One of the successful micro-channel reactor designs without heat transfer limitations was proposed for CO methanation in the presence of CO_2 and O_2 in 2005 [23]. Microstructured foils were coated with Ru/SiO_2 and Ru/Al_2O_3 catalysts. It was found, that in the presence of CO_2, the conversion of CO is higher only at temperatures between 200 and 250°C. Methanation of CO_2 dominates at temperatures >250°C [23]. In the case of CO_2 methanation, a limited number of studies are available. The reactor operation at a uniform temperature is a challenge at temperatures >250°C. Therefore a potentially interesting microchannel reactor was proposed for the flexible thermal management [19]. A porous metal felt was used as a support material for Ru and Rh catalysts and tested for CO_2 methanation. Another remarkable study on CO_2 methanation reaction was published by NASA in 2011 [28]. Results showed that an improved Microlith™ reactor design with catalytic supports has a significant impact on the performance due to its better heat and mass transfer, lower pressure drop, high surface area and short contact time compared to the traditional packed-bed system.

Recently, AM technologies have started being used for the manufacture of macro-structured catalytic supports. 3D robocasted periodic porous structures can provide several advantages such as flexible design, significantly better heat and mass transfer as well as lower pressure drop and excellent mechanical stability [20,31,32]. In this chapter, we describe the manufacture of the efficient structured catalyst for the methanation reaction. For this purpose, various 3DFD catalytic substrates were produced and functionalized with the Ni/Al_2O_3 catalytic coating using wash-coating technique. Different geometries of the structured supports were compared in CO_2 methanation reaction. The results were benchmarked with the conventional powder Ni/Al_2O_3 catalyst in a packed-bed reactor.

2.2. Experimental

2.2.1. Manufacture of macro-porous structured supports

The 316L stainless steel supports were prepared using the 3DFD technique [30]. With this technique, a highly viscous stainless steel paste was extruded through a thin nozzle. Stainless steel porous supports were built layer-by-layer by computer controlled movement in x, y and z-directions. Nozzles with a diameter of 400 and 600 µm were used to manufacture 3D-structures with 1-1 and 1-3 stacking positions (Figure 2-1). The 1-1 stacking 3DFD structure has straight fibres in the direction of the flow, while the 1-3 structure consists of ‘zigzag’ fibres in the direction of the flow. Structures were dried at room temperature for 2 days. Then they were sintered at 1300°C for 4 h in inert atmosphere and cut into cylinders with 20.1 mm diameter and 20 mm length. Before coating, all supports were

cleaned in iso-propanol for 10 minutes under ultrasonic treatment to remove light oils and dirt from the surface. Samples were dried overnight at 100°C. The overview of the manufactured structures is given in Table 2-1. Macro-porosity and specific surface area of the 3DFD supports were calculated according to listed equations in Appendix A. Where *a* is fibre thickness (mm), *n* is inter-fibre distance (mm) and *M* is axial centre difference between two fibres (mm). Stacking constant *c* refers to stacking length between two layers of fibers in z-direction considering an anisotropic pore architecture. In the case of these 3DFD supports, *c* constant of 0.00677 mm is obtained from SEM images.

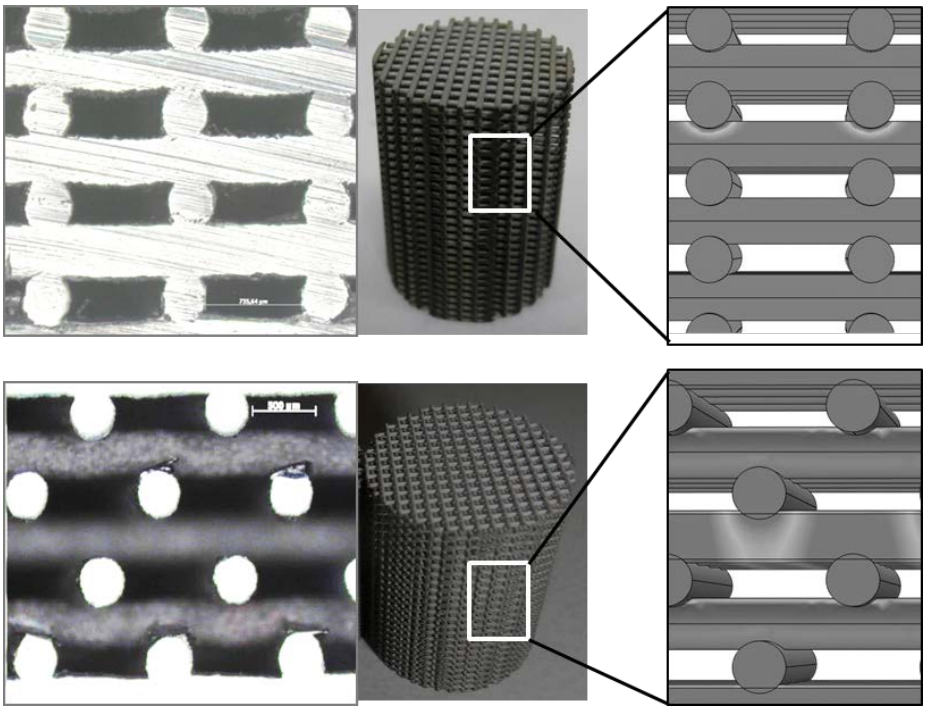

Figure 2-1. Cross-sectional images of the structures with 1-1 (up) and 1-3 (down) stacking positions.

Table 2-1. Overview and images of 3DFD structures.

Sample code[a]	Stacking position	Nozzle (mm)	Inter-fibre distance (mm)	Macro-porosity (%)	SSA[b] ($mm^2 \cdot mm^{-3}$)
4A08 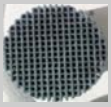	1-1	0.4	0.8	70	2.7
4A1 	1-1	0.4	1	74	2.4
4B1 	1-3	0.4	1	74	2.4
6B1 	1-3	0.6	1	67	2

[a]Sample code: first character (4 or 6) refers to the nozzle diameter (0.4 or 0.6 mm, respectively), second character refers to the stacking positions (A: 1-1 and B: 1-3), third character points inter-fibre distance (0.8 or 1 mm).

[b]SSA: specific surface area; surface area (SA, mm^2) to volume (V, mm^3) ratio per unit cell.

2.2.2. Catalyst preparation

Powder catalyst was prepared by impregnation method starting from boehmite powder, AlO(OH) (Sasol, Germany, average particle size D_{90} = 50 µm) and an aqueous solution of nickel nitrate hexahydrate (PANREAC). Boehmite (10 g) was added into the aqueous solution of nickel nitrate (5.10^{-4} M, 50 mL) under stirring and kept at room temperature for 24 h. The Ni-loading was calculated to be 12 wt.%. The mixture was dried by freeze drying (HETO Powerdry LL3000) under high vacuum at 15°C. The dried powder was calcined at 450°C for 10 h under atmospheric pressure with a heating rate of $1°C \cdot min^{-1}$. At this temperature, transformation of boehmite into γ-alumina takes place. After calcination, dried powder catalyst was sieved to achieve the particle diameter of 25 µm. For the coating preparation, Ni/Al_2O_3 powder was wet ball-milled (10 g of ZrO_2 spheres were used per gram of catalyst) at 300 rpm for 60 min (15 min milling, 45 min rest) by Planetary Micro Mill (Fritsch Pulverisette-5). Ball-milled samples were again freeze-dried and then sieved to get the particles of 3-7 µm.

Coating slurry was prepared as follows: 1-5 g PVA (Polyvinyl alcohol, Fluka Chemica, 100.000), and 0.5-2 g colloidal silica (LUDOX HS-40, Sigma Aldrich) were added to 73 ml deionised water at 60°C and left without stirring overnight. Powder Ni/Al_2O_3 catalyst (20 g, 3-7 µm) and 1 ml of acetic acid (0.2M, Merck) were added into the slurry. The solvent/catalyst ratio was 3.6-3.9 %. The mixture was stirred at room temperature for 24 h. The dip-coating of 3DFD supports was performed manually with a tank containing coating suspension and an air blow gun: the 3DFD supports were immersed into the suspension for 60 s, and the excess suspension was removed by blow gun. The

coating was repeated until the loading of ca. 0.17 - 0.19 g·cm$^{-3}_{support}$ was achieved. The catalyst loading was calculated as follows: $Loading = \frac{G_{support+cat} - G_{support}}{V_{support}}$, where, G (g) is the weight of the structured support (+catalyst) and the V (cm^3) is the volume of the structured support. Then, the samples were dried at 100°C overnight and calcined at 550°C for 4 h. After all, structured catalysts 4A08, 4A1, 4B1 and 6B1 were obtained with the Ni/Al_2O_3 loading of 0.18, 0.19, 0.17, 0.18 g·cm^{-3}, respectively. The preparation steps are given in Figure 2-2.

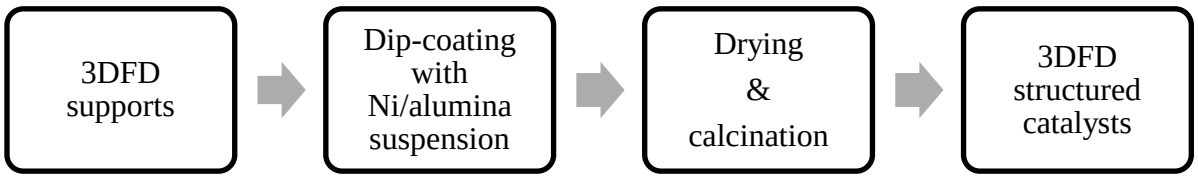

Figure 2-2. Preparation steps of the structured catalysts.

2.2.3. Characterization

The specific surface area of the catalysts was measured by N_2 sorption analyser (Quantachromie ASIQM 0002-4) at -196 °C using the BET method, each sample was degassed at 200 °C.

X-ray diffraction, XRD (PANalytical X'Pert Pro) (λ = 1.5405Å) at 40kV was used to examine the phase and crystallinity of the powder catalysts.

Reduction temperature profile of powder Ni/Al_2O_3 catalyst was performed using thermoanalyzer (TGA, NETZSCH STA-449) at 600°C, heating rate of 5°C·min^{-1}. Prior to TGA measurement, powder catalyst was reduced under 80 % H_2 flow at 450 °C for 2 h.

Particle size distribution (PSD) was detected by wet method using PSD analyser (Microtrac S3500).

Rheometer (Kinexus Rheometer) was used to determine the viscosity of the coating slurry at room temperature as a function of the shear rate.

Adhesion strength of the coating was evaluated by the weight loss after the ultrasonic treatment (Ultrasound frequency: 40kHz). The coating morphology and the thickness of the coating of the cross-section of structures were examined by scanning electron microscopy (SEM; FEG JSM6340F, JOEL) and optical microscopy (Zeiss, Stereo Discovery V12 with imager type M2m).

Energy Dispersive X-ray Fluorescence (EDXRF) spectrometer by HE XEPOS (Spectro Analytical Systems, Kleve, Germany) was used for the elemental analysis of Ni/alumina catalysts.

2.2.4. Catalytic activity and stability

The scheme of the methanation setup is presented in Figure 2-3. It is worth to mention that the setup is not optimal for this reaction and was built for the basic screening of the catalysts. A quartz

tubular reactor (24 mm diameter and 100 mm length) was used. A K-type thermocouple inserted at inlet and outlet sides of the quartz tube for continuous temperature measurements. Catalysts were packed in the middle of the reactor and fixed with quartz wool. The reactor was placed in the middle of the furnace. In order to have a fair comparison of the samples with different geometry (stacking, macro-porosity), the same amount of catalyst was used for each experiment. Before the reaction test, catalysts were activated under a continuous flow of H_2:He (80:20 %) at the total rate of 100 ml·min^{-1} (STP) and temperature of 450°C (heating rate 10°C·min^{-1}) for 2 h under atmospheric pressure. After reduction, temperature of the furnace was adjusted to the reaction temperature under continuous flow of helium. Methanation reaction was performed at temperatures between 250 and 450°C under atmospheric pressure. Carbon dioxide and hydrogen were continuously fed into the reactor together with helium carrier gas at the total rate of 100 ml·min^{-1} (STP) with a feed composition of CO_2:H_2:He = 1:4:15.

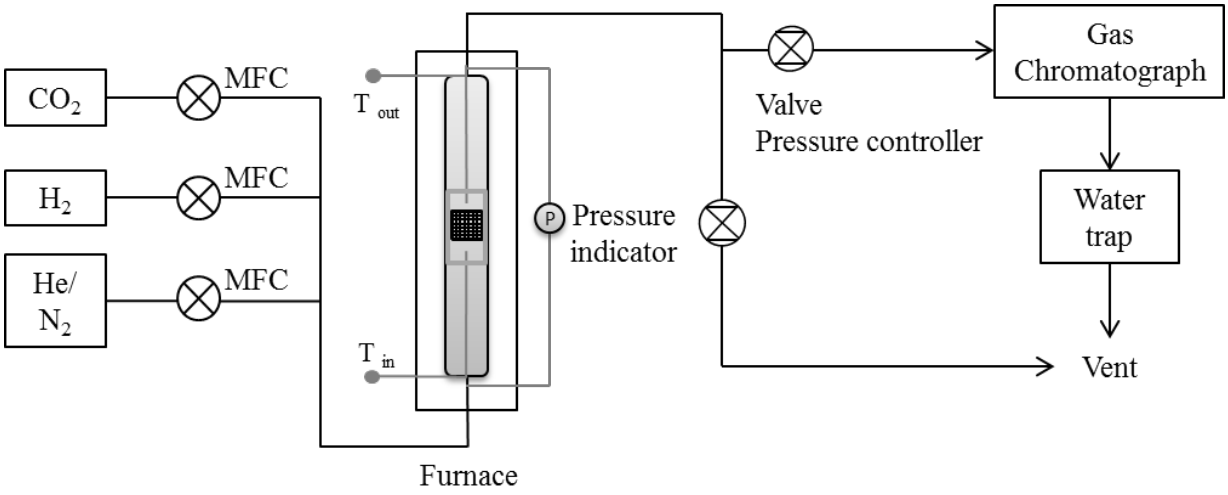

Figure 2-3. Experimental setup for methanation reaction.

Gas chromatography (450-GC, Bruker, Germany) was used for the analysis of reagents and products. The catalytic activity and stability were determined by monitoring CO_2 conversion as a function of time-on-stream. GC with flame ionization detector (FID) and thermal conductivity detector (TCD) were used to measure CH_4 and CO_2 concentrations, respectively. Temperature of both detectors was maintained at 300°C. The calibration of peak areas was measured using a known reactant gas composition without a catalyst. Conversion (X_{CO2}), selectivity (S_{CH4}) and yield (Y_{CH4}) were calculated based on peak areas from calibration using the following equations:

$$X_{CO_2} = \left[\frac{F_{CO_2 in} - F_{CO_2 outlet}}{F_{CO_2 in}}\right] * 100\ (\%) \quad (2\text{-}2)$$

$$S_{CH_4} = \left[\frac{F_{CH_4 outlet}}{F_{CH_4 outlet} + F_{CO\,outlet} + 2F_{C_2H_4 outlet} + 2F_{C_2H_6 outlet}}\right] * 100\ (\%) \quad (2\text{-}3)$$

$$Y_{CH_4} = \left[\frac{F_{CH_4 outlet}}{F_{CO_2 in}}\right] * 100\ (\%) \quad (2\text{-}4)$$

2.3. Results and discussion

2.3.1. Characterization of powder catalyst

As it was already mentioned above, Ni/Al_2O_3 catalysts were prepared by impregnation of commercial boehmite with narrow particle size distribution [33]. Nickel content was kept constant (13 wt.% according to elemental analysis), and different calcination temperatures were tested (450-550°C). The results are given in Table 2-2. The surface area of the alumina significantly dropped when the calcination temperature increased from 450 to 550°C (334 and 271 $m^2 \cdot g^{-1}$, respectively). After impregnation with nickel, surface area and pore volume decreased further due to the pore blockage which is found to be in agreement with literature [34]. However, negligible difference was recorded in pore volume and specific surface area in the case of Ni/Al_2O_3 calcined at 450 and 550°C. In order to keep the surface area higher, final catalysts were calcined at 450°C.

Table 2-2. Characteristics of the powder support and catalyst.

Powder sample	Calcination temperature (°C)	BET surface area ($m^2 \cdot g^{-1}$)	Pore volume ($cm^3 \cdot g^{-1}$)	Pore radius (nm)
γ-Al_2O_3	450	334	0.43	2.3
γ-Al_2O_3	550	271	0.44	2.5
Ni/Al_2O_3	450	164	0.30	2.5
Ni/Al_2O_3	550	143	0.32	3.1

Calcined Ni/Al_2O_3 catalyst was analysed by derivative thermo-gravimetric (DTG) method under H_2/Ar (5/95 %) atmosphere in order to determine NiO to Ni reduction profile. Temperature was increased from 25 to 600°C with a heating rate of 20°C·min^{-1}. It is known that nickel catalyst shows different reduction profile depending on the interactions between nickel and metal oxide support [35]. DTG results are given in Figure 2-4. The reduction process occurs at a temperature range of 350-520°C. A single reduction peak was observed at 478°C. This result is in agreement with the reported literature [36–38].

Figure 2-5 shows the XRD pattern of the calcined and reduced Ni/Al_2O_3 catalysts. Alumina phase evolution was studied depending on the thermal treatment conditions, and was found to be in perfect agreement with previously reported data [39]. It can be seen that after calcination, NiO and γ-Al_2O_3 phases are observed that confirms the transformation of boehmite to γ-Al_2O_3 (could not be completely distinguished with $NiAl_2O_4$). After reduction, NiO signals almost disappeared (43.1° and 62.9°), that indicates nearly full reduction of NiO. The formation of metallic Ni cannot be clearly seen due to the overlapping of the signals of alumina, $NiAl_2O_4$ and Ni^0 (44-47° and 65-69° 2Theta). However, there is a clear indication of the formation of metallic Ni, i.e. no shift of the peak at 37.1° (alumina and $NiAl_2O_4$) was detected, while there is a clear shift to “Ni-rich” direction of the signals where the signal of metallic Ni could be present: from 45.6 to 45.2° and from 66.6 to 65.9°.

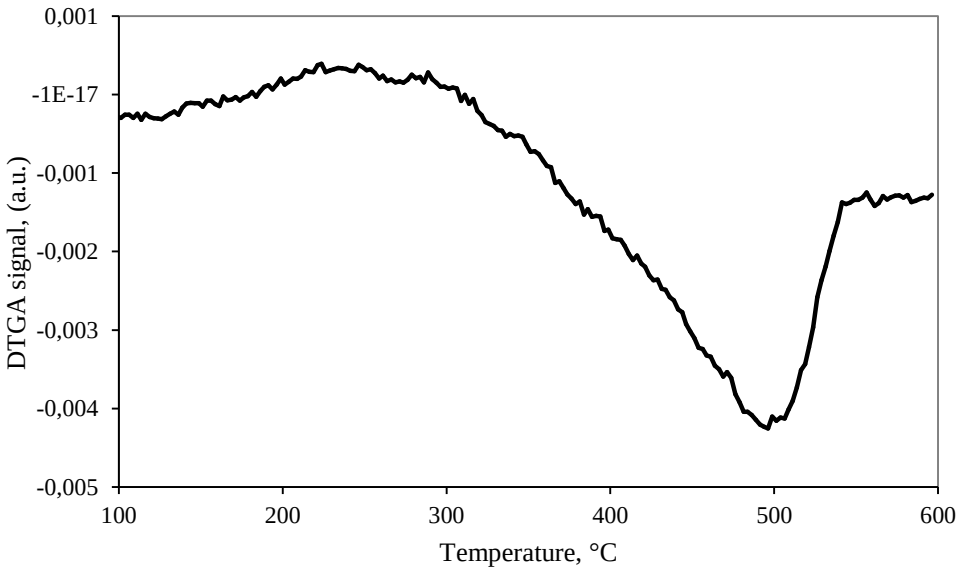

Figure 2-4. DTA profile of the powder Ni/Al_2O_3 catalyst.

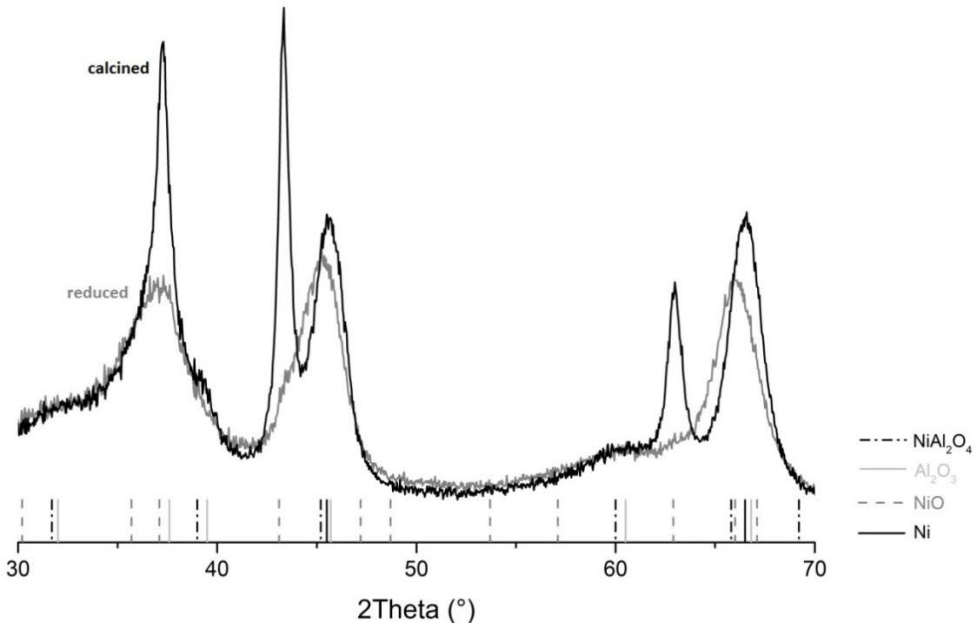

Figure 2-5. XRD patterns of calcined and reduced Ni/Al_2O_3 catalysts.

2.3.2. Characterization of the coating suspension

The coating quality depends on the coating slurry properties (solid content and viscosity). Moreover, smaller particle size results in a coating with better adhesion: for a good dip-coating, particle size below 10 µm is recommended [40–42]. Thus, Ni/Al_2O_3 particles with D_{10} = 0.6 D_{50} = 1.5, D_{90} = 3.3 and D_{99} = 7.2 µm were obtained by wet ball-milling process. The corresponding cumulative particle size distribution is shown in Figure 2-6.

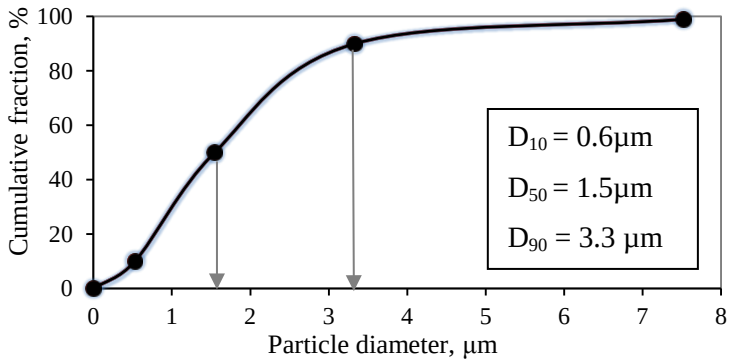

Figure 2-6. Cumulative particle size distribution of the wet-milled catalyst.

Coating suspension usually contains solid catalyst particles and binder, solvent (e.g. water), and dispersants. The binder is used to provide viscosity and sedimentally stable coating suspension [43]. The acid is added to avoid the agglomeration of the alumina particles in suspension and guarantee the suspension stability of over time [33]. Coating suspensions containing 1, 3 and 5 wt. % PVA were prepared. Rheometer was used to determine the single point viscosity at room temperature (25°C) as a function of shear rate (1, 10 and 100 s^{-1}). Figure 2-7 gives viscosities of coating suspensions versus PVA concentrations. In order to achieve homogeneous coating, viscosities between 0.03 and 0.5 Pa·s are preferred at shear rate of 10 s^{-1} [44]. Viscosity of the suspension with 3 wt.% PVA was found to be 0.13 – 0.26 Pa·s at shear rates between 10 and 100 s^{-1}. Suspensions with ≤3wt.% PVA showed pseudo-Newtonian behaviour, i.e. viscosity remained nearly constant with increasing shear rate, which is favourable in order to have a homogeneous coating.

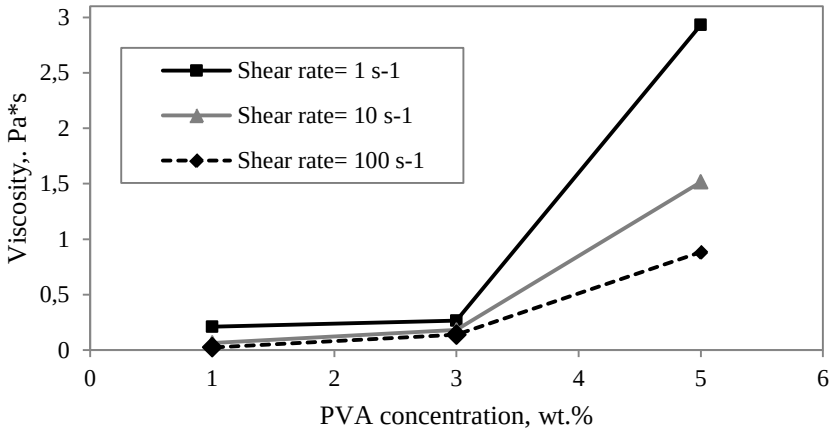

Figure 2-7. Coating suspension viscosities versus PVA concentration at different shear rates.

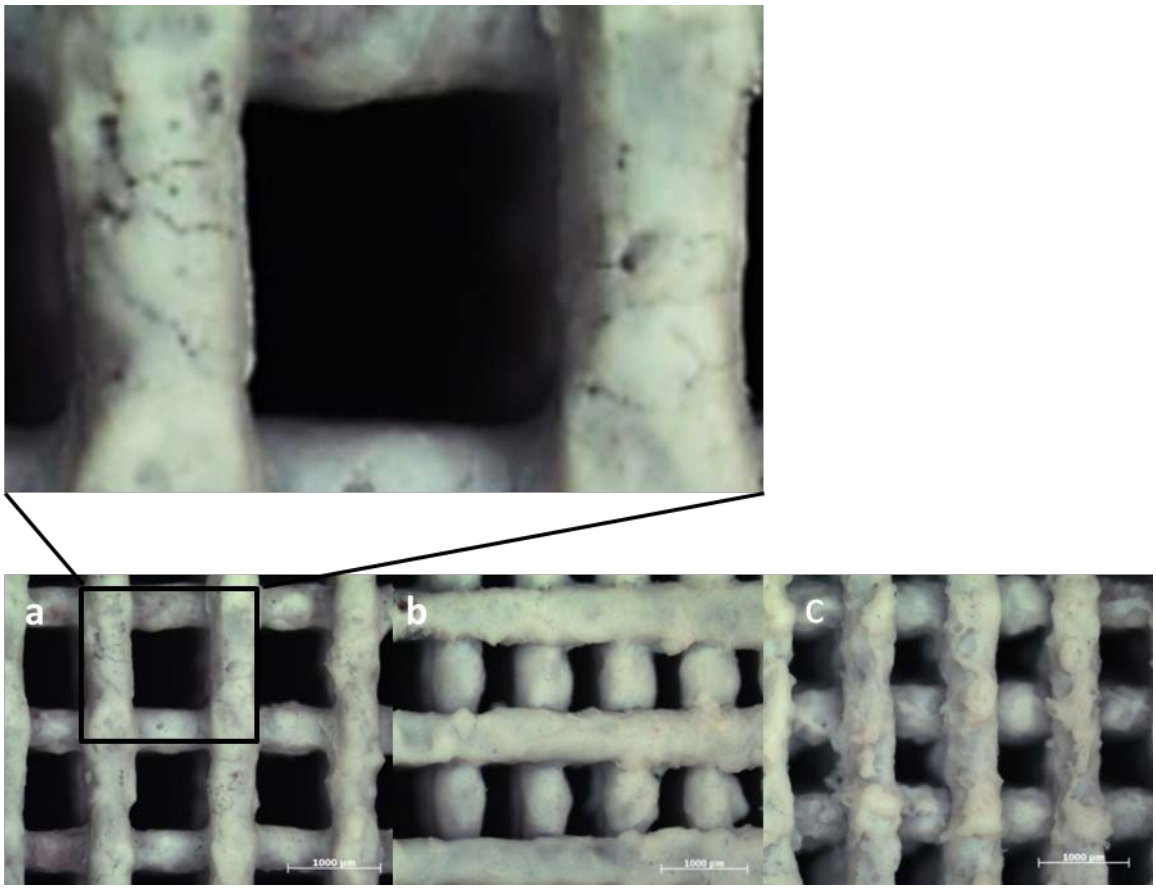

Figure 2-8. OM images of the catalytic coatings (loading ca. 0.15 g·cm^{-3}) obtained from the suspensions with different PVA content: (a) 1 wt%, (b) 3 wt%, (c) 5 wt%.

To study the effect of the PVA content in the suspension on the coating properties, Ni/Al_2O_3 suspensions with various PVA concentrations were deposited on 3DFD stainless steel supports. The amount of deposited catalysts was determined by weight difference before and after coating and calcination. According to the weight measurements, after each immersion, catalyst loading increased with increasing PVA concentration. OM images show that the coating obtained using the suspension with 1 wt.% PVA results in cracks on the surface (Figure 2-8a). Additionally, the coating made from the suspension with 5 wt.% PVA (Figure 2-8c) is observed to be non-homogeneous because of the high loading after each immersion. Less immersions were needed using the suspension with the higher PVA concentration. The results of viscosity measurements and OM images showed that using the concentration of PVA of ca. 3 wt.% in coating suspension results in optimal behaviour of the slurry and homogeneous coating (Figure 2-8b).

2.3.3. Characterization of the coating on 3DFD structures

It is known from previous studies that adhesion strength of the catalytic coating strongly depends on the binder concentration in the coating suspension [31]. In this work, colloidal SiO_2 (Ludox) was used as a binder, and effect of its concentration on the coating adhesion strength was investigated. The adhesion strength was evaluated according to a method described in the literature

[45], based on the measurement of the weight loss caused by the exposure of the sample to ultrasound. The coating thickness was measured by SEM before and after treatment. It is reported that it is more difficult to achieve a good adhesion of inorganic coatings to a metal surface than to a ceramic one. The special chemical treatment of the metal surface by e.g. acids is necessary in order to increase the surface roughness [46–48]. Coated stainless steel 3DFD structures were treated in an ultrasonic bath filled with distilled water for 1, 15, 30 and 60 min and then dried. The weight loss values are given in the Table 2-3. Results show that PVA concentration has no significant effect on adhesion strength of the coatings (first, second and third columns, Table 2-3).

Table 2-3. Effect of the suspension composition on the coating adhesion.

US treatment time (min)	Coating weight loss (wt. %)			
	1% PVA 2% SiO_2	**3% PVA 2% SiO_2**	**5% PVA 2% SiO_2**	**3% PVA 0.5% SiO_2**
1	0.6	0.1	0.4	1.3
15	2.1	0.9	1.2	4.9
30	2.5	1.1	2.5	12.5
60	2.9	2.5	3.4	17.3

After 1 h ultrasonic treatment (US), 17.3 % coating weight loss was detected in the case of the coating obtained from the suspension with 0.5wt.% SiO_2 (fourth column, Table 2-3). After addition of 2 wt.% SiO_2 into the coating slurry, the weight loss of the coating after 1h US treatment was found to be only 2.5 % (Table 2-3). This result was considered to be satisfying and no further increase of SiO_2 content was done in order to avoid the influence of SiO_2 on the catalytic properties of Ni/Al_2O_3. Based on above described results, the optimal composition of the suspension was found to be as follows: 3 % PVA, 2 % Ludox, 1 % acetic acid, 20 % catalyst powder, and water.

As it was mentioned above, the surface treatment of the stainless steel substrates could further improve the adhesion strength of catalytic coating. The stainless steel supports could be treated by various acids or mixtures, e.g. hydrofluoric and nitric acid [47]. However, due to the toxicity of HF and low corrosion resistance of 316L stainless steel, 3DFD supports were treated with 5 % nitric acid solution. Samples were placed in US bath for 10 min, then cleaned with iso-propanol. Acid treated supports were coated with the same amount of catalyst (ca. 0.15 $g \cdot cm^{-3}$), and the adhesion strength was tested. After US treatment for 10 min in water, the weight loss was found to be 1.4 and 2.5 wt.% for treated and untreated sample, respectively. This result confirms that acid treatment improves the adhesion strength due to the increased roughness of the surface. To study the effect of calcination temperature on the coating adhesion, coated 3DFD structures were calcined at 450 and 550°C. The adhesion strength was tested as described above. The results showed that calcination temperature has no influence on the adhesion strength of the coating.

Scanning electron microscopy (SEM) was used to investigate the coating morphology and the thickness. The cross-section images shows the coating on the surface of the stainless steel structures

before (Figure 2-9a) and after 1 h ultrasonic treatment (Figure 2-9b). The right light-grey part of the structure in Figure 2-9 corresponds to the stainless steel fibre and the left dark-grey part refers to the catalytic coating. The thickness of the coating was measured to be 18 and 12 µm before and after ultrasonic treatment, respectively.

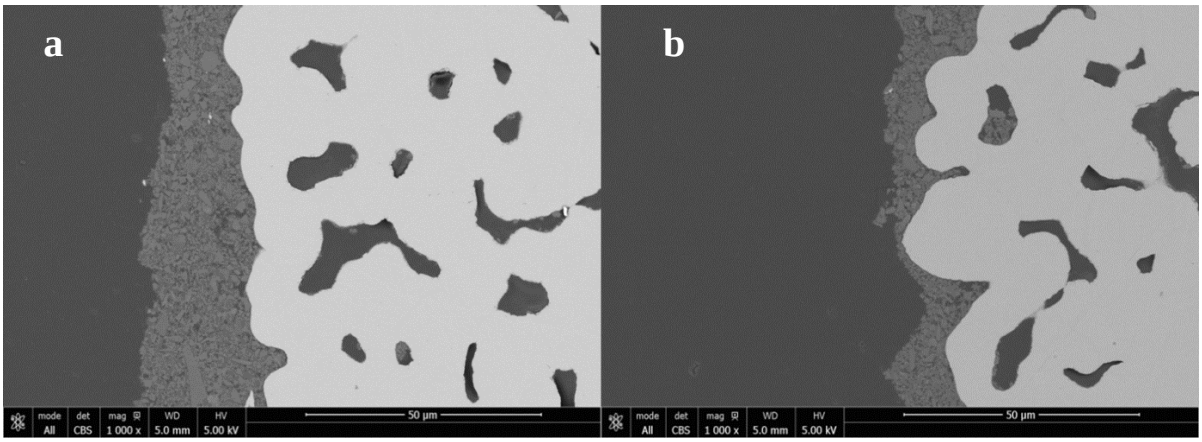

Figure 2-9. SEM images of the coated 3DFD structure: before (a) and after (b) adhesion strength test.

It is noteworthy, that the surface of the 3DFD stainless steel structures was very rough (because of sintering temperature and acid treatment), and to make the measurements and associated judgement was rather difficult; moreover, some loss of the coating could occur during the sample preparation (embedding) for SEM imaging. Thus, basically it could be concluded that there is no significant change in coating thickness before and after ultrasonic treatment.

2.3.4. Catalytic activity, selectivity and stability

The methanation reaction was carried out with powder packed-bed catalyst and coated 3DFD structures in a tubular reactor. The overall results are given in Table 2-4. The CO_2 conversion on powder catalyst at different space velocities and temperatures is plotted in Figure 2-10. At all tested temperatures, the conversion decreased slightly with the increase of the weight hourly space velocity (WHSV, h^{-1}), which is explained by the shorter contact time of the gases and catalyst in the reactor. The WHSV of the reactant gas is ranged between 750 and 2600 h^{-1} at a constant feed gas ratio (CO_2:H_2 = 1:4). Total gas feed was kept constant at 100 ml·min^{-1} by dilution. Methanation reaction on powder catalyst was performed at temperatures from 250 to 450°C. Conversion increased by ca. 20 % when temperature is changed from 250 to 300°C, while during the further increase of the temperature to 350°C, the difference was found to be only 10 %. When the temperature is raised to 400°C, no change in CO_2 conversion is observed. It is known that the Gibbs free energy (ΔG) is a negative number as long as the reaction is spontaneous. As for an exothermic reaction, after a certain temperature, reaction achieves the thermodynamic equilibrium. At reaction temperature >350°C, the thermodynamic equilibrium was reached and thus no further increase on CO_2 conversion was observed. At temperatures above 350°C, the ΔG increases rapidly and becomes positive [48], and reaction changes its way to methane reforming [49]. This explains the decreased conversion of the

CO_2 at reaction temperature >350°C. The results showed that operating temperature at 350°C was the most suitable temperature for the powder catalyst to have an effective carbon dioxide methanation. The selectivity to methane was high and stable at around 95-99 %, only small amount of by-products (CO, C_2H_4 and C_2H_6) was detected (Table 2-4).

Figure 2-11 shows the comparison of CO_2 conversion obtained with the powder packed-bed catalyst and the 3DFD structured catalysts. It can be seen that the temperature significantly affects the conversion of carbon dioxide. At temperatures above ca. 340°C, all 3DFD structured catalysts showed higher conversion (up to 90 % in the case of 6B1 sample) than that of the powdered catalyst (ca. 66 %), while at lower temperatures only the structures with 1-3 configuration showed improved CO_2 conversion. It is important to note, that in the case of the samples with the same stacking (1-1 or 1-3), macro-porosity difference does not result in significant changes of CO_2 conversion. In the case of samples with different stacking, the structured catalyst with 1-3 stacking showed a considerably higher conversion than the one with 1-1 stacking. Despite the same volume of the samples, the contact between catalysts and reactant gas in 1-3 ‘zig-zag’ structures is better than the structures with 1-1 ‘linear’ stacking. Therefore, this difference can be explained by an external mass transfer effect due to the increased effective contact surface area. This could lead to higher contact between the reactant gas and the structured channels of the structured catalyst with 1-3 stacking. The similar effect of the architecture on the mass-transfer was observed earlier for methanol-to-olefins reaction [32]. There is also an indication that the heat transfer properties of the structured catalyst with 1-3 stacking is different in comparison with structured catalyst with 1-1 stacking due to nonlinear positioning of fibres. Axial ETC of the 1-3 samples are expected to be lower than 1-1 stacking samples different due to the fibre positioning. Lower axial ETC of samples with 1-3 stacking could lead to higher increase of the actual temperature than samples with 1-1 stacking due to the heat released by the exothermic methanation reaction. Thus, at lower temperatures, this difference in both heat- and mass- transfer properties and different residence time distribution (RTD) in different architectures resulted in >40% difference in CO_2 conversion (see Figure 2-11). At temperatures above 370°C, 3DFD structured catalysts showed no geometry effect on CO_2 conversion.

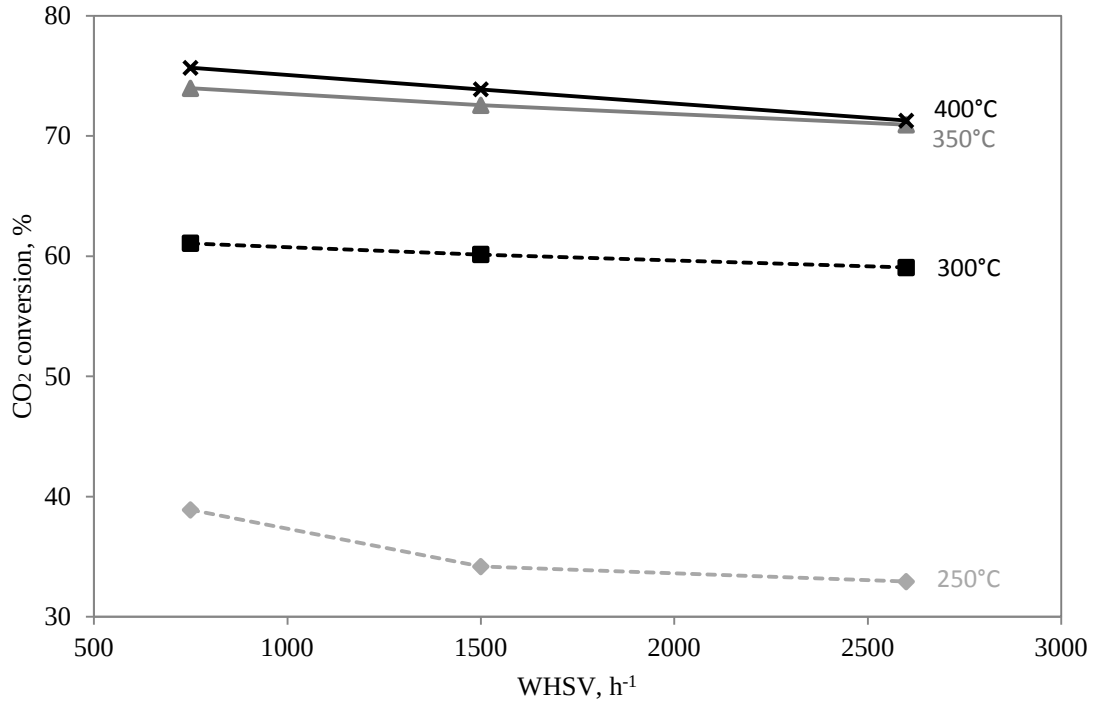

Figure 2-10. CO_2 conversion versus WHSV at different temperatures (powder Ni/Al_2O_3 catalyst).

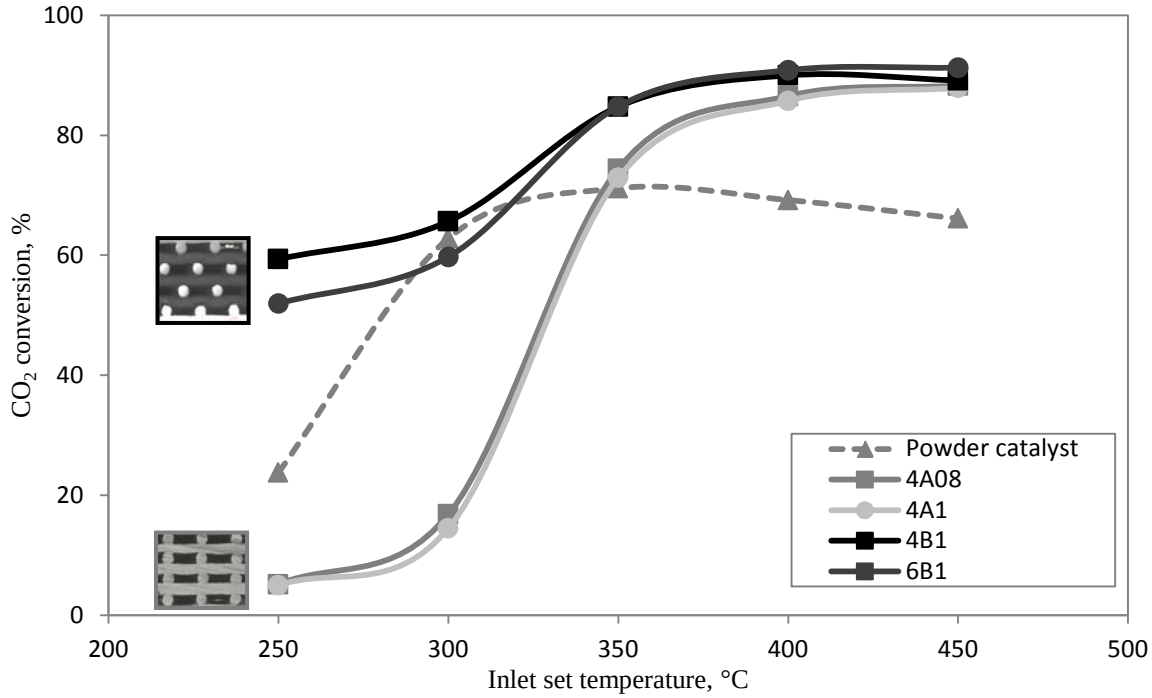

Figure 2-11. Methanation reaction at different temperatures (WHSV 1500 h^{-1}).

Table 2-4. Conversion, selectivity and yield for various Ni/Al_2O_3 catalysts.

Catalyst	WHSV (h^{-1})	Temp. inlet (°C)	Temp. outlet (°C)	CO_2 Conversion (%)	CH_4 Selectivity (%)	CH_4 Yield (%)
Powder	750	250	236	39	97	38
	1500		236	34	97	33
	2600		237	33	98	32
	750	300	284	61	95	58
	1500		283	60	97	58
	2600		278	59	98	58
	750	350	333	74	97	72
	1500		334	73	97	71
	2600		332	71	99	70
	750	400	382	76	98	74
	1500		381	74	98	73
	2600		381	71	99	70
	1500	450	450	66	97	65
4A08	1500	250	230	5	97	5
		300	277	17	99	17
		350	326	74	98	73
		400	376	87	97	84
		450	436	88	97	85
4A1	1500	250	248	5	98	5
		300	298	15	96	14
		350	349	73	98	72
		400	403	86	99	85
		450	449	88	99	87
4B1	1500	266	270	59	95	56
		294	298	66	97	64
		347	355	85	98	83
		399	413	90	98	88
		443	449	89	98	87
6B1	1500	266	264	52	96	50
		297	296	60	98	59
		349	351	85	96	82
		400	408	91	98	89
		450	450	90	98	88

In order to study the catalysts stability, methanation reaction was performed on 3DFD structured and powder catalysts at 350°C for prolonged time. Gas samples were automatically

analysed every 20 min of the reaction run. Figure 2-12 shows the CO_2 conversion as a function of time-on-stream (TOS). The initial CO_2 conversions were 80 % and 73 % for 3DFD structured catalyst (4B1 sample) and powder, respectively. Powder catalyst showed an ca.8 % decrease of CO_2 conversion already after 45 h of the experiment, while in the case of 3DFD structured catalyst, carbon dioxide conversion stayed constant at ca. 80 % during 53 h time-on-stream. Decrease of CO_2 conversion of the powder catalyst was observed probably due to the formation of carbon deposits or sintering leading to catalyst deactivation. It is suggested, that improved heat transfer of the 3DFD structured catalyst prevents temperature increases which may allow enhanced catalyst stability.

A similar effect was described in for a Microlith^{TM} based structured noble metal catalyst for Sabatier reaction [28]. The structured catalyst was found to be stable for more than 100 h TOS. It was proposed that the lack of catalyst degradation is due to the high heat transfer rate of the Microlith^{TM} catalytic substrates that permits uniform temperature distribution and avoids local hot spots that can cause metal sintering and catalyst deactivation.

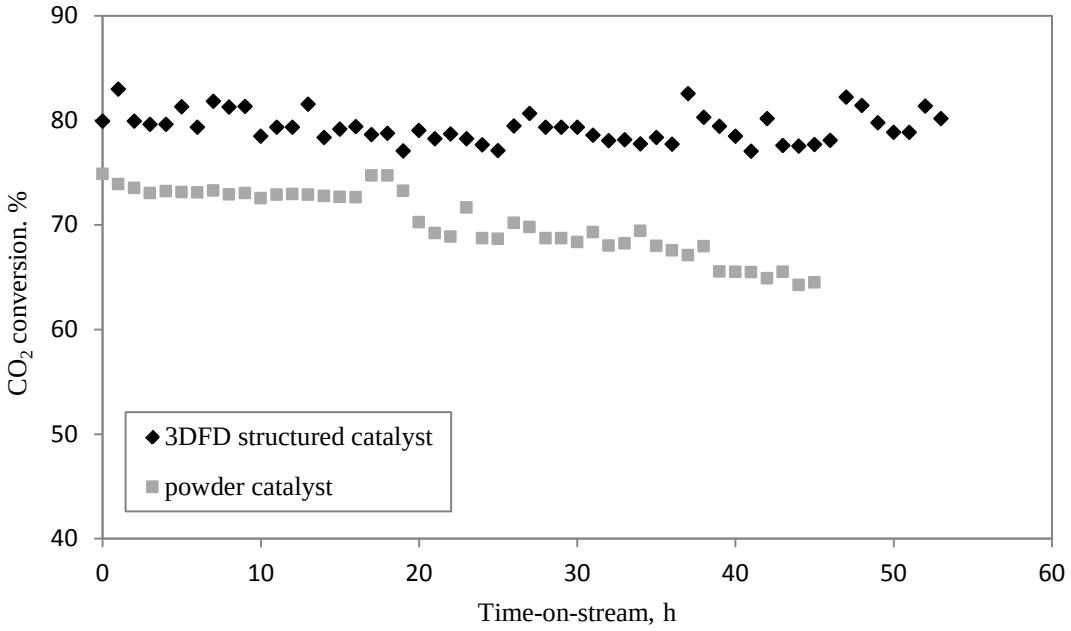

Figure 2-12. Stability test on packed-bed and 4B1 structured catalyst. Reaction conditions: 350°C, H_2/CO_2=4 and WHSV 1500 h^{-1}.

2.4. Conclusions

Ni/Al_2O_3 powder and 3DFD structured catalysts were prepared and characterized. The effect of dispersant and inorganic binder on the catalytic suspension properties was studied. It was found that dispersant concentration significantly affects the coating quality (homogeneity and thickness), whereas the inorganic binder has an influence on the coating adhesion strength. The optimal composition of the coating suspension was determined to be as follows: 3 % PVA, 2 % Ludox, 1 % acetic acid, 20 % catalyst powder, and water.

Structured 3DFD supported catalysts showed improved CO_2 conversion especially at higher temperatures and stability in CO_2 methanation reaction. The best results were obtained using the structured catalyst with 'zig-zag' architecture that can be explained by the combination of improved mass and heat transfer. This observation will be confirmed in chapter 3 by corresponding additional measurements and modelling. Additionally, the prolonged stability test and the characterization of the catalyst afterwards will be presented in chapter 5.

2.5. References

[1] W. Wang, S. Wang, X. Ma, J. Gong, Recent advances in catalytic hydrogenation of carbon dioxide., Chem. Soc. Rev. 40 (2011) 3703–3727. doi:10.1039/c1cs15008a.

[2] B. G., B. J., R. R.B., SGC report: Power-to-Gas – A technical review, 2013. doi:SGC Rapport 2013:284.

[3] W. Wang, J. Gong, Methanation of carbon dioxide: An overview, Front. Chem. Eng. China. 5 (2011) 2–10. doi:10.1007/s11705-010-0528-3.

[4] A.H. Zamani, R. Ali, W.A.W.A. Bakar, The investigation of Ru/Mn/Cu-Al_2O_3 oxide catalysts for CO_2/H_2 methanation in natural gas, J. Taiwan Inst. Chem. Eng. 45 (2014) 143–152. doi:10.1016/j.jtice.2013.04.009.

[5] A. Karelovic, P. Ruiz, CO_2 hydrogenation at low temperature over Rh/γ-Al_2O_3 catalysts: Effect of the metal particle size on catalytic performances and reaction mechanism, Appl. Catal. B Environ. 113–114 (2012) 237–249. doi:10.1016/j.apcatb.2011.11.043.

[6] M. Kuśmierz, Kinetic study on carbon dioxide hydrogenation over Ru/γ-Al_2O_3 catalysts, Catal. Today. 137 (2008) 429–432. doi:10.1016/j.cattod.2008.03.003.

[7] Z. Kowalczyk, K. Stołecki, W. Raróg-Pilecka, E. Miśkiewicz, E. Wilczkowska, Z. Karpiński, Supported ruthenium catalysts for selective methanation of carbon oxides at very low CO_x/H_2 ratios, Appl. Catal. A Gen. 137 (2008) 35–39. doi:10.1016/j.apcata.2007.12.040.

[8] S. Scire, C. Crisafulli, R. Maggiore, S. Minico, S. Galvagno, Influence of the support on CO_2 methanation over Ru catalysts: an FT-IR study, Catal. Letters. 51 (1998) 41–45.

[9] S. Hwang, J. Lee, U.G. Hong, J.H. Baik, D.J. Koh, H. Lim, I.K. Song, Methanation of carbon dioxide over mesoporous Ni-Fe-Ru-Al_2O_3 xerogel catalysts: Effect of ruthenium content, J. Ind. Eng. Chem. 19 (2013) 698–703. doi:10.1016/j.jiec.2012.10.007.

[10] H. Zhu, R. Razzaq, C. Li, Y. Muhmmad, S. Zhang, Catalytic methanation of carbon dioxide by active oxygen material $Ce_xZr_{1-x}O_2$ supported Ni-Co bimetallic nanocatalysts, Am. Inst. Chem. Eng. AIChE J. 59 (2013) 2567–2576. doi:10.1002/aic.14026.

[11] J. Zhang, Z. Xin, X. Meng, Y. Lv, M. Tao, Effect of MoO_3 on the heat resistant performances of nickel based MCM-41 methanation catalysts, Fuel. 116 (2014) 25–33. doi:10.1016/j.fuel.2013.07.102.

[12] J. Sehested, K.E. Larsen, A.L. Kustov, A.M. Frey, T. Johannessen, T. Bligaard, M.P. Andersson, J.K. Nørskov, C.H. Christensen, Discovery of technical methanation catalysts based on computational screening, Top. Catal. 45 (2007) 9–13. doi:10.1007/s11244-007-0232-9.

[13] J. Ren, X. Qin, J.-Z. Yang, Z.-F. Qin, H.-L. Guo, J.-Y. Lin, Z. Li, Methanation of carbon dioxide over Ni–M/ZrO2 (M=Fe, Co, Cu) catalysts: Effect of addition of a second metal, Fuel Process. Technol. 137 (2015) 204–211. doi:10.1016/j.fuproc.2015.04.022.

[14] G.F. Fu, J. Wang, B. Xu, H. Gao, X.L. Xu, H. Cheng, Influence of hydrothermal temperature on structure and microstructure of boehmite, Trans. Nonferrous Met. Soc. China (English Ed. 20 (2010) 221–225. doi:10.1016/S1003-6326(10)60043-X.

[15] J. Kopyscinski, T.J. Schildhauer, S.M.A. Biollaz, Methanation in a fluidized bed reactor with high initial CO partial pressure: Part I-Experimental investigation of hydrodynamics, mass transfer effects, and carbon deposition, Chem. Eng. Sci. 66 (2011) 924–934. doi:10.1016/j.ces.2010.11.042.

[16] C.H. Bartholomew, Mechanism of catalyst deactivation, Appl. Catal. A Gen. 212 (2001) 17–60. doi:http://dx.doi.org/10.1016/S0926-860X(00)00843-7.

[17] V. Tomašić, F. Jović, State-of-the-art in the monolithic catalysts/reactors, Appl. Catal. A Gen. 311 (2006) 112–121. doi:10.1016/j.apcata.2006.06.013.

[18] A. Cybulski, J.A. Moulijn, Monoliths in heterogeneous catalysis, Catal. Rev. 36 (1994) 179–270. doi:10.1080/01614949408013925.

[19] K.P. Brooks, J. Hu, H. Zhu, R.J. Kee, Methanation of carbon dioxide by hydrogen reduction using the Sabatier process in microchannel reactors, Chem. Eng. Sci. 62 (2007) 1161–1170. doi:10.1016/j.ces.2006.11.020.

[20] V. Meille, Review on methods to deposit catalysts on structured surfaces, Appl. Catal. A Gen. 315 (2006) 1–17. doi:10.1016/j.apcata.2006.08.031.

[21] Z. Liu, B. Chu, X. Zhai, Y. Jin, Y. Cheng, Total methanation of syngas to synthetic natural gas over Ni catalyst in a micro-channel reactor, Fuel. 95 (2012) 599–605. doi:10.1016/j.fuel.2011.12.045.

[22] R. Zapf, C. Becker-Willinger, K. Berresheim, H. Bolz, H. Gnaser, V. Hessel, G. Kolb, P. Löb, A.-K. Pannqitt, A. Ziogas, Alumina-based catalyst coatings within microchannels and their testing, 81 (2003) 721–729.

[23] O. Görke, P. Pfeifer, K. Schubert, Highly selective methanation by the use of a microchannel reactor, Catal. Today. 110 (2005) 132–139. doi:10.1016/j.cattod.2005.09.009.

[24] J. Hu, K.P. Brooks, J.D. Holladay, D.T. Howe, T.M. Simon, Catalyst development for microchannel reactors for martian in situ propellant production, Catal. Today. 125 (2007) 103–110. doi:10.1016/j.cattod.2007.01.067.

[25] C. Janke, M.S. Duyar, M. Hoskins, R. Farrauto, Catalytic and adsorption studies for the hydrogenation of CO_2 to methane, Appl. Catal. B Environ. 152–153 (2014) 184–191. doi:10.1016/j.apcatb.2014.01.016.

[26] C.Y. Zhao, Review on thermal transport in high porosity cellular metal foams with open cells, Int. J. Heat Mass Transf. 55 (2012) 3618–3632. doi:10.1016/j.ijheatmasstransfer.2012.03.017.

[27] M. Frey, D. Édouard, A.-C. Roger, Optimization of structured cellular foam-based catalysts for low-temperature carbon dioxide methanation in a platelet milli-reactor, Comptes Rendus Chim. 18 (2015) 283–292. doi:10.1016/j.crci.2015.01.002.

[28] C. Junaedi, K. Hawley, D. Walsh, S. Roychoudhury, M.B. Abney, J.L. Perry, Compact and lightweight sabatier reactor for carbon dioxide reduction, in: 41sr Int. Conf. Environ. Syst.,

2011.

[29] S.H.R.W. Mullens, I. Thijs, J.R. Luyten, W.L. Bouwen, EP 2 195 131 B1 - Method for producing a three-dimensional macroporous filament construct based on phase inversion and construct thereby obtained CA2696386A1, CA2696386A1, 2009.

[30] J. Luyten, S. Mullens, I. Thijs, Designing With Pores - Synthesis and Applications, KONA Powder Part. J. 28 (2010) 131–142. doi:10.14356/kona.2010012.

[31] J. Lefevere, M. Gysen, S. Mullens, V. Meynen, J. Van Noyen, The benefit of design of support architectures for zeolite coated structured catalysts for methanol-to-olefin conversion, Catal. Today. 216 (2013) 18–23. doi:10.1016/j.cattod.2013.05.020.

[32] M. Klumpp, A. Inayat, J. Schwerdtfeger, C. Körner, R.F. Singer, H. Freund, W. Schwieger, Periodic open cellular structures with ideal cubic cell geometry: Effect of porosity and cell orientation on pressure drop behavior, Chem. Eng. J. 242 (2014) 364–378. doi:10.1016/j.cej.2013.12.060.

[33] S. Abedini, N. Parvin, P. Ashtari, Preparation, characterization and microstructural optimization of a thin gamma-alumina membrane on a porous stainless steel substrate, Mater. Sci. Eng. A. 533 (2012) 1–8. doi:10.1016/j.msea.2011.11.006.

[34] A.E. Aksoylu, Z.I. Önsan, Hydrogenation of carbon oxides using coprecipitated and impregnated Ni/Al_2O_3 catalysts, Appl. Catal. A Gen. 164 (1997) 1–11. doi:10.1016/S0926-860X(97)00151-8.

[35] S. Abelló, C. Berrueco, D. Montané, High-loaded nickel-alumina catalyst for direct CO_2 hydrogenation into synthetic natural gas (SNG), Fuel. 113 (2013) 598–609. doi:10.1016/j.fuel.2013.06.012.

[36] C. Li, Y.-W. Chen, Temperature-programmed-reduction studies of nickel oxide/alumina catalysts: effects of the preparation method, Thermochim. Acta. 256 (1995) 457–465. doi:10.1016/0040-6031(94)02177-P.

[37] H. Song, J. Yang, J. Zhao, L. Chou, Methanation of carbon dioxide over a highly dispersed Ni/La_2O_3 catalyst, Chinese J. Catal. 31 (2010) 21–23. doi:10.1016/S1872-2067(09)60036-X.

[38] K.V.R. Chary, P.V. Ramana Rao, V. Venkat Rao, Catalytic functionalities of nickel supported on different polymorphs of alumina, Catal. Commun. 9 (2008) 886–893. doi:10.1016/j.catcom.2007.09.016.

[39] A. Boumaza, L. Favaro, J. Lédion, G. Sattonnay, J.B. Brubach, P. Berthet, A.M. Huntz, P. Roy, R. Tétot, Transition alumina phases induced by heat treatment of boehmite: An X-ray diffraction and infrared spectroscopy study, J. Solid State Chem. 182 (2009) 1171–1176. doi:10.1016/j.jssc.2009.02.006.

[40] J.R. Gonzalez-Velasco, M.A. Gutierrez-Ortiz, J.L. Marc, J.A. Botas, M.P. Gonzalez-Marcos, G. Blanchard, $Pt/Ce_{0.68}Zr_{0.32}O_2$ Washcoated monoliths for automotive emission control, Ind. Eng. Chem. 42 (2003) 311–317.

[41] L.C. Almeida, F.J. Echave, O. Sanz, M.A. Centeno, J.A. Odriozola, M. Montes, Washcoating of metallic monoliths and microchannel reactors, in: Stud. Surf. Sci. Catal., 2010: pp. 25–33. doi:10.1016/S0167-2991(10)75004-7.

[42] V. Meille, S. Pallier, G. Santacruzbustamante, M. Roumanie, J. Reymond, Deposition of γ-Al_2O_3 layers on structured supports for the design of new catalytic reactors, Appl. Catal. A Gen. 286 (2005) 232–238. doi:10.1016/j.apcata.2005.03.028.

[43] V.N. Antsiferov, V.D. Khramtsov, Stabilization of water suspensions of metal powders, J. Eng. Phys. Thermophys. 64 (1993) 475–478.

[44] C. Cristiani, M. Valentini, M. Merazzi, S. Neglia, P. Forzatti, Effect of ageing time on chemical and rheological evolution in γ-Al_2O_3 slurries for dip-coating, Catal. Today. 105 (2005) 492–498. doi:10.1016/j.cattod.2005.06.020.

[45] K. Ihara, K. Ohkubo, S. Yasaki, Y. Yoshino, Method of manufacturing an exhaust gas purifying catalyst, US Pat. 5,208,206. (1993).

[46] L. Kiwi-Minsker, A. Renken, Microstructured Reactors, in: Microstruct. React., 2005: pp. 2248–2264.

[47] Anders Bornmyr, Surface treatment of stainless steels, AVESTA Finish. Chem. / Pick. Handb. (2009) 1–31. http://www.misterstainless.com/assets/pickling_handbook.pdf (accessed July 27, 2015).

[48] L. Kiewidt, J. Thöming, Predicting optimal temperature profiles in single-stage fixed-bed reactors for CO_2-methanation, Chem. Eng. Sci. 132 (2015) 59–71. doi:10.1016/j.ces.2015.03.068.

[49] V. Barbarossa, G. Vanga, Methanation of carbon dioxide, Appl. Catal. A Gen. 84 (2011) N18. doi:10.1016/0926-860X(92)80119-W.

Chapter 3

Experimental and numerical investigation of heat transport and hydrodynamic properties of 3D-structured catalytic supports

Chapter 3 presents the experimental and modelling study related to the heat transport and pressure drop properties of 3D-manufactured stainless steel structured catalytic supports. The effective thermal conductivity was determined at temperatures between 50 and 500°C by diffusivity measurements. For the samples with 74 % macroporosity, at temperatures from 50 to 500°C, axial and radial effective thermal conductivities ranged between 1.78-2.5 and 1.83-2.87 $W \cdot m^{-1} \cdot K^{-1}$, respectively. The effect of geometry (fibre stacking, fibre diameter and macro-porosity) on the effective thermal conductivity was experimentally determined and compared to the modelling results. The effective thermal conductivity model studied proposed for stainless steel structures can be easily adapted to the structures made of other materials. The main parameter influencing the effective thermal conductivity was found to be the macroporosity. The effects of the geometry (fibre stacking) and the coating thickness on the pressure drop were studied experimentally. The pressure drop was measured by a manometer with air as a fluid gas. Pressure drop measurements showed that the samples with zig-zag fibre stacking (1-3 stacking) exhibit higher pressure drop values than the samples with straight fibre stacking (1-1 stacking) at the same macroporosity due to their lower open frontal area.

This chapter was adapted from the paper: Danaci S., Protasova L., Try R., Bengaouer A., Marty P., *Experimental and numerical investigation of heat transport and hydrodynamic properties of 3D-structured catalytic supports*, Appl. Therm. Eng. (2017), *in press*, http://dx.doi.org/ 10.1016/j.applthermaleng.2017.07.155

3.1. Introduction

Porous metallic materials offer a wide range of applications in industrial chemical processes [1], catalytic reactors [2] and automobile exhaust gas treatment [3]. So far, various metallic structures (monoliths, fibre felts etc.) and especially open-cell metallic foams have been investigated for the next generation mainly on heat transfer applications, but also as catalyst carriers in heat exchanger (HEX) reactors [2,4–6]. The optimal design of a metallic open cellular structure can offer multi-functional properties, such as high thermal conductivity, high porosity, large expanded surface area, strong flow-mixing capability and high mechanical strength [6].

Catalytic reactions are usually performed in packed-bed reactors with conventional catalytic materials due to economic reasons. In the packed-bed reactors, catalysts/catalytic materials have poor thermal conductivities leading to the large temperature gradient in the case of larger diameter of reactors. In the case of exothermic reactions, the heat transport in the metal based structured catalysts was found to be 2-3 times better than in conventional packed-bed catalysts, that can significantly reduce the hot spot formation and ensure advanced temperature control [7]. Moreover, at high gas velocities, existing packed-bed systems suffer from high pressure drops which are dependent on the particle size of the catalyst, its shape and packing [8]. Therefore, low pressure drops and high thermal transport are desired for new generation structured reactors.

In recent years, metallic/ceramic monoliths and foams coated with catalytically active layers have drawn great interest in the design of the structured reactors. Since the 1990s, many studies of heat transfer and pressure drop properties of metallic monoliths and foam structures used as catalytic supports for highly exothermic reactions have been reported [1–4]. A theoretical study related to heat transfer through a ceramic honeycomb monolith catalyst with square channels was performed in order to estimate the operation conditions to avoid overheating during an exothermic reaction [9]. It was found that at high gas flow velocities, the gas temperature inside the channel of the monolith noticeably increased at a distance of 1-1.5 mm from the inlet of the reactor, and sharp heat gradients formed between the channel wall and the gas stream.

In porous media, heat inside the structure is transported by multiple heat transfer mechanisms, i.e. conduction, convection and radiation. Conduction is considered to be the main heat transfer mechanism in the solid domain. In the case of metals with high thermal conductivity, conductive heat transfer dominates radiation (at low temperatures) and convection. However, propagation of thermal radiation in the porous structure can be dependent on the geometry of the solid matrix. That is why the choice of the correct geometry of the structure is of the same importance as the material.

Recently, support structures made by additive manufacturing (AM) techniques started being used for highly exothermic and endothermic reactions [11–14]. The main benefits of using AM technologies to manufacture catalytic supports are flexible design of the structures with complex geometries, material variability and adjustable porosity. In chapter 2, the advantages of the structured

catalysts were shown for highly exothermic CO_2 methanation reaction. The structured catalyst lowered the temperature increase (hot spots) and led to an enhanced catalyst stability. During stability tests (350°C, $H_2/CO_2 = 4$, WHSV 1500 h^{-1}), the initial CO_2 conversions were observed to be 80 % and 73 % for structured and powder catalysts, respectively. The powder catalyst showed an 8 % decrease of CO_2 conversion after only 45 h time-on-stream, while in the case of structured catalyst, CO_2 conversion stayed constant at ca. 80 % during 53 h time-on-stream. Therefore, it is crucial to understand the heat transport mechanisms of these newly developed support structures with different architectures. In another study, open porous structures were manufactured by using the selective electron beam melting technique to investigate the effect of porosity and cell orientation on the pressure drop [16]. The results confirmed that both porosity and cell orientation have a major effect on the pressure drop.

In this study, stainless steel structured materials with different geometries and macroporosity were manufactured by the 3DFD technique. The aim of this work was to investigate the effective thermal conductivity and the pressure drop throughout structures without taking into account any chemical reaction. The effect of fibre stacking, macroporosity and fibre diameter on effective thermal conductivity was studied experimentally and compared to modelling results. Pressure drop experiments were performed on samples with different geometries with and without coating. These pressure drop measurements were compared to the measurements on alumina beads (conventional packed-bed configuration).

3.2. Experimental

3.2.1. Samples preparation

The 316L stainless steel supports were made using additive manufacturing technology based on micro-extrusion, as previously described elsewhere [15]. A modified Computer Numerical Control (CNC) machine was used as a 3D-printer to build up the stainless steel support structures layer-by-layer by computer controlled movements in x, y and z-direction. Nozzles with diameter of 0.4 and 0.6 mm were used to manufacture the supports with inter-fibre distances between 0.6 and 1.0 mm. The cross sectional drawings of the structures with 1-1 and 1-3 stackings are given in Figure 3-1. The cross section of the fibres showed ca.3 % closed porosity. The 1-1 structure has ‘parallel’ fibres in the direction of the flow, while 1-3 structure consists of ‘zig-zag’ fibres in the direction of the flow.

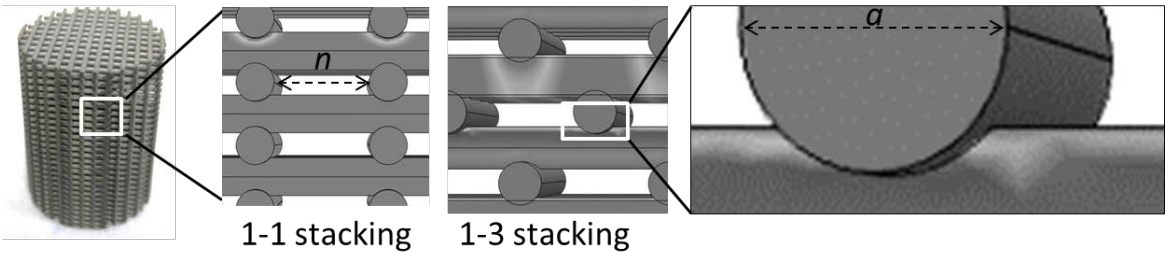

Figure 3-1. Fibre stacking (1-1) and (1-3).

Table 3-1 shows the specifications of the samples manufactured for the effective thermal conductivity and pressure drop measurements. The calculation methods for macro-porosity, specific surface area (SSA) and open frontal area (OFA) are described in Appendix A. Manufactured samples were coded as follows: fibre diameter (*a*), fibre stacking positioning (straight (1-1) or zig-zag (1-3)) and inter-fibre distance (*n*). For example, the sample 4(1-1)6 is manufactured by using the nozzle of 0.4 mm, with straight fibre positioning (stacking 1-1) and inter-fibre distance of 0.6 mm. Final structures were dried at room temperature for 2 days. Then the samples were sintered at 1300°C for 4 h under argon atmosphere.

Table 3-1. Samples specifications.

Sample codes	Macro-porosity (%)	SSA[a], (mm^{-1})	OFA[b] (%)
4(1-1)6	69	3.0	36
4(1-1)8	74	2.6	44
4(1-1)10	78	2.2	51
4(1-3)8	74	2.6	11
4(1-3)10	78	2.2	18
6(1-3)10	71	1.9	6

a: Surface area per unit of bulk volume ($mm^2 \cdot mm^{-3}$)

b: Open frontal area

For the thermal conductivity experiments, since the laser flash technique requires non-porous planar top and bottom surfaces, stainless steel discs were positioned on and under the sample to form a "sandwich" structure. The "sandwich" structures were prepared as follows (Figure 3-2): (i) the sintered stainless steel structures were cut into cylindrical shapes horizontally and vertically with a length of 4.5 mm and a diameter of 10 mm; (ii) structures were placed between two stainless steel discs of 0.5 mm thickness, and then sintered at 1300°C for 4 h under argon atmosphere. In order to avoid reflection and to obtain a good signal, both sides of structures were coated with a graphite layer.

For the pressure drop measurements, sintered stainless steel samples were cut into cylinders with 20.1 mm diameter and 20 mm length. In order to investigate the coating effect on the pressure drop, supports were dip-coated with Ni/alumina layer. Coating suspension composition was as follows: 3 wt.% PVA, 1 wt.% acetic acid, 20 wt.% Ni/Al_2O_3 powder, and water according to the procedure described before [11]. The Ni/alumina loading on the supports was varied between 0.09 and 0.19 $g_{Ni/alumina} \cdot cm^{-3}_{support}$. The loading was calculated as $(G_{support+Ni/alumina}-G_{support})/V_{support}$ where, G (g) is the weight and $V_{support}$ (cm^3) is the volume of the structured support.

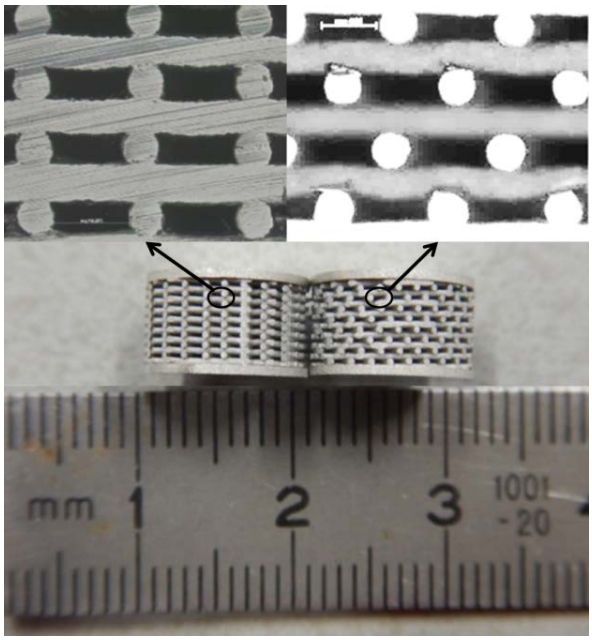

Figure 3-2. “Sandwich” design of the 4(1-1)8 (left) and 4(1-3)8 (right) structures for thermal conductivity experiments.

3.2.2. Characterization

The cross-sectional images of the structured catalyst were obtained by scanning electron microscopy (SEM; FEG JSM6340F, JOEL) and optical microscopy (Zeiss, Stereo Discovery V12) with imager (type M2m). Effective thermal conductivity was measured by Laser Micro flash instrument (Netzsch, LFA 457). Pressure drop was measured by means of TT 570 Low Res Micro manometer (DPM Buckingham).

3.2.3. Effective thermal conductivity measurements

3.2.3.1. Experimental setup

Samples with a cylindrical shape were placed in between the sample carrier (5.5 mm thick and 12.5 mm in diameter), and then were put in the furnace. The thermal diffusivity of each sample was measured under argon atmosphere (50 $ml \cdot min^{-1}$ STP) at temperatures of 50, 100, 200, 300, 400 and 500°C with a heating rate of 0.5°C·min^{-1} at ambient pressure. Scheme of the experimental setup is given in Figure 3-3. The setup consists of four main parts: furnace, laser power supply, detector and data acquisition system. The laser was used as a heat source.

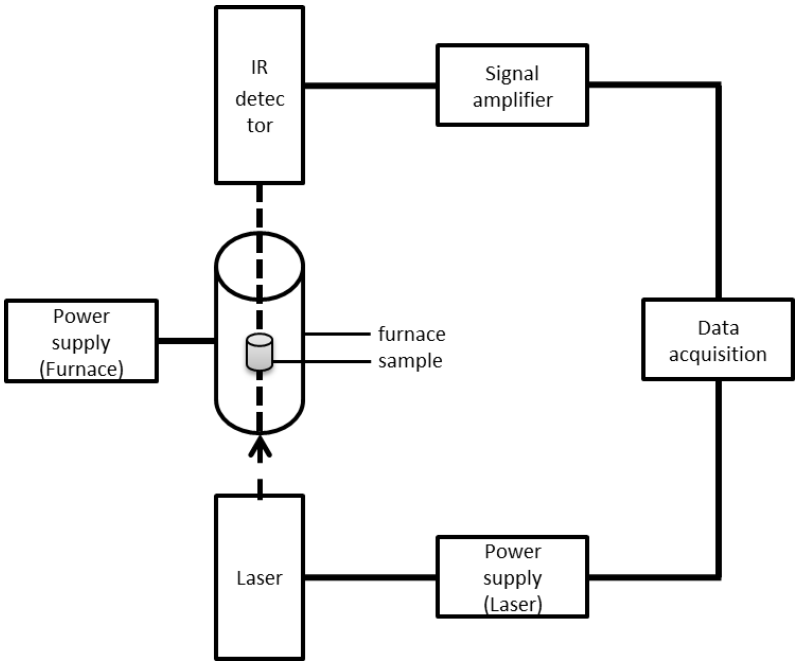

Figure 3-3. Schematic drawing of the experimental setup used for ETC measurements.

The flash method is the most widely used method for determining thermal diffusivity which was first introduced by Parker *et al.* in 1961 [17]. The rapid homogeneous heating of the front side of the sample is achieved by a laser pulse. On the back side of the sample the temperature increase is measured as a function of time. Temperature was recorded for each laser 'shot' in time. The back surface temperature (T) versus time (t) relationship was expressed by the following equations by Parker *et al.*:

$$T(L,t) = \frac{Q}{\rho C_p L}\left[1 + 2\sum_{n=1}^{\infty}(-1)^n \, exp\left(\frac{-n^2\pi^2}{L^2}\alpha t\right)\right] \quad (3\text{-}1)$$

$$\mathcal{V}\,(L,t) = \frac{T(L,t)}{T_M} \quad (3\text{-}2)$$

$$\omega \;=\; \frac{\pi^2}{L^2}\alpha t \quad (3\text{-}3)$$

where α is thermal diffusivity ($m^2 \cdot s^{-1}$), ρ density ($kg \cdot m^{-3}$) and C_p specific heat capacity ($J \cdot kg^{-1}.K^{-1}$) as a function of temperature, Q is the power on the front surface at t=0, T_M is the maximum temperature at the rear face of the sample, L is thickness of the sample in cm, V and ω are dimensionless parameters. The rear surface temperature distribution is plotted with dimensionless parameters as shown in Figure 3-4.

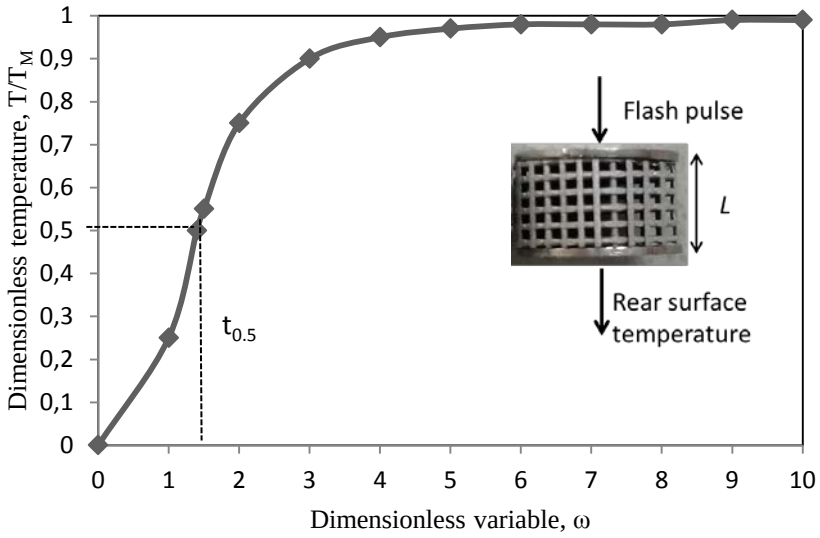

Figure 3-4. Dimensionless plot of rear surface temperature history diagram Parker *et al.* [17].

Thermal diffusivity is determined by the temperature versus time curve, where $t_{0.5}$ is the time required for the rear surface to reach half of the maximum temperature rise that is reached at $\omega = \frac{\pi^2}{L^2}\alpha t = 1.38$. Therefore, the thermal diffusivity equation is given as follows: $\alpha = 0.1388\frac{L^2}{t_{0.5}}$. The thermal conductivity (λ) is calculated using the following equation: $\lambda = \alpha(T).\rho(T).C_p(T)$. Thermal properties of 316L bulk stainless steel are given in Table 3-2. Bulk density of sample is taken as 7800 kg·m^{-3}.

Table 3-2. Thermal properties of 316L stainless steel at different temperatures [18].

Temperature, °C	**50**	**100**	**200**	**300**	**400**	**500**
C_p, J·g^{-1}·K^{-1}	485	501	512	538	556	578
λ_{solid}, W·m^{-1}·K^{-1}	14.73	15.48	16.98	18.49	19.99	21.49

Since the experiments contained multiple shots, temperature changes were recorded between two measurements. Multiple measurements were taken, and uncertainty of each parameter is determined to be as follows: effective thermal conductivity (s_{ETC}) ±4 %, temperature (s_T) ±1.2 % and geometry (s_G) ± 6%. Experimental results, temperature variations and sample size were taken into account. Combined standard uncertainty (s) was calculated as follows: $s = \sqrt{(s)_{ETC}^2 + (s)_T^2 + (s)_G^2}$ [19,20]. The total combined uncertainty was found to be 7 %.

3.2.3.1. Thermal conductivity model

For the samples with the linear fibre stacking, the axial effective conductivity can be numerically calculated according to the Equation 3-5. A unit area of a sample for axial effective conductivity calculation is given in Figure 3-5. In the area of M^2, the heat transport occurs at the

region where the two fibres intersect. The maximal area of the intersection is assumed to be a^2. The effective conductivity is related to the bulk conductivity by considering a heat transport area of a^2 for a unit cell area of M^2, where a is fibre diameter (mm) and M is axial centre distance between two fibres (mm).

$$\lambda_{axial} = \lambda_{SS\,316L} \frac{surface\ area\ of\ the\ fibres\ intersection}{unit\ area} \tag{3-4}$$

$$\lambda_{axial} = \lambda_{SS\,316L} \left(\frac{a}{M}\right)^2 \tag{3-5}$$

The optical microscope image of the structure in the axial direction of the matrix is given in Figure 3-5. In the case of 4(1-1)8 and 4(1-3)8, the structure with 1-1 stacking has 69 vertical fibres per cm^2 in the axial direction and the sample with 1-3 stacking has no direct connection between the fibres of two subsequent layers (Figure 3-1).

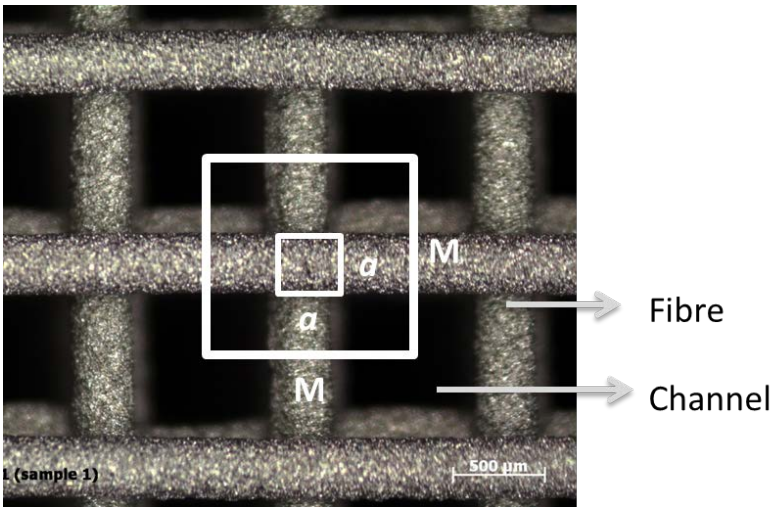

Figure 3-5. OM image of a 1-1 sample for axial ETC calculation.

The radial ETC of samples with linear stacking is calculated according to the equation 3-6.

$$\lambda_{radial} = \lambda_{SS\,316L} \frac{\pi a^2}{8M(a-c)} \tag{3-6}$$

The optical microscope image of the radial direction in the 3D-structured matrix is given in Figure 3-6, where a is fibre diameter (mm) and M is axial centre distance between two fibres (mm). The stacking factor c refers to the stacking ”depth” between two layers of fibres in z-direction, considering an anisotropic pore architecture. Stacking factor c is assumed to be a constant value for the whole sample. Due to the stacking effect (c), unit area equals to $2M\cdot(a-c)$ instead of M^2 (Figure 3-6). This difference leads to a higher λ_{radial} than λ_{axial} at the same a and M. The radial effective thermal conductivity (λ_{radial}) is calculated assuming that the heat is transmitted by conduction through the fibre cross section. The fibre density is defined as the number of fibres per square centimetre. In the case of 4(1-1)8 samples, while axial fibre density is 69 fibres per cm^2, radial fibre density is 126 fibres per

cm^2. Due to the equivalent fibre diameter of the samples with 1-1 and 1-3 stackings, the radial ETC is expected to be equivalent.

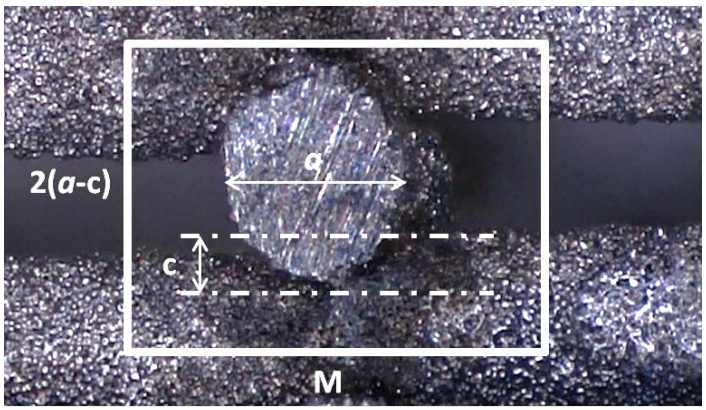

Figure 3-6. OM image of a sample for radial ETC calculation.

A steady-state model was built with COMSOL Multiphysics® for the ETC calculations of metallic supports with different stackings in the axial and radial directions without taking into account convection and radiation. A heat transfer module was applied to simulate the experimental thermal conductivity measurements by a Laser Micro flash instrument. The schematic drawing of a cylindrical shaped 3D-model of the structure is given in Figure 3-7. In the model, the temperature values between 50 and 500°C were applied to the sample. Uniform temperatures T_1 and T_2 are imposed for the top (S_t) and bottom (S_b) plates, respectively. A mesh of 10^6 elements was used for the model.

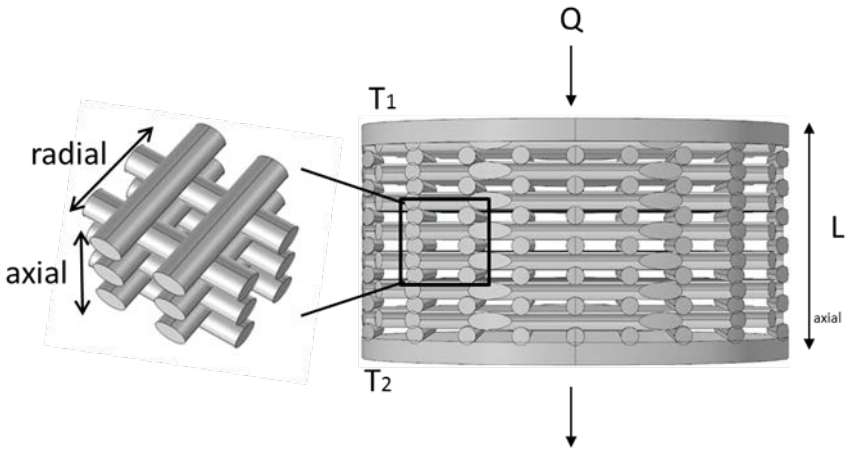

Figure 3-7. The schematic drawing of the 4(1-1)8 structure for axial thermal conductivity modelling.

In this module, the axial effective thermal conductivity (λ_{eff}) of each sample in steady-state conditions was calculated based on Fourier's law, as expressed in the following equation [21]:

$$\frac{Q}{S_{TOP/REAR}} = \lambda_{eff} \frac{\Delta T}{\Delta L} \tag{3-7}$$

where Q (W) is an amount of heat power passing through a cross section causing a temperature difference over a distance L, $Q/S_{TOP/REAR}$ ($W.m^{-2}$) is the heat flux which is related to the thermal

gradient $\Delta T/\Delta L$, $S_{TOP/REAR}$ (m^2) is the surface area of the top (S_{TOP}) and rear (S_{REAR}) plates, ΔT (K) is the temperature difference between the top and the bottom plates, and L (m) is the height of the sample.

3.2.4. Pressure drop measurements

The pressure drop (Δp) was measured as a function of the superficial velocity using an electronic micro-manometer. The experimental setup is shown in Figure 3-8. The setup was built for the basic screening of the pressure drop using different gas velocities. Air was used as a flow gas, experiments were performed at room temperature. At the inlet of the tube, a 30 mm thick glass wool layer was inserted in order to homogenize the flow. The samples of 20 mm length were centred in a 21 mm diameter tube. The samples were wrapped with a Teflon tape bandage in order to prevent the gas bypass. There were two holes with a diameter of 4 mm at top and bottom of the sample that were connected to the micro-manometer. The accuracy of the manometer was ± 0.05 Pa. The inlet flow rate was controlled by a mass flow controller. The air superficial velocity was ranged between 0.1 and 4.9 $m \cdot s^{-1}$. The Reynolds number (Re) was calculated from the equation (3-8):

$$Re = \frac{\rho V a}{\mu} \tag{3-8}$$

where a is the fibre diameter (m), V is the fluid superficial velocity ($m \cdot s^{-1}$), ρ is the fluid density ($kg \cdot m^{-3}$) and μ is the air dynamic viscosity (Pa·s).

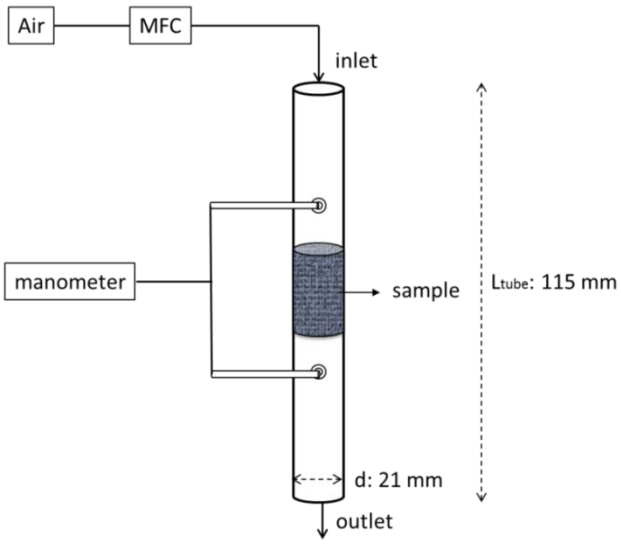

Figure 3-8. Setup for pressure drop measurements.

Measurements were performed before and after coating of the samples. For the benchmarking, a 20 mm section of the tube was filled with 3 mm alumina beads for the pressure drop measurements to simulate the packed-bed reactor. The volume of alumina beads was the same (6.3 cm^3) as the volume of the structured samples. The interest was to compare alumina beads and 3DFD structures by means of pressure drop and permeability. Permeability (K) describes how easily a fluid is able to

move through the porous material which is usually calculated using a formula known as Darcy's Law [22] by measuring the pressure drop across the structured samples (ΔP). Darcy's law, which states that a fluid flow rate is directly proportional to the pressure gradient, is shown to be accurate only at low flow velocities. At higher flow rates, Darcy's law is usually replaced by the Darcy-Forchheimer equation, which includes quadratic flow rate. Thus, Forchheimer coefficient (β) and permeability (K) were calculated as follows:

$$\frac{\Delta P}{L} = \frac{\mu}{K} V + \beta \rho V^2 \quad (3\text{-}9)$$

where ΔP is the pressure drop (Pa), L is the height of the sample (m), μ is the air dynamic viscosity (Pa·s), K is permeability (m^2), V is superficial fluid velocity ($m \cdot s^{-1}$), β is Forchheimer coefficient (m^{-1}) and ρ is fluid density ($kg \cdot m^{-3}$).

3.3. Results and discussion

3.3.1. Effective thermal conductivity measurements and modelling

Axial and radial ETC values based on experiments, numerical equations (Equation 3-5 and 3-6) and COMSOL model are listed in Tables 3-3 and 3-4. It can be seen that the numerical data based on the equations 3-5 and 3-6 agree with the experimental data. Axial and radial ETC of the samples increased with increasing temperatures due to increasing heat capacity of the bulk solid material (Table 3-3 and 3-4).

Table 3-3. Axial effective thermal conductivity.

	λ_{eff} experimental ($W \cdot m^{-1} \cdot K^{-1}$)		**λ_{eff} Eq. 3-5 ($W \cdot m^{-1} \cdot K^{-1}$)**		**λ_{eff} Comsol ($W \cdot m^{-1} \cdot k^{-1}$)**
Samples / Temp. (°C)	**4(1-1)6**	**4(1-1)8**	**4(1-1)6**	**4(1-1)8**	**4(1-1)8**
50	2.44	1.78	2.36	1.64	1.79
100	2.49	1.79	2.48	1.72	1.88
200	2.76	2.04	2.72	1.89	2.06
300	3.07	2.17	2.96	2.05	2.25
400	3.45	2.37	3.20	2.22	2.43
500	3.94	2.50	3.44	2.39	2.61

Table 3-4. Radial effective thermal conductivity.

	λ_{eff} experimental ($W \cdot m^{-1} \cdot K^{-1}$)		λ_{eff} Eq. 3-6 ($W \cdot m^{-1} \cdot K^{-1}$)		λ_{eff} Comsol ($W \cdot m^{-1} \cdot k^{-1}$)
Samples / Temp. (°C)	**4(1-1)6**	**4(1-1)8**	**4(1-1)6**	**4(1-1)8**	**4(1-1)8**
50	2.22	1.83	2.35	1.96	2.19
100	2.48	2.06	2.47	2.06	2.30
200	2.57	2.12	2.71	2.26	2.54
300	2.94	2.19	2.95	2.46	2.77
400	3.22	2.77	3.19	2.66	3.01
500	3.62	2.87	3.43	2.86	3.24

3.3.1.1. Effect of fibre stacking

Figure 3-9 shows experimental and COMSOL model results of the effect of stacking on the ETC of 4(1-1)8 and 4(1-3)8 samples. The samples were manufactured with the nozzle of 0.4 mm diameter and have a macro-porosity of 74 % and a specific surface area of 2.6 mm^{-1}. The fibre density in each structure was kept constant to investigate the stacking effect.

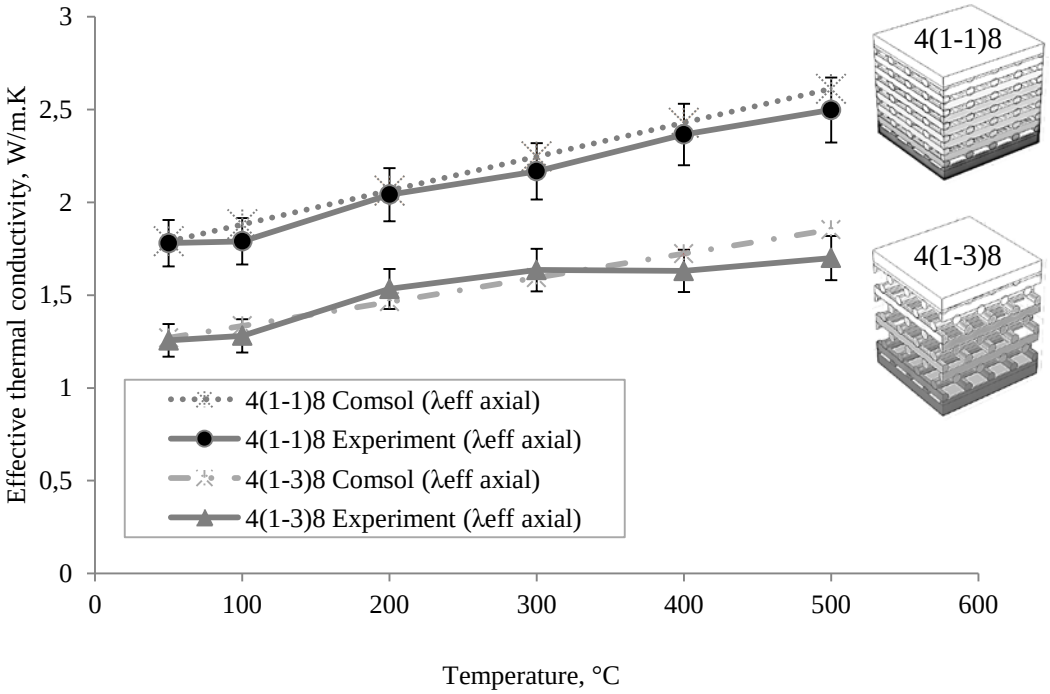

Figure 3-9. Effect of the fibre staking on effective axial ETC of 4(1-1)8 and 4(1-3)8 samples.

It can be seen that the structure with 1-1 configuration showed higher axial ETC than the structure with 1-3 stacking under the same measurement conditions due to their different geometries. The structure with 1-1 stacking has continuous fibre stackings and direct fibre connection in the axial direction, which this is not a case for 1-3 stacking samples. Therefore, the 1-3 geometry resulted in lower axial ETC. Experimental results were found to be in very good agreement with the COMSOL model.

The 3D-model allows also for the investigation of the difference in heat transport patterns of the samples with the different architectures. The images of the heat flow is given in Figures 3-10. Different sizes of the mesh (50.000 to 3.000.000 cells) were tested to check the sensitivity of the results to the mesh size. The mesh size of 1.000.000 cells was found to provide a sufficient accuracy (relative change in ETC < 10^{-4} compared to 3.000.000 cells) and a short calculation time (1.5 min). A layer of the sample was chosen in order to observe the heat flux in axial direction through fibres. The arrows show the directions of the heat flux at temperatures between 300 and 320°C. Non-linear fibre stacking (1-3) results in different temperatures along the fibre. Temperature distribution through one fibre is plotted in Figure 3-11. It is clear that fibres of the 1-1 stacking sample have more homogeneous temperature profile (ca. 305°C). At the same temperature, effective thermal conductivity of the sample with 1-3 stacking is lower than the sample with 1-1 stacking. Moreover, the temperature of the fibres show strong spatial variation in the case of 1-3 stacking.

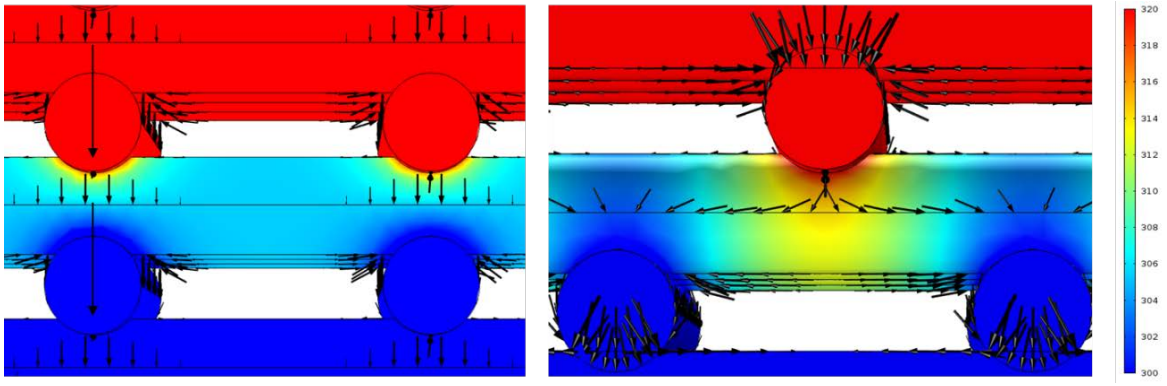

Figure 3-10. Heat flow (arrows) and temperature (colours) in linear stacking fibres in axial direction (left) and non-linear stacking fibres in axial direction (right).

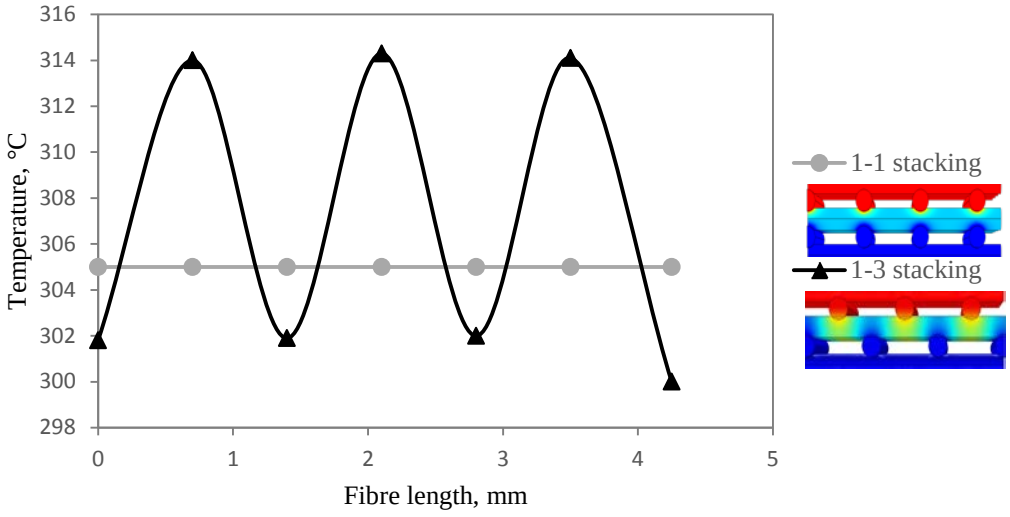

Figure 3-11. Temperature distribution model for samples 4(1-1)10 and 4(1-3)10.

Heat transport in the radial direction is a key parameter for the reactor design for exothermic reactions where heat is mainly conducted in radial direction between the reactive channel and the cooling media. Results confirmed that samples with 1-1 and 1-3 stackings show equivalent radial effective thermal conductivity due to the identical geometry in the radial direction.

3.3.1.2. Effect of macroporosity

In order to study the effect of macroporosities of samples on heat transport properties, macroporosities were varied (62, 69, 74, 78 and 81 %) by modifying interfibre distances (0.4, 0.6, 0.8, 1 and 1.2 mm) while keeping the fibre diameter constant at 0.4 mm. The corresponding structures are coded as follows: 4(1-1)4, 4(1-1)6, 4(1-1)8, 4(1-1)10 and 4(1-1)12.

The effect of macroporosity on ETC of the samples with 1-1 stacking is shown in Figure 3-12 (calculated using equations 3-5 and 3-6). It was observed that axial and radial ETC decreased with increasing macro-porosity. This is because the conduction cross section is reduced for the samples with higher macroporosity, leading to a reduced ETC (Figure 3-12). The slope of λ_{axial} was found to be higher than the λ_{radial}. The reason of the higher slope of λ_{axial} is while λ_{axial} varies with M^{-2} (Equation 3-5), λ_{radial} varies with M^{-1} (Equation 3-6).

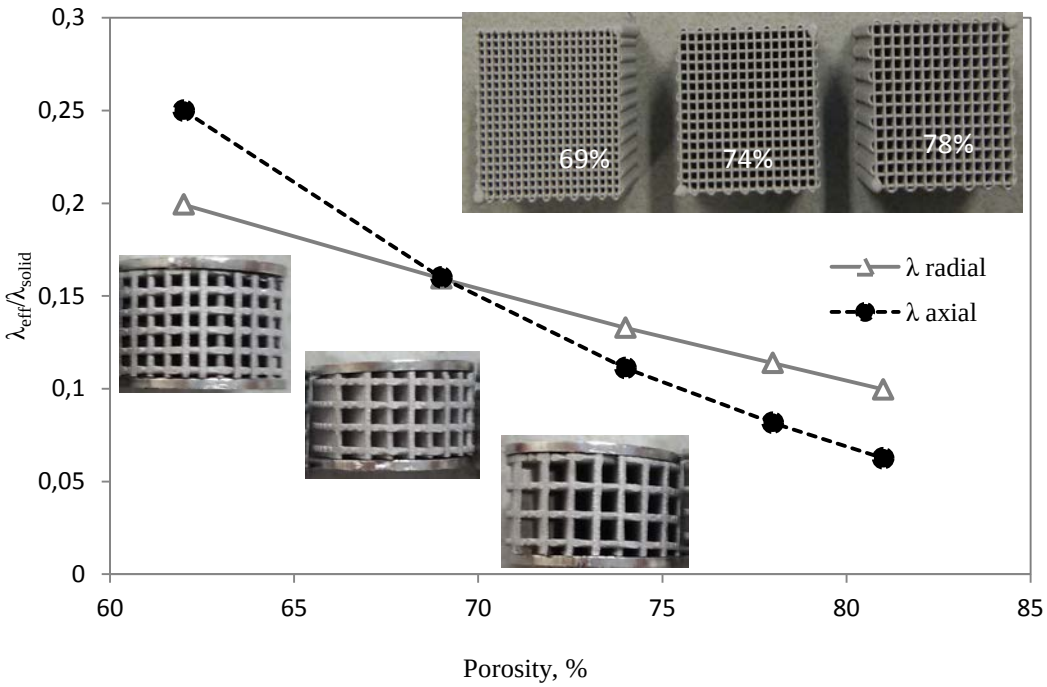

Figure 3-12. ETC of 1-1 stacking structures with different macroporosities.

The similar effect of the porosity on ETC was observed on fibre felt and foams [10,23]. It was found that the total ETC decreased with an increase of porosity under the fixed fibre diameter. This was mainly attributed to a reduced solid matrix heat conduction and reduced thermal radiation.

To study the effect of the fibre thickness on the axial and radial ETC, samples at the same porosity (70 %) with different fibre diameters, i.e. 4(1-1)6.3, 5(1-1)8, 6(1-1)9.5, 7(1-1)1.1 and 8(1-1)1.32 were compared. Results are given in Figure 3-13. It was found that the fibre diameter effect on axial and radial ETC at constant porosity was negligible. Therefore, effect of macroporosity was found to be significant for axial and radial ETC.

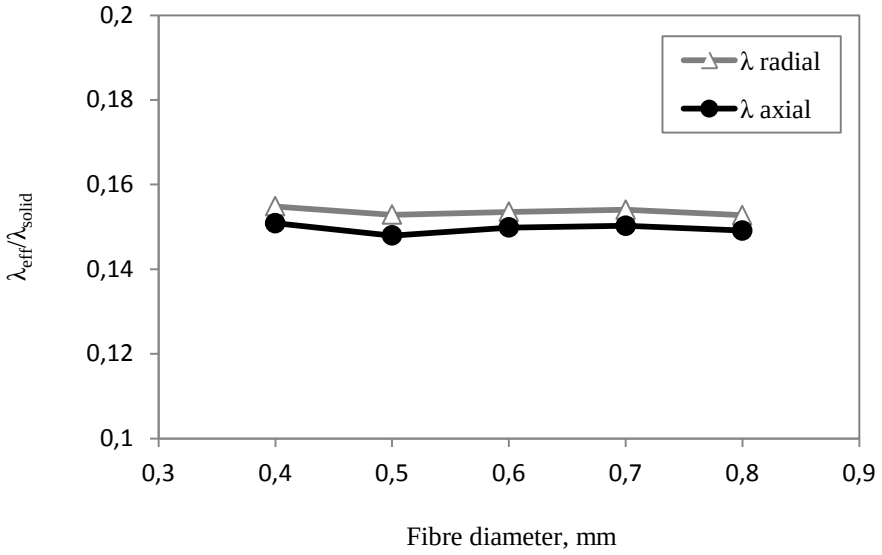

Figure 3-13. ETC of 1-1 stacking structures at 70 % macroporosity with different fibre diameters.

3.3.2. Pressure drop measurements

Tables 3-5a and 3-5b show experimental results of the pressure drop measurements (samples 4(1-1)8, 4(1-1)10, 6(1-1)10, 4(1-3)10, 6(1-3)10 and 3 mm alumina beads). The permeability and the Forchheimer coefficient were determined for each sample from the experimental results. The effect of stacking and fibre diameter on the pressure drop was studied. Samples were coated with catalyst to study the coating effect on the pressure drop. Alumina beads were used for a comparison.

Results of the pressure drop measurements on the structured samples and 3 mm alumina beads are presented in Figure 3-14. The pressure drop through the packed bed of beads was found to be 70 and 10 times higher than 1-1 and 1-3 stacking structures, respectively. The main reason was expected to be the low OFA of packed-bed of beads. In the case of beads, the tube/particle diameter ratio was calculated to be D_{tube}/d_p = 7:1. Studies regarding the wall effect on pressure drops in packed beds with D_{tube}/d_p below 10:1 was reported elsewhere [24, 25]. That is why a contribution of the wall effect in the case of 3mm alumina beads was also expected.

Table 3-5a. Experimental results of pressure drop measurements on samples with 1-1 stacking.

Sample	4(1-1)8			4(1-1)10		
Macroporosity (%)	74.30	73.76	73.22	77.87	77.40	76.94
Ni/alumina loading (g·cm^{-3})	No	0.09	0.19	no	0.1	0.2
Coating thickness (µm)	-	~8	~16	-	~8	~16
Permeability (m^2)	1.06E-06	6.74E-07	6.09E-07	1.58E-06	1.02E-06	9.60E-07
Forchheimer coefficient (m^{-1})	6.04	6.31	9.59	4.20	4.33	7.76
Velocity (m·s^{-1})	**Pressure drop (ΔP), Pa**					
0.12	2.1	4	3.3	1.3	2.7	2.1
0.25	4.7	7.3	7.4	2.8	5.1	4.6
0.37	8	11.5	12.5	4.8	7.7	8.1
0.49	11.2	15.5	17.5	7	10.4	11.7
0.62	14.9	20.1	23	9.5	13.5	15.7
0.74	18.9	24.8	29.2	12	16.5	19.8
0.87	22.6	30.3	36	14.8	19.9	24.2
0.99	26.6	35.3	42.7	17.6	23.2	29.3
1.11	31	40.8	49.7	20.6	27	34.3
1.24	35.3	46.6	56.7	23.6	31.1	39.4
2.47	86	112	143	59	75.4	103
3.71	153	202	265	107	136	194
4.95	267	320	430	182	216	322

Table 3-5b. Experimental results of pressure drop measurements on samples with 1-3 stacking and 3 mm alumina beads.

Sample	4(1-3)10			6(1-3)10			3mm beads
Macroporosity (%)	77.87	77.40	76.94	70.58	70.18	69.78	-
Ni/alumina loading (g·cm^{-3})	no	0.09	0.17	no	0.09	0.19	No
Coating thickness (µm)	-	~8	~16	-	~8	~16	-
Permeability (m^2)	4.73E-07	1.69E-07	1.63E-07	3.41E-07	1.54E-07	9.00E-08	1.71E-08
Forchheimer coefficient (m^{-1})	54.82	133.79	294.82	117.70	240.59	551.55	208.39
Velocity (m·s^{-1})	**Pressure drop (ΔP), Pa**						
0.12	7.6	12.8	10.9	11	14.6	36.6	56
0.25	18	32.5	45.5	26.5	41.3	83	204
0.37	31	58.2	90.3	46.3	80.3	158	374
0.49	44.1	84	146	70.7	128	254	552
0.62	58.7	116	210	97.3	181	372	733
0.74	75.1	153	283	126	243	500	915
0.87	92	197	367	162	317	657	1110
0.99	111	243	470	203	398	847	1330
1.11	131	294	576	256	494	1050	1560
1.24	153	350	696	298	593	1270	1770
2.47	479	1410	2400	965	2030	4500	4150
3.71	1010	2460	5230	2070	4370	-	7390
4.95	1800	4450	-	3710	-	-	-

Previous studies showed that cell orientation, porosity, open frontal area and surface roughness affect pressure drop [16, 26–28]. The dominating effect of the macro-porosity on the pressure drop was observed for the samples 6(1-3)10, 4(1-3)10, 4(1-1)8 and 4(1-3)10. Figure 3-14 shows that a decrease of the macroporosity of the sample leads to an increase of the pressure drop. The lowest pressure drop was observed for the sample 4(1-1)10 which has the highest macro-porosity (78 %). A similar macro-porosity effect was observed for samples with 1-3 stacking: 4(1-3)10 and 6(1-3)10 (see Table 3-5a and 3-5b).

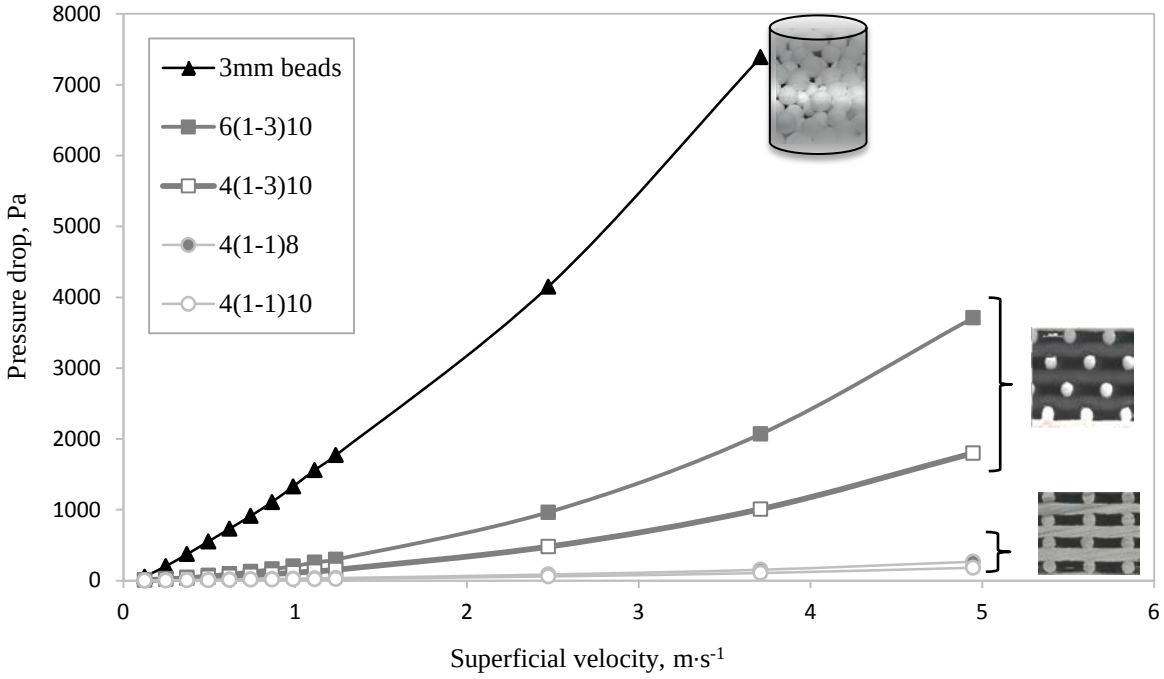

Figure 3-14. Pressure drop versus superficial velocity.

3.3.2.1. Effect of fibre stacking

The results of pressure drop measurements using samples 6(1-3)10, 4(1-3)10, 4(1-1)8 and 4(1-3)10 are given in Figure 3-15. Re numbers ranged between 2 and 127 at superficial velocities between 0.12 and 4.95 $m \cdot s^{-1}$.

In the laminar region (<15 Re), where the pressure drop increases linearly with superficial velocity, sample 4(1-1)8 shows 6 times lower pressure drop than the sample 4(1-3)8. Changing the cell orientation from 1-1 to 1-3 lead to a decrease of the OFA, that resulted in higher pressure drop. Limiting Reynolds numbers of samples with 1-3 stacking (6(1-3)10 and 4(1-3)10) were found to be 15 and 30, respectively.

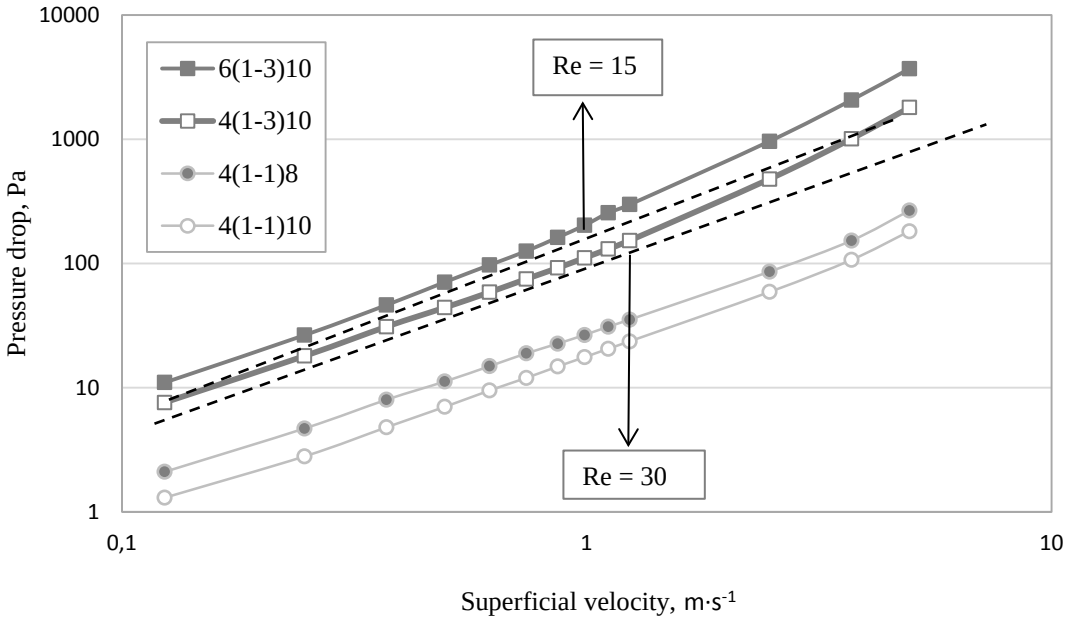

Figure 3-15. Results of pressure drop measurements with the structured samples of different stackings.

3.3.2.2. Effect of the coating

In order to investigate the effect of the coating on the pressure drop, four samples (4(1-1)10 and 4(1-3)10, two of each) were coated with a Ni/alumina slurry by a dip-coating technique to obtain two different loadings, i.e. 0.09 g·cm^{-3} (coating thickness ca. 8 µm, determined by SEM) and 0.19 g·cm^{-3} (coating thickness ca. 16 µm). Calculated macroporosity values before and after coating are given in Table 3-5. The illustration of the effect of the coating thickness on the pressure drop is given in Figure 3-16. The addition of the coating resulted in only a very small decrease in cell size and porosity. However, pressure drop was higher, due to the combination effect of increased surface roughness and decreased maco-porosity. The coating effect is more pronounced in the case of the structures with 1-3 stacking. For example, at 2.47 m·s^{-1} superficial velocity, the pressure drop of a sample with 16 µm coating was 5 times higher than the uncoated support.

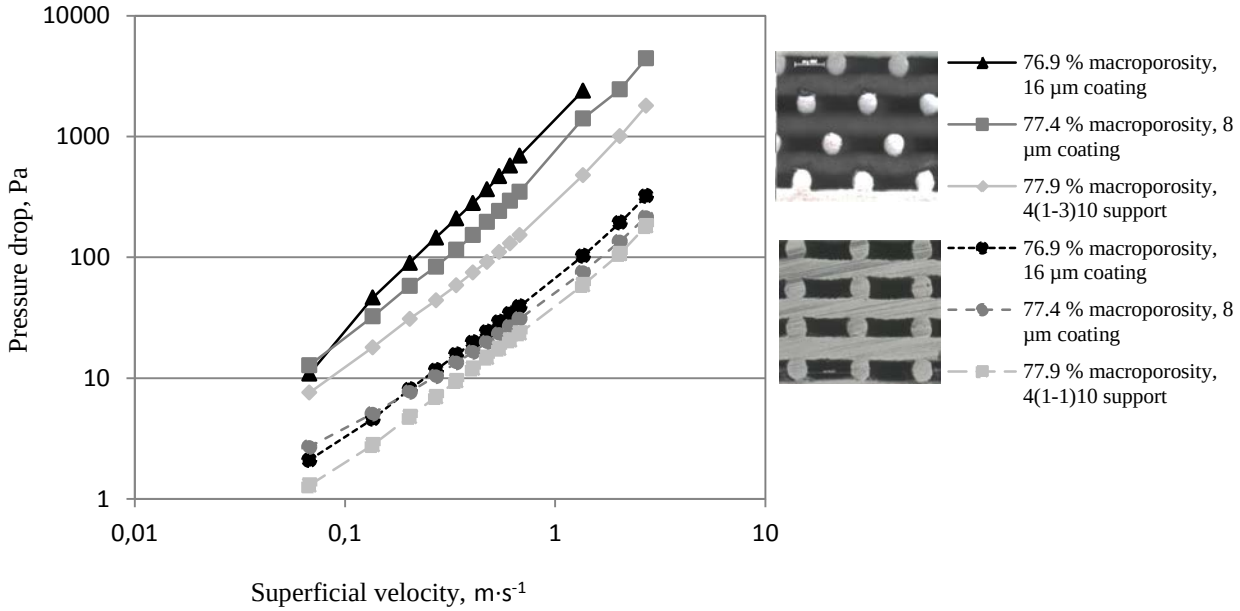

Figure 3-16. Effect of the coating thickness on the pressure drop.

3.4. Conclusions

In this chapter, the effect of the cell geometry (stacking) of stainless steel structured supports and their macroporosity on the ETC and pressure drop was studied. It was observed that the stacking (parallel or zig-zag) affects the ETC due to the difference in the connection between the fibres. Stacking factor, inter-fibre distance and fibre diameter were found to be the main parameters affecting macroporosity and therefore ETC and pressure drop. The stacking factor can be controlled by several parameters of the manufacturing technique, e.g. paste composition, printing speed, printing atmosphere, drying temperature and atmosphere. Axial ETC of samples with 1-1 stacking was found to be higher than samples with 1-3 stacking due to their linear fibre stacking in the axial direction. However, samples with different stackings have no difference in the radial ETC. The ETC decreases with increased macroporosity due to a dominant conductive heat transfer over the convective and radiative heat transfer. A model has been developed to describe the conductive heat transfer in the samples under non-adiabatic conditions in the absence of a chemical reaction. This approach suggests that the radial thermal conduction can be controlled by inter-fibre distance, fibre diameter and stacking factor. This is important for the reactor design for exothermic reactions because improved radial heat transfer can prevent the risks of thermal runaway.

Pressure drop measurements showed that samples with 1-3 stacking have higher pressure drop than the ones with 1-1 stacking at the same macroporosity due to the reduced open frontal surface area. Increasing macroporosity decreases the pressure drop allowing for the operation of the reactor at higher gas velocities. The study of the effect of the coating showed that the pressure drop increases with the increase of the surface roughness and decrease of the porosity via increasing coating thickness. In general, structured samples showed much lower pressure drop than the conventional 3mm alumina beads (simulation of the packed-bed reactor design).

This study proves that higher heat transport and lower pressure drop can be achieved using 3D-structured supports compared with conventional packed-bed reactors/catalysts. While samples with high macroporosity demonstrated low pressure drop, samples with low macroporosity showed high ETC.

The variation of structural parameters (cell orientation, stacking, fibre diameter and inter-fibre distance) allows for the modification of the geometry, cell sizes, and macroporosity therefore optimization of the heat transport and pressure drop values according to the process requirements. The heat transfer efficiency can be enhanced not only by changing the geometry of the structured catalyst but also by the use of materials with higher thermal conductivity coefficients.

3.5. References

[1] M. Noda, H. Nishitani, Flexible heat exchanger network design for chemical processes with operation mode changes, in: 16th Eur. Symp. Comput. Aided Process Eng. 9th Int. Symp. Process Syst. Eng., 2006: pp. 925–930.

[2] E. Bianchi, T. Heidig, C.G. Visconti, G. Groppi, H. Freund, E. Tronconi, An appraisal of the heat transfer properties of metallic open-cell foams for strongly exo-/endo-thermic catalytic processes in tubular reactors, Chem. Eng. J. 198–199 (2012) 512–528. doi:10.1016/j.cej.2012.05.045.

[3] I.P. Kandylas, A.M. Stamatelos, Engine exhaust system design based on heat transfer computation, Energy Convers. Manag. 40 (1999) 1057–1072. doi:10.1016/S0196-8904(99)00008-4.

[4] T.J. Lu, H.A. Stone, M.F. Ashby, Heat transfer in open-cell metal foams, Acta Mater. 46 (1998) 3619–3635. doi:10.1016/S1359-6454(98)00031-7.

[5] H.J. Xu, L. Gong, C.Y. Zhao, Y.H. Yang, Z.G. Xu, Analytical considerations of local thermal non-equilibrium conditions for thermal transport in metal foams, Int. J. Therm. Sci. 95 (2015) 73–87. doi:10.1016/j.ijthermalsci.2015.04.007.

[6] C.Y. Zhao, Review on thermal transport in high porosity cellular metal foams with open cells, Int. J. Heat Mass Transf. (2012). doi:10.1016/j.ijheatmasstransfer.2012.03.017.

[7] T. Boger, A.K. Heibel, Heat transfer in conductive monolith structures, Chem. Eng. Sci. 60 (2005) 1823–1835. doi:10.1016/j.ces.2004.11.031.

[8] V. Tomašić, F. Jović, State-of-the-art in the monolithic catalysts/reactors, Appl. Catal. A Gen. 311 (2006) 112–121. doi:10.1016/j.apcata.2006.06.013.

[9] O.P. Klenov, N.A. Chumakova, S.A. Pokrovskaya, A.S. Noskov, Modeling of heat transfer in a porous monolith catalyst with square channels, Ind. Eng. Chem. Res. (2016).

[10] W.Q. Li, Z.G. Qu, Experimental study of effective thermal conductivity of stainless steel fiber felt, Appl. Therm. Eng. 86 (2015) 119–126. doi:10.1016/j.applthermaleng.2015.04.024.

[11] S. Danaci, L. Protasova, J. Lefevere, L. Bedel, R. Guilet, P. Marty, Efficient CO_2 methanation over Ni/Al_2O_3 coated structured catalysts, Catal. Today. 273 (2016) 234–243. doi:10.1016/j.cattod.2016.04.019.

[12] J. Lefevere, M. Gysen, S. Mullens, V. Meynen, J. Van Noyen, The benefit of design of support

architectures for zeolite coated structured catalysts for methanol-to-olefin conversion, Catal. Today. 216 (2013) 18–23. doi:10.1016/j.cattod.2013.05.020.

[13] C.R. Tubio, J. Azuaje, L. Escalante, A. Coelho, F. Guitián, E. Sotelo, et al., 3D printing of a heterogeneous copper-based catalyst, J. Catal. 334 (2016) 110–115. doi:10.1016/j.jcat.2015.11.019.

[14] S. Couck, J. Lefevere, S. Mullens, L. Protasova, V. Meynen, G. Desmet, et al., CO_2, CH_4 and N_2 separation with a 3DFD-printed ZSM-5 monolith, Chem. Eng. J. 308 (2017) 719–726. doi:10.1016/j.cej.2016.09.046.

[15] J. Luyten, S. Mullens, I. Thijs, Designing With Pores - Synthesis and Applications, KONA Powder Part. J. 28 (2010) 131–142. doi:10.14356/kona.2010012.

[16] M. Klumpp, A. Inayat, J. Schwerdtfeger, C. Körner, R.F. Singer, H. Freund, et al., Periodic open cellular structures with ideal cubic cell geometry: Effect of porosity and cell orientation on pressure drop behavior, Chem. Eng. J. 242 (2014) 364–378. doi:10.1016/j.cej.2013.12.060.

[17] W.J. Parker, R.J. Jenkins, C.P. Butler, G.L. Abbott, Flash method of determining thermal diffusivity, heat capacity, and thermal conductivity, J. Appl. Phys. 32 (1961) 1679–1684. doi:10.1063/1.1728417.

[18] RCC-MRx , AFCEN-Association Française pour les Règles de Conception, de Construction et de Surveillance des Matériels des Chaudières Electronucléaires, 2010.

[19] S.L.R. Ellison, A. Williams, Quantifying Uncertainty in Analytical Measurement, Eurachem Citac Guid. CG4. 3rd (2000) 133. doi:0 948926 15 5.

[20] S. Bell, A Beginner's Guide to Uncertainty of Measurement, Meas. Good Pract. Guid. 11 (1999) 34. doi:10.1111/j.1468-3148.2007.00360.x.

[21] E.L. Clussler, Diffusion-Mass Transfer in Fluid Systems, 3rd ed., Cambridge University Press, 2007. ISBN-13 978-0-511-47892-5.

[22] S. Whitaker, Flow in porous media I: A theoretical derivation of Darcy's law, Transp. Porous Media. 1 (1986) 3–25. doi:10.1007/BF01036523.

[23] H. Yang, M. Zhao, Z.L. Gu, L.W. Jin, J.C. Chai, A further discussion on the effective thermal conductivity of metal foam : An improved model, Int. J. Heat Mass Transf. 86 (2015) 207–211. doi:10.1016/j.ijheatmasstransfer.2015.03.001.

[24] B. Eisfeld, K. Schnitzlein, The infuence of confining walls on the pressure drop in packed beds, 56 (2001) 4321–4329.

[25] N. Cheng, Wall effect on pressure drop in packed beds, Powder Technol. 210 (2011) 261–266. doi:10.1016/j.powtec.2011.03.026.

[26] J. Lefevere, A study on the impact of design of robocasted hierarchical structured catalysts on mass and heat transport , applied to methanol-to-olefins conversion, University of Antwerp, 2016.

[27] S. Kandlikar, D. Schmitt, A. Carrano, J. Taylor, Characterization of surface roughness effects on pressure drop in single-phase flow in minichannels, Phys. Fluids. (2005).

[28] G. Croce, P. D'agaro, C. Nonino, Three-dimensional roughness effect on microchannel heat transfer and pressure drop, Int. J. Heat Mass Transf. 50 (2007) 5249–5259. doi:10.1016/j.ijheatmasstransfer.2007.06.021.

Chapter 4

Manufacture of structured copper supports post-coated with Ni/alumina for CO_2 methanation

Chapter 4 describes the manufacture and optimization of the innovative copper 3D-structured supports for CO_2 methanation. The influence of the sintering temperature, atmosphere and technique (pulsed electrical current sintering versus conventional furnace sintering) was investigated. The microstructural evolution of the support was analysed by low-temperature N_2 adsorption, SEM, OM and XRD. It was found that reducing gas atmosphere during the sintering decreases the inner porosity of the fibres of the structures until ca. 0.1 %. Fibres of the sample sintered by pulsed electrical current sintering (PEC) were found to be as dense as the ones processed with conventional sintering, however PEC sintering leads in the unwanted surface oxidation. Adhesion strength of the catalytic coating on copper supports was benchmarked with previously studied stainless steel supports. Both Ni/alumina coated structured supports and conventional packed-bed catalyst were examined in CO_2 conversion to methane. No deactivation was observed after 80 h time-on-stream in the presence of 10 ppm H_2S for the coated steel and copper samples. The addition of 10 ppm H_2S to the stream did not significantly change the structured catalyst performance, although negligible carbon deposition on the catalyst surface was observed.

This chapter was adapted from the paper: Danaci S., Protasova L., Snijkers F., Bouwen W., Bengaouer A., Marty P., Innovative 3D-manufacture of copper supports post-coated with catalytic material for CO_2 methanation, Chem. Eng. Process. (2017), *submitted*.

4.1. Introduction

In recent years, methanation reaction has drawn a great interest in the context of power-to-gas (PtG) processes. The methanation reaction is a well-known exothermic catalytic process, favourable at low temperatures and high pressures. So far, catalytic methanation has been widely investigated in fixed-bed and fluidized bed reactors with conventional catalytic materials [1]. In the case of exothermic chemical reactions with packed-bed reactors, produced reaction heat can lead to the formation of hot spots in the catalyst bed, so the heat management is essential. The hot spots lead to sintering and carbon deposition on catalysts resulting in a decrease of the amount of catalyst active sites [2].

Latterly, structured catalysts attracted a great interest for exothermic reactions due to their better heat- and mass-transfer properties. In recent years, AM started being used for the manufacture of the macro-structured catalytic supports for highly exothermic and endothermic reactions [3–5]. In chapter 2, we proposed to use 3DFD structured catalysts for CO_2 methanation. Above-mentioned limitations of the conventional systems, i.e. temperature regulation limitations, catalysts deactivation (active phase sintering, carbon deposition), high pressure drop and inefficient use of the catalyst due to channelling and bypass phenomena can be overcome by using structured catalysts and reactors. For example, a unique felt structured catalyst for methanation and rWGS reactions was proposed by Hu *et al*. Porous FeCrAlY felt was used as a substrate and wash-coated with methanation catalyst. This micro-structured reactor achieved 78 % conversion at GHSV of 18.000 h^{-1} and temperature of 300°C in methanation reaction [6].

Previously, 3DFD manufactured structured catalysts were investigated at VITO for $DeNO_x$ process and the conversion of methanol to light olefins [5,7]. The main benefits of AM technologies for the manufacture of catalytic supports are the flexible design of complex geometries, material variability and adjustable properties (e.g. porosity) of structures. 3DFD method is based on the continuous micro-extrusion which is described in detail elsewhere [8]. The method allows for the control of the porosity of macro-structured supports via precise distances between the extruded struts. Metallic or ceramic pastes are extruded through a thin nozzle, so the structures are built layer-by-layer. Depending on the material, “green” structures can be sintered using conventional sintering techniques in high temperature ovens, under air/inert/reducing atmosphere. Structured catalysts can be manufactured by direct printing (struts are made of catalyst material) or in two steps: manufacturing of a support structure and then coating the structure with the catalyst layer. Architecture, macro-porosity and material of the structured support play a great role in the catalytic process.

In chapter 2, methanation reaction was studied at temperatures between 250 and 450°C on 3DFD manufactured stainless steel supports coated with Ni/Al_2O_3 catalyst in two different architectures (zig-zag and linear fibre stacking). At low temperatures, effect of the geometry of the structured support on heat- and mass- transfer and thus on CO_2 conversion was observed. Structured

catalyst lowered the temperature increase and led to the enhanced catalyst stability. During stability tests (350°C, H_2/CO_2 = 4, WHSV 1500 h^{-1}), the initial CO_2 conversions were observed to be 80 % and 73 % for structured and powder catalysts, respectively. Powder catalyst showed 8 % decrease of CO_2 conversion already after 45 h time-on-stream, while in the case of structured catalyst, CO_2 conversion stayed constant at ca. 80 % during 53 h time-on-stream.

In this chapter, we report about the manufacture of copper structures as catalytic supports. The reason of using copper is to improve heat exchange between the catalyst and the reactor wall. The heat removal from the catalyst to the cooled wall affects conversion rate and lowers the catalyst deactivation.

Previously, AM copper materials have been fabricated starting from powder with LS, EBM and binder jetting techniques, however no data has been reported on the manufacture of such structures with the method similar to 3DFD technique due to the challenging post-treatment procedure. The structured copper supports were successfully manufactured by 3DFD technique and coated with Ni/alumina catalyst for the tests of CO_2 methanation at laboratory scale. Copper supports were chosen as a possible alternative to stainless steel supports due to high thermal conductivity of copper in comparison with 316L stainless steel (385 and 15 $W \cdot m^{-1} \cdot K^{-1}$, respectively). Adhesion strength of the catalytic coating on copper supports was benchmarked with stainless steel supports described in chapter 2. Density of the struts is also an important parameter for the efficient heat transfer. Therefore, in this work, additional attention was paid to the effect of sintering temperature and atmosphere on the properties of copper 3DFD structures.

4.2. Experimental

4.2.1. Manufacture of macro-porous copper structured supports and coating

Manufacture process of the 3D-structured catalysts consists of the following steps: (i) paste preparation and structure manufacturing, (ii) thermal treatment of the structure and (iii) catalytic coating and post-treatment.

Copper paste was prepared from a spherical copper powder (Sigma-Aldrich, 14-25 μm). The corresponding cumulative particle size distribution (PSD) of the copper powder was determined by PSD analyser (Microtrac S3500) to be as follows: D_{10} = 8.15 μm, D_{50} = 14.02 μm, D_{90} = 22.56 μm and D_{99} = 33.82 μm. Copper powder (88 wt.%) sieved to <25 μm to avoid nozzle blockage was mixed in a planetary intensive mixer (Thinky ARE-250, Japan) with organic binder (12 wt.%) at 1950 rpm for 8 min. 3DFD technique was used for the manufacture of the copper structures. Copper paste was extruded through a nozzle with a diameter of 400 μm, and inter-fibre distance was set at 800 μm (Figure 4-1). Samples consist of ‘zigzag’ crossed fibres in the direction of the flow (1-3 fibre stacking). This geometry was chosen due to the results of CO_2 conversion on structured catalysts reported in chapter 2.

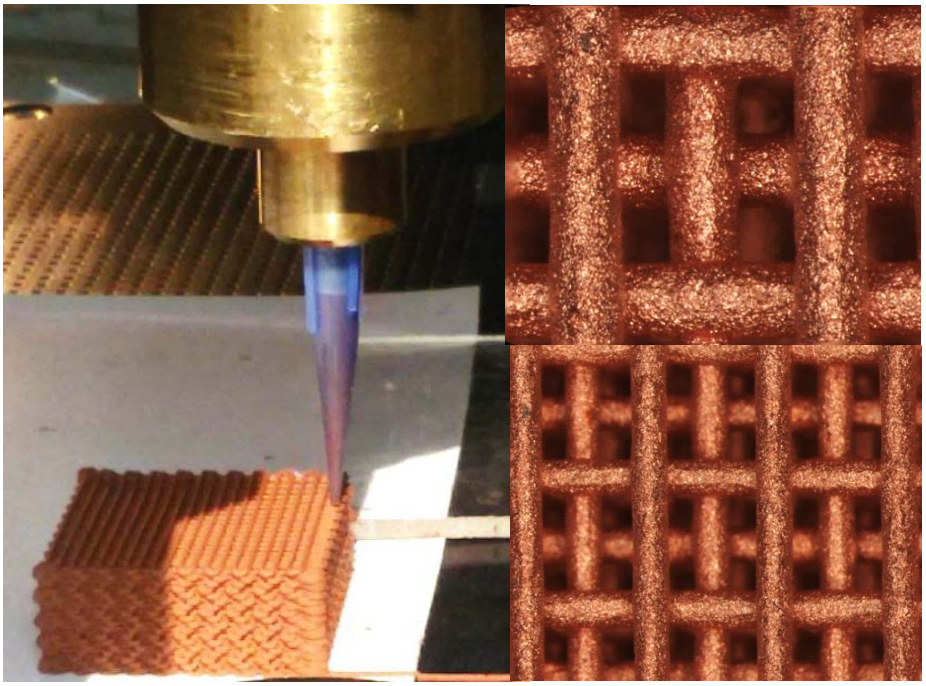

Figure 4-1. 3DFD manufacture (left) and optical microscope images of 3D-copper supports (right).

Manufactured samples were dried at room temperature for 2 days. Conventional furnace sintering (CS) and pulsed electric current sintering (PECS) were used to sinter the catalytic supports. In the case of furnace sintering in a cylindrical oven, samples were calcined at 550°C for 2 h with a heating rate of 1°C·min^{-1} (de-binding process). Then, they were sintered at temperatures between 880 and 1000°C for 5 h with a heating rate of 5°C·min^{-1} under 80 L·min^{-1} N_2 or N_2:H_2 (1:1) atmosphere. In order to avoid the surface oxidation, samples were kept in the furnace until the room temperature was reached. Detailed sintering profile is given in Figure 4-2. In the case of PECS, samples were sintered in the FAST furnace (HP D 25, FCT Systeme, Rauenstein, Germany) in maintained vacuum of ~100 Pa. PECs also known as Spark Plasma Sintering (SPS) employs a pulsed DC current to heat up an electrically conductive tool. High pulsed DC current generates heat internally. This technique provides very high heating and cooling rates. Detailed PEC sintering temperature profile is given in Figure 4-3. After thermal treatment, samples were cut into cylinders with 20.05 mm diameter and 15 mm length. In order to monitor the temperature changes, 2 mm cylindrical holes were made in the centre of the samples for the thermocouple positioning. Structured supports had 70 % macro-porosity and 2.7 mm^{-1} surface area. 316L type stainless steel supports were also prepared for comparison as described elsewhere [9].

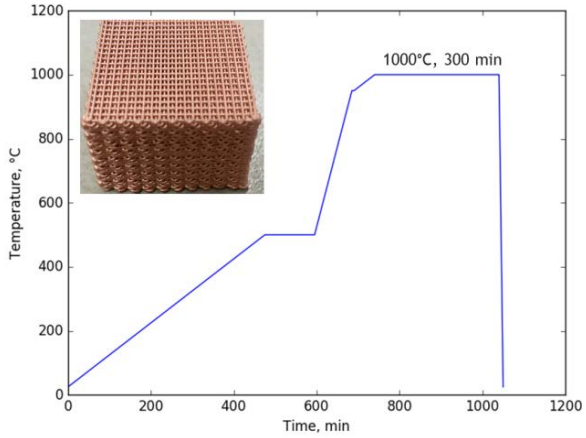

Figure 4-2. Conventional sintering (16 h).

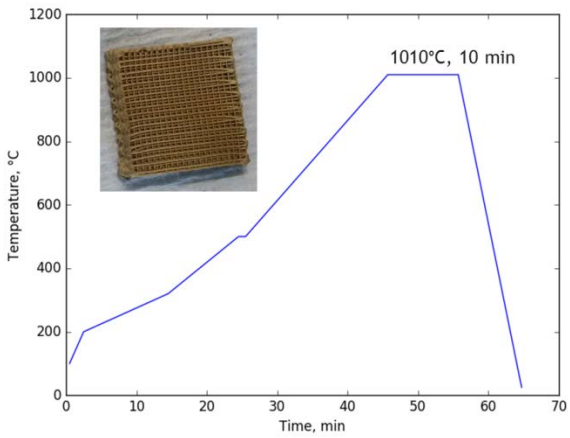

Figure 4-3. PEC sintering (65 min.).

Powder Ni/Al_2O_3 catalyst was prepared according to the procedure described in [9] by impregnation of boehmite powder AlO(OH) (Sasol, Germany, particle size D_{90}=50 μm) with an aqueous solution of nickel nitrate hexahydrate (PANREAC). Before coating, all supports were cleaned with iso-propanol for 10 minutes under ultrasonic treatment to remove dirt from the surface. Samples were dried overnight at 100°C.

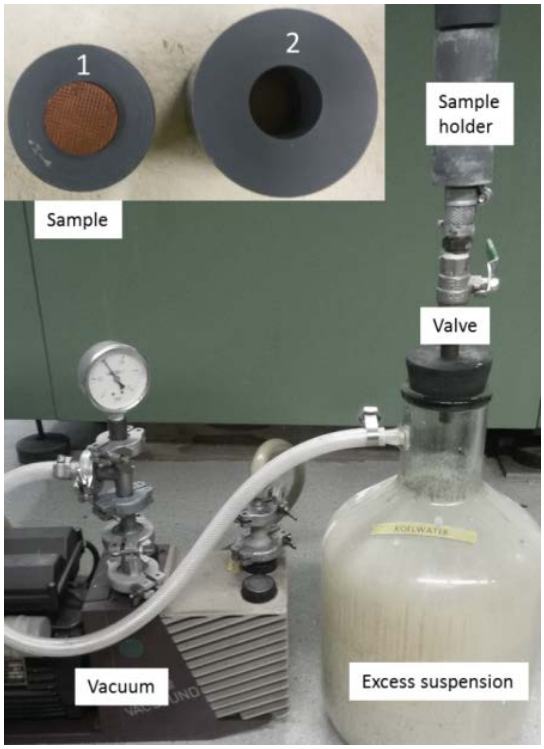

Figure 4-4. Wash-coating set-up.

Coating slurry was prepared as follows: 3 g polyvinyl alcohol (PVA, Fluka Chemica, 100.000), and 1 ml 0.2 M acetic acid (Merck) were added to 74 ml deionised water, the mixture was stirred at 60°C for 2 h and left without stirring overnight. Powder Ni/Al_2O_3 catalyst (20 wt.%) and 4 ml (2 wt.%) colloidal silica (LUDOX HS-40, Sigma Aldrich) were added into the slurry. The mixture

was stirred at room temperature for 24 h. Sintered copper samples were coated with resulting suspension of Ni/Al_2O_3 (BET 236 $m^2 \cdot g^{-1}$, average particle size 3 μm, Ni content 12 wt.%) by wash-coating technique. Wash-coating set-up is shown in Figure 4-4. A support was placed in the sample holder; calculated amount of coating suspension was added on the holder, excess suspension was removed by releasing the valve under the vacuum. Samples were dried overnight and calcined at 500°C for 2 h. Stainless steel supports were coated in the same way. Catalyst loadings for stainless steel and copper supports are given in Table 4-1.

Table 4-1. Catalyst loadings for 316L type stainless steel (left) and copper (right) supports.

Supports / Catalyst Loading	3D-SS support	3D-Cu support
	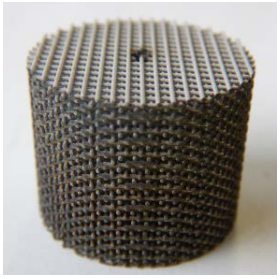	
Ni/Al_2O_3 catalyst (g)	1.2	1.0

4.2.2. Characterization

The cross-sections of the samples were examined by scanning electron microscopy (SEM; FEG JSM6340F, JOEL) and Optical Microscopy (Zeiss, Stereo Discovery V12) with imager (type M2m). X-ray diffraction was used to examine the phase and crystallinity of the copper structures after sintering, using the XRD (PANalytical X'Pert Pro, λ = 1.5405Å) at 40kV.

Viscosity of the coating suspension as a function of the shear rate was determined by rheometer (kinexus rheometer, Malvern Instruments, Worcestershire, UK). Shear rates were varied between 0.01 and 1000 s^{-1} at a temperature of 25°C.

Adhesion strength of the coating was determined by measuring weight loss before and after ultrasonic treatment (US) (40kHz ultrasonic frequency).

The apparent specific surface area of the different sintered supports was measured by N_2 sorption at −196°C using the BET method (Autosorb-1, Quantachrome, Germany).

Profilometer was used to examine the average surface roughness of the fibres by Veeco - Bruker (3D microscope, a confocal microscope/white light interferometer).

Thermogravimetric analysis (TGA) was recorded using a STA 449C Jupiter (Netzsch, Germany) and performed in dry air (70 $ml \cdot min^{-1}$). The spent catalysts were heated from ambient temperature to 600°C with a heating rate of $5°C \cdot min^{-1}$. The TGA equipment was coupled online to a mass spectrometer Omnistar GSD 301 O2 (Pfeiffer Vacuum, Germany).

4.2.3. Catalytic activity and stability

A quartz tubular reactor (24 mm diameter and 100 mm length) was used. K-type thermocouples installed at inlet and outlet of the quartz tube for the continuous temperature measurements of the gas and the structured catalyst was used (see Figure 4-5). Catalysts were packed in the middle of the reactor and fixed with quartz wool. In order to have the fair comparison of the samples, powder catalyst (1.2 g) was diluted with 3 mm alumina beads to get the same volume as structured catalysts. Before the reaction test, catalysts were activated under a continuous flow of H_2/N_2 (80/20 vol.%) at the total rate of 100 ml·min^{-1} (STP) and temperature of 450°C (heating rate 10°C·min^{-1}) for 3h under atmospheric pressure. After reduction, temperature of the furnace was adjusted to the reaction temperature under continuous flow of nitrogen. Methanation reaction was performed at temperatures between 280 and 500°C under atmospheric pressure. Carbon dioxide and hydrogen were continuously fed into the reactor together with nitrogen carrier gas at the total rate of 100 ml·min^{-1} (STP) resulting in GHSV of 1300 h^{-1} with a feed composition of CO_2:H_2:N_2 = 1:4:5.

The catalytic stability was determined by monitoring CO_2 conversion as a function of time-on-stream. Stability test was performed under 10 ppm hydrogen sulphide (H_2S) containing feed gas at 450°C for 96 h. Gas chromatography (450-GC, Bruker, Germany) was used for the analysis of reagents and products. Flame ionization detector (FID) and thermal conductivity detector (TCD) were used to measure CH_4 and CO_2 concentrations, respectively. Temperature of the detectors was maintained at 300°C. The calibration was performed using a known gas mixture without a catalyst.

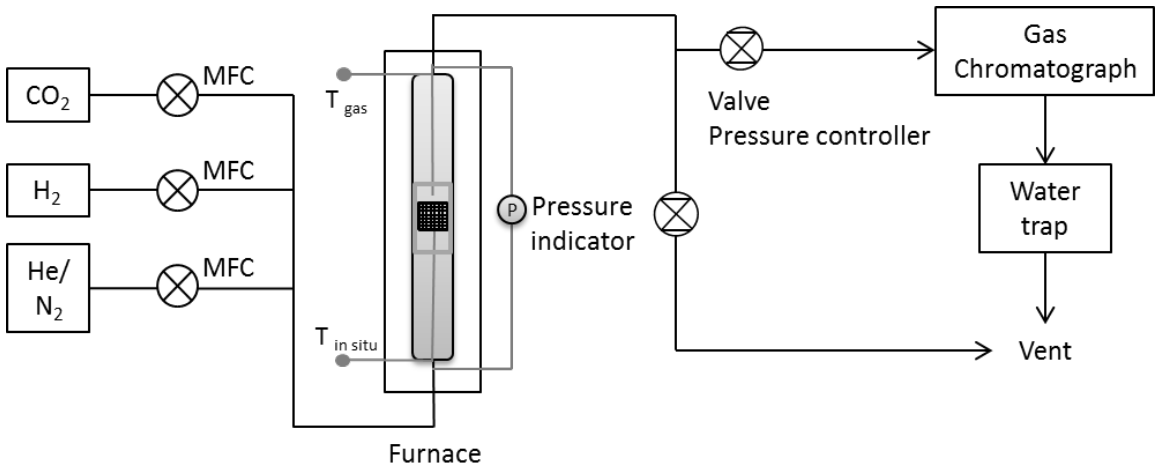

Figure 4-5. Experimental setup.

Conversion (X_{CO2}), selectivity (S_{CH4}) and productivity (P_{CH4}) were calculated using the following equations:

$$X_{CO_2} = \left[\frac{F_{CO_2 in} - F_{CO_2 outlet}}{F_{CO_2 in}}\right] * 100\ (\%) \quad (4\text{-}1)$$

$$S_{CH_4} = \left[\frac{F_{CH_4 outlet}}{F_{CH_4 outlet} + F_{CO\ outlet} + 2F_{C_2H_4 outlet} + 2F_{C_2H_6 outlet}}\right] * 100\ (\%) \quad (4\text{-}2)$$

$$P_{CH_4} = \left[\frac{F_{\ CH_4 outlet}}{m_{catalyst}}\right]\left(\frac{mmol}{g.h}\right) \quad (4\text{-}3)$$

where F is the molar flow rate and m is the mass of Ni/alumina catalyst. GHSV was calculated from the total inlet volumetric flow rate divided by the inserted sample volume V_{sample} (volume of the copper or stainless steel supports).

$$GHSV = \left[\frac{Q_{reactant}}{V_{sample} * k_{number\ of\ samples}}\right] \ (h^{-1}) \quad (4\text{-}4)$$

4.3. Results and discussion

4.3.1. Characterization of copper support structures

Two important parameters of the copper supports were investigated in this study. A low inner porosity in the fibres is desired in order to have a high thermal conductivity and thus better temperature control. Another crucial parameter is the surface roughness which is important to achieve an adhesive coating layer on the surface of the support.

Scanning electron microscopy (SEM) images of the cross sections of the fibres are given in Figure 4-6. The inner porosity of the structures was determined from SEM images using the open source software 'ImageJ'. Inner porosity and surface roughness data of the sintered samples are given in Table 4-2. Figure 4-6a shows the fibre cross section of the copper sample after calcination at 550°C for 2 h under N_2 atmosphere. Highly porous fibres can be seen in both Figures 4-6a and 4-6b. These very fragile samples were formed at the temperature below 880°C by conventional sintering method. N_2 low-temperature sorption analysis of these two samples showed specific surface areas of 1 and 1.2 $m^2 \cdot g^{-1}$, respectively.

Sintering temperature effect was investigated by sintering copper structures at 880, 960 and 1000°C under 80 $L \cdot min^{-1}$ N_2 gas flow. The SEM results are shown in Figures 4-6b, 4-6c and 4-6d. The samples sintered at the temperature >1000°C exhibited lower inner porosity compared to those sintered at <1000°C. It can be seen that an increase of the temperature from 960 to 1000°C significantly reduces the inner porosity (from 10.6 to 2.5 %). Strong bonding between the copper particles in the whole structure was achieved after sintering at a temperature >990°C, which is closer to the melting temperature of copper (ca. 1083°C) [10,11]. Furthermore, N_2 low-temperature sorption analysis proved the change of the micro-structure by reduction of the surface area (Table 4-2). Average surface roughness of the fibres was examined using an optical profilometer. Surface roughness images are given in Figure 4-7. In contrast to the temperature effect on inner porosity, no significant effect on surface roughness was observed.

The effect of the sintering atmosphere on the properties of the structured copper supports was studied by changing inert (N_2) atmosphere to a reducing atmosphere (H_2:N_2). In order to have dense

fibres with a good quality, there should be minimum amount of binder (carbon source) in the paste, and oxidation should be avoided. Oxidation can occur by air, moisture or carbon dioxide during the paste preparation, 3D-manufacturing step and drying. Hydrogen as a reducing gas can prevent the oxidation and minimise the oxide content in the fibres of the structure. Figures 6d and 6f present the samples sintered at 1000°C under nitrogen and reducing atmosphere (H_2:N_2 = 1:1), respectively. It can be seen that denser copper fibres were achieved under reducing atmosphere. Inner porosity of the fibres decreased after sintering in H_2:N_2, from 2.5 to 0.1 %, and surface roughness slightly decreased from 6.9 to 5.9 µm.

Table 4-2. Inner porosity and surface roughness of copper and stainless steel structures sintered at different conditions.

Sample	**Sintering**	**Temperature (°C), duration (h)**	**Atmosphere**	**BET surface area (m^2/g)**	**Inner porosity (%)**	**Surface roughness (Ra, µm)**
Copper (b)	Furnace	880, 5	N_2	1.2	10.6	7.0
Copper (c)	Furnace	960, 5	N_2	n.a.	7.1	n.a
Copper (d)	Furnace	1000, 5	N_2	0.3	2.5	6.9
Copper (e)	PEC	1000, 0.167	Vacuum	n.a.	3.8	n.a.
Copper (f)	Furnace	1000, 5	N_2:H_2	n.a.	0.1	5.9
316L stainless steel	Furnace	1300, 4	N_2	n.a.	2.6	6.3

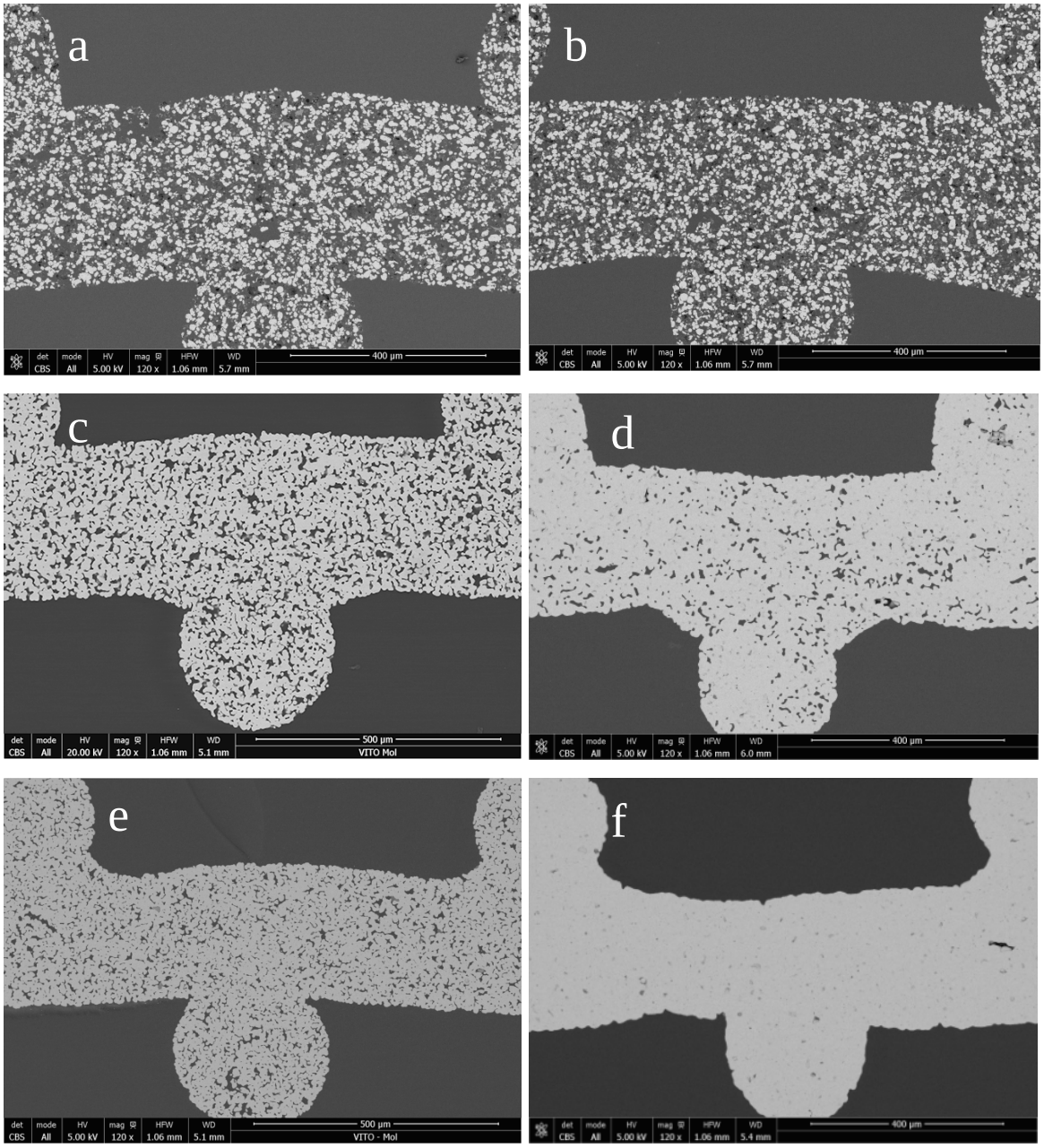

Figure 4-6. SEM images of the cross-sections of the fibres of copper 3DFD structures (a) calcined at 550°C, 2 h, under N_2; (b) sintered at 880°C, 5 h, under N_2; (c) sintered at 960°C, 5 h, under N_2; (d) sintered at 1000°C, 5 h, under N_2; (e) sintered by PECS at 1010°C, 10 min, under vacuum; (f) sintered at 1000°C, 5 h, under H_2:N_2 (1:1).

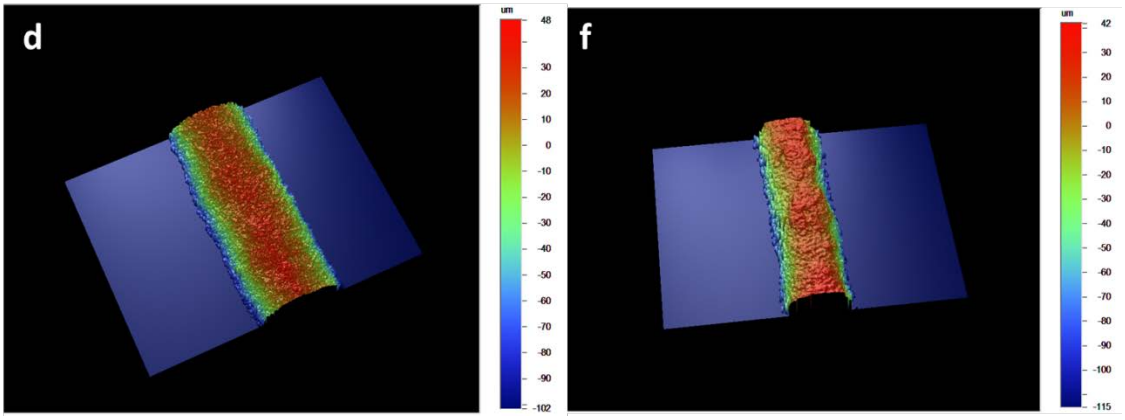

Figure 4-7. Sintering atmosphere effect on the surface roughness of the fibres (d) sintered at 1000°C, 5h, under N_2 and (f) sintered at 1000°C, 5h, under H_2:N_2 (1:1).

SEM results showed that PEC sintered sample (Figure 4-6e) is as dense as conventionally sintered sample (Figure 4-6d), however 'greenish' surface was observed (see Figure 4-3). It was reported before that the colour formed on copper surface is a function of copper oxide layer thickness [12]. Copper (I) oxide on the surface of the PEC sintered sample was detected by XRD analysis (Figure 4-8). Surface oxidation could be prevented by sintering in reducing atmosphere.

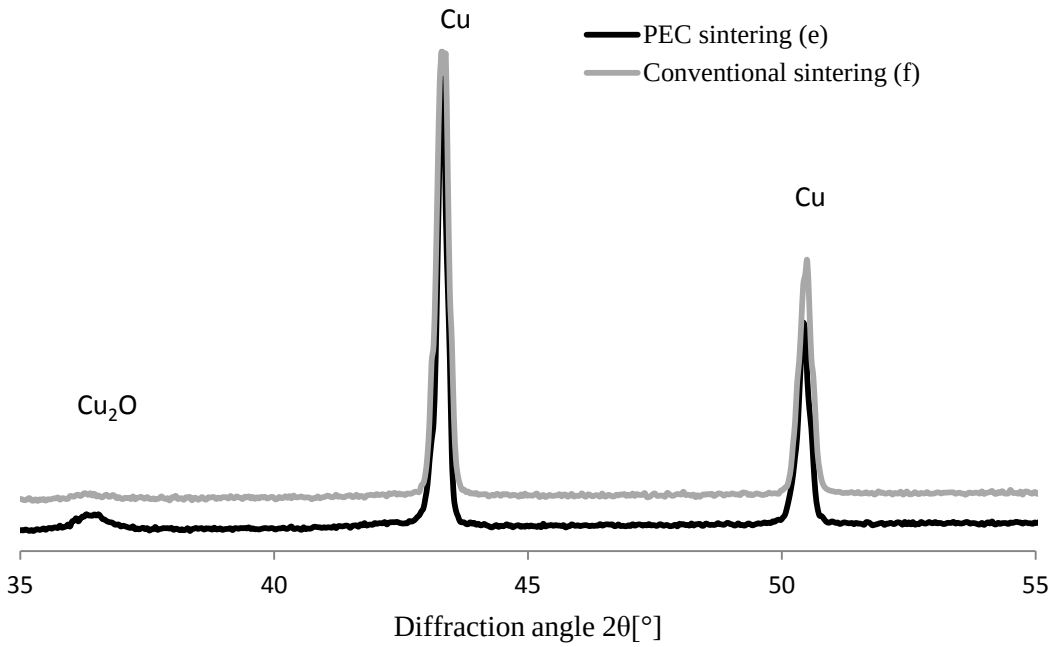

Figure 4-8. XRD patterns of the PEC sintered (Figure 4-6e) and furnace sintered under H_2 atmosphere (Figure 4-6f) samples.

4.3.2. Characterization of catalytic coating

Sintered structured copper supports were coated with Ni/alumina suspension. Figure 4-9 shows the rheological properties of the coating suspension. Rheometer was used to determine the single point viscosity at room temperature as a function of shear rate (0.001, 0.1, 10 and 1000 s^{-1}). From one side, coating suspension is expected to have high viscosity at low shear rates to avoid leaking through the macro-pores of the sample. On the other hand, coating suspension should have lower viscosity at higher shear rates so that the excess suspension can be easily removed from the sample. Therefore, rheology of the coating suspension should be set according to the geometry of the support and coating technique.

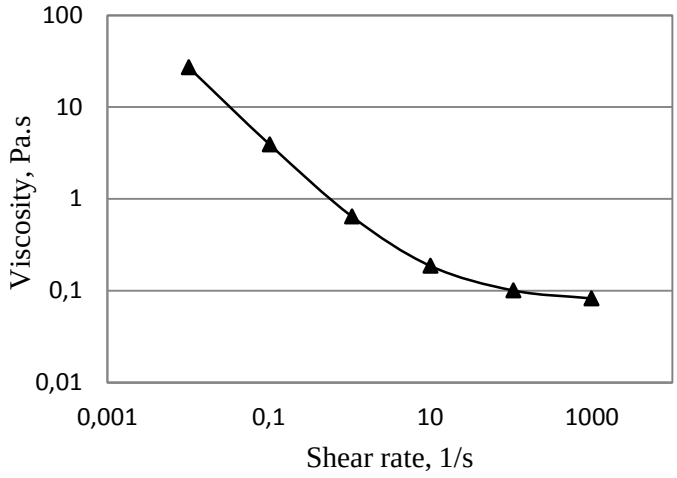

Figure 4-9. Viscosity of Ni/alumina coating suspension.

It is known that the adhesion strength of the catalytic coating strongly depends not only on the coating suspension but also on the nature of the support.. It was reported that the weight loss of ca.6 % after 30 min of treatment with petroleum ether was considered as an adhesive alumina coating on FeCrAl metallic supports [13,14]. In order to test the adhesion strength of the coating, coated structures were treated in a high-intensity ultrasonic bath in distilled water for 1, 15, 30 and 60 minutes. The weight loss values are given in Table 4-3. In literature, to increase the adhesion strength, metallic supports are usually treated by chemicals (etching) [15] or calcined at high temperatures [16] to increase the surface roughness of the substrate. Furthermore, nanoparticles in the coating suspension can occupy the unevenness's of the substrate surface, therefore improve the adhesion strength. Copper structured catalyst coated with Ni/alumina suspension had a weight loss of 17 % after 1 minute of US treatment. After 60 min of US treatment, a weight loss of 43 % was measured. An increase of the colloidal silica content in the suspension from 0.5 to 2 % improved the adhesion strength significantly (14 % weight loss after 60 min US treatment). Despite a similar surface roughness, the stainless steel structures coated with Ni/alumina showed much higher adhesion strength than copper samples. The reason is the nature of the support material.

Table 4-3. Effect of the support on the coating adhesion.

Catalyst:	**Ni/alumina-3D-Cu**	**Ni/alumina-3D-Cu**	**Ni/alumina-3D-SS**
Sintering temperature	1000, $N_2 + H_2$	1000, $N_2 + H_2$	1300, N_2
Inner porosity, %	0.1	0.1	2.6
Roughness, Ra	5.85	5.85	6.3
SiO_2, %	0.5	2	2
U.S. time, min:	**Coating weight loss, wt.%**		
1	17.2	0.8	2
15	33.8	3.9	2.4
30	40.8	11.3	2.5
60	43.6	14.2	2.9

4.3.3. Catalytic activity and characterization of spent catalyst

Methanation reactions were carried out with powder Ni/Al_2O_3 catalyst, coated 3D-SS and 3D-Cu structures in a tubular reactor at temperatures between 280 and 500°C. An overview of the results is given in Table 4-4. The productivity of the catalysts was plotted taking into account the in-situ temperatures (Figure 4-10). It can be seen in Table 4-4 that the selectivity of the structured catalysts to methane slightly increased with increasing temperature from 280 to 450°C. Main by-products were recorded to be CO and C_2H_4. This means that the improvement of CO methanation activity at temperatures between 280 and 450°C can lead to high CH_4 selectivity in CO_2 methanation. In the case of structured catalysts, selectivity decreased by ca. 15 % at the reaction temperatures above 450°C. According to our equilibrium calculations, selectivity reaches the corresponding equilibrium value at 400°C. The highest selectivity to methane was found to be 98 % at 400°C for all samples. Above 450°C, the formation of ethylene and carbon monoxide is favoured, therefore methane selectivity and carbon dioxide conversion decreased.

Figure 4-10 shows the methane productivity of powder and structured catalysts. Methane productivity reached a maximum at ca. 450°C. Results show that the temperature of 450°C is optimal for this reaction (highest CH_4 selectivity 98 % and highest CO_2 conversion of ca. 50 %). The 3D-SS catalyst showed slightly higher CO_2 conversion (ca. 3%) than 3D-Cu catalyst due to higher catalysts loading (Table 4-1) on 3D-SS sample than on 3D-Cu one. Catalytic results demonstrated that structured and powder catalysts showed very similar methane yield and carbon dioxide conversion. Methane productivities of the catalysts were calculated and found to be 4.5, 4.1 and 3.8 $mmol_{CH4} \cdot g_{cat}^{-1} h^{-1}$ for 3D-Cu, 3D-SS and powder catalyst, respectively. Methane productivity of structured catalysts was found to be slightly higher than powder catalysts.

Figure 4-11 shows the results of the stability tests on structured catalysts. The experiment was performed at 450°C with a feed gas composition of CO_2:H_2:N_2 =1:4:5 in the presence of 10 ppm H_2S,

for 80 h. It was observed that the addition of 10 ppm H_2S to the stream did not significantly change the performance of the structured catalysts: CO_2 conversion stayed at ca. 50 %. 3D-Cu and 3D-SS samples showed methane selectivity of 97.4 and 97.7 %, respectively, CO was detected as a by-product. No selectivity fluctuation was observed during the stability test. The experimental results showed that both 3D-SS and 3D-Cu catalysts had comparable stability during 80 h time-on-stream. Similar effect was observed in our previous study. While powder catalyst showed 8 % decrease of CO_2 conversion already after 45 h time-on-stream, structured catalyst showed a stable CO_2 conversion during 53 h time-on-stream.

Table 4-4. CO_2 conversion, methane selectivity and methane productivity for packed-bed and structured catalysts at GHSV= 1300 h^{-1}, 1 bar.

Sample	$T_{gas\ inlet}$ (°C)	$T_{in\ situ}$ (°C)	Conversion (%)	Selectivity (%)	Productivity ($mmol \cdot g^{-1} h^{-1}$)
Ni/Al_2O_3 powder	280	269	3	56	0.40
	300	291	4	76	0.45
	330	334	5	87	0.58
	350	356	9	91	0.95
	400	401	29	97	2.72
	450	445	43	97	3.69
	500	503	45	84	3.79
3D-SS	280	287	6	91	0.69
	300	307	10	94	1.06
	350	355	26	97	2.54
	400	405	40	98	3.59
	450	440	49	98	4.11
	500	497	47	84	3.71
3D-Cu	280	282	3	89	0.44
	300	301	7	93	0.87
	350	350	22	97	2.55
	400	400	38	98	4.10
	450	450	44	97	4.44
	500	499	45	83	4.22

Ni/alumina coating was removed from the structured samples tested in the presence of 10 ppm H_2S by intensive ultrasonic treatment in deionized water for 6h. The BET surface area of the fresh and spent catalysts was measured (Figure 4-12). The BET surface area of the spent catalysts was found to be lower than the one of the fresh samples. The biggest decrease of the surface area (by ca. 150 m2·g-1) was observed between fresh and spent catalysts. It is known from literature that reduction of the catalyst can affect the surface area [17]. The surface area can also decrease due to the carbon deposition on the catalyst surface leading to the pore blockage [18,19], crystalline phase transitions leading to sintering of catalytic supports and sintering of metallic species during the reaction run. It can be seen that the decrease of the specific surface area became more severe with increased time on stream. In the case of 3D-SS sample, increase of the reaction time from 24 to 80 h leads to a decrease of the surface area by ca. 50 m2·g-1. However, no significant effect on the conversion was observed (Figure 4-11).

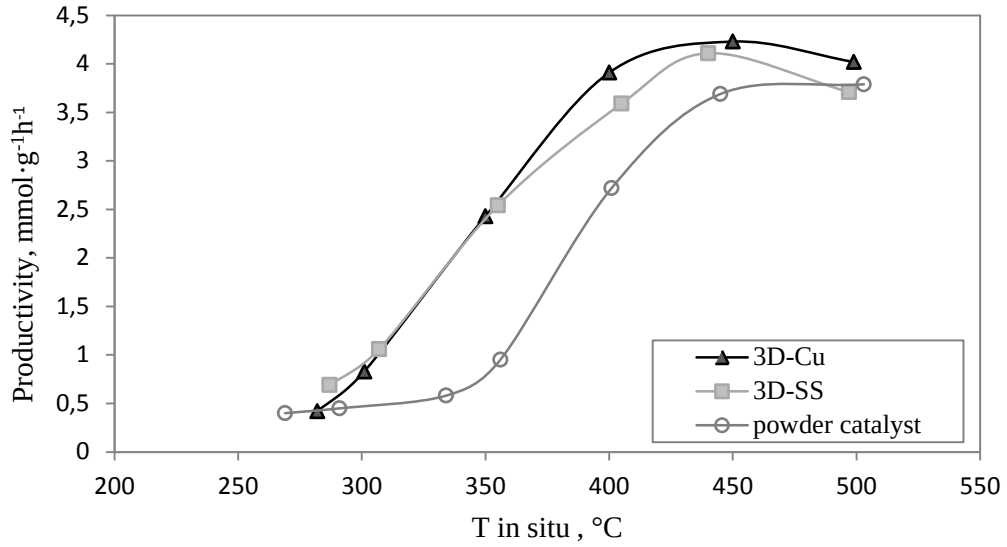

Figure 4-10. Methane productivity versus temperature for Ni/Al_2O_3 powder, 3D-SS and 3D-Cu structured catalysts (GHSV= 1300 h^{-1}, 1 bar).

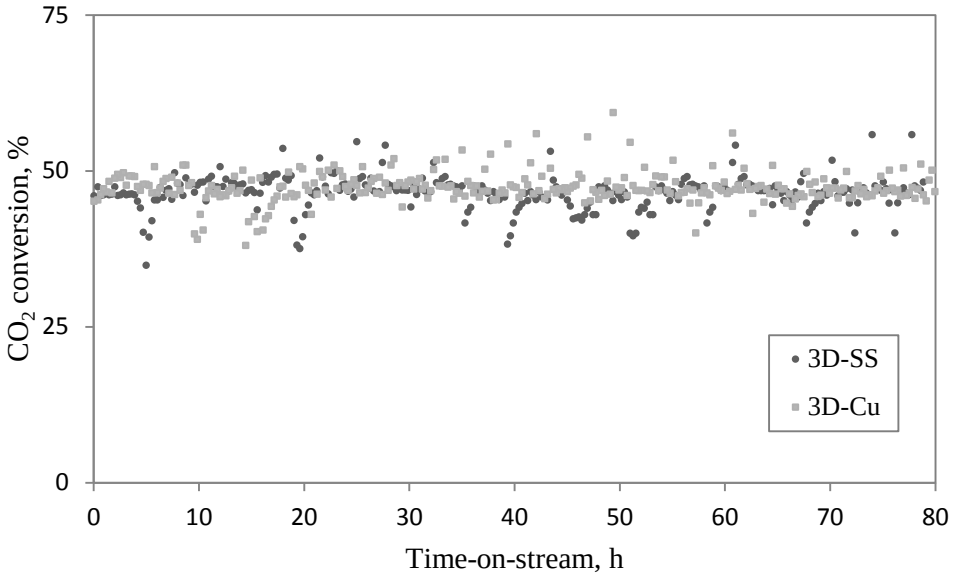

Figure 4-11. Lab-scale stability test of the structured catalysts in the presence of 10 ppm H_2S (450°C, 1 bar, GHSV= 1300 h^{-1}).

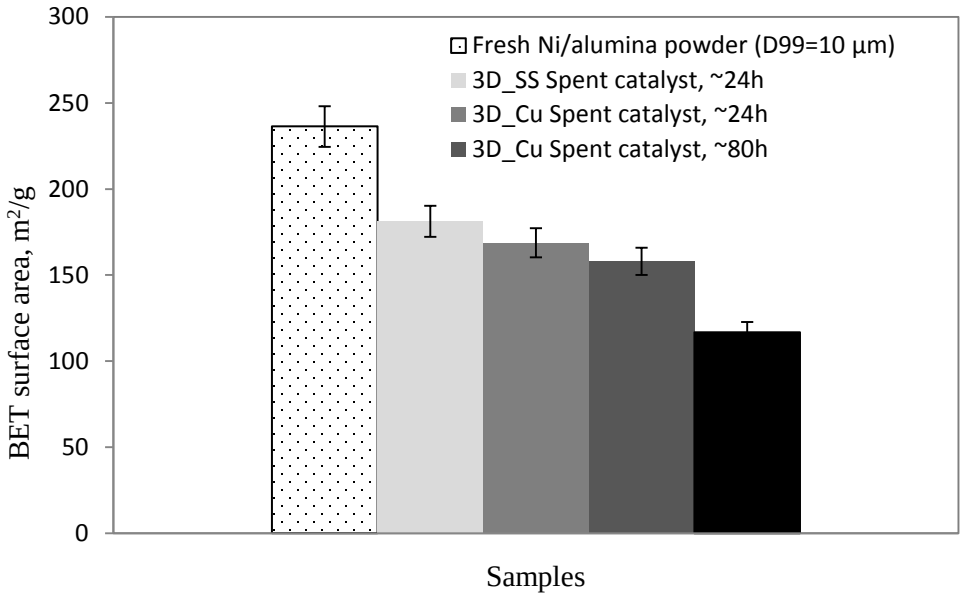

Figure 4-12. BET specific surface area values of freshly calcined and spent Ni/alumina catalysts.

Figure 4-13 shows the DTGA-MS results of freshly calcined and spent catalysts. The DTGA-T plot of the spent catalyst gave a peak at ca. 275°C with 0.44 % weight loss. This negligible weight loss can be an indication of oxidation of the deposited amorphous carbon species on the catalyst surface. Total weight losses of the fresh and spent catalysts were recorded to be ca. 3 and 6 %, respectively.

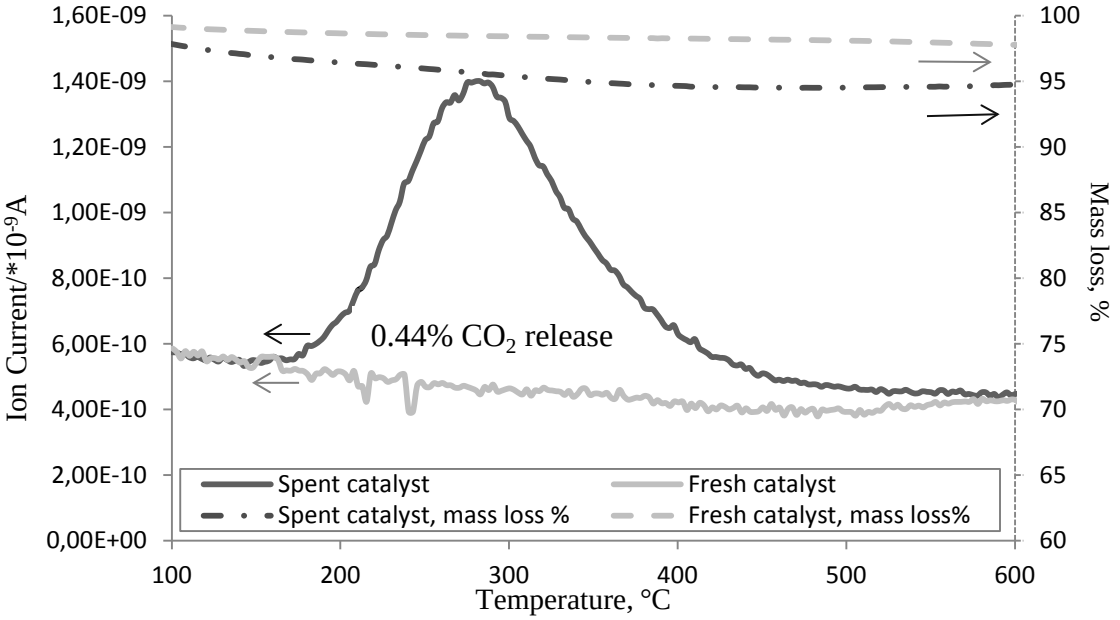

Figure 4-13. DTGA-MS of fresh and spent catalysts.

It is reported in literature, that carbon deposition starts from the formation of amorphous (C_β, 250–500°C) and graphitic (C_γ, 150–250°C) carbon islands [20], that further leads to either encapsulation of the metallic active phase causing the decrease of the catalytic activity or formation of filamentous carbon which does not encapsulate nickel active sites, causing only a slight decrease of the catalytic

activity [21]. Therefore, it is possible to conclude that the second route took place. DTGA-MS and N_2 low-temperature sorption results were found to be in a good agreement with the stability of the catalytic activity of the structured catalysts.

4.4. Conclusions

In this chapter, innovative 3DFD copper supports were developed and manufactured. Calcination and sintering at different temperatures were investigated. Both sintering temperature and atmosphere were found to affect the morphology of the struts of the structures. The optimal sintering conditions were found to be as follows: 1000°C, 5 h, under H_2:N_2 (1:1) atmosphere in conventional high-temperature oven. PEC sintering technique provides quick heating and sintering (10 minutes instead of 5 h), however undesired surface oxidation was detected. The result demonstrates the feasibility of using 3DFD to manufacture copper supports/structures with complex geometries. In future, optimized PEC sintering technique can be integrated with 3D-printing technology, especially for the sintering of conductive materials. Adhesion strength of the coating was found to be better on stainless steel than on copper supports, however the latter can be improved by the addition of inorganic binder (e.g. colloidal silica, $AlPO_4$, bentonite) or by increasing the surface roughness.

In CO_2 methanation, with diluted reactant gas and under atmospheric pressure, copper and stainless steel supported Ni/alumina catalysts showed slightly higher productivity than powder Ni/alumina catalysts. 80 h stability test showed that an addition of 10 ppm H_2S to the stream did not significantly change the structured catalysts performance. Innovative porous structures were found to be promising as catalytic supports providing the improved temperature control with the efficient use of the catalyst. The further work highlighted in chapter 5 is devoted to testing structured catalysts in CO_2 methanation reaction in the pilot-scale reactor at CEA-Liten in Grenoble with reactant gases without dilution and under high pressure.

4.5. References

[1] J. Kopyscinski, T.J. Schildhauer, S.M.A. Biollaz, Methanation in a fluidized bed reactor with high initial CO partial pressure: Part I-Experimental investigation of hydrodynamics, mass transfer effects, and carbon deposition, Chem. Eng. Sci. 66 (2011) 924–934. doi:10.1016/j.ces.2010.11.042.

[2] C.H. Bartholomew, Mechanism of catalyst deactivation, Appl. Catal. A Gen. 212 (2001) 17–60. doi:http://dx.doi.org/10.1016/S0926-860X(00)00843-7.

[3] J. Lefevere, M. Gysen, S. Mullens, V. Meynen, J. Van Noyen, The benefit of design of support architectures for zeolite coated structured catalysts for methanol-to-olefin conversion, Catal. Today. 216 (2013) 18–23. doi:10.1016/j.cattod.2013.05.020.

[4] C.R. Tubio, J. Azuaje, L. Escalante, A. Coelho, F. Guitián, E. Sotelo, A. Gil, 3D printing of a heterogeneous copper-based catalyst, J. Catal. 334 (2016) 110–115. doi:10.1016/j.jcat.2015.11.019.

[5] S. Couck, J. Lefevere, S. Mullens, L. Protasova, V. Meynen, G. Desmet, G. V. Baron, J.F.M. Denayer, CO_2 adsorption with a 3DFD-printed ZSM-5 monolith, Chem. Eng. J. 308 (2017)

719–726. doi:10.1016/j.cej.2016.09.046.

[6] J. Hu, K.P. Brooks, J.D. Holladay, D.T. Howe, T.M. Simon, Catalyst development for microchannel reactors for martian in situ propellant production, Catal. Today. 125 (2007) 103–110. doi:10.1016/j.cattod.2007.01.067.

[7] J. Van Noyen, A. De Wilde, M. Schroeven, S. Mullens, J. Luyten, Ceramic processing techniques for catalyst design: Formation, properties, and catalytic example of ZSM-5 on 3-dimensional fiber deposition support structures, Int. J. Appl. Ceram. Technol. 9 (2012) 902–910. doi:10.1111/j.1744-7402.2012.02781.x.

[8] J. Luyten, S. Mullens, I. Thijs, Designing With Pores - Synthesis and Applications, KONA Powder Part. J. 28 (2010) 131–142. doi:10.14356/kona.2010012.

[9] S. Danaci, L. Protasova, J. Lefevere, L. Bedel, R. Guilet, P. Marty, Efficient CO_2 methanation over Ni/Al_2O_3 coated structured catalysts, Catal. Today. 273 (2016) 234–243. doi:10.1016/j.cattod.2016.04.019.

[10] Y. Bai, C.B. Williams, An exploration of binder jetting of copper, Rapid Prototyp. J. 21 (2015) 177–185. doi:10.1108/RPJ-12-2014-0180.

[11] L. Xu, C. Srinivasakannan, J. Peng, S. Guo, H. Xia, Study on characteristics of microwave melting of copper powder, J. Alloys Compd. 701 (2017) 236–243. doi:10.1016/j.jallcom.2017.01.097.

[12] U.R. Evans, H.A. Miley, Measurements of oxide films on copper and iron, in: Nature, 1937: p. 283.

[13] Y. Han, D. Xu, C. Lu, N. Li, J. Zhou, Y. Hu, H. Huang, Preparation of alumina coatings on metallic nickel substrate using a room-temperature wet chemical pretreatment method, Mater. Chem. Phys. 127 (2011) 7–11. doi:10.1016/j.matchemphys.2011.01.014.

[14] S. Zhao, J. Zhang, D. Weng, X. Wu, A method to form well-adhered γ-Al_2O_3 layers on FeCrAl metallic supports, Surf. Coatings Technol. 167 (2003) 97–105. doi:10.1016/S0257-8972(02)00859-9.

[15] L. Giani, C. Cristiani, G. Groppi, E. Tronconi, Washcoating method for Pd/γ-Al_2O_3 deposition on metallic foams, Appl. Catal. B Environ. 62 (2006) 121–131. doi:10.1016/j.apcatb.2005.07.003.

[16] S. Kressirer, L.N. Protasova, M.H.J.M. de Croon, V. Hessel, D. Kralisch, Removal and renewal of catalytic coatings from lab- and pilot-scale microreactors, accompanied by life cycle assessment and cost analysis, Green Chem. 14 (2012) 3034–3046. doi:10.1039/c2gc35803d.

[17] Y. Gao, F. Meng, K. Ji, Y. Song, Z. Li, Slurry phase methanation of carbon monoxide over nanosized Ni-Al_2O_3 catalysts prepared by microwave-assisted solution combustion, Appl. Catal. A Gen. 510 (2016) 74–83. doi:10.1016/j.apcata.2015.11.006.

[18] L. Zhu, S. Yin, X. Wang, Y. Liu, S. Wang, L. Zhu, S. Yin, X. Wang, Y. Liu, S. Wang, The catalytic properties evolution of HZSM-5 in the conversion of methanol to gasoline, RSC Adv. 0 (2013) 1–3. doi:10.1039/x0xx00000x.

[19] P. Li, Y.H. Park, D.J. Moon, N.C. Park, Y.C. Kim, Carbon deposition onto Ni-based catalysts for combined steam/CO_2 reforming of methane, J. Nanosci. Nanotechnol. 16 (2016) 1562–1566. doi:10.1166/jnn.2016.12006.

[20] A. Kambolis, D. Ferri, Y. Lu, S.N. Yannopoulos, S. Pokrant, D. Rentsch, O. Kröcher, Structural modification of Ni/γ-Al_2O_3 with boron for enhanced carbon resistance during CO methanation, ChemCatChem. 7 (2015) 3261–3265. doi:10.1002/cctc.201500567.

[21] I. Luisetto, S. Tuti, C. Battocchio, S. Lo Mastro, A. Sodo, Ni/CeO_2–Al_2O_3 catalysts for the dry reforming of methane: The effect of $CeAlO_3$ content and nickel crystallite size on catalytic activity and coke resistance, Appl. Catal. A Gen. 500 (2015) 12–22.

Chapter 5

Structured catalysts for CO_2 methanation - a scale-up study

Chapter 5 presents the scale-up study of Ni/Alumina coated structured metal supports manufactured by 3DFD technique. Ni/Al_2O_3 catalysts with nickel loading of 12 wt.% were synthesized by a conventional impregnation method using two different alumina powders. Structured metal supports were coated with Ni/alumina catalysts and then inserted into a single channelled tubular reactor for the reaction tests. Lab- and pilot-scale experiments were performed, and the results were compared by means of the productivity. In pilot-scale experiments, methane productivity was achieved to be 255.8 $mmol \cdot g_{Ni}^{-1} \cdot h^{-1}$ which was found to be 3 times higher than the lab-scale reactor. The catalyst showed high stability for 80 h time-on-stream. The influence of the temperature, pressure and flow rate was investigated. Fresh and spent catalysts were characterized by N_2 adsorption, XRD, XPS, TPR, SEM and TGA. It was proven that the change of the alumina support affects the catalytic performance of the catalysts.

This chapter was adapted from Danaci S., Protasova L., Mertens M., Xin Q., Jouve M., Bengaouer A., Marty P., *Structured catalysts for CO_2 methanation – A scale-up study*, Appl. Catal. A Gen., *to be submitted*.

5.1. Introduction

The conversion of CO_2 to methane is a promising process in Power-to-gas (PtG) applications [1,2]. Methanation reactors in PtG applications can be divided into different categories. Regarding their technological development, they can be classified as: commercialised, demonstration and R&D scale reactors. Considering methane production, several ongoing PtG projects have been identified woldwide. One of the planned PtG platforms is the Jupiter 1000 to be built at the *Fos sur Mer* harbour nearby Marseille in France in 2020 [3]. An intensified methanation reactor will be used in the process and CO_2 from industrial flue gas will be employed. The methanation reactor technology will be provided by CEA Liten, Grenoble. The produced methane will be stored in the natural gas grid. More details about PtG plants can be found elsewhere [3–9]. Industrial scale methanation reactors usually have operating pressures ranging between 10-77 bars. The lifetime of their conventional Ni/alumina catalysts is generally between 2 and 4 years [10].

For exothermic chemical reactions, using a packed-bed reactor can lead to hot-spots and catalyst deactivation due to the sintering of the catalyst. It is essential to remove the produced heat from the reactor more efficiently. In recent years, great interest has been shown in structured catalysts/reactors, e.g. metal based structured catalysts such as metallic plates [11], foils [12,13], microfibrous materials [14], monoliths [15], foams [16,17] and additive manufacturing (AM) materials [18,19] due to a number advantages over conventional reactors for exothermic reactions. It is interesting and useful to compare the performance of different reactor types.

In our previous chapters, methanation reactions were studied at temperatures between 250 and 450°C on AM manufactured supports with different architectures coated with Ni/Al_2O_3 catalysts [18]. At low temperatures, the effect of the geometry of the structured support on heat and mass transfer and thus on CO_2 conversion was observed. Structured catalysts showed ca. 89 % CO_2 conversion without showing any geometry effect at high temperatures (above 370°C). The structured catalyst lowered the temperature increase (hot spots) and enhanced the stability of the catalyst. During stability tests (350°C, $H_2/CO_2 = 4$, WHSV 1500 h^{-1}), the initial CO_2 conversions were observed to be 80 % and 73 % for structured and powder catalysts, respectively. The powder catalyst showed an 8 % decrease of CO_2 conversion after only 45 h time-on-stream. In the case of the structured catalyst, CO_2 conversion stayed constant at ca. 80 % during 53 h time-on-stream. In a recent study with Ni/CeO_2 coated honeycomb, structured catalysts showed a similar high stability during 124 h time-on-stream for the methanation reaction [20].

In this chapter, we studied the additive manufactured stainless steel and copper supports coated with two different Ni/alumina catalysts. A single channelled reactor was designed for pilot-scale experiments at CEA, Liten. The effects of the reduction temperature and alumina precursor for CO_2 conversion were studied. Improved methane productivity and stability were achieved by 3D-structured catalysts in pilot-scale experiments.

5.2. Experimental

5.2.1. Support manufacturing, catalyst and coating preparation

The 316L type stainless steel (Carpenter Technology, US, <25 µm powder) and copper (Sigma-Aldrich, 14-25 µm powder) were used to manufacture structured supports using 3-Dimensional Fibre Deposition (3DFD) solid free forming technique as described elsewhere [21]. Nozzles with a diameter of 400 µm were used to manufacture 3D-structures with 1-1 and 1-3 stackings (Figure 5-1 and 5-2). Porous supports were built up layer-by-layer by computer controlled movements in x, y and z-directions. Structures were dried at room temperature for 2 days. Then, stainless steel and copper supports were sintered at 1030°C for 4 h under vacuum and at 1000°C for 5 h under H_2:N_2 (1:1) atmosphere, respectively. After sintering, periodic porous structures were obtained. Supports were cut into cylinders with 20.1 mm diameter and 30 mm length. In order to monitor the temperature changes, 2 mm cylindrical holes were made in the centre of the samples for the multipoint thermocouple placement. Before coating, all supports were cleaned in iso-propanol for 10 minutes under ultrasonic treatment to remove the traces of fat and dirt on the surface coming from cutting process. Before coating, samples were dried overnight at 100°C.

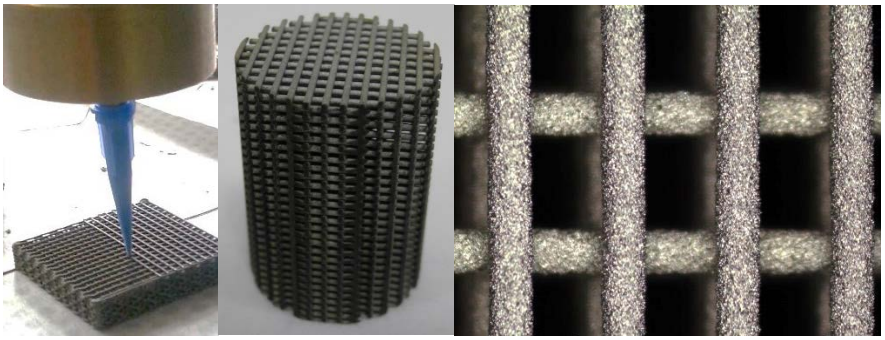

Figure 5-1. 3DFD manufactured and sintered 316L type stainless steel support (3D-SS) in 1-1 stacking.

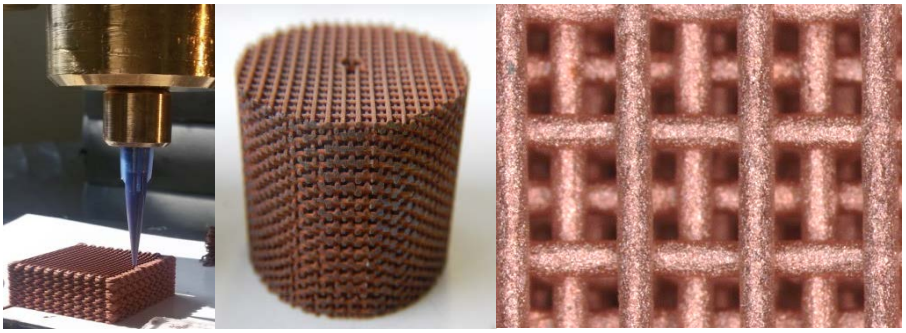

Figure 5-2. 3DFD manufactured and sintered copper support (3D-Cu) in 1-3 stacking.

Nickel/alumina catalysts with 12wt% Ni loading were prepared by impregnation of two powders: boehmite AlO(OH) (Sasol, Germany, average particle size D_{90}=50 µm) and γ-Al_2O_3 (Sasol,

Puralox TM100/150UF, average particle size D_{90}=4-6 μm), with aqueous solution of nickel nitrate hexahydrate (PANREAC). Either boehmite or γ-alumina (10g) was added into an aqueous solution of nickel nitrate (0.41 M, 50 mL) under stirring and kept at room temperature for 24 h. The Ni loading was calculated to be 12 wt.% and confirmed by ICP-AES analysis. The mixtures were dried by freeze drying (HETO Powerdry LL3000) under high vacuum at 15°C. Dried nickel impregnated γ-Al_2O_3 powder was calcined at 500°C for 4 h, and nickel impregnated boehmite powder was calcined at 450-500°C for 4-10 h under atmospheric pressure with a heating rate of 1-2°C·min^{-1}. After calcination, Ni/Al_2O_3 powder catalysts were wet ball-milled (10 g of ZrO_2 spheres were used per gram of catalyst) at 300 rpm for 60 min (15 min milling, 45 min rest) by Planetary Micro Mill (Fritsch Pulverisette-5). Ball-milled samples were again freeze-dried. For the coating preparation, dried powder catalysts were sieved to achieve the particle diameter of 10 μm.

Metal supports were coated with Ni/Al_2O_3 layer by dip-coating technique, manually. Coating slurry was prepared as follows: 4 g PVA (Polyvinyl alcohol, Fluka Chemica, 100.000) and 1 ml of acetic acid (0.2 M, Merck) were added to 73 ml deionised water at 60°C for 2 h and left without stirring overnight. Powder Ni/Al_2O_3 catalyst (20 wt.%) and 4 ml (2 wt.%) colloidal silica (LUDOX HS-40, Sigma Aldrich) were added into the slurry. The mixture was stirred at room temperature for 24 h. A support was placed on between two pieces of the sample holder on vacuum coating apparatus. Certain amount of coating suspension was added onto the holder. Excess suspension was removed by releasing the valve under vacuum. Coating was repeated few times in order to achieve 0.18 - 0.2 g·cm^{-3} catalyst loading. Samples were dried overnight and calcined at 500°C for 4 h for de-binding. The sample specifications of the powder and structured catalysts are summarised in Table 5-1.

Table 5-1. Sample specifications and experimental conditions.

Ni/Al_2O_3 sample code[a]	**Nickel content (Ni wt.%)**	**Alumina source[P] / catalyst source[S]**	**Calcination[P] / de-binding[S] (temperature, time)**	**Support macro-porosity (%)**	**Catalyst amount[P] / loading[S] (g)**	**Reduction (temp., time, gases, flow, pressure)**	**Structured reactor length (mm), volume (L)**
Ni-BOE-P	12	Boehmite, AlO(OH)	450, 10h	n.a.	1	450 and 600, 3 h, (15:85% = H_2:He), 100 ml/min, 1 bars	20, 0.006
Ni-γ-P	12	Puralox, γ-Al_2O_3	500, 4h	n.a.	1	600, 3h (15:85% = H_2:He), 100 ml/min, 1 bars	20, 0.006
Evonik Octolyst 1001	14-17	n.a.	n.a.	n.a.	1	600, 3h (15:85% = H_2:He), 100 ml/min, 1 bars	20, 0.006
Ni-BOE-3DSS	12	Ni-BOE-P	550, 4h	74	2.4	325, 7h (60:40% = H_2:Ar), 2 Nl/min. 2.5 bars	120, 0.037
Ni-BOE-3DCu	12	Ni-BOE-P	550, 4h	74	4.0	325, 7h (60:40% = H_2:Ar), 2 Nl/min, 2.5 bars	220, 0.069
Ni-γ-3DSS	12	Ni-γ-P	500, 4h	82	10	Pre-reduction: 600, 3h, (15:85% = H_2:He), 100 ml/min, 1 bars Reduction: 325, 7h, (15:85% = H_2:Ar), 2 Nl/min, 2.5 bars	290, 0.091

[a] Sample code: first character refers to the Ni/Al_2O_3 catalyst, second character refers to the alumina source (BOE: AlO(OH) and γ: γ-Al_2O_3), third character refers to the form of the catalyst (P: powder, 3DSS: 3D-Stainless steel and 3DCu: 3D-Copper).

[P]: Powder Ni-BOE-P, Ni-γ-P and Evonik Octolyst 1001 catalysts.

[S]: Structured Ni-BOE-3DSS, Ni-BOE-3DCu and Ni-γ-3DSS catalysts

5.2.2. Characterization

The apparent specific surface area was measured by N_2 sorption at −196°C using the BET method (Autosorb-1, Quantachrome, Germany).

Nickel content in the catalysts was determined by ICP-AES elemental analysis (Perkin-Elmer Optima 3000 dv).

X-ray diffraction (XRD) was used to examine the phase and crystallinity of the catalysts (PANalytical X'Pert Pro, λ = 1.5405Å at 40kV).

Chemical surface analysis of the reduced catalyst was performed by a X-ray Photoelectron Spectrometer (XPS), K-Alpha-Thermo Scientific.

The catalysts were examined by scanning electron microscopy (SEM; FEG JSM6340F, JOEL) and support structures by Optical Microscopy (Zeiss, Stereo Discovery V12 with imager type M2m).

Temperature programmed reduction (TPR) of the catalysts were done to investigate the reducibility of the catalysts; on a Quantachrome iQ. Prior to the measurement, about 20 mg of the sample was outgassed at 200°C for 16 h. After cooling, the sample was first pretreated at 250 °C under a He flow for 1 h. Subsequently, the sample was reduced with 5 % H_2/Ar at a flow rate of 25 mL·min^{-1} and then the temperature was raised from 100°C to 800°C with a heating rate of 10°C·min^{-1}. The hydrogen consumption was continuously monitored using a thermal conductivity detector (TCD). The final TCD signal was normalized by the catalyst weight used during the measurement.

Thermogravimetric analysis (TGA) was performed on a STA 449C Jupiter (Netzsch, Germany) and performed in dry air (70 ml·min^{-1}). The catalysts were heated to 600°C with a heating rate of 5°C·min^{-1}. The TGA equipment was coupled online to a mass spectrometer Omnistar GSD 301 O2 (Pfeiffer Vacuum, Germany).

5.2.3. Catalytic activity and stability

Lab-scale experiments were performed in a quartz tubular reactor (24 mm diameter and 100 mm length) surrounded by an electrical furnace and equipped with a K-type thermocouple. Catalysts were packed in the middle of the reactor and fixed with quartz wool. After reduction, temperature of the furnace was adjusted to the reaction temperature under continuous flow of nitrogen. Methanation reaction was performed at temperatures between 280 and 500°C under atmospheric pressure. Carbon dioxide and hydrogen were continuously fed into the reactor together with nitrogen carrier gas at the total rate of 100 ml·min^{-1} (STP) resulting in GHSV of 1300 h^{-1} with feed composition of CO_2:H_2:N_2 = 1:4:5. Gas chromatography (450-GC, Bruker, Germany) was used for the analysis of reagents and products. Flame ionization detector (FID) and thermal conductivity detector (TCD) were used to measure CH_4 and CO_2 concentrations, respectively. The temperature of both detectors was maintained at 300°C.

Pilot-scale experiments were performed in a 316L type stainless steel tubular reactor with the length of 290 mm, inner diameter of 20.1 mm, and the wall thickness of 2 mm. A vertical cross-section of the pilot methanation reactor is given in Figure 5-3. The reactor (ca. 90 cm^3) was equipped with a multipoint thermocouples assembly. Eight thermocouples, located in the same tube or assembly, were used to monitor catalyst bed temperatures. This assembly thermocouple is located in the centre of the tube. The locations of the different thermocouples from the inlet to the outlet of the reactor are as follows: 7.5, 9.5, 13.5, 18.5, 25 and 34.5 cm. Catalytic structures were packed in the middle of the reactor and fixed with commercial aluminium foams to provide temperature and flow homogeneity. The sample specifications and experimental conditions are summarised in Table 5-1.

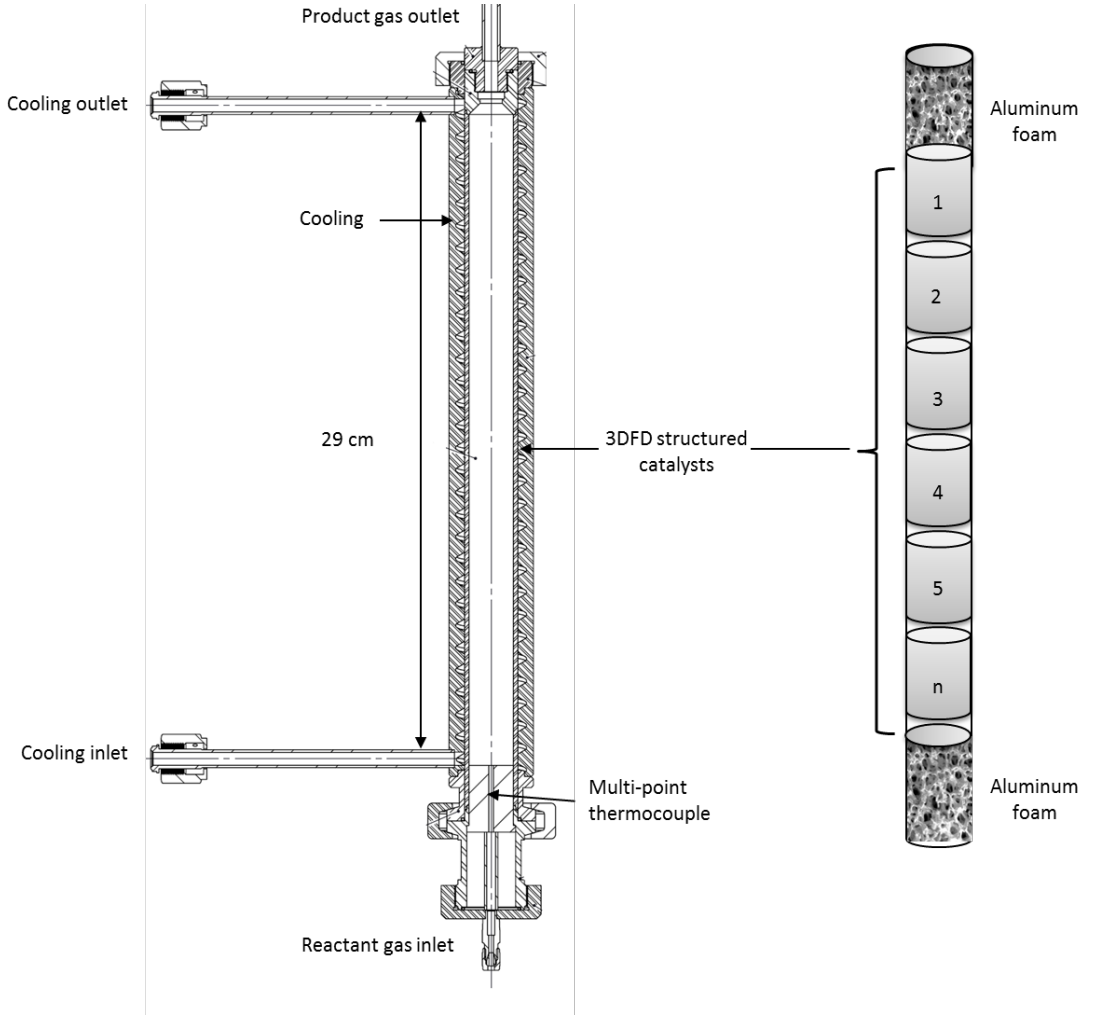

Figure 5-3. Reactor configuration.

The experimental setup given in Figure 5-4 consists of a catalytic reactor, a gas conditioning equipment (valves, heat exchanger and water trap/condenser), a pressure indicator and regulator (1 to 10 bars), an oil thermo-regulator (Huber Thermofluid DW-Therm 30-330°C), a mass flow controller of CO_2, H_2 and Ar flows up to 3, 10 and 10 $Nl \cdot min^{-1}$, respectively and a micro-GC. The catalytic reactor is surrounded by a safety cabinet. The oil thermo-regulator controls the temperature and flow of the oil.

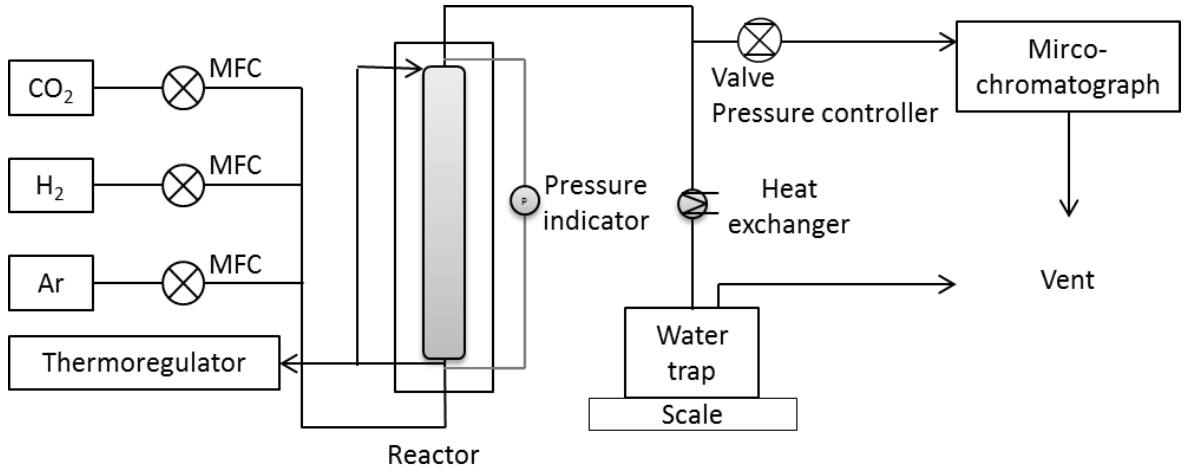

Figure 5-4. Experimental setup for the pilot tests.

Before the reaction test, catalysts were activated under a continuous flow of H_2:Ar (4:1) at the total rate of 1 Nl·min^{-1} (STP) and temperature of 325°C (heating rate 10°C·min^{-1}) for 7 h at 2.5 bars. After reduction, temperature of the furnace was adjusted to the reaction temperature under continuous flow of argon. Methanation reaction was performed at temperatures between 280 and 325°C. Carbon dioxide and hydrogen were continuously fed into the reactor together at the total rate of 0.25-1 Nl·min^{-1} (STP) with feed composition of CO_2:H_2 = 1:4.

A micro-GC (SRA R2000) was used for the analysis of reagents and products. TCD was used to measure CH_4, CO_2 and CO concentrations. The peaks from C_2H_4 and C_2H_6 were indistinguishable from each other. The calibration of peak areas was performed using a known reactant gas composition using calibration gas cylinders. Conversion, selectivity and productivity were calculated using the following equations:

$$X_{CO_2} = \left[\frac{F_{CO_2 in} - F_{CO_2 outlet}}{F_{CO_2 in}}\right] * 100\ (\%) \quad (5\text{-}1)$$

$$S_{CH_4} = \left[\frac{F_{CH_4 outlet}}{F_{CH_4 outlet} + F_{CO\,outlet} + 2F_{C_2H_4 outlet} + 2F_{C_2H_6 outlet}}\right] * 100\ (\%) \quad (5\text{-}2)$$

$$P_{CH_4} = \left[\frac{F_{CH_4 outlet}}{m_{Ni}}\right]\left(\frac{mmol}{g.h}\right) \quad (5\text{-}3)$$

where F is the molar flow rate and m_{Ni} is the mass of nickel. GHSV was calculated from $Q_{reactant}$ total inlet volumetric flow rate divided by the inserted sample volume V_{sample} (volume of copper or stainless steel supports).

$$GHSV = \left[\frac{Q_{reactant}}{V_{sample} * k_{number\ of\ samples}}\right] \ (h^{-1}) \quad (5\text{-}4)$$

Alternatively, calculations of conversion rate from micro-GC data can be calculated from carbon balance (mass balance) using the following equations:

$$X_{CO_2} = \left[\frac{F_{CH_4 outlet} + F_{CO outlet} + 2F_{C2H4 outlet} + 2F_{C2H6 outlet}}{F_{CH_4 outlet} + F_{CO_2 inlet} + F_{CO outlet} + 2F_{C2H4 outlet} + 2F_{C2H6 outlet}}\right] * 100\ (\%) \quad (5\text{-}5)$$

5.3. Results and discussion

5.3.1. Characterization of fresh catalysts

Figure 5-5 shows the XRD pattern of the fresh, calcined and reduced Ni-γ-P. The broad peaks at 45-54° indicated that nickel oxide was present in an amorphous state or highly dispersed on the support. NiO/Ni peak at 51.8° of calcined catalysts became sharper due to the change of NiO crystallite form after increasing calcination temperature from 500 to 700°C. Peak attributed to NiO/Ni at 69° became sharper after the reduction of the catalyst at 700°C for 3 h.

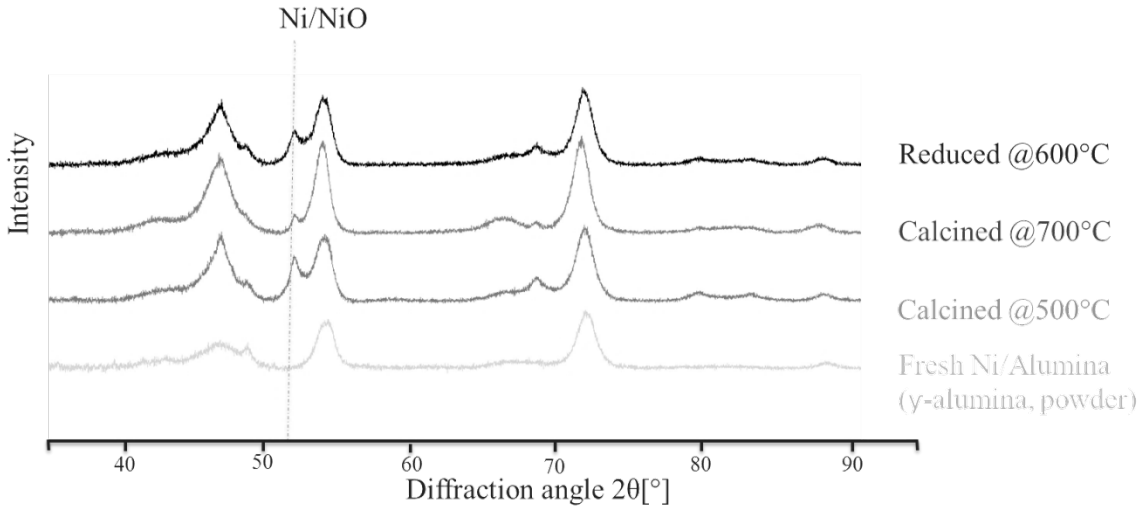

Figure 5-5. XRD patterns of the Ni-γ-P catalyst.

Figure 5-6 presents the X-ray photoelectron spectroscopy (XPS) spectra of Ni-BOE-P, reduced at 450 and 600°C. The XPS was used to determine the chemical composition of the catalyst surface and to better understand the role of the metal interactions with catalyst support. It is reported in literature that three kinds of Ni could be inferred from the binding energies. The binding energy of Ni $2p_{3/2}$ in $NiAl_2O_4$ is 857.0 eV, in the case of NiO intimately interacting with support is 856.0 eV and for bulk NiO the binding energy is 854.0 eV [22,23]. Ni/alumina made of boehmite and reduced at 450°C showed the Ni $2p_{3/2}$ binding energy at 856.48 eV, that can be attributed to NiO closely interacting with alumina support. The same catalyst reduced at 600°C showed Ni $2p_{3/2}$ binding energy at 858.20 eV, closer to the binding energy of the species in $NiAl_2O_4$ spinel. With the increase of the reduction temperature from 450 to 600°C, the Ni $2p_{3/2}$ binding energy was shifted by 1.72 eV to higher binding energy which can be dedicated to very strong interaction between Ni species and the Al_2O_3 support. Though the spinel peak was not detected by XRD measurements due to overlapping, XPS results were found to be consistent with the results of XRD examination.

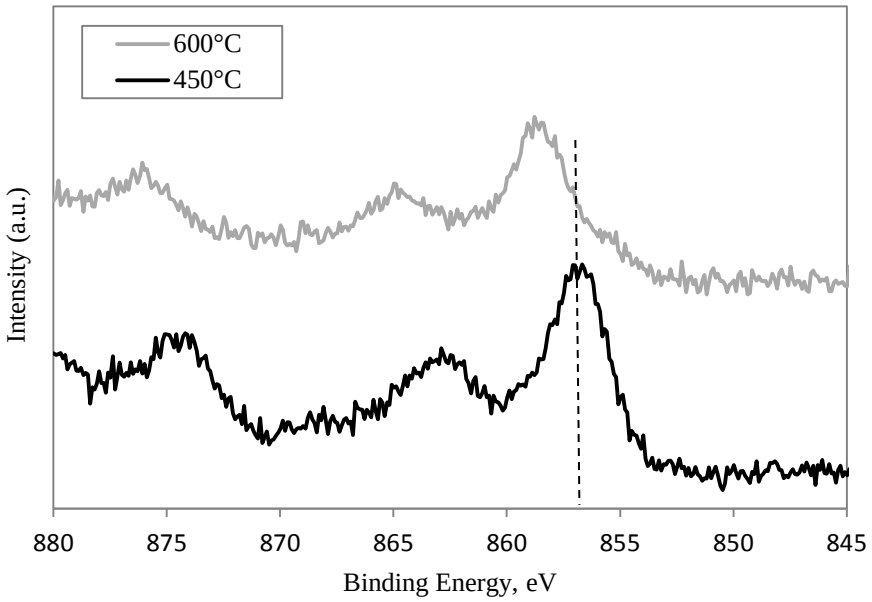

Figure 5-6. XPS spectra of Ni-BOE-P catalysts reduced at 450 and 600°C.

Table 5-2 shows the surface atomic ratios and the binding energies of Ni $2p_{3/2}$ core-level obtained from XPS spectra. The C/Al atomic ratio of the samples after different reduction treatments remains unchanged corresponding to the carbon contamination. The O/Al atomic ratio was calculated to be ca. 1.56 which is very close to the theoretical stoichiometric atomic ratio of alumina (Al_2O_3). The Ni/Al atomic ratio indicates the dispersity of nickel that the catalyst reduced at 600°C was found to be less than reduced at 450°C. The reason could be the nickel sintering at reduction temperature of 600°C or inhomogeneity of the catalysts due to limitations of XPS technique, these hypotheses can take into account only considering the small measured area of the catalysts surface.

Table 5-2. XPS analysis of Ni-BOE-P catalyst after reduction at 450°C and 600°C.

Sample	C/Al	Ni/Al	O/Al	Ni $2p_{3/2}$ (BE, eV)
After reduction at 450°C	0.81	0.07	1.57	856.48
After reduction at 600°C	0.73	0.04	1.55	858.20

Figure 5-7 shows the temperature-programmed reduction (TPR) analysis of the Ni-BOE-P, Ni-γ-P and commercial Evonik Octolyst 1001 catalysts. The TPR was used to characterize the catalysts with respect to the interactions between nickel species and alumina support and to understand the effect of the alumina type on reducibility. The low temperature peaks are attributed to the reduction of bulk NiO and high temperature peaks are attributed to the reduction of NiO in intimate contact with the oxide supports [22–25]. Calcined Ni-BOE-P showed low temperature single sharp peak of H_2 consumption at ca. 510°C and high temperature broad peak at temperatures 600-800°C. The first peak is assigned to the reduction of bulk NiO which interacts weakly with alumina support. The second broad peak is attributed to the reduction of $NiAl_2O_4$. The catalyst reduced at 600°C showed broad reduction peak at 250 to 500°C and the high temperature peak was shifted to the higher

temperatures due to the strong contact with support by increasing calcination temperature. Formation of $NiAl_2O_4$ decreases the reducibility at low temperatures. The formation of $NiAl_2O_4$ spinel species is expected to be due to the interactions between the impregnation solution and the boehmite followed by the heat treatment. During impregnation, formation of Ni and Al cations occupies the sites of the lattice, and lead to formation of spinel structures ($Metal^{+2}Al_2^{+3}O_4^{-2}$). It also has been explained that active NiO reacts with Al_2O_3 to transform into Nickel aluminate spinel structure during heat treatment at high temperature [26,27] and prolonged calcination time can alter the texture and promotes the $NiAl_2O_4$ formation [28].

The high temperature reduction peak of Ni-γ-P catalysts reduced at 600°C was not affected by the prior calcination. Broader low temperature reduction peak corresponding to NiO weakly interacting with catalyst support was observed on reduced Ni-γ-P. Both Ni-γ-P and commercial Evonik Octolyst 1001 (14-17 wt.%Ni) catalysts showed broad reduction peak starting at 250°C therefore demonstrated the best reducibility at low temperatures. It has been explained that changing the nickel loading, nickel species interacts differently with Al_2O_3. Above 12 wt.%Ni on alumina, the alumina is saturated with Ni, and bulk NiO is formed on the alumina surface [29].

In summary, Ni-BOE-P showed high temperature reduction TPR peaks. The impregnation of boehmite with nickel followed by the calcination at 450°C resulted in $NiAl_2O_4$ spinel formation that decreases the reducibility of the catalyst. High reducibility at low temperatures was achieved with the Ni-γ-P catalyst.

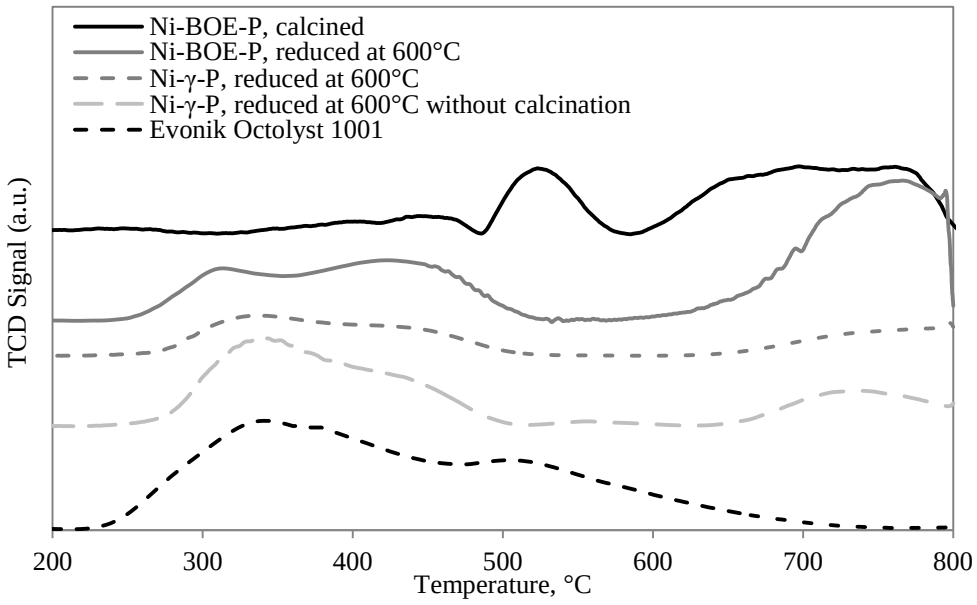

Figure 5-7. TPR results of the catalysts.

5.3.2. Catalytic activity

5.3.2.1. Lab-scale experiments

Lab-scale experiments were performed in a quartz tubular reactor. Figure 5-8 illustrates the CO_2 conversion of powder Ni/Al_2O_3 catalysts reduced at the different temperatures as a function of the reaction temperature. Reaction conditions are given in Table 5-1. It can be seen that catalytic CO_2 conversion at 450°C improved by ca. 18 % when the reduction temperature is increased from 450 to 600°C. This is because of the increased amount of metallic Ni in the catalyst reduced at higher temperature.

At the same conditions, commercial Evonik Octolyst 1001 (14-17 wt.%Ni, SSA 246 $m^2 \cdot g^{-1}$) and Ni-γ-P (12 wt.%Ni, SSA 72 $m^2 \cdot g^{-1}$) catalysts reduced at 600°C were compared. Commercial catalyst showed high catalytic activity already at 250°C. At 350°C, both catalysts showed similar catalytic activity.

Lab-scale measurements also showed that Ni-γ-P gave a much higher CO_2 conversion than Ni-BOE-P catalyst and conversion started at a lower temperature. The selectivities of all catalysts were constant (ca. 98%) at the temperature <400°C. In the case of Ni-BOE-P catalyst reduced at 450°C, selectivity was found to be only 80 %. Main by-products were detected to be CO and C_2H_4.

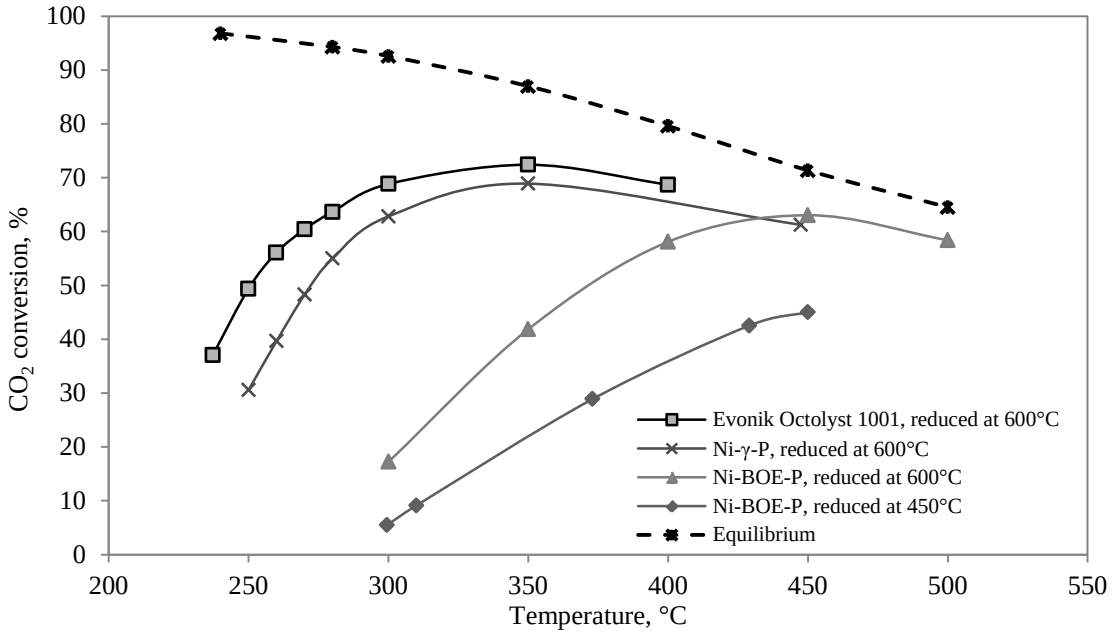

Figure 5-8. Conversion of CO_2 versus temperature for Ni-BOE-P, Ni-γ-P and commercial catalysts, (GHSV = 1300 h^{-1}, 1 bars) at lab-scale reactor.

5.3.2.2. Pilot-scale experiments

Methanation reaction was performed at temperatures between 280 and 330°C under pressure of 1.5-15 bars. Carbon dioxide and hydrogen were continuously fed into the reactor at the total rate

0.25 – 3.75 $Nl \cdot min^{-1}$ (STP) with a feed composition of CO_2:H_2 = 1:4. Table 5-3 presents the pilot-scale experimental conditions and results of the structured catalysts (CO_2 conversion, selectivity, yield and CH_4 productivity). Catalysts were reduced at the conditions listed in Table 5-1. In the case of Ni-BOE-3DSS, Ni-BOE-3DCu and Ni-γ-3DSS catalysts, a contribution effect on CO_2 conversion was expected due to the increased residence time of the reactant gases by increasing the reactor lengths (120, 220 and 290 mm, respectively). In the case of Ni-BOE-3DSS and Ni-BOE-3DCu catalysts overall activity was found to be very similar as described in chapter 4. By-product compounds were observed to be 2-5 % CO, negligible amount of C_2H_4/C_2H_6 (<0.001 %). However, at the CO_2 conversion lower than ca.10 %, methane selectivity was measured to be below 80 % for both Ni-BOE-3DSS and Ni-BOE-3DCu catalysts.

The illustration of the effect of the pressure on CO_2 conversion and CH_4 selectivity and productivity for the Ni-BOE-3DSS catalyst is given in Figure 5-9. Increasing pressure (from 1.5 to 6.5 bars) resulted in 13 % increase of CO_2 conversion and 60 $mmol \cdot g_{Ni}^{-1}.h^{-1}$ increase of productivity. At 330°C and 6.5 bars, CO_2 conversion and methane productivity were calculated to be 35 % and 153.3 $mmol \cdot g_{Ni}^{-1}.h^{-1}$, respectively. Increasing pressure increases the partial pressure of the reactant gases and therefore thermodynamic equilibrium conversion, as well as the reaction rate. Thus, with the increase of the pressure at constant flow rate, the CO_2 conversion and methane productivity were increased. By-product compounds were observed to be 5 % CO, negligible amount of C_2H_4/C_2H_6 (<0.001 %). All the structured catalysts showed a similar trend of CO_2 conversion by an increase of a pressure.

Table 5-3. Experimental results of the Ni-BOE-3DSS, Ni-BOE-3DCu and Ni-γ-3DSS catalysts.

Catalyst	T_{set} (°C)	$T_{in\text{-}situ,\ max}$ (°C)	P (bars)	Flow (Nl/min)	GHSV (h^{-1})	X_{CO2} (%)	S_{CH4} (%)	Y_{CH4} (%)	Productivity ($mmol \cdot g_{Ni}^{-1} \cdot h^{-1}$)
Ni-BOE-3DSS	325	315	2.5	1	1622	9	41	3	56
		315	5		1622	11	60	7	130
		316	6		1622	13	65	10	186
		320	5	0.5	811	20	91	18	167
	330	320	1.5	0.25	405	22	91	20	93
		320	2.5		405	25	93	24	107
		320	5		405	29	95	28	130
		320	6		405	32	95	30	139
		320	6.5		405	35	95	33	153
Ni-BOE-3DCu	325	317	1.5	1	870	7	60	4	77
		317	2.5		870	8	68	5	88
		317	5		870	9	77	7	98
		318	10		870	11	84	9	118
		318	15		870	13	88	11	142
	330	321	15		870	15	89	13	168
	325	318	5	0,5	435	11	86	9	59
	325	318	15	0.25	217	26	95	25	74
Ni-γ-3DSS	325	306.1	5	1	659	18	82	15	83
	328	320.3	15	3.75	2473	15	84	13	256
		318.2		1	659	31	96	30	141
		317.9		0.5	330	45	98	44	102
	328	317.5	5	3.75	1102	10	84	8	154
	325	318.6	1.5	3.75	2473	7	63	4	127
	328	317.2	10	0.25	165	50	99	50	56
	325	314.3			165	49	99	50	57
	320	309.5			165	47	99	47	53
	300	290.1			165	38	99	38	46
	280	271.1		1	659	6	89	5	27
	290	280.6			659	8	90	7	34
	300	290.6			659	10	91	9.1	46
	320	310.1			659	19	93	18	86

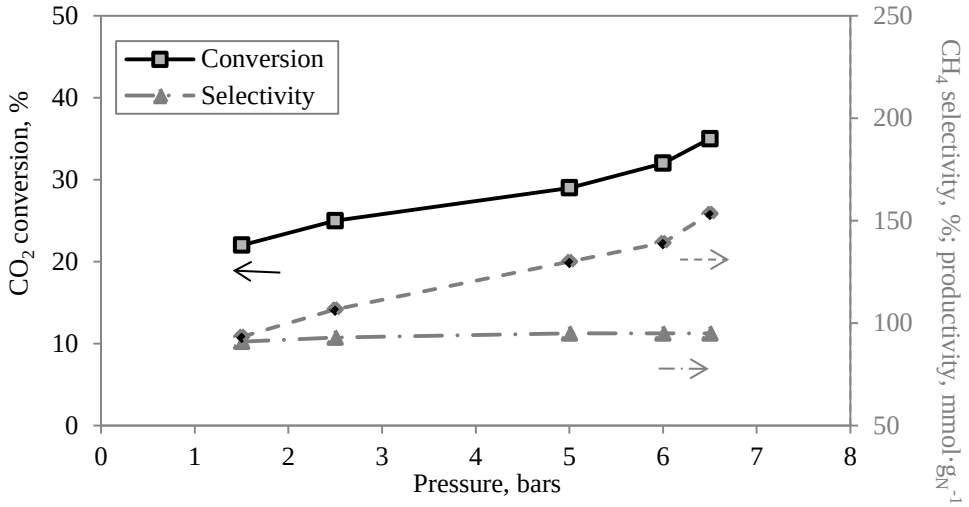

Figure 5-9. CO_2 conversion, methane selectivity and productivity versus pressure for Ni-BOE-3DSS catalyst at 330°C, 0.25 Nl·min^{-1}.

The GHSV effect on CO_2 conversion and CH_4 selectivity and productivity for Ni-γ-3DSS catalyst is given in Figure 5-10. The pressure and temperature were kept constant at 15 bars and at 328°C, respectively. The total gas flow rate was ranged between 0.5 and 3.75 Nl·min^{-1}. Conversion of CO_2 was achieved to be 45 % with a productivity of 102 mmol·g_{Ni}^{-1}.h^{-1} at GHSV of 330 h^{-1}. An increase of GHSV from 330 to 2473 h^{-1} led to an increase of productivity from 102 to 256 mmol·g_{Ni}^{-1}.h^{-1} and a decrease in CO_2 conversion from 45 to 15 %. For the continuous production in large-scale industrial plants, high activity at a higher GHSV is desired. Productivity is directly linked to the molar flow rate (mmol.h^{-1}) of products. Thus, an increase of the molar flow rate of reactants increases the methane productivity. As expected, a similar effect of GHSV was observed of all the structured catalysts.

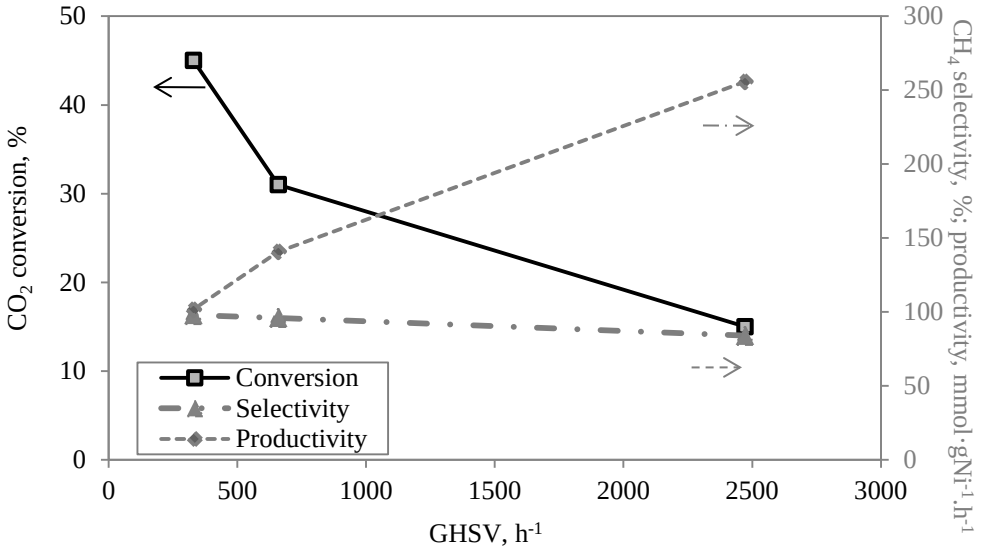

Figure 5-10. CO_2 conversion, methane selectivity and productivity versus GHSV for Ni-γ-3DSS catalyst at 328°C, 15 bars.

The effect of the temperature on CO_2 conversion and CH_4 selectivity for Ni-γ-3DSS catalyst is given in Figure 5-11. The result shows that CO_2 conversion and CH_4 selectivity is a function of the reaction temperature. The conversion of CO_2 at 10 bars gradually increased with the temperature (from 280 to 330°C). In the case of lab-scale experiments, catalyst was found to be active at temperatures above 300°C as given in Figure 5-8. Due to the limitation of the maximum temperature of the oil thermo-regulator, the set temperature could not exceed 330°C. Therefore, the highest CO_2 conversion was achieved to be 50 % at 328°C, 10 bars. During these measurements, the temperature along the reactor was monitored by multipoint thermocouple. Measured temperatures are given in Figure 5-12. Temperature all along the reactor was observed to be homogeneous. No hot-spots formation was observed at the highest CO_2 conversion of 50 %. It was reported that in the case of packed bed of Evonik Octolyst 1001 catalyst, the temperature at the centre of the catalytic bed went up to 520°C at the set temperature of 250°C, so the hot-spot temperature was found to be ca. 270°C [30].

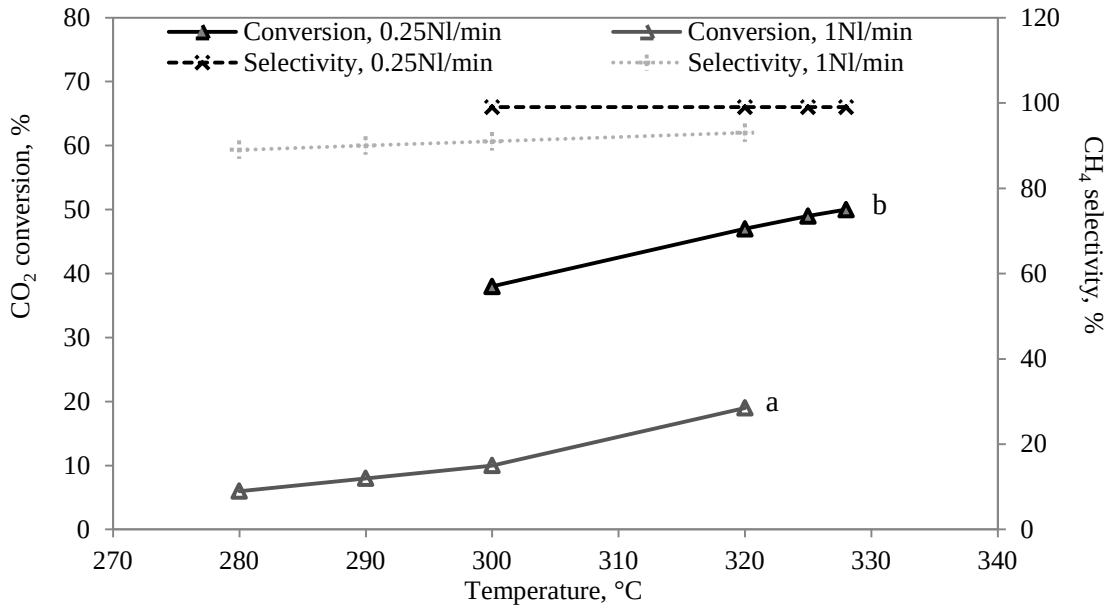

Figure 5-11. CO_2 conversion and CH_4 selectivity versus temperature for Ni-γ-3DSS catalyst at 10 bars.

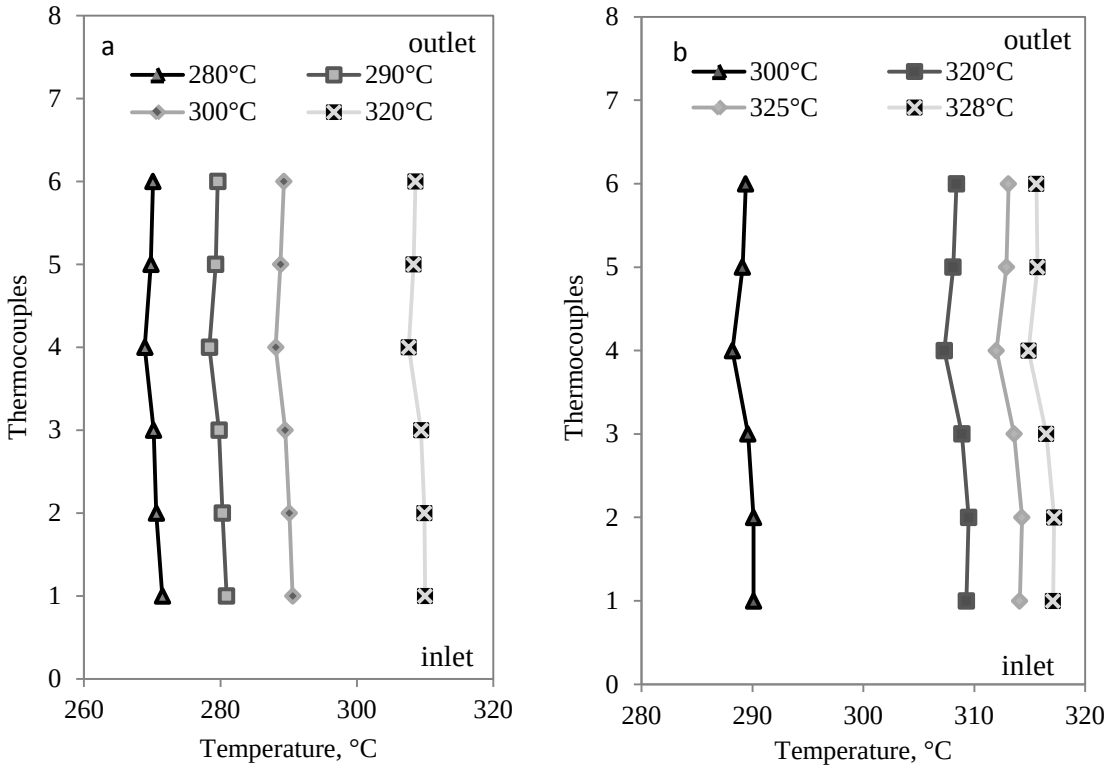

Figure 5-12. Reactor temperature profiles during methanation test at 10 bars, 1 Nl·min^{-1} (a) and 0.25 Nl·min^{-1} (b).

5.3.3. Characterization of spent catalysts

The SEM images of calcined, reduced and spent Ni-γ-P catalyst and reduced Ni-BOE-P catalysts are given in Figure 5-13. As for the calcined Ni-γ-P catalyst before reduction, it was difficult to distinguish NiO, Ni aluminate and alumina particles. After the reduction, uniformly distributed nickel particles (red arrows) of 10-20 nm diameters are clearly visible at the Figure 5-13b. After the reaction, the size of the nickel particles stays the same and no carbon deposits were observed on the SEM images of the catalyst. Regarding Ni-BOE-P catalysts, the accumulated dark spots with a diameter above 20 nm indicates the formed nickel aluminate spinel. The spinel $NiAl_2O_4$ formation on Ni-BOE-P catalysts was confirmed by XPS, TPR and SEM analysis.

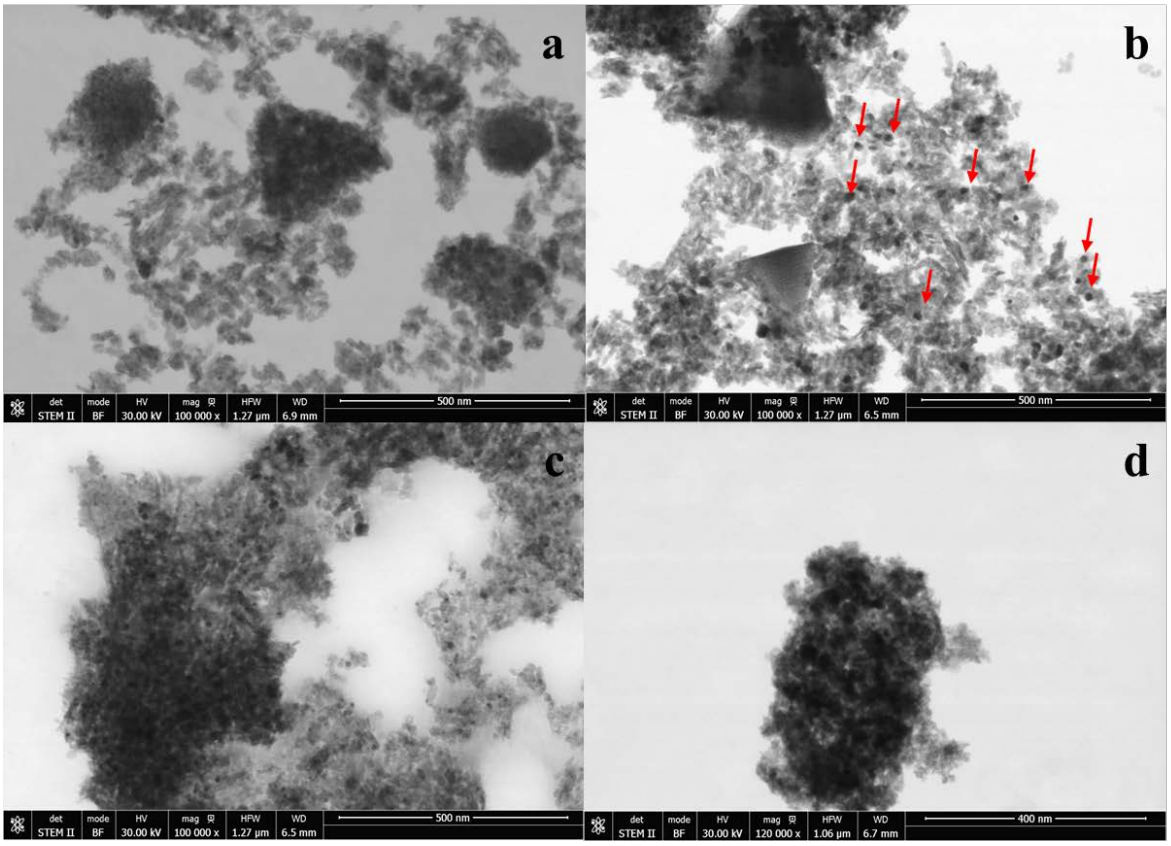

Figure 5-13. SEM images of calcined (a), reduced (b), spent (c) Ni-γ-P catalysts and reduced (d) Ni-BOE-P catalysts.

For the analysis, Ni/alumina coating was removed from the Ni-BOE-3DCu catalyst by ultrasonic treatment in deionised water for 6 h. The BET surface areas of fresh and spent catalysts are given in Table 5-4. The BET surface area of the fresh Ni-BOE-3DCu catalyst was measured to be 236 $m^2 \cdot g^{-1}$. After pilot-scale experiments, the BET surface area decreased by 42 $m^2 \cdot g^{-1}$. The reasons could be sintering of support, metallic phase or pore blockage due to carbon deposition during the reaction.

Table 5-4. BET specific surface area of fresh and spent Ni/alumina catalysts.

Catalyst	Form	BET surface are ($m^2 \cdot g^{-1}$)	Micropore volume ($cm^3 \cdot g^{-1}$)	Pore diameter (nm)
Ni-BOE-P	Fresh	236	n.a.	n.a.
Ni-BOE-3DCu	Spent	194	n.a.	n.a.
Evonik Octolyst 1001	Fresh	246	n.a.	n.a.
Ni-γ-P	Fresh	72	0.029	3.821

Figure 5-14 presents the DTGA-MS results of the abovementioned spent Ni-BOE-3DCu catalyst. The peak with a weight loss of 0.81 wt.% was observed at temperatures between 250 and 450°C which corresponds to CO_2 release due to the oxidation of carbon deposits. Similar effect was

described in the previous chapter that Ni-BOE-3DCu spent catalyst showed 0.44 wt.% weight loss at DTGA-MS measurements.

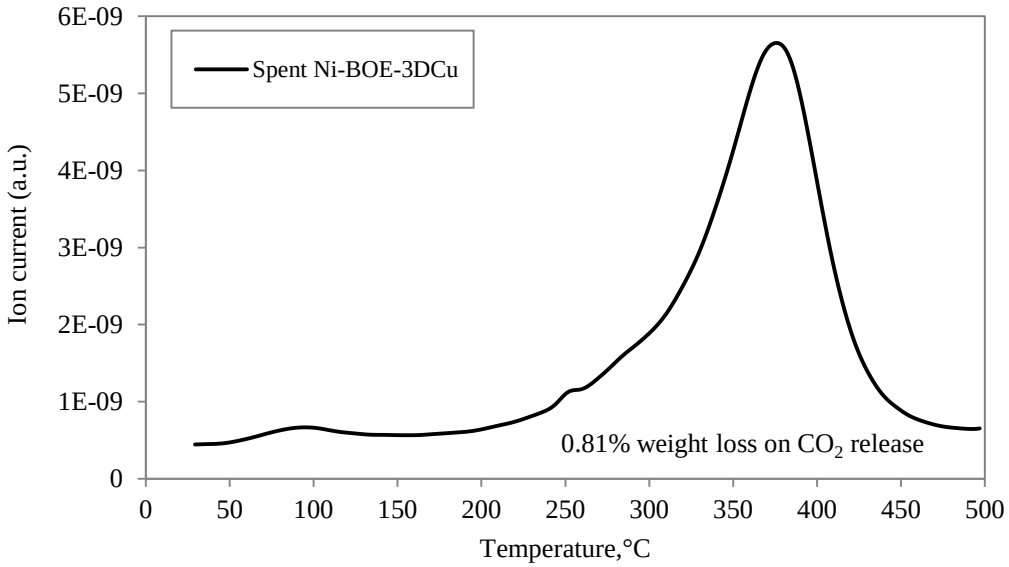

Figure 5-14. DTGA-MS of spent Ni-BOE-3DCu catalyst.

5.3.4. Methane productivity

The highest methane productivity of Ni-BOE-3DSS, Ni-BOE-3DCu and Ni-γ-3DSS catalysts was found to be 185.8, 168.3 and 255.8 mmol·g_{Ni}^{-1}.h^{-1}, respectively. The values of productivity of the structured catalysts from this work and coated open cellular foams (OFC) in literature are compared in Table 5-5. In the case of the lab-scale experiments, boehmite based catalysts have not shown high catalytic activity at low temperatures (<300°C). That is why the productivities of Ni-BOE-P and Ni-BOE-3DSS catalysts were compared at the temperature of 400°C. Structured catalysts showed slightly higher methane productivity than the powders in packed-bed configuration at the same conditions. The productivity of the Ni-γ-P and Ni-γ-3DSS catalysts was found to be ca. 2 times higher than the Ni-BOE-P and Ni-BOE-3DSS catalysts. The reason could be the starting materials (AlO(OH) and γ-Al_2O_3), that affects the metal-support interactions and reducibility of the catalysts. A clear increase of methane productivity with increase of pressures is observed on the pilot-scale.

The results of the productivity were compared with previously reported studies. Methanation reaction was performed with commercial Evonik Octolyst 1001 coated onto aluminium OCF [30]. CO_2 conversion of 22 % was achieved at 300°C, 5 bars and 5 Nl·min^{-1} flow. Selectivity was recorded to be 95 %. Frey *et al.* studied the methanation reaction with Ni/ceria-zirconia coated aluminium OCF structured catalyst [31]. In this study, the productivity of the OCF catalyst was found to be slightly higher than the packed-bed of the same catalyst. The productivity of the Evonik Octolyst 1001 Al OCF was found to be ca. 4 and 2 times higher than Ni-γ-3DSS and Ni/CZ/Al OCF catalysts, respectively. It has to be mentioned that no direct comparison can be made between 3D-SS, 3D-Cu

and OCF structured catalysts due to the difference in support material, cell geometry, macro-porosity, coating thickness, type of active catalyst and oxide etc.

To conclude, the highest methane productivity was achieved with the Ni-γ-3DSS catalyst. The scale-up possibility of the structured catalysts was proved by the tests in the pilot single-channel reactor. Methane productivity of 256 mmol·g_{Ni}^{-1}·h^{-1} was achieved at 328°C, 15 bars. This productivity value is ca. 3 times higher than the results obtained in the lab-scale reactor, and comparable with literature data.

Table 5-5. Comparison of 3D structured catalysts in CO_2 methanation.

Catalyst	Tests	Temperature (°C)	CO_2 flow (Nl· min^{-1}· g_{Ni}^{-1})	Productivity (mmol· g_{Ni}^{-1}· h^{-1})	References
Ni-BOE-P	Lab-scale	400	0.083	30.8	Present study
Ni-BOE-3DSS			0.083	36.2	
Ni-γ-P		300	0.083	66.8	
Ni-γ-P-3DSS			0.083	74.1	
Ni-γ-3DSS	Pilot-scale	325 (1.5 bars)	0.625	126.7	Present study
		328 (5 bars)	0.625	154.2	
		328 (15 bars)	0.625	255.8	
Ni/CZ/ Aluminium OCF		309 (5 bars)	0.790	580	[31]
Evonik Octolyst 1001 Aluminium OCF		300 (5 bars)	0.695	975	[30]

5.3.5. Catalyst stability

In order to study the catalysts stability, methanation reaction was performed with the Ni-γ-3DSS structured catalyst at 320°C, 10 bars in H_2:CO_2 = 4:1 mixture without dilution. The temperature was recorded every 30 seconds of the reaction run. Figure 5-15 shows the CO_2 conversion and maximum temperature as a function of TOS. The initial CO_2 conversion was 25 %. After 80 h, CO_2 conversion decreased only by ca. 3.6 %. The maximum temperature was recorded as 309.5±0.3°C. Therefore, it can be seen that no hot-spot formation occurred during 80 h TOS. During the last 40 h only 1 % activity loss was recorded. It was found to be a promising result in comparison with previously reported data: e.g. a stability test on commercial powder Evonik Octolyst 1001 was performed for methanation reaction in a multichannel structured reactor [30]. The maximum temperature was recorded to be 500°C, and the initial CO_2 conversion was 86 %. After 80 h TOS, a 13.6 % decrease of CO_2 conversion was observed. It is reported that carbon deposition, sintering of the

catalytic support and metallic phase can lead to a decrease of catalytic activity during the reaction run [12,32–34].

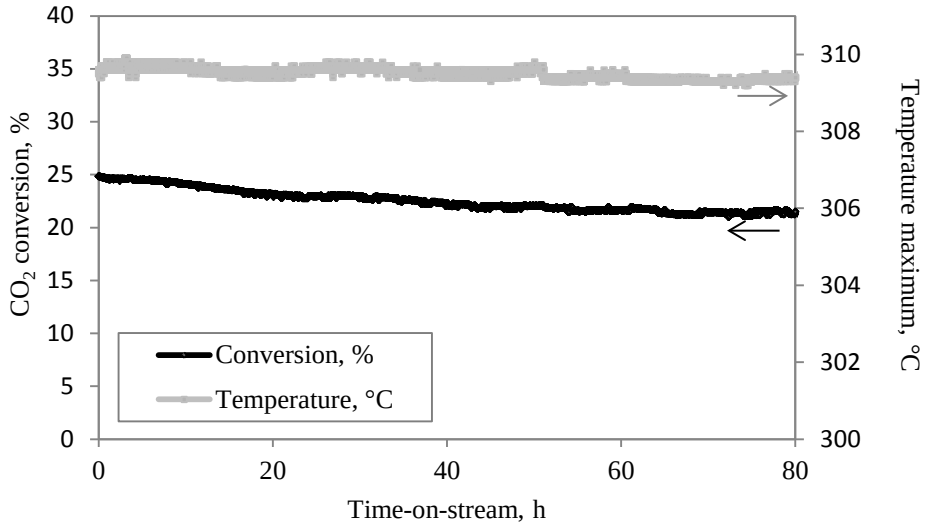

Figure 5-15. Stability of Ni-γ-3DSS catalyst at 320°C, 10 bars in pure H_2:CO_2 = 4:1 for 80 h TOS.

5.4. Conclusions

This chapter describes the innovative 3DFD structured supports that were developed, manufactured and coated with Ni/alumina catalysts made of different alumina precursors. The type of alumina support affected the catalytic performance due to their different physical properties (pore size, specific surface area, reducibility, crystallinity). Characterization of the catalysts showed that nickel aluminate spinel formation occurred on Ni-BOE catalysts leading to an increase of the reduction temperature. The lab-scale experiments showed that in the presence of aluminates, reduction temperature and reducibility of the catalyst decreases. Nickel aluminate formation can be avoided by using Ni/alumina catalysts made of γ-alumina precursors which were calcined and reduced at 500°C.

3D-structured catalysts were scaled up in a pilot-scale reactor at CEA Liten, Grenoble. Pilot-scale experimental results were found to be in agreement with lab-scale tests. The highest methane productivity was achieved with Ni-γ-3DSS catalysts. Methane productivity was calculated to be 256 $mmol \cdot g_{Ni}^{-1} \cdot h^{-1}$ which was ca. 3 times higher than results obtained in the lab-scale reactor. The Ni-γ-3DSS catalysts showed high stability for 80 h time-on-stream with non-diluted feed gas under pressure of 15 bars. No hot-spots formation was recorded during the reaction and a low amount of carbon deposits was detected.

5.5. References

[1] K. Altfeld, D. Pinchbeck, Admissible hydrogen concentrations in natural gas systems, (2013). www.gas-for-energy.com.

[2] O. Teller, J.-P. Nicolai, M. Lafoz, D. Laing, R. Tamme, A. Schroeder Pederson, M. Andersson, C. Folke, C. Bourdil, M. Conte, G. Gigliucci, I. Fastelli, M. Vona, M. Rey Porto, T. Hackensellner, R. Knapp, H.J. Seifert, M. Noe, M. Sander, J. Lugaro, M. Lippert, P. Hall, R. Saliger, A. Harby, M. Pihlatie, N. Omar, J.-M. Durand, P. Clerens, Joint EASE / EERA recommendations for a European Energy Storage Technology Development Roadmap towards 2030, 2013. http://www.ease-storage.eu/tl_files/ease-documents/Stakeholders/ES Roadmap 2030/EASE-EERA ES Tech Dev Roadmap 2030 Final 2013.03.11.pdf.

[3] The project Jupiter 1000, Demonstr. Massive Renew. Energy Storage into Transm. Gas Grid. (2017). http://www.jupiter1000.com/en/projet.html (accessed May 24, 2017).

[4] T.J. Schildhauer, S.M. Biollaz, Synthetic natural gas from coal, dry biomass, and power-to-gas applications, John Wiley & Sons, Paul Scherrer Institut, Villigen/Switzerland, 2016.

[5] M. Götz, J. Lefebvre, F. Mörs, A. McDaniel Koch, F. Graf, S. Bajohr, R. Reimert, T. Kolb, Renewable Power-to-Gas: A technological and economic review, Renew. Energy. 85 (2016) 1371–1390. doi:10.1016/j.renene.2015.07.066.

[6] P. Collet, E. Flottes, A. Favre, L. Raynal, H. Pierre, S. Capela, C. Peregrina, Techno-economic and life cycle assessment of methane production via biogas upgrading and power to gas technology, Appl. Energy. (2016). doi:10.1016/j.apenergy.2016.08.181.

[7] O.S. Buchholz, A.G.J. Van Der Ham, R. Veneman, D.W.F. Brilman, S.R.A. Kersten, Power-to-Gas: Storing surplus electrical energy a design study, Energy Procedia. 63 (2014) 7993–8009. doi:10.1016/j.egypro.2014.11.836.

[8] J. Vandewalle, K. Bruninx, W. D'Haeseleer, Effects of large-scale power to gas conversion on the power, gas and carbon sectors and their interactions, Energy Convers. Manag. 94 (2015) 28–39. doi:10.1016/j.enconman.2015.01.038.

[9] D. Türks, H. Mena, U. Armbruster, A. Martin, Methanation of CO_2 on Ni/Al_2O_3 in a Structured Fixed-Bed Reactor—A Scale-Up Study, Catalysts. 7 (2017) 152. doi:10.3390/catal7050152.

[10] L.F. Albright, Albright's Chemical Engineering Handbook, CRC Press, 2008. https://books.google.com/books?id=HYB3Udjx_FYC&pgis=1 (accessed May 22, 2016).

[11] Z. Liu, B. Chu, X. Zhai, Y. Jin, Y. Cheng, Total methanation of syngas to synthetic natural gas over Ni catalyst in a micro-channel reactor, Fuel. 95 (2012) 599–605. doi:10.1016/j.fuel.2011.12.045.

[12] R. Zapf, C. Becker-Willinger, K. Berresheim, H. Bolz, H. Gnaser, V. Hessel, G. Kolb, P. Löb, A.-K. Pannqitt, A. Ziogas, Alumina-based catalyst coatings within microchannels and their testing, 81 (2003) 721–729.

[13] O. Görke, P. Pfeifer, K. Schubert, Highly selective methanation by the use of a microchannel reactor, Catal. Today. 110 (2005) 132–139. doi:10.1016/j.cattod.2005.09.009.

[14] J. Hu, K.P. Brooks, J.D. Holladay, D.T. Howe, T.M. Simon, Catalyst development for microchannel reactors for martian in situ propellant production, Catal. Today. 125 (2007) 103–110. doi:10.1016/j.cattod.2007.01.067.

[15] C. Janke, M.S. Duyar, M. Hoskins, R. Farrauto, Catalytic and adsorption studies for the hydrogenation of CO_2 to methane, Appl. Catal. B Environ. 152–153 (2014) 184–191. doi:10.1016/j.apcatb.2014.01.016.

[16] C.Y. Zhao, Review on thermal transport in high porosity cellular metal foams with open cells, Int. J. Heat Mass Transf. 55 (2012) 3618–3632. doi:10.1016/j.ijheatmasstransfer.2012.03.017.

[17] M. Frey, D. Édouard, A.-C. Roger, Optimization of structured cellular foam-based catalysts for low-temperature carbon dioxide methanation in a platelet milli-reactor, Comptes Rendus Chim. 18 (2015) 283–292. doi:10.1016/j.crci.2015.01.002.

[18] S. Danaci, L. Protasova, J. Lefevere, L. Bedel, R. Guilet, P. Marty, Efficient CO_2 methanation over Ni/Al_2O_3 coated structured catalysts, Catal. Today. 273 (2016) 234–243.

doi:10.1016/j.cattod.2016.04.019.

[19] J. Lefevere, M. Gysen, S. Mullens, V. Meynen, J. Van Noyen, The benefit of design of support architectures for zeolite coated structured catalysts for methanol-to-olefin conversion, Catal. Today. 216 (2013) 18–23. doi:10.1016/j.cattod.2013.05.020.

[20] C. Fukuhara, K. Hayakawa, Y. Suzuki, W. Kawasaki, R. Watanabe, A novel nickel-based structured catalyst for CO_2 methanation: A honeycomb-type Ni/CeO_2 catalyst to transform greenhouse gas into useful resources, Appl. Catal. A Gen. 532 (2017) 12–18. doi:10.1016/j.apcata.2016.11.036.

[21] J. Luyten, S. Mullens, I. Thijs, Designing With Pores - Synthesis and Applications, KONA Powder Part. J. 28 (2010) 131–142. doi:10.14356/kona.2010012.

[22] Z. Hou, O. Yokota, T. Tanaka, T. Yashima, Characterization of Ca-promoted $Ni/\alpha\text{-}Al_2O_3$ catalyst for CH_4 reforming with CO_2, Appl. Catal. A Gen. 253 (2003) 381–387. doi:10.1016/S0926-860X(03)00543-X.

[23] F. Meng, Z. Li, J. Liu, X. Cui, H. Zheng, Effect of promoter Ce on the structure and catalytic performance of Ni/Al_2O_3 catalyst for CO methanation in slurry-bed reactor, J. Nat. Gas Sci. Eng. 23 (2015) 250–258. doi:10.1016/j.jngse.2015.01.041.

[24] F.W. Chang, M.S. Kuo, M.T. Tsay, M.C. Hsieh, Hydrogenation of CO_2 over nickel catalysts on rice husk ash-alumina prepared by incipient wetness impregnation, Appl. Catal. A Gen. 247 (2003) 309–320. doi:10.1016/S0926-860X(03)00181-9.

[25] J. Requies, M. a. Cabrero, V.L. Barrio, J.F. Cambra, M.B. Güemez, P.L. Arias, V. La Parola, M. a. Peña, J.L.G. Fierro, Nickel/alumina catalysts modified by basic oxides for the production of synthesis gas by methane partial oxidation, Catal. Today. 116 (2006) 304–312. doi:10.1016/j.cattod.2006.05.084.

[26] O.S. Joo, K.D. Jung, CH_4 dry reforming on alumina-supported nickel catalyst, Bull. Korean Chem. Soc. 23 (2002) 1149–1153. doi:10.5012/bkcs.2002.23.8.1149.

[27] M. Javanmardi, R. Emadi, H. Ashrafi, Synthesis of nickel aluminate nanoceramic compound from aluminum and nickel carbonate by mechanical alloying with subsequent annealing, Trans. Nonferrous Met. Soc. China. 26 (2016) 2910–2915. doi:10.1016/S1003-6326(16)64420-5.

[28] M. Mohammadpour Amini, L. Torkian, Preparation of nickel aluminate spinel by microwave heating, Mater. Lett. 57 (2002) 639–642. doi:10.1016/S0167-577X(02)00845-5.

[29] C. Li, Y.-W. Chen, Temperature-programmed-reduction studies of nickel oxide/alumina catalysts: effects of the preparation method, Thermochim. Acta. 256 (1995) 457–465. doi:10.1016/0040-6031(94)02177-P.

[30] J. Ducamp, Conception et optimisation d ’un réacteur-échangeur structuré pour l’hydrogénation du dioxyde de carbone en méthane de synthèse dédié à la filière de stockage d’énergie électrique renouvelable, l’université de Strasbourg, 2015.

[31] M. Frey, A. Bengaouer, G. Geffraye, D. Edouard, A.-C. Roger, Aluminium open cell foams as efficient support for CO_2 methanation catalyst: pilot scale reaction results, Energy Technol. (2017). doi:10.1002/ente.201700188.

[32] L. Zhu, S. Yin, X. Wang, Y. Liu, S. Wang, L. Zhu, S. Yin, X. Wang, Y. Liu, S. Wang, The catalytic properties evolution of HZSM-5 in the conversion of methanol to gasoline, RSC Adv. 0 (2013) 1–3. doi:10.1039/x0xx00000x.

[33] P. Li, Y.H. Park, D.J. Moon, N.C. Park, Y.C. Kim, Carbon deposition onto Ni-based catalysts for combined steam/CO_2 reforming of methane, J. Nanosci. Nanotechnol. 16 (2016) 1562–1566. doi:10.1166/jnn.2016.12006.

[34] Y. Gao, F. Meng, K. Ji, Y. Song, Z. Li, Slurry phase methanation of carbon monoxide over

nanosized Ni-Al_2O_3 catalysts prepared by microwave-assisted solution combustion, Appl. Catal. A Gen. 510 (2016) 74–83. doi:10.1016/j.apcata.2015.11.006.

Conclusions and outlook

In the present study we investigated the potential of 3D-printing technology for the manufacture of structured supports for CO_2 conversion into CH_4. The motivation of the thesis is to study the possibility of overcoming the industrial issues and limitations of CO_2 methanation such as temperature control, catalyst deactivation and high pressure drops. Therefore, 3DFD structured supports were proposed as an alternative to conventional packed-beds and open porous structures such as monoliths and foams.

3DFD technique was used to manufacture metallic support structures. This manufacturing technique enables the production of ceramic and metallic macro-porous structures with high specific surface areas where fibre thickness, geometry, inter-fibre distance (pore size), surface roughness and layer stacking (architecture) can be varied. Furthermore, the variation of the structural parameters allows for the optimization of the heat transfer and pressure drop values according to the process requirements. It is also noteworthy that a wide range of materials can be shaped into porous structures using the 3DFD technique e.g. metals and alloys, oxide supports, carbon-based materials and novel advanced materials such as graphene oxide composites.

Nickel/alumina coated stainless steel structured supports were manufactured and tested in the lab-scale reactor for CO_2 methanation reactions. It was found that the properties of the Ni/alumina-containing coating suspension (binder, viscosity, pH) affected the properties of the catalytic coating. The effect of the fibre positioning (1-1 and 1-3 stacking) on CO_2 conversion was compared. The high conversion at low temperatures was achieved by using structures with 1-3 stacking due to the higher mass transfer properties in these samples. Lower axial heat-transport of the structures with 1-3 stacking could also lead to an increase of the temperature in the structured catalyst and therefore increase of CO_2 conversion. At temperatures above 350°C, all structured catalysts showed similar CO_2 conversion.

The heat transport and pressure drop properties of AM structured catalytic supports were described based on experimental and numerical data. The structures with 1-1 configuration showed higher axial ETC than structures with 1-3 stacking due to the linear fibre stacking in the direction of the heat flux. In general, the macro-porosity was found to be the main parameter affecting ETC and pressure drop. Improved radial ETC can prevent the risks of thermal runaway due to the improved heat transfer between the reaction and cooling channels. Radial ETC is an important parameter for the reactor design which can be controlled by inter-fibre distance, fibre diameter and stacking factor. The cell orientation, porosity, open frontal area and surface roughness affect the pressure drop. The measurements showed that the samples with 1-3 fibre stacking have higher pressure drop values than the samples with 1-1 fibre stacking at the same macro-porosity due to their lower open frontal areas.

However, the pressure drop through the structures even with 1-3 architecture was found to be 10 times lower than conventional packed-beds with 3mm alumina beads.

Structured copper supports were manufactured as an alternative to stainless steel structures because of their higher thermal conductivity. Copper paste with an alcohol based binder was prepared for the manufacturing of support structures. Sintering temperature and atmosphere affected the morphology of the copper fibres. To enhance the thermal conductivity of the structures, dense fibres with ca. 0.1 % inner fibre porosity were achieved by controlling the sintering temperature and atmosphere. The homogeneous coating on the structures was obtained by optimizing the coating suspension. However, the coating on stainless steel supports was found to be more adhesive than on copper ones due to the nature of the support.

It was proved that preparation techniques and materials play a crucial role in catalyst preparation and have a strong effect on the activity of catalysts. Nickel/alumina catalysts with two different alumina powders were prepared by impregnation. Catalysts prepared from boehmite exhibited nickel alumina spinel formation showing a higher reduction temperature. This can be overcome by using γ-alumina for the catalyst preparation. Structured catalysts were tested in lab and pilot reactors. In the pilot reactor, methane productivity increased by a factor of 2 compared to the lab scale tests. Furthermore, no hot-spots formation was observed during 80 h TOS using Ni/alumina structured catalyst. Stability test showed only 3.6 % deactivation under undiluted reactant gas with a pressure of 15 bars. The highest methane productivity of 256 $mmol \cdot g_{Ni}^{-1} \cdot h^{-1}$ was achieved by using Ni/alumina supported on stainless steel structured catalysts in the pilot-scale reactor.

The use of structured catalysts/reactors showed advantages over conventional catalysts/reactors such as relatively low pressure drops, high mass- and heat-transfer properties and design flexibility. Structured catalysts were successfully implemented in the pilot scale reactor for the production of methane. This study demonstrates the real potential of 3DFD structured supports over conventional reactor designs.

Outlook and recommendations

For better temperature control, support structures were manufactured from copper. In order to improve the adhesion strength of the copper structures, a study aiming to improve the adhesion strength of the coating by chemical or physical treatments on copper surfaces is highly recommended. Furthermore, structured supports could be manufactured from other commercially attractive metals and alloys with high thermal conductivity (e.g. aluminium). We were able to successfully print pure aluminium 3DFD structures. However, sintering of them was found to be a challenge due to their ease of oxidation. The use of aluminium alloys could overcome the sintering issue. In the case of sintering of such conductive materials, PEC or plasma sintering can be used. Direct bulk printing of 3DFD structured catalysts made of catalytic materials (metal/oxide type catalysts, zeolites, carbon-based materials) offer a high catalyst loading in the structured reactor and an easier preparation procedure

(one-step). Moreover, this eliminates the coating adhesion issues. The disadvantage of such bulk structured catalysts is low mechanical strength (depending on the material and post-treatment) and lower heat transfer efficiency when compared with metal-based coated structured catalysts. Therefore, the process requirements determines what type of structured catalyst is suitable.

Furthermore, catalyst deactivation is one of the major issues in industrial catalytic processes. Further investigations on the catalyst deactivation to understand the fundamentals and mechanisms of the deactivation process for designing stable catalysts are highly recommended. The prevention of the deactivation by optimizing catalysts (using bimetallic catalysts etc.) or by optimizing processes (minimizing the formation of carbon precursors etc.) for CO_2 methanation also needs to be studied. Attention also needs to be paid to the regeneration of catalysts (e.g. removal of carbon deposits).

Further experiments could also be performed on the different architecture of structured supports for the improved temperature control in the different regions of structured catalysts. Structures with graded porosity were proposed for CO_2 methanation. The graded structures have a macro-porosity increasing from the edge to the centre of the structures. These structures are proposed in order to reduce hot-spots formation. The higher porosity in the middle of the structure (core of the reactor) provides lower catalyst loading, thus lower conversion of CO_2, and consequently lower temperature rise. Graded, multi-channel graded and spiral structures (Figure 6-1) were designed, manufactured and proposed to be used as alternative supports for CO_2 methanation. Preliminary experiments proved that graded structures could be a promising alternative: the measurements showed that at the average macro porosity of 66 %, graded structures exhibited a slightly higher pressure drop, however, higher CO_2 conversion compared to structures with ‘even’ porosity. Further investigations on graded structures by modelling studies are to be done for CO_2 methanation.

Figure 6-1. Graded (left), multi-channel graded (middle) and spiral (right) 3D-manufactured structures.

Therefore, high attention should be paid to a modelling study which will allow the exploration of the limitations of structured catalysts/reactors. The modelling of structured catalysts needs to take

into account the reaction kinetics and the properties of the catalysts/reactors. Therefore, structured catalysts can be designed and optimized considering the results of the modelling study. Designed structures can be manufactured by the 3DFD technique and integrated into reactors (milli- and micro-reactors, multi-channelled or plasma reactors) taking into account the requirements of the chemical processes. It is noteworthy that 3DFD structured catalysts can be used not only for gas phase reactions, but also for liquid-liquid and liquid-gas reactions for the production of valuable (fine) chemicals. The first promising results on hydrogenation and carbonylation of liquid substrates were obtained at VITO, and will be published soon.

Regarding the potential implementation of 3DFD structured catalysts in industry, it can be mentioned that a lot of work is currently being carried out on the scale-up of the 3DFD technology (e.g. using multi-nozzle or array-nozzle printers with higher printing speed and advanced process control). These developments along with longer catalyst life-time and higher efficiency will make 3DFD structured catalysts more commercially attractive and therefore a real alternative to existing conventional reactors.

Appendix A. Calculation of specific surface area, porosity and open frontal area

Figure A.1 shows a unit cell of a sample. Structures are anisotropic in z-direction due to the printing effect (stacking). Stacking factor *c* refers to a stacking length between two layers of fibres in the z-direction considering an anisotropic pore architecture. The stacking factor changes depending on paste composition, fibre thickness and inter-fibre distance. In this work, *c* factor of ~0.006 mm was determined from optical microscope (OM) images. Fibre diameter is $a = M - n$ (mm), *n* is inter-fibre distance (mm) and *M* is axial centre distance between two fibres (mm).

Specific surface area (SSA, $mm^2 \cdot mm^{-3}$) and macro-porosity (ε, %) of the 3DFD support were calculated using Equations A.8 and A.9, respectively. S_c is the loss of the surface area of two connected fibres (mm^2), S_f is the surface area of two fibres (mm^2), V_{cell} is the unit cell volume (mm^3), V_{fibre} is the fibre volume (mm^3) and *Vc* is the volume of the intersection of two fibres (mm^3) at the same fibre diameter. *Vc* is a function of *c*. Stacking factor *c* can be in the range of $0 \leq c \leq a$. In order to obtain continuous porous structures, $c \neq 0$ and $c = a$ are technically not possible. While c is $0 < c < a$, circular cone volume or elliptic cone volume can be assumed for the calculation of *Vc*. In this study circular cone volume was assumed for the porosity calculation of the structures.

The open frontal area (OFA, %) of 1-1 and 1-3 stacking structures was calculated by dividing their respective frontal open pore areas (n^2 and $(n-a)^2$) by using the frontal unit cell area (M^2).

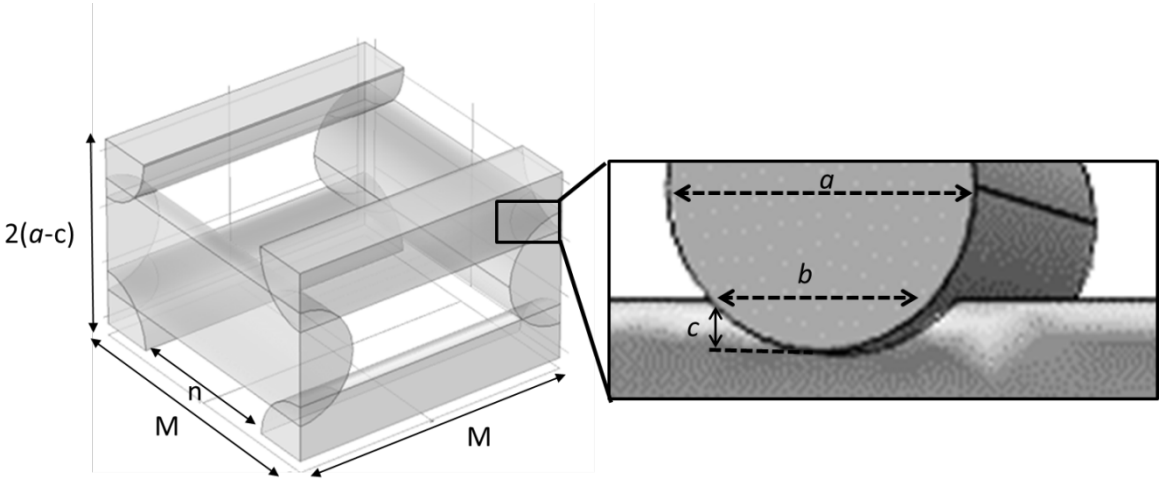

Figure A.1. A unit cell of a sample.

$$b = 2\sqrt{2ac - c^2}\ (mm) \qquad \text{Eq. (A.1)}$$

$$S_c = \frac{\pi\ a * b}{4}\ (mm^2) \qquad \text{Eq. (A.2)}$$

$$S_f = \pi M a\ (mm^2) \qquad \text{Eq. (A.3)}$$

$$V_{cell} = 2(a - c)M^2\ (mm^3) \qquad \text{Eq. (A.4)}$$

$$V_{fibre} = \frac{\pi M a^2}{4} \ (mm^3)$$ Eq. (A.5)

$$V_c = 2 * \pi * \left(\frac{b}{2}\right)^2 * \frac{c}{3} \ (mm^3)$$ Eq. (A.6)

$$SSA = \frac{2(S_f - 2S_c)}{V_{cell}} \ (mm^2 \cdot mm^{-3})$$ Eq. (A.7)

$$SSA = \frac{\pi a\left(M - \sqrt{2ac - c^2}\right)}{M^2(a - c)} \ (mm^2 \cdot mm^{-3})$$ Eq. (A.8)

$$Porosity = \left(1 - \frac{2(V_{fibre} - V_c)}{V_{cell}}\right) * 100 \ (\%)$$ Eq. (A.9)

$$OFA_{(1-1)stacking} = (\frac{n}{M})^2 * 100 \quad (\%)$$ Eq. (A.10)

$$OFA_{(1-3)stacking} = (\frac{n - a}{M})^2 * 100 \ (\%)$$ Eq. (A.11)

List of figures

List of tables

List of publications and conferences

Publications

Danaci S., Protasova L., Lefevere J., Bedel L., Guilet R., Marty P., Efficient CO_2 methanation over Ni/Al_2O_3 coated structured catalysts, Catal. Today. 273 (2016) 234–243.

Danaci S., Protasova L., Try R., Bengaouer A., Marty P., Experimental and numerical investigation of heat transport and hydrodynamic properties of 3D-structured catalytic supports, Appl. Therm. Eng. (2017), *in press.*

Danaci S., Protasova L., Snijkers F., Bouwen W., Bengaouer A., Marty P., Innovative 3D-manufacture of copper supports post-coated with catalytic material for CO_2 methanation, Chem. Eng. Process. (2017), *submitted.*

Middelkoop V., Slater T., Danaci S., Protasova L., Petit C., Onyenkeadi V., Burnett T., Saha B., Kellici S., Next frontiers in catalytic materials: 3D printed graphene supported nano-composite heterogeneous catalyst, ACS Catalysis. (2017), *to be submitted*.

Danaci S., Protasova L., Mertens M., Xin Q., Jouve M., Bengaouer A., Marty P., Structured catalysts for CO_2 methanation – A scale-up study, Appl. Catal. A Gen. (2017), *to be submitted*.

Patents

S. Danaci, L. Protasova, F. Snijkers, Devices for through-flow of fluids comprising graded porous structures, app. number: EP17163707.7 (29.03.2017).

Conferences

Poster, Ni/alumina structured catalysts for CO_2 methanation, I-SUP Conference, (2014), Antwerp, Belgium.

Poster, Ni/alumina structured catalysts for CO_2 methanation, CEOPS-EMR (European Materials Research Society), (2015), Lille, France.

Oral, Efficient 3D-structured catalysts for CO_2 methanation, ECCE10 conference, (2015), Nice, France.

Oral, Optimization and integration of catalytic porous structures for CO_2 methanation, NCCC 17th Conference, (2017), Noordwijkerhout, Netherlands.

Index